

2015

Reconstructing Past Variations in Erosion and Sediment Transport using Uranium-Series Isotopes

Ashley Neil Martin
University of Wollongong

Follow this and additional works at: <https://ro.uow.edu.au/theses>

University of Wollongong

Copyright Warning

You may print or download ONE copy of this document for the purpose of your own research or study. The University does not authorise you to copy, communicate or otherwise make available electronically to any other person any copyright material contained on this site.

You are reminded of the following: This work is copyright. Apart from any use permitted under the Copyright Act 1968, no part of this work may be reproduced by any process, nor may any other exclusive right be exercised, without the permission of the author. Copyright owners are entitled to take legal action against persons who infringe their copyright. A reproduction of material that is protected by copyright may be a copyright infringement. A court may impose penalties and award damages in relation to offences and infringements relating to copyright material.

Higher penalties may apply, and higher damages may be awarded, for offences and infringements involving the conversion of material into digital or electronic form.

Unless otherwise indicated, the views expressed in this thesis are those of the author and do not necessarily represent the views of the University of Wollongong.

Recommended Citation

Martin, Ashley Neil, Reconstructing Past Variations in Erosion and Sediment Transport using Uranium-Series Isotopes, Doctor of Philosophy thesis, School of Earth and Environmental Sciences, University of Wollongong, 2015. <https://ro.uow.edu.au/theses/4949>

Reconstructing Past Variations in Erosion and Sediment Transport using Uranium-Series Isotopes

A thesis submitted in partial fulfilment of the requirements for the degree of

Doctor of Philosophy

from

University of Wollongong

by

ASHLEY NEIL MARTIN MChem.

School of Earth and Environmental Sciences,

Faculty of Science Medicine and Health,

July 2015



I, Ashley Neil Martin, declare that this thesis, submitted in partial fulfilment of the requirements for the award of Doctor of Philosophy, in the School of Earth and Environmental Sciences, University of Wollongong, is wholly my own work unless otherwise referenced or acknowledged. The document has not been submitted for qualifications at any other academic institution.

Ashley Neil Martin

23 July 2015.

Table of contents

Table of contents	3
Table of figures	8
Table of tables	16
Abbreviations	20
Acknowledgements	21
Abstract	23
Thesis outline	25
1. Introduction	26
1.1 Background	26
1.2 Rates of sediment transport in hillslope and fluvial systems	28
1.2.1 Rates of denudation and regolith production	30
1.2.2 Hillslope transport	32
1.2.3 Fluvial transport	34
1.3 Comminution dating	37
1.3.1 Background theory	40
1.3.2 Comminution age equation	44
1.3.3 Sample pre-treatment	45
1.3.4 Direct-recoil fraction	47
1.3.5 Applications	54
1.3.6 Uncertainties	58
1.4 Study area	67
1.4.1 Climate	68
1.4.2 Hydrology	71
1.4.3 Catchments	71

1.4.4	Gulf palaeoenvironments	74
1.4.5	Palaeoclimate and past vegetation changes	74
1.5	References	78
2.	Evaluating the removal of non-detrital matter from soils and sediment using uranium isotopes	98
2.1	Abstract	99
2.2	Introduction	100
2.3	Conceptual model.....	103
2.4	Experimental methods and approach.....	106
2.5	Analytical techniques	111
2.6	Results	113
2.6.1	Uranium isotope and concentration measurements	113
2.6.2	Physical Analyses	120
2.7	Discussion	122
2.7.1	Validation of the methodology	122
2.7.2	The addition of a complexing agent.....	123
2.7.3	Mild HF/HCl etching procedure	124
2.7.4	Evaluation of other procedures	127
2.7.5	The effect of sequential extraction and etching procedures on the surface properties of soil	128
2.7.6	Calculated ages	129
2.8	Conclusions	130
	Acknowledgements.....	133
	References.....	133
3.	Controls on ($^{234}\text{U}/^{238}\text{U}$) in fine-grained sediments from the Gulf of Carpentaria, tropical northern Australia	140

Abstract	141
3.1 Introduction	142
3.2 Study area	146
3.3 Methods	152
3.3.1 Sample collection	152
3.3.2 Sample preparation and analytical techniques	154
3.3.3 Spatial Analysis	156
3.3.4 Statistical analyses	157
3.4 Results and discussion	158
3.4.1 Detrital uranium in river sediments	158
3.1.1 Geometric properties of detrital river sediments	164
3.1.2 Initial ($^{234}\text{U}/^{238}\text{U}$) activity ratio of source rocks	166
3.1.3 Direct-recoil fraction of ^{234}U in river sediments	172
3.1.4 Preferential leaching effects	175
3.1.5 Aeolian input	176
3.1.6 Sediment residence times in the Gulf of Carpentaria drainage basin	180
3.2 Conclusions	183
3.3 Acknowledgements	184
3.4 References	185
4. Late Quaternary sediment dynamics inferred from U isotope variations in tropical monsoonal Australia	199
Abstract	200
4.1 Introduction	201
4.2 Study area	203
4.2.1 Hydrology of the Gulf	203
4.2.2 Gulf of Carpentaria drainage basin	205
4.2.3 Palaeoclimate in northern Australia	207

4.3	Methods	209
4.3.1	Sampling and sample preparation	209
4.3.2	Analytical techniques	210
4.3.3	Depositional age chronology	211
4.4	Results	214
4.4.1	Uranium isotopes	214
4.4.2	Surface area measurements	219
4.5	Discussion	219
4.5.1	Grain size variations.....	219
4.5.2	Reduced direct-recoil of ^{234}U in core sediments	221
4.5.3	Comparison of two cores from the Gulf of Carpentaria	224
4.5.4	Comminution ages in the Gulf of Carpentaria	225
4.5.5	Variations in sediment provenance during glacial and inter-glacial periods	234
4.6	Conclusions and summary.....	242
	Acknowledgements.....	244
	References.....	245
5.	Summary and future perspectives.....	257
5.1	Sampling and sample pre-treatment	257
5.2	Initial activity ratio of the parent material	260
5.3	Sediment-routing system	262
5.4	Comminution dating of sedimentary deposits.....	263
5.4.1	Reduced direct recoil in core sediments	263
5.4.2	Past variations in sediment residence times	264
5.5	Future work	265
5.5.1	Initial activity ratio of the parent material	265
5.5.2	Sediment budgeting and comminution dating	267
5.5.3	Direct-recoil fraction.....	268

5.5.4	Aeolian input.....	268
5.6	Final conclusions.....	269
5.7	References.....	270
6.	Appendix A.....	275
6.1	Analytical techniques.....	275
6.1.1	Sample preparation.....	275
6.1.2	Sample weighing.....	276
6.1.3	Acid dissolution.....	277
6.1.4	Column chromatography.....	278
6.1.5	Mass spectrometry.....	280
6.1.6	Surface area analysis.....	282
6.2	Analytical data.....	287
6.2.1	Blanks data.....	287
6.2.2	Standard data.....	288
6.2.3	Chromatography.....	289
6.3	Field work.....	290
6.3.1	Fluvial sediment.....	291
6.3.2	Bedrock samples.....	307
6.4	Unreported experiments.....	312
6.4.1	Neodymium chromatography experiments.....	312
6.4.2	Sequential extraction experiments.....	313
6.5	Uranium measurements summary.....	317
	References.....	321
7.	Appendix B.....	325

Table of figures

Figure 1.1A) Sketch depicting the sediment residence time (T_{res}) of a hillslope section depicting the potential pathways of sediment particles (stars) from incipient bedrock weathering at t_0 , including the duration of regolith storage during soil production (T_1), and downhill creep (T_2); B) Sketch (oblique view) of the fluvial system depicting potential routes (dashed lines) of sediment particles including durations of fluvial transport (T_3), floodplain storage (T_4), and deltaic storage (T_5) (modified from Malmon et al., 2003).....	29
Figure 1.2 Schematic diagram of the direct ejection of ^{234}U (via the short-lived ^{234}Th) into the surrounding medium following the alpha decay of ^{238}U . The dark grey area represents the ^{234}U -depleted outer-rind of the detrital minerals. The light grey area represents the inner-core of the detrital minerals where loss by direct recoil does not occur, and $(^{234}\text{U}/^{238}\text{U}) = 1$. Figure modified from DePaolo et al. (2006).....	38
Figure 1.3 Evolution of the $(^{234}\text{U}/^{238}\text{U})$ in sediment grains as a function of time for: sand grains ($> 63\mu\text{m}$), silts ($2-63\mu\text{m}$), and clays ($<2\mu\text{m}$) (modified from DePaolo et al., 2006).	39
Figure 1.4 Analogy of the U-series decay chain represented by a series of buckets feeding into each other (modified from Bourdon et al., 2003). The size of the outlet in each bucket represents the decay constant of each nuclide, and the levels of each bucket represent the abundances of each nuclide. If the bucket of a daughter nuclide is emptied, the time required to refill the bucket to its original level depends upon the decay constant of the daughter nuclide.....	42
Figure 1.5 Modelled $(^{234}\text{U}/^{238}\text{U})$ activity ratio vs time resulting from the direct recoil of ^{234}U (via the short-lived ^{234}Th) with direct-recoil fractions of 0.2, 0.3 and 0.5 (modified from DePaolo et al. 2006).....	48

Figure 1.6 Schematic representation of (palaeo) sediment residence times from $t = 0$ at the soil-bedrock interface, including storage in the weathering profile, fluvial transport and sedimentary deposit. Circle sizes represent an idealised fluvial system in which sediment residence times increase linearly downstream. Applied to sedimentary deposits, depositional ages can be subtracted from comminution ages to calculate palaeo sediment residence times.

..... 55

Figure 1.7 Conceptual diagram depicting the different types of alpha recoil tracks where preferential leaching of ^{234}U nuclides (stars) could occur 1: direct-ejection; 2: Post-comminution implantation from adjacent grains; 3: leaching from pre-existing recoil tracks at time zero; and 4: recoil tracks located at a depth greater than 50 nm from the mineral surface (modified from Lee, 2009).

..... 60

Figure 1.8A) Initial loss of ^{234}U due to preferential leaching from type 3 recoil tracks, leading to an initial activity ratio of 0.98. B) Percentage difference between apparent comminution ages and true ages due to preferential leaching.

..... 63

Figure 1.9 Model of direct-recoil fraction varying linearly from 0.20 – 0.30 over 1000 ka, where error bars represent comminution ages subtracted from real ages.

..... 65

Figure 1.10A) The Gulf of Carpentaria showing delineated catchment areas, major fluvial channels and core locations (+); B) Sahul during Last Glacial Maximum (sea level: -125 m below present sea level) and where grey lines showing modern shorelines; and C) Regional setting showing key palaeoclimate study sites. The solid lines delineate catchment areas, and labelled dashed lines depict the -53 and -59 m isobaths.

..... 67

Figure 1.11 Total precipitation during the austral summer (DJF: December/January/February) and winter (JJA: June/July/August). Maps obtained using Climate Reanalyzer (<http://cci-reanalyzer.org>), Climate Change Institute, University of Maine, USA and the ERA-Interim dataset (1979-2015).

..... 70

Figure 2.1 The three domains present in soils and sediment in terms of their respective ($^{234}\text{U}/^{238}\text{U}$) activity ratios and the two scenarios for ^{234}U -depletion: 1) direct ejection of ^{234}U (via the short-lived ^{234}Th); and 2) preferential leaching of ^{234}U from alpha-recoil tracks which are embedded as a result of direct ejection of ^{234}U from adjacent grains.	101
Figure 2.2 The hypothetical progression of the ($^{234}\text{U}/^{238}\text{U}$) activity ratio of the solid residue during the removal of non-detrital matter from the detrital minerals (modified from Lee, 2009).	105
Figure 2.3A) ($^{234}\text{U}/^{238}\text{U}$) activity ratio of the solid residues; B) Percentage of U extracted in reagent solutions (relative to the amount of U in the untreated sample). All error bars represent 2σ internal standard error. Operationally-defined fractions are: exchangeable (F1), acid-soluble (F2), reducible (F3), oxidisable (F4) and refractory (F5). The error shown represents the 2σ internal standard error.	115
Figure 2.4A) ($^{234}\text{U}/^{238}\text{U}$) activity ratios of the solid residues following mild HF/HCl etching in Exp. 3 on the soil sample (diamonds), river sediment (filled circles), marine sediment (unfilled circles) and rock standard BCR-2 (squares); B) The percentage of U extracted in reagent solutions in Exp. 3 using the soil sample (relative to the amount of U in the untreated sample). All error bars represent 2σ internal standard error and most are hidden by the symbols.	117
Figure 2.5 Relative volume change as a function of particle size following: sequential extraction in Exp. 1, compared to the $<63\text{ }\mu\text{m}$ fraction of the untreated soil, and mild HF/HCl etching in Exp. 3 (24 h), compared to the particle-size distribution following sequential extraction in Exp. 1.	121
Figure 3.1A) Sketch depicting the sediment residence time (T_{res}) of a hillslope section depicting the potential pathways of sediment particles (stars) from incipient bedrock weathering, soil production, and creep during regolith storage (T_{regolith}); B) Sketch (oblique view) of the fluvial system depicting potential routes (dashed lines) of sediment particles	

during fluvial transport including alluvial storage (T_{alluvial}), and deltaic storage (T_{delta}) (modified from Malmon et al., 2003).	143
Figure 3.2. Spatial data for the Gulf of Carpentaria drainage basin including: A) Major channels (5 th order streams and above) and labelled drainage basins (areas shown in pink); B) Digital elevation model (Gallant et al., 2014) with labelled sediment sampling sites (yellow stars); C) Catchment lithology with labelled sampling sites of bedrock (black stars) (Raymond et al., 2012); and D) Mean annual rainfall (BOM, 2009).	148
Figure 3.3A) Bedrock outcrop sampled from the Flinders River catchment (B-6, 17°44.21'S 144°32.01'E); B) Mud drapes (R-12, Einasleigh River, 19°12.38'S 144°22.70'E); and C) Sediment sampled from a 100 m reach of a dry channel (R-18, Leichhardt River, 20°46.63'S 139°29.69'E).	153
Figure 3.4. Linear regression models of catchment area (A) vs mean discharge (Q) for the following basins (DNRM, 2014): Archer/Mitchell (ARC/MIT), Gilbert/Staaten/Norman (GIL/NOR), Flinders (FLI), Leichhardt (LEI) Rivers.	157
Figure 3.5 Box plot of ($^{234}\text{U}/^{238}\text{U}$) activity ratios (A) for <63 μm river sediments from the tropical monsoonal Gulf (this study), Murrumbidgee River in southeastern Australia (Dosseto et al., 2010), Flinders Ranges in semi-arid South Australia (Handley et al., 2013b), and Cooper Creek in arid central Australia (Handley et al., 2013a). Outliers (outside 1.5 times the interquartile range) are represented as open circles. Upper and lower limits represent the interquartile range.....	164
Figure 3.6 Surface roughness (λ) vs fractal dimension (D) for fluvial sediments from the Gulf of Carpentaria drainage basin	166
Figure 3.7 Bedrock sampling sites (stars) with the ($^{234}\text{U}/^{238}\text{U}$) activity ratio shown above. Solid black lines represent faults, dashed black lines represent concealed faults, red lines represent shear zones and the dashed red lines represent concealed shear zones. Geological data are derived from Raymond et al. (2012).	170

Figure 3.8 Direct-recoil fraction (f_a) as a function of mean grain diameter (d) for <63 μm sediments measured in this study, Site 984 (DePaolo et al., 2006), KRF: King River Fan (Lee et al., 2010), Dome C ice core in Antarctica (Aciego et al., 2011), and the Murrumbidgee River (Dosseto et al., 2010).	174
Figure 3.9 Box plot of specific surface area of sediments from the Gulf catchments where (in order from northeast to southwest) northeast: Archer River and Mitchell River, southeast: Staaten River and Gilbert River, and southwest: Norman River, Flinders River, and Leichhardt River.	178
Figure 3.10 Sediment residence times as a function of catchment area in the Gulf of Carpentaria drainage basin.	183
Figure 4.1A) The Gulf of Carpentaria with delineated catchment areas (red curves), major fluvial channels (blue lines), and core locations (+ symbols) shown; B) Sahul during Last Glacial Maximum when sea level was -125 m bpsl and where grey lines show modern shorelines; and C) Regional setting showing key palaeoclimate study sites. In all figures, the red line represents the Gulf of Carpentaria catchment area, and labelled dashed lines depict the -53 and -59 m contour lines.	205
Figure 4.2A) Age-depth model for the Gulf of Carpentaria cores A) MD32 and B) MD33. The depositional ages are from Reeves et al. (2008) (\blacklozenge), inferred depositional ages from the palaeo environmental record (\diamond), and stratigraphic units (<i>italics</i>). Error bars not shown are hidden by markers.	213
Figure 4.3 Uranium isotope data, sedimentation rates for cores MD32 and MD33 from the Gulf of Carpentaria. Gulf level represents the maximum water depth in the Gulf of Carpentaria. Particle size distribution and surface area data for core MD32.	217
Figure 4.4 Mean diameter of MD32 core sediments as a function of the ($^{234}\text{U}/^{238}\text{U}$) activity ratio (errors not shown are within the marker size).	220

Figure 4.5a) Specific surface area, b) fractal dimension of <63 μm sediments, and c) total pore volume as a function of depth in core MD32. Errors not shown are within the symbol size.	224
Figure 4.6 ($^{234}\text{U}/^{238}\text{U}$) as a function of the ^{234}U decay rate (in a^{-1}) and the depositional age (in ka) for the MD32 core sediments.....	230
Figure 4.7 Modelled ($^{234}\text{U}/^{238}\text{U}$) activity ratios of sediments deposited in the Gulf as a function of the relative contribution of the south (S) catchments.....	239
Figure 4.8 Predicted discharge of the southern (S) catchments relative to the modern discharge based on the ($^{234}\text{U}/^{238}\text{U}$) activity ratios of sediments deposited in MD32 and Equation 6. Only order of magnitude changes in relative palaeodischarge are considered due to large uncertainty in palaeodischarge estimates.....	240
Figure 6.1 Various types of physiosorption isotherms.	284
Figure 6.2 Upstream (A) and downstream (B) views from sample point for R-01	293
Figure 6.3 Downstream (A) upstream (B) views of McLeod River for wet sample R-02. Downstream (C) and upstream (D).....	294
Figure 6.4	295
Figure 6.5 Downstream (A) and upstream (B) views for the Palmer River (R-04).....	295
Figure 6.6	296
Figure 6.7 Downstream and B: Upstream.....	297
Figure 6.8 A: Upstream B: Downstream	297
Figure 6.9 Upstream (A) and downstream (B) views of sample location for GOC-R-8.	298
Figure 6.10 Upstream (A) and downstream (B) views of sample location for GOC-R-9... ..	298
Figure 6.11	299

Figure 6.12 Upstream (A) and downstream (B) views of sample location for GOC-R-11.	300
Figure 6.13 Upstream (A) and downstream (B) views of sample location for GOC-R-16.	300
Figure 6.14 Upstream (A) and downstream (B) views of sample location for GOC-R-13.	301
Figure 6.15 Sediment sampled from silt dried on the top of boulders.....	302
Figure 6.16 Upstream (A) and downstream (B) views of sample location for GOC-R-14.	302
Figure 6.17 Upstream (A) and downstream (B) views of sample location for GOC-R-16W.	
C) Sample point for muddy “gully deposits” for “GOC-R-15E; and d) Side-view of “gully”.	
.....	303
Figure 6.18 Upstream (A) and downstream (B) views of sample location for GOC-R-16.	304
Figure 6.19 A) Upstream view of sample location for GOC-R-17; B) Filled sample bag and typical example of sampled sediment for GOC-R-17.....	304
Figure 6.20 Upstream (A) and downstream (B) views of sample location for GOC-R-18.	305
Figure 6.21A) Upstream view of sample location for GOC-R-19; B) Filled sample bag and typical example of sampled sediment for GOC-R-19.....	306
Figure 6.22A) Upstream view of sample location for GOC-R-20; B) Filled sample bag and typical example of sampled sediment for GOC-R-20.....	306
Figure 6.23A) Sampling point of GOC-B-1 from boulder shown by yellow notebook; B) Side-view of sample location for GOC-B-1	308
Figure 6.24 Sampling point of GOC-B-2 from boulder shown by yellow notebook; B) Side- view of sample location for GOC-B-2.....	308
Figure 6.25 Sampling point of GOC-B-5 from road cut shown by yellow notebook; B) Side- view of sample location for GOC-B-5	309
Figure 6.26 Sampling point of GOC-B-6 from outcrop shown by yellow notebook.	310

Figure 6.27 Sampling point of GOC-B-10 from road cut shown by yellow notebook; B) Side-view of sample location for GOC-B-10	310
Figure 6.28 Sampled rock for GOC-B-1; B) Side-view of sample location for GOC-B-01, as shown by the hammer.	311
Figure 6.29 Sampling point of GOC-B-22 from road cut shown by yellow notebook; B) Side-view of sample location for GOC-B-22 shown by hammer.....	311
Figure 6.30 Percentage of U extracted into solution as a function of reaction time using the following reagents: A) NaOAc at 6, 8, 10 and 24 h; B) $\text{NH}_2\text{OH}\cdot\text{HCl}$ at 5, 8, 10 and 24 h; C) $\text{H}_2\text{O}_2/\text{HNO}_3$ at 1, 2 and 3 h; D) $\text{H}_2\text{O}_2/\text{HNO}_3$ at 3, 4 and 5 h. The error bars represent 1σ standard deviation and where not shown, are hidden by the markers.	316

Table of tables

Table 1.1 Recoil ranges calculated from LSS theory (Hashimoto et al., 1985; Dosseto and Schaller, 2016)	50
Table 2.1 Reagents and conditions used in the sequential extraction procedures developed by Tessier et al. (1979) and Schultz et al. (1998).	108
Table 2.2 ($^{234}\text{U}/^{238}\text{U}$) activity ratio, and U concentration of the untreated soil (< 63 μm fraction).....	113
Table 2.3 ($^{234}\text{U}/^{238}\text{U}$) activity ratio of rock standard BCR-2 following leaching experiments	117
Table 2.4 ($^{234}\text{U}/^{238}\text{U}$) activity ratios and the cumulative percentage of U extracted (relative to the amount of U in the untreated soil) in Experiments 1 – 7.	119
Table 2.5 Amount of mass removed per gram of soil in Experiments 1, 2, 4, and 5.	120
Table 2.6 Particle size and surface area properties of the <63 μm fraction of the untreated soil sample, and following Experiments 1, 3 and 4.	122
Table 2.7 Recommended sample pre-treatment procedure.....	126
Table 2.8 Comminution ages calculated following the various sample pre-treatment procedures.	130
Table 2.9 Recommended sample pre-treatment procedure for comminution dating.....	132
Table 3.1 Morphometric parameters for each sub-catchment: catchment area (A), average slope, mean annual rainfall (P), discharge (Q), and lithology.	151
Table 3.2. U concentration, U isotope, surface area, mineralogy, and particle size data for <63 μm river sediments.	161

Table 3.3 Pearson's correlation matrix ^a for measured parameters for <63 µm river sediments	162
Table 3.4 U isotope and concentration data for <63 µm river sediments from the northern and southern catchments draining to the Gulf of Carpentaria	163
Table 3.5 The (²³⁴ U/ ²³⁸ U) activity ratios of bedrock samples	169
Table 3.6 Bootstrap results for measured initial activity ratios of bedrock samples ^a	172
Table 3.7 Average (²³⁴ U/ ²³⁸ U) activity ratios of bedrock samples.....	172
Table 3.8 Recoil lengths for typical minerals/mineral groups.....	174
Table 3.9 The <63µm river sediments from the Gulf of Carpentaria drainage basin for which the (²³⁴ U/ ²³⁸ U) activity ratios (<i>A</i>) could not be accounted for by the direct-recoil fraction (<i>f_a</i>)	175
Table 3.10 Reported leaching coefficients (<i>w</i> ₂₃₈) for ²³⁸ U in tropical watersheds.....	176
Table 3.11 Relative contribution of denudation vs aeolian deposition to sediments in the Gulf of Carpentaria drainage basin	179
Table 3.12 Comminution age parameters and associated uncertainties for river sediment GOC-R-7.....	182
Table 3.13 The average residence time of <63 µm sediment in catchments draining to the Gulf of Carpentaria	182
Table 4.1 U and surface area measurements for <63 µm detrital core sediments from the Gulf of Carpentaria	218
Table 4.2 Statistical summary of (²³⁴ U/ ²³⁸ U) activity ratios and mean grain size for cores MD32 and MD33	225
Table 4.3 Reported leaching coefficients (<i>w</i> ₂₃₈) for ²³⁸ U in tropical watersheds.....	226

Table 4.4 Estimated initial activity ratio of source rocks in the Gulf of Carpentaria drainage basin during glacial vs interglacial periods.....	228
Table 4.5 Comminution age parameter uncertainties for core sediment MD32-6d	233
Table 4.6 Sediment residence times for <63 µm sediments from core MD32 during interglacial periods in the Gulf of Carpentaria	233
Table 4.7 Average sediment residence time of catchments in the Gulf of Carpentaria drainage basin (Chapter 3).....	234
Table 4.8 Average ($^{234}\text{U}/^{238}\text{U}$) activity ratios and U concentrations for <63 µm sediments from the northern and southern catchments draining to the Gulf.....	235
Table 4.9 Sediment yield and input parameters, and mass balance mixing factors.....	237
Table 4.10 Predicted ($^{234}\text{U}/^{238}\text{U}$) in the Gulf as a function of the discharge of the northern (N) and southern (S) catchments relative to present.....	239
Table 5.1 Recommended sample pre-treatment procedure for comminution dating.....	260
Table 5.2 The ($^{234}\text{U}/^{238}\text{U}$) activity ratios of bedrock samples	266
Table 6.1 Sequential extraction procedure from Lee (2009) where the operationally-defined fractions are F0: water soluble F1: exchangeable, F2: acid soluble, F3: reducible, and F4: oxidisable.	276
Table 6.2 Column chromatography used to separate U, which is modified from Luo et al. (1997).....	279
Table 6.3 Amount of U in total procedure blanks	288
Table 6.4 ($^{234}\text{U}/^{238}\text{U}$) of rock standards shown with 2σ standard error.....	289
Table 6.5 Percentage of U, Th, and Nd eluted in each fraction.....	290
Table 6.6 Fluvial sediment samples collected	292

Table 6.7 Fieldwork numbers are corresponding sample numbers used in Chapter 3.	307
Table 6.8 ($^{234}\text{U}/^{238}\text{U}$) activity ratios and U concentrations for all samples from Chapter 2	318
Table 6.9 ($^{234}\text{U}/^{238}\text{U}$) activity ratios and U concentrations for all samples from Chapter 3	319
Table 6.10 ($^{234}\text{U}/^{238}\text{U}$) activity ratios and U concentrations for all samples from Chapter 4	
.....	320

Abbreviations

$(^{234}\text{U}/^{238}\text{U})$

$^{234}\text{U}/^{238}\text{U}$ activity ratio

λ_{234}

^{234}U decay constant

$t_{1/2}$

Half life

f_{α}

Direct-recoil fraction

BET

Brunauer–Emmett–Teller theory

S_{BET}

BET specific surface area

S_{geo}

Geometric surface area

D

Fractal Dimension

λ

Surface roughness

Acknowledgements

I would like to take this opportunity to acknowledge and thank the people who have contributed to the completion of this PhD thesis. Above all, I would like to thank my parents for teaching me to read and write, and more importantly – supporting me in whatever I have chosen to do. Thanks also to my sister Rebekah for supporting me throughout.

I would first like to thank my principal supervisor A/Prof. Dr. Anthony Dosseto for providing the opportunity for me to carry out a PhD, and his significant role in my development as an isotope geochemist. Thanks also to Prof. Allan Chivas for introducing me to my study area, the Gulf of Carpentaria, providing samples and assisting with field work – I have learned much from his rigorous scientific and grammatical insights. Thanks to Dr. Jan-Hendrik “Henne” May for providing positive inspiration in harder times and for helping me to open the black box of GIS. Although no longer a co-supervisor, Dr. Maxime Aubert is thanked for his early contributions to my PhD before continuing his career at another university. Dr. John Jansen is thanked for his geomorphic expertise and guidance. Dr. Chris Richardson, Dr. Lili Yu and Les Kinsley are thanked for providing technical expertise.

Davide Menozzi is thanked for accompanying me as a friend, fellow PhD student and an office mate for over three years. Thanks also to fellow PhD students at the University of Wollongong for sharing this experience. Finally, thanks to the ANZGG 2012 and INQUA ECR 2013 conferences for providing the opportunity to meet Monika Markowska who has since become my best friend and partner.

Funding for this thesis was provided by a postgraduate scholarship to myself, and an Australian Research Council (ARC) Future Fellowship grant No. FT0990447 to Anthony Dosseto, and an ARC Discovery Grant No. DP1093708 to Anthony Dosseto and Allan Chivas.

“It is better to be lucky. But I would rather be exact. Then when luck comes you are ready.”

Ernest Hemingway (1952), *The Old Man and the Sea*

...but as this is a scientific thesis, the quote which should be attributed to the first source:

“Chance favours the prepared mind.”

Louis Pasteur (1854), Lecture at the University of Lille

Abstract

Uranium-series (U-series) isotopes are fractionated in soils, sediments and natural waters by erosion and weathering processes. Recent applications of U-series isotopes to sedimentary deposits have enabled the landscape response to glacial-interglacial climate change to be studied. This thesis focuses on the developing *comminution dating* (or the *comminution age*) technique that utilises U isotopes to constrain the time elapsed since mineral grains were reduced to ca. $<63\ \mu\text{m}$ in size. Applied to hillslope and fluvial systems, the comminution age represents the *sediment residence time*, and applied to sedimentary deposits of known depositional age, the *palaeo sediment residence time* can be constrained.

Non-detrital matter e.g. carbonates, organic matter, and clay minerals must be removed to isolate detrital minerals and calculate accurate comminution ages. In Chapter 2, existing sample pre-treatment methods were evaluated by monitoring the ($^{234}\text{U}/^{238}\text{U}$) activity ratio (where parentheses denote activity ratio) and using a novel mild HF/HCl etching procedure. This further decreased the activity ratio of soil and sediment samples following sequential extraction, indicating that removal of non-detrital matter was incomplete. Particle-size distribution measurements indicate that the decrease in the ($^{234}\text{U}/^{238}\text{U}$) was likely due to the dissolution of clay minerals. Although tests on a rock standard revealed a small amount of preferential leaching of ^{234}U ($<1\%$), an additional mild HF/HCl etch following sequential extraction is recommended for comminution dating studies.

In Chapter 3, the ($^{234}\text{U}/^{238}\text{U}$) and surface area properties of the $<63\ \mu\text{m}$ detrital fraction of river sediments from seven large catchments in the Gulf of Carpentaria drainage basin, northern Australia were measured to infer comminution ages. Bedrock outcrops in the upper catchments were sampled to test the assumption that the parent material is in secular equilibrium where ($^{234}\text{U}/^{238}\text{U}$) = 1. Rocks were generally depleted in ^{234}U , and there was a

general trend between bedrock grain size and ($^{234}\text{U}/^{238}\text{U}$). This suggests that loss of ^{234}U by direct-recoil processes may occur in bedrock as well as in sediment, but a larger database of different rock types is required to confirm this hypothesis. Considerations of mass fluxes estimated that the aeolian fraction of sediments could be up to 24%. Thus, sediment residence times in our study area are considered to represent fluvial-aeolian processes. Finally, inferred sediment residence times in catchments ranged from <1 to 190 ± 80 ka. The average sediment residence time was 88 ± 35 ka, suggesting that catchments may be currently reworking of sediment that was accumulated over the last glacial cycle, which was a period of reduced rainfall and fluvial activity in N Australia. This highlights that the long duration of sedimentary storage in large, low-relief shield basins.

In Chapter 4, comminution dating was applied to two sedimentary cores from the Gulf of Carpentaria in northern Australia, spanning the past 120 ka. Past variations in sediment residence times are expected to result from past changes in the strength of the Indo-Australian monsoon. The ($^{234}\text{U}/^{238}\text{U}$) were low during Marine Isotope Stage (MIS) 5 and MIS 1, but higher throughout much of MIS 2 to 4. In addition, many sediments deposited during glacial periods remained close to secular equilibrium. Lower ($^{234}\text{U}/^{238}\text{U}$) were then recorded following the termination of the Last Glacial Maximum (LGM) from around 20 ka onwards to present. The average inferred sediment residence time during MIS 5 and post-LGM was 41 ± 18 ka. However, residence times could not be calculated for sediments deposited during glacial periods due to their lack of ^{234}U depletion, suggesting rapid sediment transport. Based on the ($^{234}\text{U}/^{238}\text{U}$) and U concentrations of river sediments measured in Chapter 3, variations in the ($^{234}\text{U}/^{238}\text{U}$) of core sediments were interpreted to represent variations in sediment provenance between the N and S catchments due to the north/southwards migration of the Indo-Australian monsoon. This suggests that rather than perturb net erosion rates, Late Quaternary climate change in N Australia may simply reorganise the spatial distribution of discharge and sediment provenance.

Thesis outline

Chapter 1 introduces the general context of the thesis in Section 1.1, and reviews the application of geochronological techniques for constraining the rates and timescales of Earth-surface processes in Section 1.2. Section 1.3 introduces the background theory and models for the behavior of the uranium-series nuclides at the Earth's surface. Following this, the general theory, measured parameters, and applications of comminution dating are discussed in Section 1.3. Finally, the study area for Chapters 3 and 4 is introduced in Section 1.4.

In Chapter 2, sample pre-treatment methods for the comminution dating technique were evaluated using the ($^{234}\text{U}/^{238}\text{U}$) activity ratio and a novel mild HF/HCl etching procedure. In Chapter 3, sediment residence times inferred by comminution dating were assessed in seven large catchments from the Gulf of Carpentaria drainage basin, northern Australia. In addition, near-surface bedrock samples were collected to test the assumption that the parent material is in *secular equilibrium* whereby ($^{234}\text{U}/^{238}\text{U}$) = 1. In Chapter 4, comminution dating was applied to sedimentary deposits from the Gulf of Carpentaria, northern Australia to assess how past variations in climate affected sediment transport.

In Chapter 5, the main findings and conclusions from Chapters 2, 3 and 4 are summarised and future perspectives for the comminution dating technique are discussed.

Appendix A contains a description of analytical techniques and data in Section A.1, and Section A.2 contains additional data that were not reported in Chapters 2, 3 and 4. Appendix B contains the published manuscript of Chapter 2: Martin, A.N., Dosseto, A., Kinsley, L.P.J., 2015. Evaluating the removal of non-detrital matter from soils and sediment using uranium isotopes. *Chemical Geology* 396, 124-133.

1. Introduction

1.1 Background

Chemical weathering of silicate minerals removes carbon dioxide (CO₂) from the atmosphere by forming carbonate minerals that ultimately store CO₂ in sedimentary deposits (Berner et al., 1983). The amount of atmospheric CO₂ depends on the balance between the rate of organic carbon oxidation during physical weathering (Hilton et al., 2014; Hilton et al., 2011), the rate of chemical weathering reactions, and the timescales of sediment transport processes. Chemical weathering rates are well studied (Kump et al., 2000; Raymo and Ruddiman, 1992; West et al., 2005), but the timescales of sediment transport are poorly constrained. Modelling approaches suggest that the duration of temporary sediment storage in large fluvial systems could be up to 1 Ma (Castelltort and Van Den Driessche, 2003; Métivier and Gaudemer, 1999). If weathering continues during intervals of temporary storage, this will affect the rate of global CO₂ drawdown (Bouchez et al., 2012). Long durations of sediment transport in large fluvial systems may explain the relatively stable silicate weathering flux throughout the Late Quaternary (Willenbring and von Blanckenburg, 2010; von Blanckenburg et al., 2015). This is because the duration of sediment transport in large fluvial system may be much greater than the timescale of glacial-interglacial climate change, and large catchments may be buffered to such changes (Allen, 2008). Thus, empirical measurements of the duration of sediment transport are required to test modelling predictions to improve our understanding of the global carbon cycle.

Recent anthropogenic impacts also threaten to disrupt the current balance of processes operating Earth-surface; for instance, agriculture and land clearing have increased soil erosion rates by orders of magnitude (Montgomery, 2007), and dams have restricted sediment transport from the continents to the oceans, increasing the risk of coastal erosion in

many areas (Syvitski et al., 2005). In addition, the effects of potential climate change on erosional and sediment transport processes remain largely unknown. By constraining past variations in the rates and timescales of Earth-surface processes, it is possible to construct a baseline with which to reference modern landscape perturbations.

The residence time of sediment, i.e. *sediment residence time*, is a key parameter in large hillslope-fluvial systems that integrates storage in the regolith, hillslope, fluvial channel and alluvial deposits (Malmon et al., 2003). This thesis aims to develop an innovative geochronological technique known as *comminution dating* or *comminution age* technique (DePaolo et al., 2006), which can be used to constrain the sediment residence time. Current knowledge of the rates and timescales of sediment production and transport are summarised in Section 1.2. The background theory and applications of comminution dating are given in Section 1.3. The study area for Chapters 3 and 4, Gulf of Carpentaria in northern Australia, is then introduced in Section 1.4.

1.2 Rates of sediment transport in hillslope and fluvial systems

The fluvial system can be classified into three idealised subsystems: the erosion, transfer and sedimentation zones (Schumm, 1977). The erosion zone ideally represents the catchment headwaters and considers the transport of sediment from hillslopes to fluvial channels. Sediment residence times in this zone are dependent upon the rates of regolith production, and downslope hillslope transport, i.e. creep (Figure 1.1A). In the transfer zone, sediment is transported downstream from the catchment headwaters to the sedimentation zone. Sediment residence times also depend on the duration of storage in alluvial deposits, such as floodplains, channels bars, and the valley floor (Figure 1.1B). In the sedimentation zone, sediment residence times are controlled by the duration of deltaic storage that results from lateral channel migration. In an ideal system, sediment residence times should increase linearly from the erosion zone to the sedimentation zone. Recently developed geochronological techniques such as cosmogenic nuclides and uranium-series (U-series) isotopes have enabled the rates of erosional and sediment transport processes to be quantified. These are discussed in Sections 1.2.1, 1.2.2, and 1.2.3, respectively.

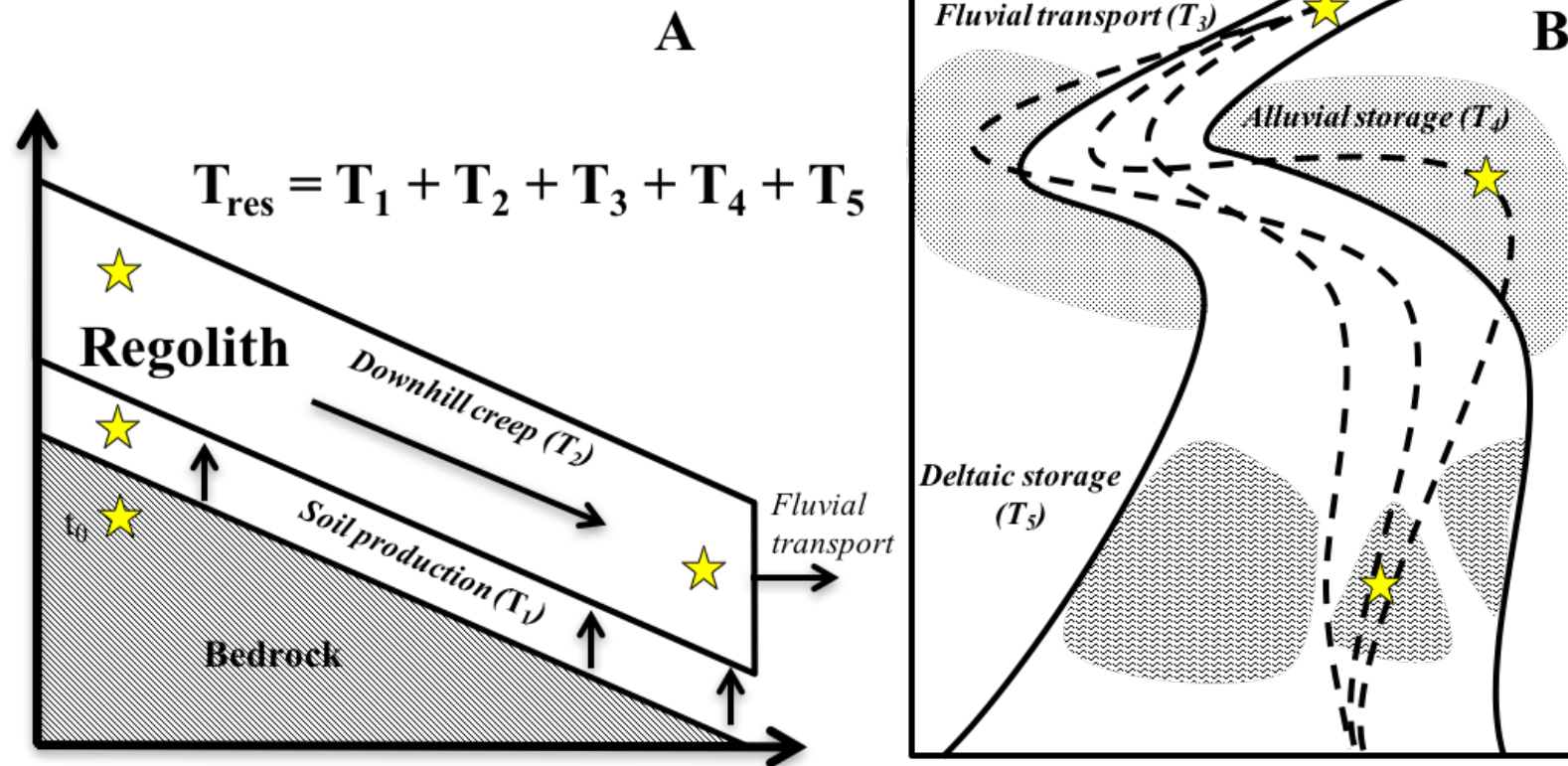


Figure 1.1A) Sketch depicting the sediment residence time (T_{res}) of a hillslope section depicting the potential pathways of sediment particles (stars) from incipient bedrock weathering at t_0 , including the duration of regolith storage during soil production (T_1), and downhill creep (T_2); B) Sketch (oblique view) of the fluvial system depicting potential routes (dashed lines) of sediment particles including durations of fluvial transport (T_3), floodplain storage (T_4), and deltaic storage (T_5) (modified from Malmon et al., 2003).

1.2.1 Rates of denudation and regolith production

The residence time of sediment in the weathering profile is dependent on the duration of regolith storage during soil production from bedrock and downhill creep (T_1 and T_2 , Figure 1.1A). Therefore, the duration of regolith storage is expected to be a function of the rate surface lowering by denudation. Denudation represents surface lowering caused by erosion and mass wasting processes. The rate of denudation can be measured by *in-situ* cosmogenic nuclide, e.g. ^{10}Be , ^{26}Al and ^{21}Ne , which are formed by cosmic radiation and typically measured in quartz grains (Lal, 1991; Portenga and Bierman, 2011; Willenbring et al., 2013). Denudation rates rely on estimating the production rate of cosmogenic nuclides in minerals (Lal, 1991), which are dependent on depth below Earth's surface, elevation and latitude. By assuming *steady-state erosion* whereby the rate of denudation is constant over millennial timescales, cosmogenic nuclide concentrations in bedrock samples can be related to production rates to calculate denudation rates. Applied to sediment samples, this method can be used to infer average catchment-wide denudation rates (Bierman and Steig, 1995).

Denudation rates are controlled by slope to a first-order approximation (Willenbring et al., 2013), but this relationship is complicated due to local variables, such as catchment lithology and climate. Changes in climate have little effect on denudation rates, unless erosion is increased by glaciation (Riebe et al., 2001). Global denudation rates may have rapidly increased since ~2 Ma due to periodic Quaternary glaciations (Herman et al., 2013). However, these data may be biased by the analytical limitations of thermochronometry, namely that slow exhumation rates are harder to measure in younger rocks.

Denudation rates derived from cosmogenic nuclide concentrations can also be used to calculate regolith production rates by assuming that the regolith thickness is in steady-state (Heimsath et al., 1997). This is applicable in regolith-mantled landscapes where there is a relationship between soil thickness and curvature (Dietrich et al., 1995). This approach

provides quantitative evidence to show that the regolith production rates decline exponentially with increasing soil thickness, known as the *soil production function* (Heimsath et al., 1997). In some cases, regolith production rates reach a maximum at a certain soil thickness and display a “humped” profile, for instance, in Arnhem Land in northern Australia (Heimsath et al., 2009). Another method for constraining regolith production rates is by measuring cosmogenic meteoric ^{10}Be concentrations, which accumulates in the regolith from precipitation and fallout. Meteoric ^{10}Be measurements at ridgetop soils in the Susquehanna Shale Hills Critical Zone Observatory in PA, USA indicate minimum regolith residence times from 9 – 11 ka (West et al., 2013).

Regolith production rates and timescales can also be estimated using U-series isotopes, which measure the time elapsed since the onset of physical or chemical weathering at the soil-bedrock interface (Bourdon et al., 2003; Chabaux et al., 2003; Dosseto, 2014), and do not require steady state soil thickness to be assumed. Studies of granitic lithologies from Brazil, Burkina Faso, and Australia indicate that there is a weak relationship between regolith production rates and climate (Dequincey et al., 2002; Dosseto et al., 2008b; Mathieu et al., 1995). This is consistent with the weak relationship between climate and denudation rates measured by cosmogenic nuclides (Riebe et al., 2001). Lithology has been quantitatively shown to be a more important control as regolith production rates in Puerto Rico were three times greater for a volcanic lithology, compared to a granitic lithology (Dosseto et al., 2012; Dosseto et al., 2007). Soil production rates of ridgetop soils in Susquehanna Shale Hills Critical Zone Observatory were $40 - 45 \text{ m Ma}^{-1}$, which equates to residence times of 11 – 13 ka (Ma et al., 2013). Interestingly, these residence times inferred by U-series isotopes were similar to estimates from meteoric ^{10}Be measurements (West et al., 2013). Based on current understanding of rates of soil production and denudation, short sediment residence times are expected in areas that are high-relief, glaciated, and/or volcanic lithologies.

1.2.2 Hillslope transport

Regolith produced from the bedrock is transported down hillslopes in a process termed *creep* (Figure 1.1A) (Carson and Kirkby, 1972). Creep is a diffusive process that is proportional to the hillslope gradient (Carson and Kirkby, 1970; Dietrich, 1995). The rate of creep is also depth-dependent as it is controlled by vertical mixing processes, such as bioturbation and tree-throw (Heimsath et al., 2002). However, a linear diffusion transport may only be applicable for areas with low relief since landslides dominate in weathering-limited landscapes with steeper terrain. The rate of hillslope transport in landslide-prone regions depends on the depth of landslide event since deeper landslides, which involve bedrock failure, transport larger volumes of material than shallow landslides (Larsen et al., 2010). Frequent (deep and shallow) landslides on steep hillslopes thus erode at fast rates and short hillslope residence times are expected in these regions.

In-situ cosmogenic nuclides quantitatively show that the diffusive rate of hillslope transport/creep is dependent on slope (Heimsath et al., 2002). Hillslope residence times are therefore expected to be inversely proportional to slope, similar to regolith production rates. In low-relief environments, such as desert piedmonts, sediment transport rates are slow and sediment grains can remain on the piedmont slope for timescales >10 ka (Nichols et al., 2002).

The timescales of hillslope transport can also be constrained by measuring meteoric ^{10}Be , which accumulates on hillslopes from precipitation (Pavich et al., 1986). This approach shows long hillslope residence times of 1 – 5 Ma in the Appalachian Mountains, USA (Pavich, 1989). Meteoric ^{10}Be measurements can be coupled with mineral-derived ^9Be measurements to provide more accurate constraints on the rate of hillslope transport. This is because the $^{10}\text{Be}/^9\text{Be}$ ratio combines a tracer of known flux to Earth's surface (^{10}Be) with a tracer that is dependent the weathering rate release from rocks (von Blanckenburg et al.,

2012). This approach was applied to the same study area as Pavich (1989) to derive similar hillslope residence times of 1 – 3 Ma (Bacon et al., 2012). In the Susquehanna Shale Hills Critical Zone Observatory, slow hillslope transport rates of 2 m ka^{-1} were inferred (West et al., 2013), indicating hillslope residence timescales of ca. 10 ka.

The timescales of hillslope transport can also be estimated using U-series isotopes by comparing the residence times of soils in catchment headwaters and fluvial channels. Long hillslope residence times of ca. 200 ka are inferred for the Murrumbidgee River in southeastern Australia (Suresh et al., 2014). Sediment residence times of 300 – 2,000 ka in a small catchment in southeastern Australia were also attributed to long hillslope residence times (Dosseto et al., 2014). In contrast, short residence times of 5 ka are inferred for fluvial sediment from small catchments in Puerto Rico. However, the studied weathering profiles in Puerto Rico are $>3 \text{ m}$ in depth, and residence times of 5 ka imply erosion rates of $>600 \text{ mm ka}^{-1}$, which is 6 – 12 greater than regolith production rates determined from cosmogenic nuclides (Brown et al., 1995; Riebe et al., 2003). To account for this, it was suggested that landslides in Puerto Rico mobilise sediment from deep in the weathering profile, and “bypass” sediment transport in the weathering profile, leading to shorter residence times.

Both U-series and meteoric ^{10}Be approaches show that hillslope residence times are generally 200 – 3,000 ka in temperate, transport-limited environments. However, this does not appear to be the case for a transport-limited environment with active landslides, e.g. Puerto Rico. Further studies are required to quantify the timescales of hillslope transport. In particular, studies are required to investigate the effect of hillslope-channel connectivity on sediment residence times.

1.2.3 Fluvial transport

In the transfer zone of the fluvial system, sediment residence times are dependent upon the duration of alluvial storage. Sediment is stored at the base of hillslopes (colluvium) and alluvial deposits, such as valley floors, point bars, channel floors, and floodplains (Dietrich et al., 1982; Reneau et al., 1990). The amount of sediment stored in alluvial deposits commonly exceeds the sediment load (Trimble, 1977; Walling, 1983), and long sediment residence times are likely.

Sediment budgets are typically used to assess sediment transport, but there is a discrepancy between erosion rates and sediment yields at catchment outlets, which has been termed *the sediment delivery problem* (Walling, 1983). This is explained by sediment storage in a catchment as outlined above. In addition, sediment budget approaches suffers from spatial and temporal clumping (Walling, 1983). Spatial clumping results from point measurements in a catchment that do not properly represent catchment-wide processes outlined above. Temporal clumping results from the timescales of measurements that typically only span a few decades at most, and are not sufficiently long to capture long-term variability.

Radionuclides (e.g. ^7Be , ^{137}Cs and ^{210}Pb) are present in the atmosphere due to post-1950s nuclear weapons testing and nuclear power accidents (Jones, 1981). When these fallout from the atmosphere onto Earth's surface, *fallout radionuclides* can be used to constrain short-term (<100 a) sediment transport and erosion rates (Ritchie et al., 1974; Wallbrink and Murray, 1993). As sediment eroded from the upper surface will contain a higher concentration of fallout radionuclides compared to sub-surface material, denudation and sediment transport rates can be derived. This was verified by showing that recently-eroded alluvial gullies have low concentrations of fallout radionuclides (Olley et al., 1993).

In mountainous regions, fallout radionuclides show that once entering high gradient streams, suspended sediment is transported tens of kilometres within less than a decade (Bonniwell et

al., 1999). However in large, low gradient systems, such as the Mississippi River, the majority of sediment did not contain fallout radionuclides (Scott et al., 1985). This is due to the increased alluvial storage capacity in large catchments, and the majority of sediment being derived from alluvial reworking. This provides further evidence of significant alluvial storage in large fluvial systems.

Dating techniques such as optically stimulated luminescence and thermo-luminescence can estimate the age of deposition. The sediment residence time can be constrained by using a catchment-wide assessment of depositional ages. For a small catchment in New Zealand, Phillips et al. (2007) showed that the half-life of removal for in-channel deposits was >2 ka, and the majority of sediment deposited on the floodplain remains there for >10 ka. However, this approach is time-consuming and logistically impractical – particularly for large catchments.

Concentrations of in-situ cosmogenic nuclides do not generally increase downstream and this is attributed to the majority of cosmogenic nuclide dosing occurs before sediment enters the fluvial system (Matmon et al., 2003; Wittmann et al., 2009). This agrees with studies discussed in Section 1.2.2 that suggest long durations of hillslope storage (Bacon et al., 2012; Pavich, 1989), and hillslope storage represents a significant proportion of the sediment residence time (Dosseto et al., 2014; Suresh et al., 2014).

Measurements of U-series isotopes in fluvial sediment integrate the timescales of regolith production, hillslope transport and any alluvial storage (Bourdon et al., 2003; Dosseto et al., 2008a; Vigier et al., 2001). The U-series approach has been applied to a wide range of geomorphic settings and these are discussed below.

In a large, recently-glaciated catchment in northern Canada, sediment residence times of 10 – 30 ka correlate with the time elapsed since glacial retreat during the Last Glacial Maximum (Vigier et al., 2001). Other studies in Canada also show that the sediment loads of

modern rivers are still adjusting to glaciation during the Last Glacial Maximum and are remobilising Quaternary sediment (Church and Slaymaker, 1989). This suggests that widespread glaciation during the Last Glacial Maximum inhibited regolith production, and the bulk of the modern sediment was created during glacial retreat.

Sediment residence times are short for small catchments in weathering-limited environments, e.g. 1 – 6 ka in Iceland (Vigier et al., 2006), which are attributed to high rates of denudation and chemical weathering. This was used to show that erosional and weathering processes were in steady-state. Much longer residence times were inferred (40 – 90 ka) in catchments draining the Deccan Traps, India (Vigier et al., 2005). These longer residence times for the Deccan Traps vs Icelandic catchments were attributed to the absence of glaciers during the Last Glacial Maximum in the Deccan Traps.

In the Amazon River basin (Rio Madeira), sediment residence times increase downstream with increasing distance from the Andes from 4 to 20 ka at the confluence of the Rio Madeira River with Amazon River with (Dosseto et al., 2006). The almost linear increase in residence times with distance from the Andes reflects that sediment is continually stored and reworked in the floodplain. Moreover, this suggests that the duration of regolith storage in the Andes is relatively short compared to floodplain storage further downstream. Residence times then decreased downstream at the delta to 6 ka due to mixing. Sediment residence times are 400 ± 180 ka in the Murrumbidgee River, southeastern Australia (Suresh et al., 2014), which is an order of magnitude than sediment residence times in the Amazon River; as residence times do not increase downstream, this is attributed to much longer duration of hillslope storage in low-relief southeastern Australia, compared to the high-relief Andes. However, large uncertainties in sediment residence times from Suresh et al. (2014) limit possible insights.

In summary, denudation rates are well constrained for regolith profiles, but controls on regolith production rates are not well constrained and require further studies. Long hillslope residence times indicate hillslope transport processes must be considered when assessing sediment residence times of fluvial sediment. For instance, hillslope transport processes could explain the order of magnitude difference between sediment residence times in the Amazon River vs Murrumbidgee River. In addition to storage on hillslopes, alluvial storage also appears to be significant in large fluvial systems; however, the controls on the duration of alluvial storage are largely unknown. This thesis aims to assess the relationship between sediment residence times and climate in modern catchments. By applying comminution dating to sedimentary deposits, the effects of past climate change on sediment residence times can also be assessed.

1.3 Comminution dating

The *comminution dating* (or *comminution age*) technique is a developing application of the uranium (U) isotopes, which is based on the disequilibrium between ^{234}U and ^{238}U in fine-grained detrital minerals (DePaolo et al., 2006). Comminution is defined as “to reduce to powder” and comminution ages are modelled on the loss of ^{234}U by direct recoil following the alpha decay of ^{238}U in fine-grained minerals (Figure 1.2). Since the length of direct recoil is around 30 nm in silicates, the loss of ^{234}U by direct recoil is only measureable in fine-grained detrital sediments with high surface-area-to-volume ratios, which is typically $\sim 63\ \mu\text{m}$ (Kigoshi, 1971; DePaolo et al., 2006). Therefore, comminution ages represent the time elapsed since detrital grains were reduced to $<63\ \mu\text{m}$ in size.

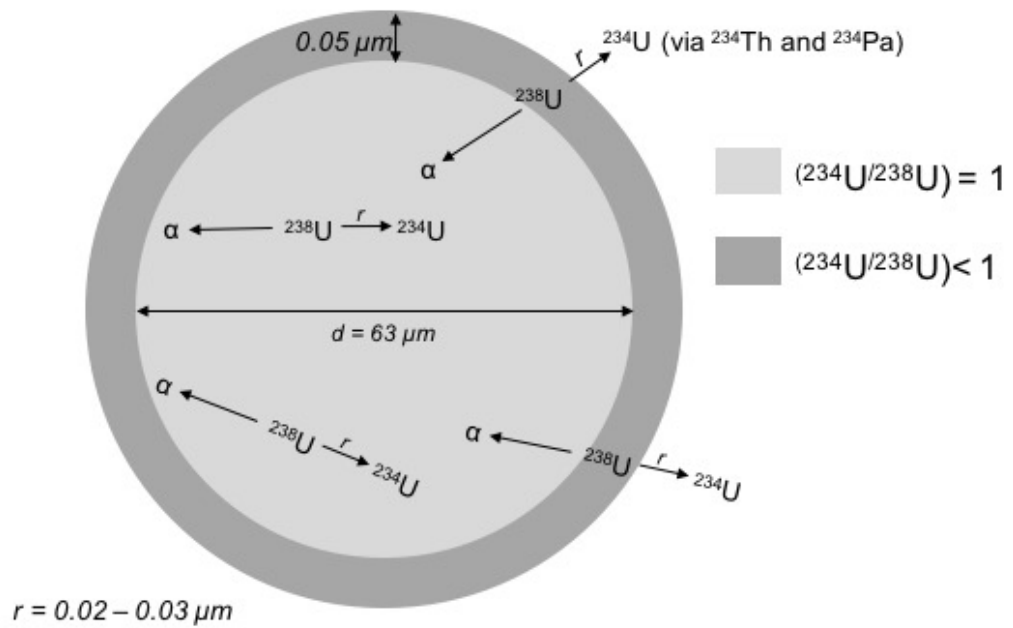
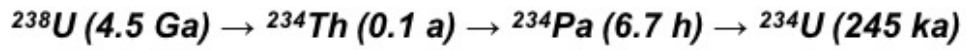


Figure 1.2 Schematic diagram of the direct ejection of ^{234}U (via the short-lived ^{234}Th) into the surrounding medium following the alpha decay of ^{238}U . The dark grey area represents the ^{234}U -depleted outer-rind of the detrital minerals. The light grey area represents the inner-core of the detrital minerals where loss by direct recoil does not occur, and $(^{234}\text{U}/^{238}\text{U}) = 1$. Figure modified from DePaolo et al. (2006).

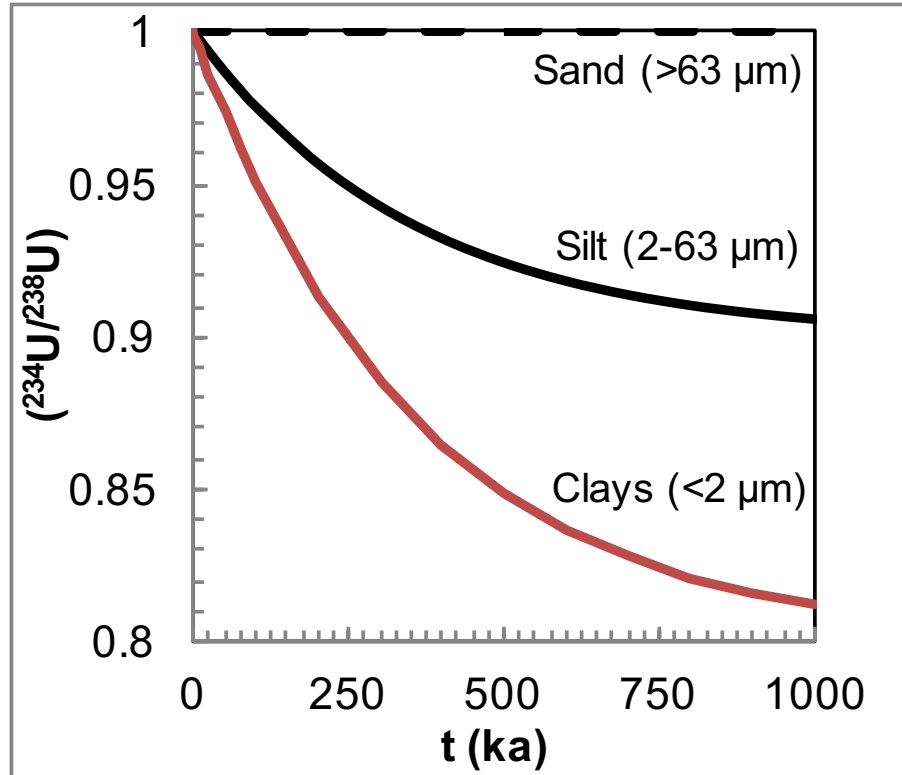


Figure 1.3 Evolution of the $(^{234}\text{U}/^{238}\text{U})$ in sediment grains as a function of time for: sand grains ($> 63\mu\text{m}$), silts ($2-63\ \mu\text{m}$), and clays ($<2\ \mu\text{m}$) (modified from DePaolo et al., 2006).

An alpha particle is emitted during the radioactive decay of ^{238}U and the daughter nuclide, ^{234}Th , is recoiled to obey the conservation of energy, which is termed *alpha recoil*. If the distance between the parent nuclide and the grain boundary is less than the recoil length of ^{234}Th , and correctly orientated, the daughter nuclide is emitted into the surrounding medium, which is termed *direct ejection*. The fraction of ^{234}Th nuclides that are lost by direct ejection is termed the *direct-recoil fraction* (Kigoshi, 1971). The short-lived ^{234}Th ($t_{1/2} = 24$ days) is considered to instantly decay to ^{234}U via the unstable ^{234}Pa ($t_{1/2} = 6.7$ h) and direct ejection therefore results in ^{234}U - ^{238}U disequilibrium.

The general concepts of U-series radioactive disequilibria are introduced in Section 1.3.1, and the basis for the comminution dating equation is outlined in Section 1.3.2. Sample pre-treatment procedures for comminution dating are discussed in Section 1.3.3. The accuracy of

comminution ages is dependent upon estimating the direct-recoil fraction and this is discussed in Section 1.3.4. Applications of comminution dating in the literature are reviewed in Section 1.3.5. As comminution dating is a developing technique, issues and uncertainties are discussed in Section 1.3.6.

1.3.1 Background theory

The potential of U-series radioactive disequilibria as geochronological tools has been known since the 1960s (Rosholt et al., 1966). However, advances were limited by analytical capabilities for accurately measuring low concentrations of radionuclides. Recent developments in analytical techniques, such as thermal ionization mass spectrometric (TIMS) and multi-collector inductively coupled plasma mass spectrometry (MC-ICPMS), have removed these limitations (Goldstein and Stirling, 2003). These subsequent advances in U-series geochemistry are discussed in this section.

The U-series isotopes are fractionated by weathering processes, and the following order of reactivity is generally observed in the natural environment (Bourdon et al., 2003; Chabaux et al., 2003; Dosseto, 2014): $^{234}\text{U} > ^{238}\text{U} > ^{230}\text{Th} > ^{232}\text{Th}$. The U-series isotopes also undergo radioactive decay on similar timescales to weathering and erosional processes. As the initial isotopic composition of closed systems is known (discussed in Section 1.3.1.1), the U-series isotopes are ideal chronometers for dating such processes (Chabaux et al., 2003). By modelling changes in the abundances of U-series isotopes, the time since the onset of chemical weathering can be constrained i.e., the *weathering age* (Dosseto et al., 2012), or the *sediment residence time* (Dosseto et al., 2008a). The low temperature behaviour of uranium (U) at the Earth's surface is discussed in Section 1.3.1.2, and models that account for the abundances of nuclides in soils and sediment are discussed in Section 1.3.1.3.

1.3.1.1 Secular equilibrium

It is assumed that the initial activity ratio of the parent material is known at time zero and ^{234}U and ^{238}U are in *secular equilibrium*. In closed systems where the half-life of the daughter is much shorter than the parent, as is the case with ^{234}U and ^{238}U , the abundance of the parent is constant, and the abundance of the daughter is dependent upon the rate of radioactive decay (Figure 1.4). If the system remains closed for approximately four half-lives of the daughter nuclide, the ratio of nuclides remains constant and the system is in secular equilibrium. As the half-life of ^{234}U is $245,250 \pm 490$ a (Cheng et al., 2000), the parent material will be in secular equilibrium if undisturbed for >1000 ka whereby $(^{234}\text{U}/^{238}\text{U}) = 1$ (where parentheses denote activity ratio). The comminution dating technique assumes that the unweathered material is in secular equilibrium if older than 1 Ma, which may be bedrock or >63 μm detrital sediment. The radiometric clock then begins following the formation of <63 μm at the soil-bedrock interface, or following the comminution of >63 μm detrital grains.

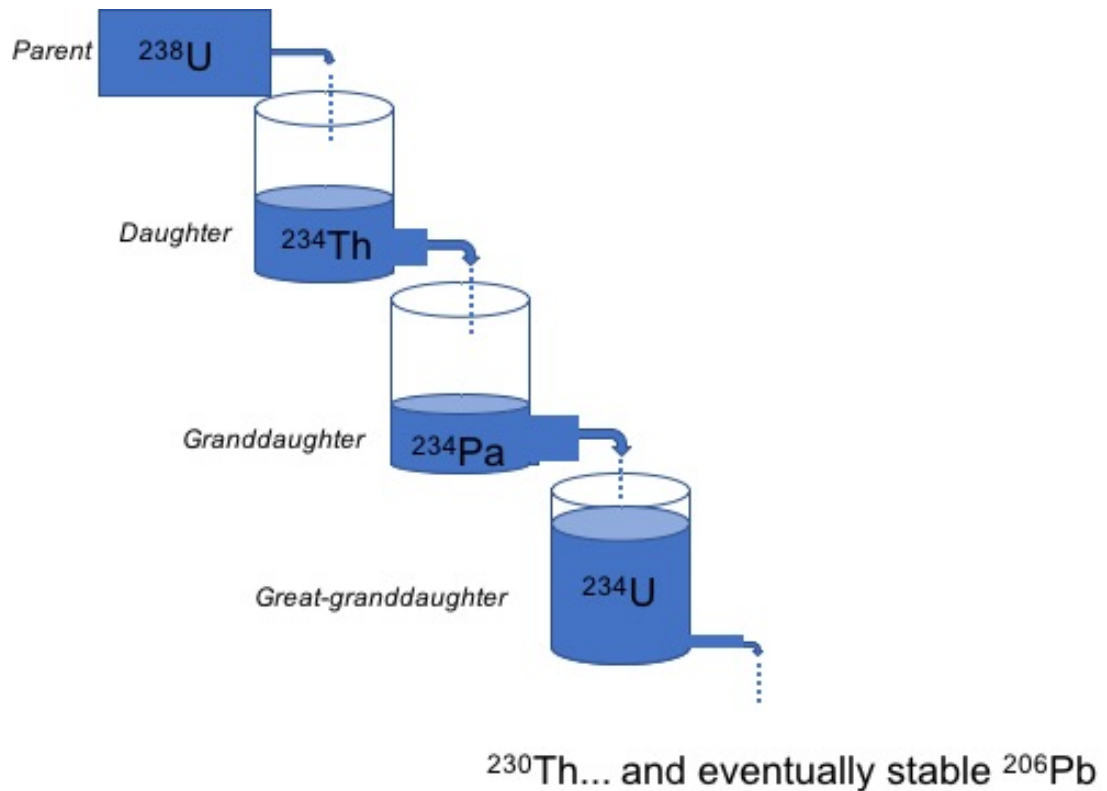


Figure 1.4 Analogy of the U-series decay chain represented by a series of buckets feeding into each other (modified from Bourdon et al., 2003). The size of the outlet in each bucket represents the decay constant of each nuclide, and the levels of each bucket represent the abundances of each nuclide. If the bucket of a daughter nuclide is emptied, the time required to refill the bucket to its original level depends upon the decay constant of the daughter nuclide.

1.3.1.2 Nuclide reactivity and distribution

The reactivity of U is strongly dependent on redox conditions, and is stable at oxidation states +4 and +6 (Langmuir, 1978). Under reducing conditions, e.g. Earth's interior, U^{4+} is generally insoluble; whereas under oxidising conditions, e.g. the Earth's surface, U^{6+} typically exists as the uranyl ion UO_2^{2+} and forms soluble carbonyl complexes (Langmuir, 1978).

The abundance of U is low in common rock-forming minerals due to the large radii of the U^{4+} and U^{6+} ions (Dahlkamp, 1993). In accessory minerals, U concentrations are higher due

to the similar ionic radii of U with major cations, such as Zr^{4+} in zircon. As U is more mobile in oxidising conditions, fluid-rock interactions may deposit aqueous U species onto reduced species such as iron (II) (Fe^{2+}). This results in higher U concentrations on mineral grain boundaries and along microfractures (Tieh and Ledger, 1981). In common silicate minerals such as quartz and feldspar, U concentrations are low and can be considered as “background U” (Tieh and Ledger, 1981).

A disequilibrium between ^{234}U and ^{238}U is typically observed in solids and solutes at Earth's surface (Bourdon et al., 2003; Chabaux et al., 2003; Dosseto, 2014; Dosseto et al., 2008a). A excess of ^{234}U is generally observed in solutions, and there has been a constant excess of ^{234}U in the oceans for the past 800 ka (Henderson, 2002). The greater mobility of ^{234}U relative to ^{238}U is associated with the alpha decay of ^{238}U (discussed later in Section 1.3.4). Leaching models have been developed to constrain the timescales of weathering and erosion processes based on the abundance of ^{234}U and ^{238}U nuclides in soils, and sediments.

1.3.1.3 Nuclide loss/gain models

A leaching model was first devised by Latham and Schwarcz (1987) to account for $(^{234}U/^{238}U) \leq 1$ in weathered silicate rocks. This assumes that the unweathered solid is initially in secular equilibrium with respect to ^{238}U and ^{234}U (discussed later in Section 1.3.2). At time zero, secular equilibrium is disturbed by weathering processes leaching U. Variation of the abundance of ^{238}U nuclides in silicate minerals with time is given as:

$$\frac{dN_{238}}{dt} = -w_{238}N_{238} \quad (1)$$

where N_{238} is the number of atoms of ^{238}U , and w_{238} is a leaching coefficient for ^{238}U that describe the rate of ^{238}U loss (in a^{-1}). Loss of ^{238}U via radioactive decay is considered negligible on the timescale of soil and fluvial processes (<1 Ma), as $\lambda_{234} \gg \lambda_{238}$. The abundance of ^{234}U nuclides with time is given as:

$$\frac{dN_{234}}{dt} = \lambda_{238}N_{238} - \lambda_{234}N_{234} - w_{234}N_{234} \quad (2)$$

where N_{234} is the number of atoms of ^{234}U , and w_{234} (in a^{-1}), λ_{234} and λ_{238} (in a^{-1}) are the leaching constants and decay constant for ^{234}U and ^{238}U , respectively.

Equation 2 assumes that all ^{234}U produced by the decay of ^{238}U remains in the solid; however, ^{234}U is also lost by direct ejection (as outlined later in Section 3.1.4). Thus, Scott et al. (1992) modified Equation 2 to account for the loss of ^{234}U by alpha recoil:

$$\frac{dN_{234}}{dt} = (1 - f_\alpha)\lambda_{238}N_{238} - \lambda_{234}N_{234} - w_{234}N_{234} \quad (3)$$

where $(1 - f_\alpha)$ represents the fraction of ^{234}U that remains in the solid following the alpha decay of ^{238}U .

1.3.2 Comminution age equation

DePaolo et al. (2006) suggested a modified version of Equation 3 to account for the abundances of ^{234}U and ^{238}U in fine-grained detrital minerals where it is assumed that the leaching rate of ^{234}U and ^{238}U is equal ($w_4 = w_8$):

$$A = (1 - f_\alpha) + [(A_0 - (1 - f_\alpha))e^{-\lambda_{234}t_{comm}}] \quad (4)$$

where t_{comm} is the comminution age, A and A_0 are the measured and initial ($^{234}\text{U}/^{238}\text{U}$) activity ratios, respectively. By rearranging Equation 4 in terms of t , the comminution age equation is given as (DePaolo et al., 2006):

$$t_{comm} = \frac{-1}{\lambda_{234}} \ln \left[\frac{A - (1 - f_\alpha)}{A_0 - (1 - f_\alpha)} \right] \quad (5)$$

1.3.3 Sample pre-treatment

To determine accurate comminution ages, the detrital minerals must be isolated. This is because the U isotope composition of non-detrital matter, which represents weathering products such as carbonates, iron oxides and organic matter, is not related to the loss of ^{234}U by direct recoil. It should also be ensured that sample pre-treatment procedures do not affect the surface area properties, and/or dissolve the ^{234}U -depleted outer-rind of detrital minerals.

Sequential extraction procedures were designed to assess the fractionation of trace metals in operationally-defined phases (Bacon and Davidson, 2008; Gleyzes et al., 2002). This is achieved by sequentially removing non-detrital matter using chemical reagents leaving the “residual fraction”. This is the fraction of interest for comminution dating since this represents the isolated detrital minerals. The original procedure was developed by Tessier et al. (1979) and is herein referred to as “Tessier’s procedure”. However, this method has since been modified frequently, leading to a wide range of procedures and a difficulty in cross-comparing results. To overcome this, Schultz et al. (1998) attempted to establish a common procedure, herein referred to as “Schultz’ procedure”. Operationally-defined phases removed in sequential extraction procedures are discussed below, and typical chemical reagents used to remove non-detrital phases are also given.

The *exchangeable fraction* (F1) refers to elements bound relatively weakly to the surface of the grain by either physical dipole-dipole interactions (adsorption) or weak electrostatic interactions. Only a small fraction of the U-series isotopes is expected to be found in F1 unless the depositional environment was particularly U-rich or contaminated. F1 is removed by the addition of a neutral salt which disrupts the ionic composition and affects sorption-desorption processes and Mg^{2+} has been noted to be particularly effective at competing with trace metals for surface sites (O'Connor and Kester, 1975). Although both Schultz’ and Tessier’s procedure utilise MgCl_2 , Lee (2009) recommends MgNO_3 as selectivity issues

have been noted with the chloride ion which can be avoided using a nitrate ion (Leleyter and Probst, 1999).

The *acid-soluble fraction* (F2) is pH dependant and dissolved by acidic solutions. Ca- and/or Mg-bearing minerals such calcite and dolomite are targeted, and F2 is commonly referred to as 'carbonates'. A significant amount of U can be incorporated into these minerals by surface adsorption and/ or co-precipitation processes. This fraction will be especially significant in marine sediment and sediment from arid environments due to evaporative processes. Acidic reagents easily remove F2 but selectivity is an issue as most acidic reagents also attack Fe/Mn oxides and/or organic compounds; however, for comminution dating, reagents must only be selective between detrital and non-detrital matter. A buffer solution of acetic acid and sodium acetate at pH 5 was found to be the optimum balance between selectivity and completeness. Schultz et al. (1998) modified the removal of this fraction by carrying out the procedure in two separate two-hour batches to minimise readsorption and ensure the correct pH of the buffer solution was maintained.

The *reducible fraction* (F3) targets iron (Fe) and manganese (Mn) oxides, hydroxides and oxyhydroxides. These compounds are formed in oxidising weathering environments, whereby Fe^{2+} is rapidly oxidised to form amorphous phases such as ferrihydrite (Lee and Baik, 2009). Crystalline phases, such as goethite, form by slower reactions, but have a greater affinity for U compared to amorphous phases and subsequently have higher U concentrations. As oxides are unstable under anoxic conditions, a reducing agent is used to remove them and coulometry experiments have shown that $\text{NH}_2\text{OH}\cdot\text{HCl}/\text{AcOH}$ is particularly selective towards the reducible fraction (Tessier et al., 1979).

The *oxidisable fraction* (F4) primarily consists of organic matter. F4 can be U-rich due to the chelating ability of most organic acids, which strongly bind with heavy metals. Furthermore, sulphur-containing bacteria can reduce mobile U^{6+} and deposit immobile U^{4+} .

F4 is typically removed by heating in a furnace or a chemical oxidising agent. Removal of F4 using $\text{H}_2\text{O}_2/\text{HNO}_3$ at an acidic pH minimise readsorption of U hydrolysis reactions which form insoluble heavy metal complexes (Tessier et al., 1979); however, NaOCl has been shown to be more effective in some cases, particularly in soils (Anderson, 1963; Shuman, 1983).

Remaining matter following removal of operationally-defined phases is referred to as the *residual fraction*. This is considered to be comprise only detrital and clay minerals, but the removal of non-detrital matter may be incomplete (Bacon and Davidson, 2008; Gleyzes et al., 2002). This is problematic for comminution dating since the U isotope composition of non-detrital matter is not related to the loss of ^{234}U by direct recoil.

Another issue associated with sequential extraction procedures is readsorption (also referred to as *redistribution*), which refers to the re-deposition of released metals to the solid-phase via physical dipole-dipole interactions (physiosorption), electrostatic attraction or inorganic precipitation. Ethylenediaminetetraacetic acid (H_4EDTA) was tested in a sequential extraction procedure and had a minimal effect on the recovery of U, but dramatically increased the recovery of Cm and Pu indicating that U was outcompeted for binding with EDTA by elements with a greater affinity for the ligand (Schultz et al., 1998). Under alkaline conditions however, EDDS and EDTA were more effective than citrate, but less effective than the acidic citrate solution. As the majority of sequential extraction procedures are carried out under acidic conditions, sodium citrate is an ideal complexing agent to test to inhibit the readsorption of U (Blanco et al., 2004).

1.3.4 Direct-recoil fraction

The direct-recoil fraction accounts for the fraction of ^{234}U nuclides lost by direct ejection, as outlined in Section 1.3. Following approximately four half-lives of ^{234}U (ca. 1000 ka), the detrital minerals will be in a new steady-state disequilibrium that accounts for the loss of

^{234}U by direct ejection, and is dependent on the direct-recoil fraction (Figure 1.5). The magnitude of the direct-recoil fraction is dependent upon the surface-area properties of the detrital minerals. The recoil length is an important parameter in all direct-recoil models and firstly, this is discussed in Section 1.3.4.1. There are various models for estimating the direct-recoil fraction, and these are outlined in the Sections 1.3.4.2 to 1.3.4.5.

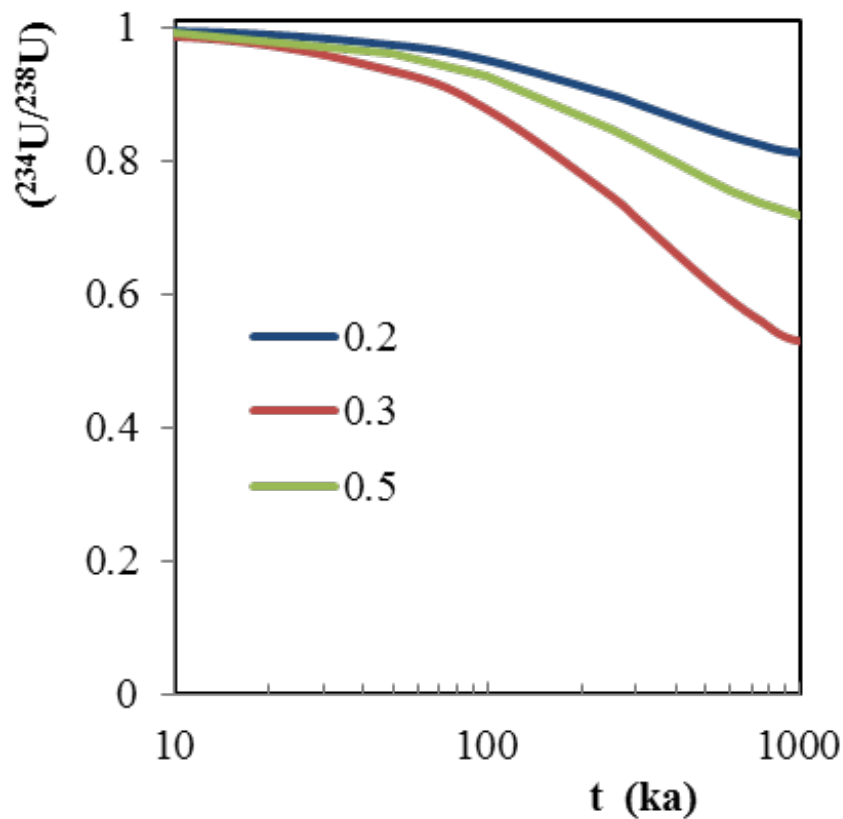


Figure 1.5 Modelled ($^{234}\text{U}/^{238}\text{U}$) activity ratio vs time resulting from the direct recoil of ^{234}U (via the short-lived ^{234}Th) with direct-recoil fractions of 0.2, 0.3 and 0.5 (modified from DePaolo et al. 2006)

1.3.4.1 Recoil length

The recoil length of ^{234}Th during the alpha decay of ^{238}U is an important control on the magnitude of the direct-recoil fraction. During alpha recoil, the daughter nuclide travels through the host lattice and is subject to nuclear and electronic interactions that are

dependent on the sample mineralogy; nuclear interactions are more important for heavy elements such as U and Th.

Recoil lengths can be predicted from Lindhard-Scharff-Schiott (LSS) Theory, which considers the relative masses and abundance of the target electrons and nuclei (Lindhard and Scharff, 1961). The equation for predicting the recoil length is given as (Hashimoto et al., 1985):

$$R = CA_2 \left[\frac{(Z_1^{2/3} + Z_2^{2/3})}{Z_1 Z_2} E_r \right]^{2/3} \quad (6)$$

where $Z_{1,2}$ and A_2 are the atomic and mass numbers of recoiling atom I and constituent atom 2 (in g mol⁻¹), E_r is energy of the alpha recoil atom 1 (in keV), and C is a constant. The recoil distance in Equation 6 is given in $\mu\text{g cm}^{-2}$ and converted to a distance using the mineral density. For heterogeneous materials, such as silicate minerals, the equation for predicting the recoil length (R) is given as:

$$\frac{1}{R} = \sum_i \frac{X_i}{(R_t)_i} \quad (7)$$

where X_i and $(R_t)_i$ are the fraction of the total mass and projected range of the i^{th} component (where $a_i + b_i = c_i$), respectively. The recoil lengths of selected common minerals are given below in Table 1.1. Recoil lengths can also be predicted from software that considers the stopping and range of ions in matter, known as SRIM (Ziegler et al., 1996). Recoil lengths of some typical minerals that were calculated using SRIM software are included in Table 1.1.

In comminution dating studies, the recoil length of ²³⁴Th is typically assumed to range from 30 – 40 nm e.g. values of 34 and 30 nm were assumed in Lee et al. (2010), and Dosseto et al. (2010), respectively. Table 1.1 shows that these assumed values could overestimate the

recoil length, especially considering U-rich minerals such as zircon have shorter recoil lengths of 23 nm, and a recoil length of 25 nm is assumed in this thesis. However, for comminution ages from different studies to be comparable, efforts should be made to estimate the recoil length from the sample mineralogy.

Table 1.1 Recoil ranges calculated from LSS theory (Hashimoto et al., 1985; Dosseto and Schaller, 2016)

Mineral	Chemical structure	Density (g cm ⁻³)	Recoil length (nm)
Albite	NaAlSi ₃ O ₈	2.62	30.0 ^b
Kaolinite	Al ₂ Si ₂ O ₅ (OH) ₄	2.63	30.0 ^b
Quartz	SiO ₂	2.65	27.2 ^a
Calcite	CaCO ₃	2.71	29.8 ^b
Muscovite	KAl ₂ Si ₃ O ₁₀ (OH) ₂	2.93	24.6 ^a
Biotite	K(Mg,Fe) ₃ AlSi ₃ O ₁₀ (F,OH) ₂	3.00	24.7 ^a
Zircon	ZrSiO ₄	4.65	22.7 ^b
Triuranium octoxide	U ₃ O ₈	8.50	17.8 ^a
Thorium dioxide	ThO ₂	9.86	15.8 ^a

^aLSS theory from Hashimoto (1985)

^bSRIM from Maher et al. (2006)

1.3.4.2 Geometric direct-recoil fraction model

The direct-recoil fraction was initially estimated by considering the probability of ²³⁴U loss from an ideal sphere with a uniform grain size distribution (Kigoshi, 1971):

$$f_{\alpha} = \frac{3}{4} \left(\frac{R}{r} - \frac{R^3}{12r^3} \right) \quad (8)$$

where R is recoil length (in μm) and r is the grain radius (in μm). However, the geometric approach underestimates the direct-recoil fraction as it does not consider *surface roughness* of grains, which represents the ratio of the actual surface area to the geometric surface area of mineral grains. The average value reported for freshly-ground minerals over a range of particle sizes is seven (Brantley and Mellott, 2000; White and Peterson, 1990), and surface

roughness values of up to 600 are reported for weathered silicates (White et al., 1996). Thus the geometric model was extended to take into account surface roughness, and the length-to-width ratio of mineral grains i.e. the *aspect ratio*, given as (DePaolo et al., 2006):

$$f_{\alpha} = \int_{\frac{R}{2}}^{r_{max}} X(r)\beta(r)\lambda(r) \frac{3}{4} \left(\frac{R}{r} - \frac{R^3}{12r^3} \right) dr \quad (9)$$

where r is the radius (in μm), $X(r)$ is the proportion of the size fraction with radius r , β is the dimensionless aspect ratio, and λ is the dimensionless surface roughness. A similar equation that also considers the grain size distribution was proposed by Maher et al. (2006):

$$f_{\alpha} = \sum_n \lambda \beta X_{\bar{d}} \frac{3}{2} \left(\frac{R}{\bar{d}} - \frac{R^3}{3\bar{d}^3} \right) \quad (10)$$

where \bar{d} is the mean particle diameter (in μm), and $X_{\bar{d}}$ is the proportion of the size fraction with mean particle diameter \bar{d} . Lee et al. (2010) showed that assuming a constant surface roughness value for all grain sizes is not valid. Larger grain size fractions required larger surface roughness values for comminution ages to be consistent with independently constrained ages. This is because the surface roughness of minerals is related to the density of *dissolution reactive sites*, which decreases with decreasing grain diameter (White and Peterson, 1990; Anbeek et al., 1994). An alternative geometric model was proposed by Lee et al. (2010) to consider surface roughness, and is given as:

$$f_{\alpha} = \frac{RK}{8r} \lambda \quad (10)$$

where R the recoil length (in μm), r is the grain radius (in μm), λ is the dimensionless surface roughness, and K is a dimensionless grain shape factor, e.g. $K = 6$ for a sphere (Cartwright, 1962).

1.3.4.3 BET surface area direct-recoil fraction model

Maher et al. (2006) proposed that the direct-recoil-fraction could be constrained using the specific surface area calculated using Brunauer–Emmett–Teller (BET) theory (Brunauer et al., 1938). The BET specific surface area is measured using N₂ gas sorption measurements, and details regarding the procedure are given in Appendix A. The BET model for estimating the direct-recoil fraction is given as:

$$f_{\alpha} = \frac{1}{4} S_{BET} \rho R \quad (11)$$

where S_{BET} is the specific surface area of the mineral grains (in m² g⁻¹), ρ is the density of solid phase (in g m⁻³). The BET model is preferred to the geometric approaches of calculating the direct-recoil fraction as assumptions regarding surface roughness and particle shapes are not required. However, the BET model overestimates the direct-recoil fraction as the N₂ gas sorption technique measures the surface area on a length-scale of a N₂ molecule (ca. 0.3 nm diameter) that is approximately two order of magnitude smaller than the length scale of alpha recoil (Hashimoto et al., 1985).

1.3.4.4 Fractal direct-recoil fraction model

To account for the BET model overestimating the direct-recoil fraction, Bourdon et al. (2009) proposed a fractal correction that was based on the model from Semkow (1991). The fractal model is given as:

$$f_{\alpha} = \frac{1}{4} S_{BET} \rho R \left[\frac{2^{D-1}}{4-D} \left(\frac{a}{R} \right)^{D-2} \right] \quad (12)$$

where D is the fractal dimension of the mineral grains and a is the adsorbate gas diameter (in m). Note that the fractal direct-recoil model should only be applied to mesoporous materials. The fractal dimension can be calculated from gas sorption isotherms by several methods,

which are outlined in Appendix A. The fractal model was successfully applied to constrain the accumulation of ^{234}U in ice, resulting from the direct ejection of ^{234}U from dust trapped within the ice. Handley et al. (2013a; 2013b) applied the fractal model to alluvial deposits, but found that calculated comminution ages were less than depositional ages.

1.3.4.5 Other approaches

The direct-recoil fraction could be measured by using the ($^{234}\text{U}/^{238}\text{U}$) activity ratio of $<63\ \mu\text{m}$ material that is $>1\ \text{Ma}$; as shown by Figure 1.5, a steady-state disequilibrium is reached following $1\ \text{Ma}$ for ^{234}U and ^{238}U (DePaolo et al., 2006). Thus, the direct-recoil fraction is given as:

$$f_{\alpha} = 1 - A \quad (13)$$

where A represents the ($^{234}\text{U}/^{238}\text{U}$) activity ratio of fine-grained sediment that has a comminution age of $>1\ \text{Ma}$. This method could also be applied to shorter-lived isotopes in the ^{238}U decay chain, for instance, by measuring the ($^{226}\text{Ra}/^{230}\text{Th}$) activity ratio. However, this would be more complicated than using ^{234}U and ^{238}U as the different chemical properties of ^{226}Ra and ^{230}Th would have to be taken into account. Furthermore, ^{226}Ra and ^{230}Th will have undergone alpha recoil multiple times, respectively, due to alpha decay from the parent ^{238}U , and may be unevenly distributed at grain boundaries.

Maher et al. (2006) suggested that the direct-recoil fraction could be measured by dissolving the ^{234}U -depleted outer-rind of detrital minerals with a strong acid. The direct-recoil is then given as:

$$f_{\alpha} = 1 - A_L \left(\frac{[\text{U}]_L}{[\text{U}]_{\text{solid}}} \right) \quad (14)$$

where A_L is the ($^{234}\text{U}/^{238}\text{U}$) activity ratio of the leachate, and $[U]_L/[U]_{\text{solid}}$ is the fraction of U leached. This approach assumes that the unleached U in the solid has ($^{234}\text{U}/^{238}\text{U}$) = 1, and secondly, that only the outer-rind of detrital minerals is removed during leaching. Despite these uncertainties, estimates of the direct-recoil fraction using this approach were in a similar range to direct-recoil fraction values estimated using geometric and BET models (Maher et al., 2006). This approach requires further testing to confirm that ($^{234}\text{U}/^{238}\text{U}$) = 1 for the leached solid, following etching.

1.3.5 Applications

Comminution dating of soils and sediments aims to constrain the time elapsed since the formation of <63 μm particles (DePaolo et al., 2006). Applied to hillslope-fluvial systems, these ages are referred to as *sediment residence times*. If the depositional ages of a sedimentary deposit is known, the *palaeo sediment residence time* can be constrained by subtracting the depositional age from the comminution age (Figure 1.6).

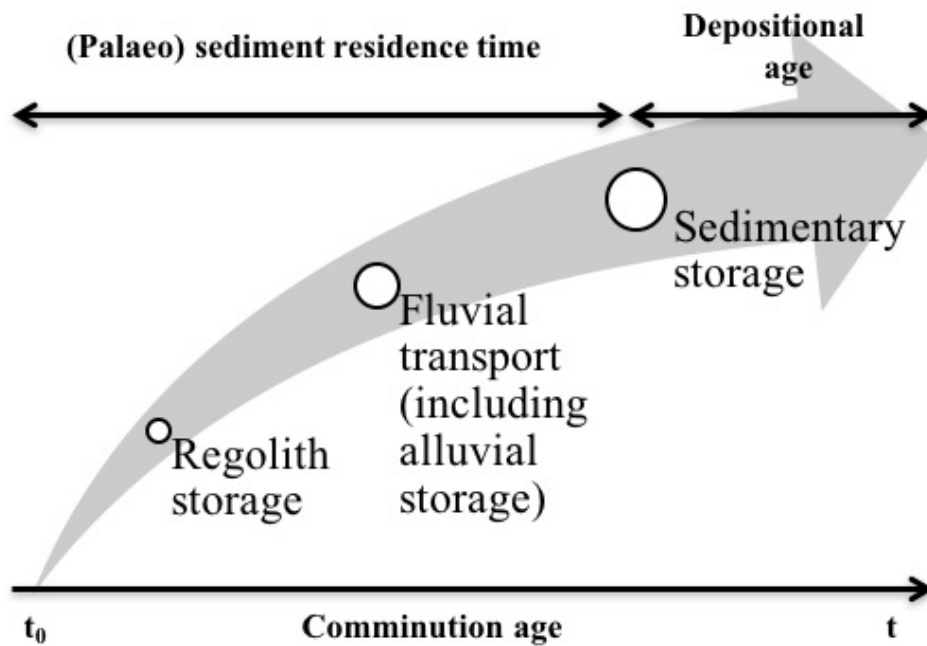


Figure 1.6 Schematic representation of (palaeo) sediment residence times from $t = 0$ at the soil-bedrock interface, including storage in the weathering profile, fluvial transport and sedimentary deposit. Circle sizes represent an idealised fluvial system in which sediment residence times increase linearly downstream. Applied to sedimentary deposits, depositional ages can be subtracted from comminution ages to calculate palaeo sediment residence times.

The comminution dating technique was first applied to a sedimentary core from the North Atlantic (DePaolo et al., 2006). U activity ratios were lower during glacial periods, and higher during interglacial periods. These variations correlated with the Nd and Sr isotope record of the core, showing that sediment provenance oscillated between nearby volcanic rocks (Iceland) during inter-glacial periods and a distal continental source (Europe) during glacial periods. Long transport times for glacial periods were inferred to represent the reworking of sediment from subaerially exposed continental shelf areas; short transport times for interglacial periods was attributed to the rapid erosion and transport of sediment from Iceland within <10 ka.

Dosseto et al. (2010) applied the technique to palaeo-channel deposits in southeastern Australia. In contrast to DePaolo et al., (2006), residence times were shorter during glacial periods and longer during interglacials. Variations in sediment residence times were attributed to decreased rainfall/vegetation cover during glacial periods increasing the erosion of younger hillslope sediment. Whereas increased vegetation cover during interglacials was inferred to reduce hillslope erosion, and increased reworking of older sediment from alluvial deposits.

Lee et al. (2010) attempted to calibrate the technique by studying an alluvial glacial outwash deposit where the transport time was assumed to be minimal and thus comminution ages should represent depositional ages. However, ages calculated using the geometric model were typically less than independently constrained depositional ages. This was attributed to the invalid assumption of a constant surface roughness factor for all sediments. Thus, the surface roughness of sediments should be calculated when using the geometric model. Since this requires grain size distribution and BET surface measurements, the calculation of comminution ages using the BET direct-recoil model is preferred. Issues regarding constraining the direct-recoil fraction using the geometric model are discussed in Section 1.3.4.2.

Comminution dating was applied to an alluvial deposit in the Flinders Ranges, southern Australia using the fractal direct-recoil model (Handley et al., 2013b). Inferred ages were less than depositional ages, and decreased with depth. This was attributed to sediment samples comprising a mixture of fluvial sediment material and aeolian material. In addition, Handley et al. (2013b) found that near-surface bedrock samples were not in secular equilibrium, suggesting that preferential leaching of ^{234}U had occurred. However, even if sediment samples comprised 100% aeolian material, and the bedrock was not in secular equilibrium, comminution ages should still be greater than depositional ages. This suggests that either 1) ^{234}U -rich non-detrital matter was incompletely removed during sample pre-

treatment non-detrital matter, and/or the direct-recoil fraction was incorrectly estimated. Inferred comminution ages of sediment from palaeochannel deposits in the Lake Eyre basin, central Australia were also less than depositional ages (Handley et al., 2013a). Furthermore, ages could not be produced for many samples as the direct-recoil fraction could not account for the measured ($^{234}\text{U}/^{238}\text{U}$) activity ratio. Comminution dating of sediments from the Lake Eyre basin is likely complicated by the fact that clay minerals travel as mud aggregates, and are resistant to disaggregation (Maroulis and Nanson, 1996); estimating the direct-recoil fraction will therefore be affected by imprecise surface area or particle size distribution measurements. Monte Carlo simulations of comminution ages for a synthetic sample show that if input parameters are known with 1 % of their true value, the weighted geometric and fractal models yield comminution ages with relative errors of 2.4 and 0.5 %, respectively.

In contrast to results from sedimentary deposits, comminution dating of ice cores successfully provided an independent method for determining the ages of ice layers (Aciego et al., 2011). Ages were calculated by constraining the rate at which ^{234}U is ejected into the surrounding ice from mineral dust trapped in the ice. For a core in Antarctica, ages calculated using the fractal model were consistent with estimates from other proxies, such as dated tephra layers. Recently, this approach was applied to evaluate the residence time of ground ice in permafrost cores in central Alaska, USA (Ewing et al., 2015). This showed that the ages of ice were up to 200 ka, and consistent with ^{14}C radiocarbon dating that showed organic material within the ice was >40 ka BP. However, errors in estimated ages were up to ca. 100 ka due to uncertainties in the direct-recoil fraction, and the role of secondary coatings on detrital minerals.

In summary, comminution dating is useful as a relative proxy for discerning large variations in sediment transport (DePaolo et al., 2006; Dosseto et al., 2010). Results from DePaolo et al. (2006) likely correlated especially well with glacial-interglacial cycles as sediment was sourced from two areas with strongly contrasting sediment transport histories. Comminution

dating also shows great promise for determining depositional ages for ice cores. However, comminution ages are currently not useful when applied to deposits with complex transport histories and variable grain size distribution. The application of the technique is limited by uncertainties and these are outlined in the following section.

1.3.6 Uncertainties

Uncertainties regarding the comminution dating method are discussed in the following sections. These include: the starting point for comminution in Section 1.3.6.1, isolating the detrital minerals in Section 1.3.6.2, preferential leaching of ^{234}U in Section 1.3.6.3, the initial activity ratio of the parent material in Section 1.3.6.3, estimation of the direct-recoil fraction in 1.3.6.4, mineral dissolution in Section 1.3.6.5, and aeolian input in Section 1.3.6.6.

1.3.6.1 Initial conditions for comminution ages

Comminution ages are typically regarded to represent the time elapsed since grains were reduced in size $<63\ \mu\text{m}$ at the soil-bedrock interface (DePaolo et al., 2006; Dosseto et al., 2010). However, it is also possible that the grain sizes of minerals are already sufficiently small in the bedrock for the direct-recoil of ^{234}U to be significant. The loss of recoiled ^{234}U nuclides could only occur if the rock has sufficiently porosity and/or fracture density for water/air movement (Fleischer, 1982). This effect may be significant for permeable rocks in which the majority of minerals are $<63\ \mu\text{m}$, e.g. siltstone, mudstone and claystone (Folk, 1974). In addition, rocks with high concentrations of accessory minerals, such as zircon and apatite, may also be affected. This is because these minerals are typically fine-grained (Farley et al., 1996), and U rich (Tieh and Ledger, 1981). Likewise, it is possible that mineral grains are not sufficiently reduced in size upon the breakdown of the bedrock for direct-recoil to become significant. If the radiometric clock is starting at different points within soil profiles and/or fluvial systems, comminution ages inferred for different catchments may not be comparable.

There is conflicting evidence to support whether or not the parent material is in secular equilibrium, but this has not been extensively tested. Data from bedrocks indicate that this assumption may not be true (e.g., Rosholt, 1983), with the exception of young volcanic rocks (e.g., Dosseto et al., 2003; Handley et al., 2011). However, glacial sediments were in secular equilibrium and support this hypothesis (DePaolo et al., 2012), assuming that the composition of the glacial sediments represents that of the bedrock. If the parent material is not in secular equilibrium, this can be accounted for by adjusting the initial activity ratio. For instance, assuming that $(^{234}\text{U}/^{238}\text{U})_{\text{initial}} = 1$, $(^{234}\text{U}/^{238}\text{U})_{\text{measured}} = 0.90$, and a direct-recoil fraction of 0.40 yields a comminution age of 100 ka. For the same hypothetical sample, assuming that $(^{234}\text{U}/^{238}\text{U})_{\text{initial}} = 0.95$ decreases the comminution age by 45% to 55 ka. Thus comminution ages are highly sensitive to U isotope disequilibrium in the parent material.

Further work is required to assess the initial activity of parent material on a catchment-wide scale. To address this, near-surface bedrock samples were sampled from catchment headwaters draining to the Gulf of Carpentaria in Chapter 3.

1.3.6.2 Isolating the detrital minerals

Sequential extraction procedures are currently used in comminution dating studies to isolate the detrital minerals, as outlined in Section 1.3.3. However, it is difficult to compare results from different studies as each comminution dating study has used different sample pre-treatment methods and the development of a standardised procedure is required. Furthermore, it is not clear whether the removal of non-detrital matter is complete, and investigations are required to determine this. Lee (2009) suggested that the removal of non-detrital matter could be monitored by measuring the $(^{234}\text{U}/^{238}\text{U})$ activity ratio of the solid residue throughout a sample pre-treatment procedure. Experiments of this nature were carried out and further details are given in Chapter 2.

1.3.6.3 Preferential leaching

Preferential leaching represents the leaching of labile ^{234}U from damaged lattice sites formed by alpha recoil, referred to as *alpha-recoil tracks* (Huang and Walker, 1967). It is possible that the *preferential leaching* of ^{234}U is occurring in the parent material, which represents bedrock or coarse-grained sediment ($>63\ \mu\text{m}$), and/or fine-grained sediment (Fleischer, 1980). Four types of tracks were classified by Lee (2009) (Figure 1.8): 1) ^{234}U directly-ejected out of the grain; 2) implanted ^{234}U following direct ejection from adjacent grains; 3) ^{234}U recoiled within the interior of the sediment protolith and alpha-recoil track exposed following comminution; and 4) ^{234}U recoiled at depths greater than 50 nm from the mineral surface.

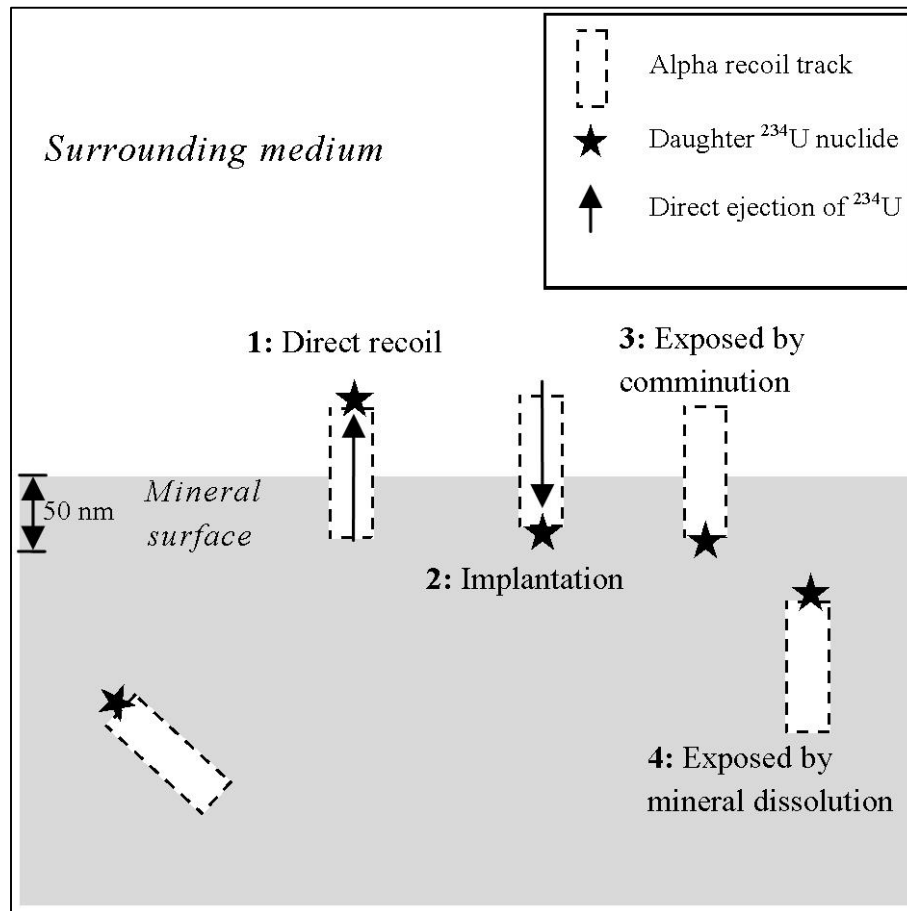


Figure 1.7 Conceptual diagram depicting the different types of alpha recoil tracks where preferential leaching of ^{234}U nuclides (stars) could occur 1: direct-ejection; 2: Post-comminution implantation from

adjacent grains; 3: leaching from pre-existing recoil tracks at time zero; and 4: recoil tracks located at a depth greater than 50 nm from the mineral surface (modified from Lee, 2009).

Type 1 recoil tracks are accounted for by the direct-recoil fraction, and nuclides from type 2 tracks are expected to be lost within 200 a (Fleischer, 1980). Therefore, nuclide loss from types 1 and 2 do not affect the accuracy of comminution ages. However, the exposure of type 3 and 4 tracks will result in a loss of labile ^{234}U as these tracks are not exposed at time zero. Preferential leaching from types 3 and 4 tracks is further discussed below.

The importance of preferential leaching from type 3 and 4 recoil tracks is firstly dependent on the age of the minerals; in newly formed minerals, the majority of ^{234}U nuclides will not have undergone alpha recoil and be in undamaged lattice sites that are less susceptible to leaching. However, after four half-lives of the daughter (ca. 1 Ma for ^{234}U), the majority of ^{234}U nuclides will be formed from the alpha decay of ^{238}U and reside in damaged lattice sites.

In older minerals, the leachability of the ^{234}U nuclides will therefore depend on the *annealing rate* of the alpha-recoil tracks. Annealing refers to the ability of the mineral to self-heal and spontaneously repair the damaged lattice site over time. The annealing rate of alpha-recoil tracks can be estimated by comparing the relative dissolution between different daughter-parent combinations with varying decay rates for the daughter nuclide. Based on the greater fractionation observed between ^{228}Th and ^{232}Th , compared to ^{234}Th and ^{234}U , and the half-lives of the daughter nuclides, the average timescale of annealing for alpha-recoil tracks was estimated to be ca. 15 ka by (Eyal and Fleischer, 1985a, b).

The percentage of ^{234}U nuclides that may be susceptible to preferential leaching can then be estimated by considering the relative rates of annealing and alpha decay, as given as (DePaolo et al., 2006; Maher et al., 2006):

$$\frac{\lambda_{234}}{\lambda_{\text{annealing}}} \quad (15)$$

where λ_{234} and $\lambda_{annealing}$ are the decay constant for ^{234}U in (a^{-1}), and the annealing rate of alpha recoil tracks (a^{-1}), respectively. By considering that $1/\tau_{annealing} = 1/15 \text{ ka}^{-1}$, it would be expected that ca. 5% of recoiled ^{234}U nuclides remain in damaged lattice sites that are not repaired by annealing.

The magnitude of ^{234}U loss from recoil tracks is currently unknown; the effects of preferential leaching can be assessed by considering a hypothetical sample with a direct-recoil fraction of 0.1 and initial activity ratio of 0.980 to simulate a small amount of ^{234}U loss due to weathering processes in the parent material (Figure 1.7). After 10 ka, the measured activity would be 0.978 and the apparent age would be 89 ka, representing an error of 79 ka and a relative error of 790 %. After 500 ka has elapsed, the measured activity would be 0.919 and the apparent age would be 690 ka, representing an error of 190 ka and 38 %. Therefore, the effects of preferential leaching may be more important for younger samples. Quantifying the initial loss of ^{234}U in the parent material and fine-grained sediment ($<63 \mu\text{m}$) is therefore a key research goal.

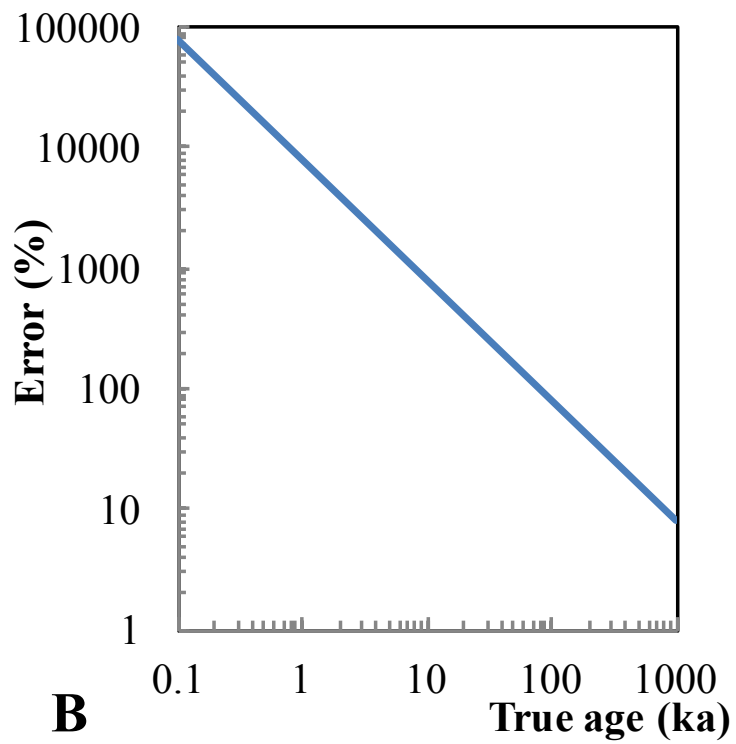
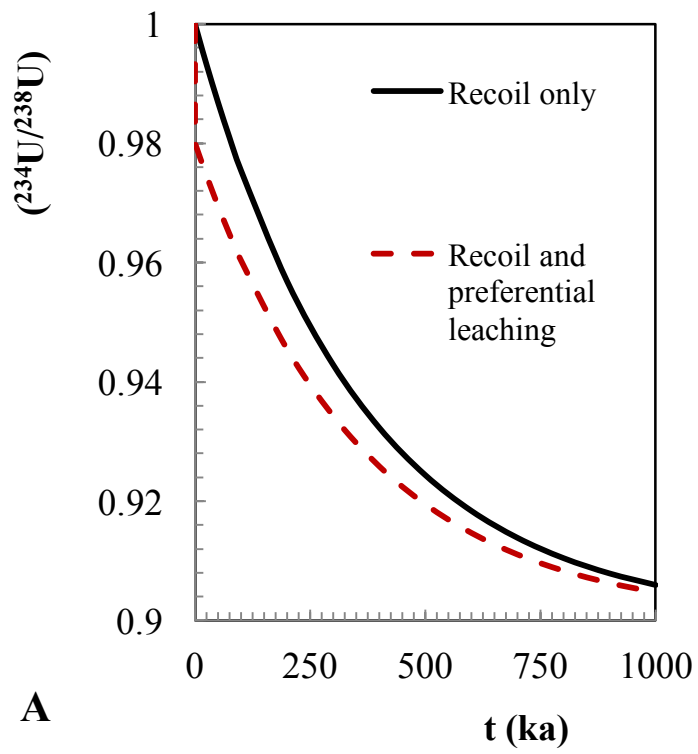


Figure 1.8A) Initial loss of ^{234}U due to preferential leaching from type 3 recoil tracks, leading to an initial activity ratio of 0.98. B) Percentage difference between apparent comminution ages and true ages due to preferential leaching.

Preferential leaching from type 4 tracks could occur as the grain surface is removed by mineral dissolution. DePaolo et al. (2006) evaluated this by considering the time required to remove a surface layer L (30 nm) for a sample with a comminution age of 354 ka, given as:

$$\frac{\tau_{recoil}}{\tau_{dissolution}} = \frac{R}{\lambda_{234} L \rho} \quad (16)$$

where λ_{234} is the rate of formation for the ^{234}U -depleted outer rind (in a^{-1}), ρ is the mineral density (2.70 kg m^{-3}), R is the mineral dissolution rate ($2.50 \times 10^{-18} \text{ mol m}^{-2} \text{ s}^{-1}$), and τ_{recoil} and $\tau_{dissolution}$ are the timescales of direct recoil and mineral dissolution (in ka), respectively. By considering $\tau_{dissolution} = 354 \text{ ka}$, DePaolo et al. (2006) suggested that ^{234}U depletion mainly results from direct recoil. However, in the case of higher mineral dissolution rates, the comminution age equation should be modified as (Dosseto and Schaller, 2016):

$$t_{comm} = \frac{-1}{\lambda_{234}} \ln \left[\left(\frac{A - (1 - f_d)(1 - f_d)}{(A_0 - (1 - f_d)(1 - f_d))} \right) \right] \quad (17)$$

where f_d is the fraction of ^{234}U released from type 4 recoil tracks during dissolution. The rate of ^{234}U release from type 4 recoil tracks will depend on the dissolution rate and surface area of minerals.

1.3.6.4 Accurately estimating the direct-recoil fraction

In summary, uncertainties regarding surface roughness and particle shapes limit the use of geometric models (Lee et al., 2010). Therefore, direct-recoil models based on surface area measurements are more reliable. However, the BET specific surface area overestimates the surface area relevant to recoil and a fractal correction is required.

In this thesis, it is assumed that further comminution is not significant once particles become $< 63 \text{ }\mu\text{m}$, and the direct-recoil fraction thus remains constant. Flume experiments show that the abrasion of the suspended load in fluvial systems is limited (Attal and Lavé, 2009), and

therefore, the assumption appears to be reasonable. In addition, it is assumed that mineral dissolution effects are not significant on the timescales of alpha recoil, as outlined in Section 3.2.

The effects of increasing surface roughness can be assessed by allowing the direct-recoil fraction to vary linearly between 0.20 and 0.30 from 0 – 1000 ka (Figure 1.10), which represents the typical range of reported values (DePaolo et al., 2006; Dosseto et al., 2010). If the direct-recoil fraction is increasing over time, comminution ages should be regarded as minimum ages. Furthermore, the discrepancy between true ages and calculated ages increases over time, and is particularly significant from ca. 200 ka onwards.

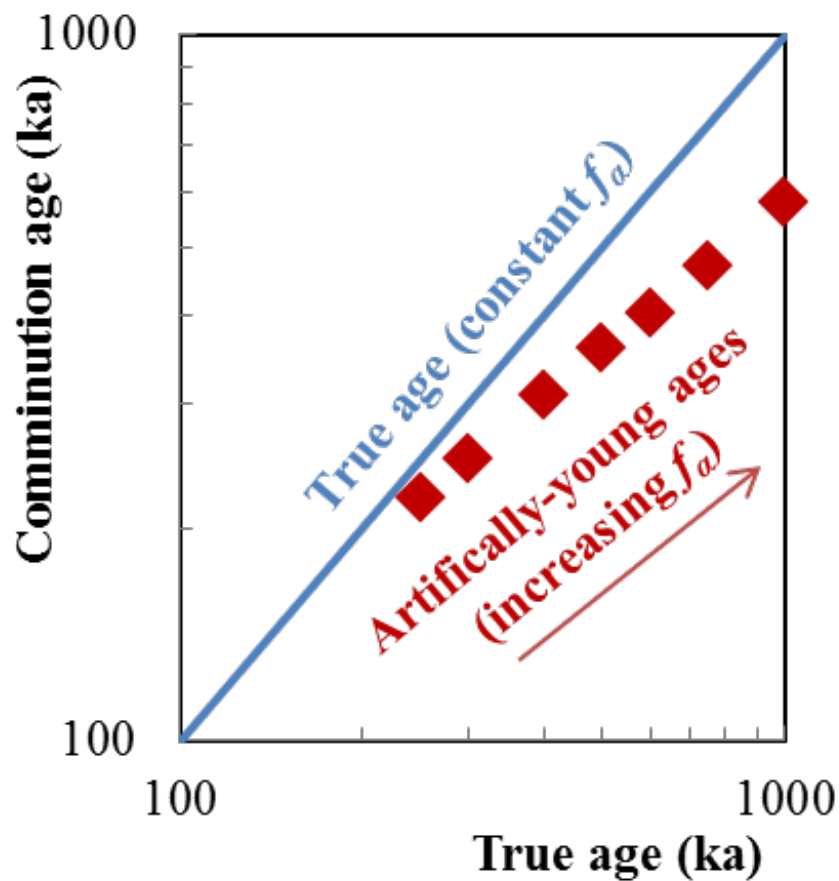


Figure 1.9 Model of direct-recoil fraction varying linearly from 0.20 – 0.30 over 1000 ka, where error bars represent comminution ages subtracted from real ages.

1.3.6.5 Aeolian input

Aeolian input can affect comminution ages by providing allochthonous <63 µm material that is not related to the process being studied, such as hillslope and fluvial transport processes. For instance, the addition of dust to a regolith profile provides fine-grained material that is not related to hillslope processes and may skew expected relationships between the sediment residence time and parameters. Potential aeolian contribution and the effect on sediment residence times must therefore be assessed.

Dosseto et al. (2010) suggested aeolian contribution should lead to short sediment residence times in palaeochannel deposits of the Murrumbidgee River, southeastern Australia. This is because palaeo sediment residence times were shortest during the LGM when dust deposition rates are expected to have been at a maximum. Thus, dust and fluvial components were assumed to be $(^{234}\text{U}/^{238}\text{U}) = 1.00$ and 0.94 (the latter similar to interglacial sediments with lowest possible dust contribution), respectively. In this case, a minimum dust contribution of ~80 wt% would be required to yield $(^{234}\text{U}/^{238}\text{U}) = 0.99$ as observed for LGM sediment. This was considered unlikely since the palaeochannel discharge during the LGM was estimated to be greater than the modern channel.

Handley et al. (2013b) sampled a sand dune from the Flinders Ranges, South Australia and found that aeolian material had a much shorter sediment residence time when compared to the average sediment residence time for valley-fill alluvial deposits. Suresh et al. (2014) attempted to assess aeolian contribution to fluvial sediment from the Murrumbidgee River using a binary mixing model for concentrations and isotopic ratios; no relationships were found, but only one dust sample was used and more samples are likely required.

1.4 Study area

In this thesis, comminution dating was applied to the Gulf of Carpentaria (herein termed ‘the Gulf’), which is an epicontinental sea located between northern Australia and New Guinea (Figure 1.11A). The Gulf is an interesting area to study the effects of climate on sediment transport for the following reasons: 1) the region is tectonically stable allowing past variations in sediment transport to be attributed to past climate change (Torgersen et al., 1983); 2) rainfall is mainly sourced from the Indo-Australian monsoon and past variations in the strength of monsoon are expected to produce large variations in sediment transport (Magee et al., 2004; Muller et al., 2012; Suppiah, 1992; Williams et al., 2009); and 3) sedimentary deposits in the Gulf have detailed depositional age chronologies that cover the last glacial-interglacial cycle, and Late Quaternary palaeoenvironments are well understood (Chivas et al., 2001; Reeves et al., 2008; Torgersen et al., 1983; Torgersen et al., 1988); for instance, the extent of Lake Carpentaria shown in Figure 1.11B.



Figure 1.10A) The Gulf of Carpentaria showing delineated catchment areas, major fluvial channels and core locations (+); B) Sahul during Last Glacial Maximum (sea level: -125 m below present sea level) and

where grey lines showing modern shorelines; and C) Regional setting showing key palaeoclimate study sites. The solid lines delineate catchment areas, and labelled dashed lines depict the -53 and -59 m isobaths.

In the Gulf of Carpentaria, samples are available from sedimentary cores with known depositional ages (cores MD32 and MD33 from Chivas et al. (2001) and Reeves et al. (2008) as shown in Figure 1.11A), which allows palaeo sediment residence times to be calculated from comminution ages (Figure 1.6). The effect of Late Quaternary climate change can be inferred from nearby palaeoclimate records at Lynch's Crater (Kershaw et al., 2007b; Turney et al., 2004), and core Fr95-17 (van Der Kaars and De Deckker, 2002), (Figure 1.11C). These palaeoclimate records are discussed further in Section 1.4.4. Combined with palaeoenvironmental data from the Gulf (Chivas et al., 2001; Reeves et al., 2008), sediment dynamics inferred from comminution dating can be placed in context of past environmental changes.

Previous application of comminution dating to the Murrumbidgee River in temperate southeastern Australia showed shorter residence times during glacial periods and longer residence times during interglacial periods (Dosseto et al., 2010). By studying sedimentary deposits from the Gulf, the landscape response of tropical and temperate Australia to Late Quaternary climate change can be broadly assessed.

Descriptions of the modern climate, hydrology, catchments, palaeoenvironments, and palaeoclimate for the Gulf and northern Australia are given in the following sections.

1.4.1 Climate

Rainfall in northern Australia ranges from 400 – 2000 mm a⁻¹ (BOM, 2009), and is largely controlled by the Indo-Australian monsoon, which is typically active from December to March (Reeves et al., 2008). The Indo-Australian monsoon provides the majority of the annual precipitation in northern Australia and is primarily driven by the inter-tropical

convergence zone (ITCZ) (Suppiah, 1992) (Figure 1.11). The ITCZ is the low pressure component of the equatorial Hadley Cell and is characterised by intense rainfall and thunderstorms. The position of the ITCZ is controlled by the position of sun's zenith point and migrates south towards Australia during the austral summer from November to February (Figure 1.11). The northern migration of the ITCZ, and subtropical high pressure ridge, leads to dry conditions from March to October in northern Australia. In the Gulf, rainfall from the Coral Sea/Pacific Ocean is further limited due to orographic lifting by the Great Dividing Range in the east.

The monsoon in northern Australia is facilitated by the formation of *thermal lows*, which are caused by the reflection of solar radiation to the lower atmosphere (Suppiah, 1992). Thermal lows form in areas which receive intense solar radiation, cloudless skies and have a high surface albedo. In Australia, there are two areas where heat lows are predominant: the Pilbara region in Western Australia and Cloncurry in western Queensland. These form in the months leading up the austral summer (October to December), and they trigger monsoonal circulation.

Monsoonal activity in northern Australia can be classified into three types (Gentili, 1971): true, pseudo and quasi-monsoons. In north-western Australia, a *pseudo-monsoon* is formed by the Pilbara thermal low, and deflects southeastern trade winds to form northwesterly wind; the *quasi-monsoon* is formed by a similar mechanism but is due to the Clonclurry thermal low. The *true monsoon* is caused by the asymmetric heating of land and the oceans in summer and considered to only represent the area north of 20°S.

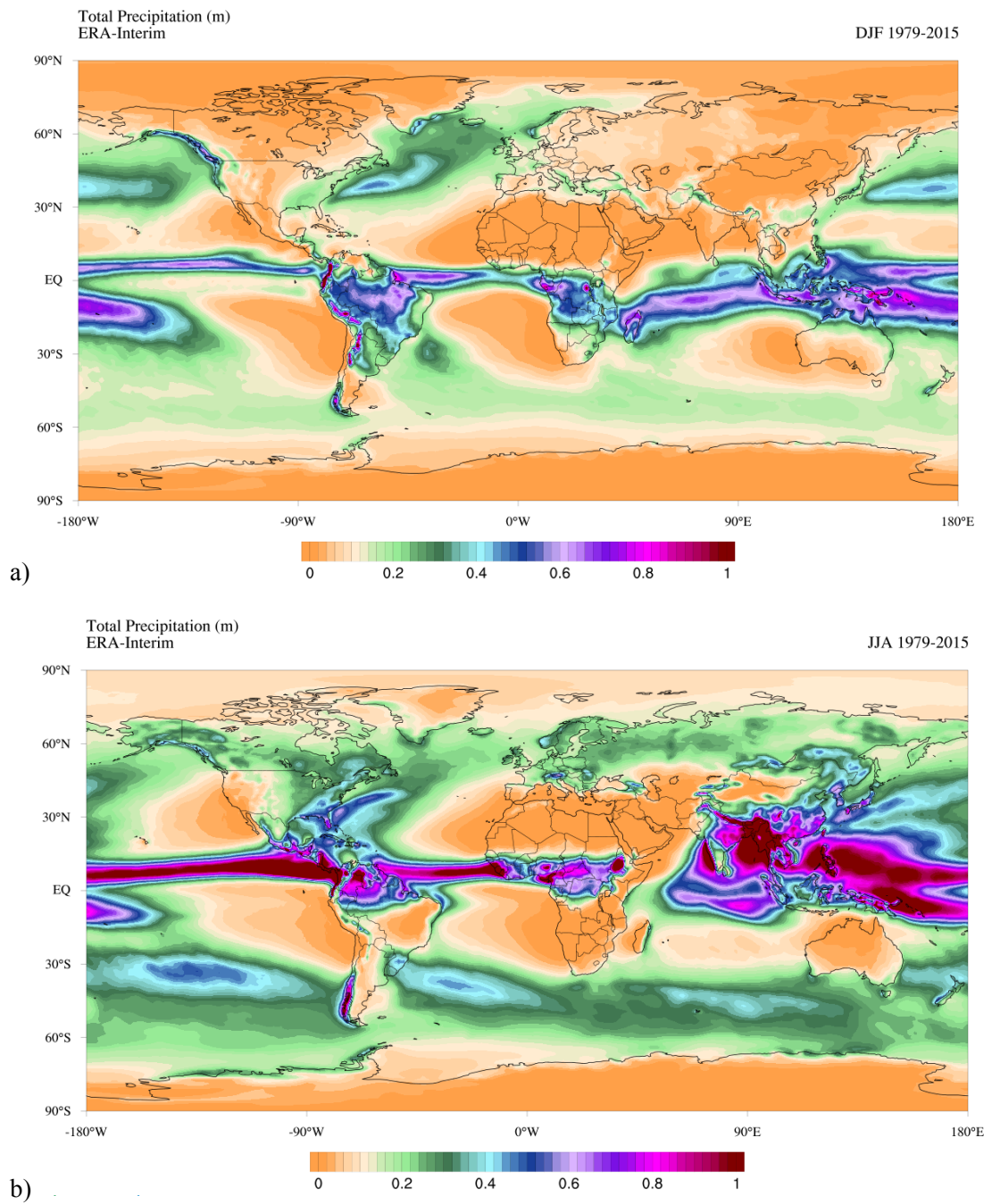


Figure 1.11 Total precipitation during the austral summer (DJF: December/January/February) and winter (JJA: June/July/August). Maps obtained using Climate Reanalyzer (<http://cci-reanalyzer.org>), Climate Change Institute, University of Maine, USA and the ERA-Interim dataset (1979-2015).

1.4.2 Hydrology

The Gulf is located between the landmasses of Australia and New Guinea and extends from 10 – 18°S. The water body covers an area of ca. 230,000 km² and has a maximum depth of ca. 70 m in the central-eastern section. The Gulf is located at an important junction between the Indian and Pacific Oceans, and is in close proximity to the Indo-Pacific Warm Pool, which is thought to play an important role in driving glacial-interglacial cycles (Visser et al., 2003).

Diurnal tides enter the Gulf from the northwest and circulate clockwise; more frequent, semi-diurnal tides are also present, but they are focussed on the northern section of the Gulf (Wolanski, 1993). North-westerly trade winds are prevalent during the summer monsoon and result in a clockwise circulation. Occasionally, weak south-easterly trade winds produce a counter-clockwise circulation. Overall, this results in a clockwise residual current. Seasonal changes in wind patterns create sea-level fluctuations of 0.5 m in coastal areas.

The Gulf is semi-enclosed from the Coral Sea by the Torres Strait to the east (-12 m below present sea level), and the Arafura Sea/Indian Ocean by the Arafura Sill to the west (-53 m below present sea level). During low sea-level stands, the continental shelf of the Gulf was exposed and formed a land-bridge between Australia and New Guinea.

1.4.3 Catchments

The Gulf of Carpentaria drainage basin extends from 8 – 22°S and has a catchment area of 1,130,000 km², which represents an area equivalent to 15% of the Australian continent. The maximum elevation in the drainage basin is ca. 1600 m on Great Dividing Range in the east. Long-term denudation rates in northern Australia are generally held to be low. No denudation rates are available for bedrock surfaces in the Gulf of Carpentaria drainage basin, but bedrock denudation rates in northern Australia are generally slow, <4 m Ma⁻¹ (Belton et

al., 2004; Bierman and Caffee, 2002). No denudation rates derived from cosmogenic nuclide concentrations are available Gulf of Carpentaria drainage, but dating of basalt surfaces in the Flinders River indicate an average denudation rate of 20 m Ma^{-1} (Coventry et al., 1985), which supports catchment-wide denudation rates derived from cosmogenic nuclides in northeastern Australia of $15 - 20 \text{ m Ma}^{-1}$ (Nichols et al., 2014).

Fluvial channels in Gulf catchments are generally wide (50 – 100 m), sandy, low sinuosity, and anabranching, with extensive floodplains (Nanson et al., 1991). Floodplain units comprise muds, muddy-sands, and sands, with various depositional ages that reflect Late Quaternary climate fluctuations discussed in Section 1.4.3. Channel reaches can be partly filled with recently deposited, unconsolidated sand and/or expose older floodplain units. Fluvial megafans have formed in the downstream areas of many catchments, and these are discussed in Section 1.4.4.1.

Alluvial gullying of floodplains is noted to be a major source of sediment to modern channels, and this is noted to be extensive for the Mitchell River (Brooks et al., 2009). Fallout radionuclide measurements of ^{137}Cs confirmed that sediment is mainly sourced from alluvial gully and channel bank erosion in Gulf catchments (Caitcheon et al., 2012). Shellberg et al. (2010) propose that land clearing and cattle grazing has initiated and/or increased alluvial gully erosion; however, historical records note the presence of deep gullies in Gulf catchments before European settlement (Gilbert, 1845; Leichhardt, 1847).

Detailed geological and morphometric information regarding the study catchments are given in Chapter 3.

1.4.3.1 Fluvial megafans

Fluvial megafans are large, fan-shaped, depositional features that develop in the downstream portions of catchments and laterally migrate from the exit of the erosion zone (or topographic front) in the upstream area (DeCelles and Cavazza, 1999). Although similar to alluvial fans, fluvial megafans are distinguished by their large areas of 1000 – 10000 km², low gradients of 0.10 – 0.01° and sedimentary deposits are typically water-laid and absent of sediment gravity flows observed in alluvial fans (DeCelles and Cavazza, 1999; Leier et al., 2005). In a broader sense, fluvial megafans can be considered as *distributive fluvial systems*, which represent aggradational depositional systems that are dominated by distributive planforms in both subaerial and subaqueous settings (Weissmann et al., 2010).

Interestingly, fluvial megafans are only found in areas with large seasonal fluctuations in discharge, typically due to seasonal or monsoonal rainfall, and are absent in tropical areas with consistent rainfall throughout the year (Leier et al., 2005). Not all rivers that undergo large fluctuations in discharge form fluvial megafans and climate is therefore not the only control on fluvial megafan formation. This is because space is required for channels to migrate laterally, and valleys or neighbouring channels can constrict the formation of fluvial megafans.

In the Gulf of Carpentaria drainage basin, fluvial megafans have been noted in the Mitchell River (Brooks et al., 2009), Gilbert River (Nanson et al., 1991), and Flinders River (Weissmann et al., 2010). Megafans in the Gulf are formed in the lower ca. 100 km of catchments and are ca. 50 – 100 km in length at the widest point downstream. Geological strata of megafans vary in age from Holocene to Pre-Pliocene, and the megafans are suggested to have formed due to Late Quaternary climatic fluctuations (Brooks et al., 2009). These sedimentary features are expected to represent sediment sinks in the hillslope-fluvial system and may have long sediment residence times.

1.4.4 Gulf palaeoenvironments

Throughout the Late Quaternary, palaeoenvironments and depositional environments have existed in the Gulf, including open marine, shallow marine (Torres Strait closed), brackish lake (Torres Strait and Arafura Sill closed), freshwater lake ('Lake Carpentaria') and sub-aerial exposure (Chivas et al., 2001; Reeves et al., 2008). During the last interglacial in MIS 5, the Gulf was a shallow marine environment until falling sea levels caused the formation of a brackish lake during the MIS 5/4 transition. Estuarine conditions, with occasional sub-aerial exposure of the Gulf floor, were present until the MIS 4/3 transition. Lake Carpentaria then persisted until the MIS 2 termination when rising sea levels led to marine waters re-entering the Gulf. A more detailed review of palaeoenvironments throughout the Late Quaternary is given in Chapter 4.

1.4.5 Palaeoclimate and past vegetation changes

Palaeoclimatic records indicate that northern Australia experienced generally wet interglacial and dry glacial periods throughout the Late Quaternary (Nanson et al., 1992). Sedimentary records in the Gulf extend back to ca. 120 ka and past climates in northern

Australia during this period are outlined here. Key palaeoclimatic sites include the Gilbert River in the Gulf of Carpentaria drainage basin, and the Lake Eyre drainage basin in central Australia. Although Lake Eyre is located in the arid Australian interior, the drainage basin extends to the southern limit of the Gulf of Carpentaria basin and is fed by monsoonal rains.

Detailed pollen records are available from the nearby Lynch's Crater in northeastern Australia (Kershaw et al., 1993; Moss and Kershaw, 2000; Kershaw et al., 2007b; Moss and Kershaw, 2007), and marine core Fr95-17, which is located offshore from Cape Range in northwestern Australia (van der Kaars et al., 2006). Although this is further away from the Gulf than Lynch's Crater, the regional climate at Cape Range is more analogous to the Gulf than Lynch's Crater. This is because Lynch's Crater is located to the east of the Great Dividing Range and is not affected by the rain shadow to the west of the Great Dividing Range.

During MIS 5d – 5c, alluvial deposits of coarse sands from the Gilbert River indicate that large, laterally migrating channels were present in northern Australia (Nanson et al., 2005). Continuous filling of Lake Eyre during MIS 5 indicates that monsoonal rains extended to the arid Australian interior (Magee et al., 2004). The climate at this time was likely humid, with abundant monsoonal rainfall and *Eucalyptus* woodland (van der Kaars et al., 2006).

Various records suggest the cessation of pluvial conditions and the onset of aridity during MIS 5b at 100 – 90 ka. Calcrete and gypcrete deposits in the Gilbert River indicate the onset of aridity at ca. 90 ka, but alluvial deposits of coarse sand in the Gilbert River indicate pluvial conditions persisted until ca. 85 ka (Nanson et al., 2005). Deposition of aeolian material and dune building in the Gregory lakes in northwestern Australia is inferred from 99 ± 17 ka onwards (Bowler et al., 2001). Lake Eyre shallowed from 100 ka onwards, and eventually dried at 75 – 70 ka (Magee et al., 2004).

Arid conditions are inferred until sub-pluvial conditions returned during MIS 4 at around 65 ka. This is indicated by alluvial deposits in the Gilbert River from 65 – 50 ka (Nanson et al., 2005), and filling of Lake Eyre at 65 – 60 ka (Magee et al., 2004). Following this, the deposition of mud from 50 ka onwards in the Gilbert River indicates the decline of pluvial conditions and the onset of arid conditions (Nanson et al., 2005), which is consistent with pollen and geochemical evidence from the Gulf (Reeves et al., 2008; Torgersen et al., 1988). Palaeo-shorelines and the $\delta^{13}\text{C}$ and $\delta^{18}\text{O}$ composition of egg shells in Lake Eyre indicate that a major hydrological shift to aridity occurred at ca. 50 ka (Cohen et al., 2015; Magee et al., 2004; Miller et al., 1997). This coincides with the extinction of megafauna (Roberts et al., 2001), vegetation change from C_3 to C_4 plants (Miller et al., 2005), and the arrival of humans (Bowler et al., 2003) – possibly leading to increased fire burning of vegetation (Rule et al., 2012).

During the Last Glacial Maximum (LGM), the sea level was ca. 125 m below present around northern Australia, sea-surface temperatures were 1 – 3 °C cooler (Reeves et al., 2013), and the proportion of the continental land mass covered by the oceans was reduced from ca. 78 % at present to 64 % (De Deckker et al., 2003). Pollen evidence from northwestern Australia suggests that 32 – 20 ka represented the driest regional conditions of the past 100 ka with low rainfall resulting in mainly grassland vegetation (van der Kaars et al., 2006). In the Gulf, Lake Carpentaria contracted to the -63 m contour for the period 23 – 19 ka.

Wetter conditions returned to northern Australia between the Last Glacial Maximum and the Holocene, but the exact timing is unclear and variable between study sites. In the Gilbert River, mud deposits in the uppermost 3 – 6 m of the floodplain indicate the establishment of wetter conditions post-LGM (Nanson et al., 2005). In the Flores Sea, ^{232}Th fluxes in sedimentary deposits increase from 18 – 15 ka, indicating enhanced rainfall and increased continental runoff (Muller et al., 2012). This may suggest that the Indo-Australian monsoon

was active at low latitudes from 18 ka onwards. In northwestern Australia, pollen records indicate increased summer rainfall from 20 ka onwards at Cape Range (van der Kaars et al., 2006). This is supported by evidence from core MD98-2167, which is located offshore from the Kimberley and suggests increased rainfall from 21 ka (Kershaw et al., 2007a). Alluvial deposits from northwestern Australia suggest that an active flood regime was established by 14 ka, caused by reactivation of the monsoon that was stronger than at present (Wyrwoll and Miller, 2001). In northeastern Australia, *Eucalyptus* woodland was re-established at 17 ka in Lake Euramoo (Haberle, 2005).

During the Holocene, there is evidence that wetter conditions were established in northern Australia based on evidence from alluvial deposits in north-western Australia from 12 – 5 ka (Wende et al., 1997), and palaeo-flood deposits in northern Australia ca. 9 – 4 ka (Nott and Price, 1999). The Gulf was terrestrial during the glacial low-stand and marine waters re-entered the Gulf around 9 ka (Reeves et al., 2008). Pollen evidence suggests the modern vegetation surrounding the Gulf was established by 7.5 ka (Shulmeister, 1992).

Speleothem deposits from the Kimberley in northwestern Australia indicate variable monsoon activity during the Holocene (Denniston et al., 2013); the monsoon is inferred to be active in the early-Holocene, decreased by 4 ka, further decreased from 2 to 1 ka, and then re-strengthened at 1 ka. Present conditions are inferred to be wetter than during the LGM, but floodplain deposits indicate that rivers are not as powerful as during MIS 3 and 5 (Nanson et al., 2005).

Past variations in the palaeoclimate of northern Australia are expected to be recorded in the sedimentary deposits in the Gulf. The abundance of monsoonal rainfall in the Gulf is particularly sensitive to the north/southwards migration of ITCZ during glacial-interglacial cycle, particularly in the southern portion of the basin (Suppiah, 1992). Therefore, glacial-interglacial climate change has likely affected the relative contribution of the southern and

northern catchments to sediment deposited in the Gulf. These changes should result in extreme variations in sediment residence times.

1.5 References

Aciego, S., Bourdon, B., Schwander, J., Baur, H. and Forieri, A. (2011) Toward a radiometric ice clock: Uranium ages of the Dome C ice core. *Quaternary Science Reviews* 30, 2389-2397.

Allen, P.A. (2008). From landscapes into geological history. *Nature*, 451, 274-276.

Anbeek, C., Van Breemen, N., Meijer, E.L. and Van Der Plas, L. (1994) The dissolution of naturally weathered feldspar and quartz. *Geochimica et Cosmochimica Acta* 58, 4601-4613.

Attal, M. and Lavé, J. (2009) Pebble abrasion during fluvial transport: Experimental results and implications for the evolution of the sediment load along rivers. *Journal of Geophysical Research: Earth Surface* (2003–2012) 114.

Bacon, A.R., Richter, D.d., Bierman, P.R. and Rood, D.H. (2012) Coupling meteoric ^{10}Be with pedogenic losses of ^9Be to improve soil residence time estimates on an ancient North American interfluve. *Geology* 40, 847-850.

Bacon, J.R. and Davidson, C.M. (2008) Is there a future for sequential chemical extraction? *Analyst* 133, 25-46.

Belton, D.X., Brown, R.W., Kohn, B.P., Fink, D. and Farley, K.A. (2004) Quantitative resolution of the debate over antiquity of the central Australian landscape: implications for the tectonic and geomorphic stability of cratonic interiors. *Earth and Planetary Science Letters* 219, 21-34.

Berner, R.A., Lasaga, A.C. and Garrels, R.M. (1983) The carbonate-silicate geochemical cycle and its effect on atmospheric carbon dioxide over the past 100 million years. *American Journal of Science* 283, 641-683.

Bierman, P.R. and Caffee, M. (2002) Cosmogenic exposure and erosion history of Australian bedrock landforms. *Geological Society of America Bulletin* 114, 787-803.

Blanco, P., Vera Tomé, F. and Lozano, J.C. (2004) Sequential extraction for radionuclide fractionation in soil samples: A comparative study. *Applied Radiation and Isotopes* 61, 345-350.

BOM (2009) Mean monthly and mean annual rainfall data (base climatological datasets) Bureau of Meteorology.

Bonniwell, E.C., Matisoff, G. and Whiting, P.J. (1999) Determining the times and distances of particle transit in a mountain stream using fallout radionuclides. *Geomorphology* 27, 75-92.

Bouchez, J., Gaillardet, J., Lupker, M., Louvat, P., France-Lanord, C., Maurice, L., Armijos, E. and Moquet, J.-S. (2012) Floodplains of large rivers: Weathering reactors or simple silos? *Chemical Geology* 332–333, 166-184.

Bourdon, B., Bureau, S., Andersen, M.B., Pili, E. and Hubert, A. (2009) Weathering rates from top to bottom in a carbonate environment. *Chemical Geology* 258, 275-287.

Bourdon, B., Turner, S., Henderson, G.M. and Lundstrom, C.C. (2003).

Bowler, J.M., Johnston, H., Olley, J.M., Prescott, J.R., Roberts, R.G., Shawcross, W. and Spooner, N.A. (2003) New ages for human occupation and climatic change at Lake Mungo, Australia. *Nature* 421, 837-840.

- Bowler, J.M., Wyrwoll, K.-H. and Lu, Y. (2001) Variations of the northwest Australian summer monsoon over the last 300,000 years: the paleohydrological record of the Gregory (Mulan) Lakes System. *Quaternary International* 83, 63-80.
- Brantley, S.L. and Mellott, N.P. (2000) Surface area and porosity of primary silicate minerals. *American Mineralogist* 85, 1767-1783.
- Brooks, A.P., Shellberg, J.G., Knight, J. and Spencer, J. (2009) Alluvial gully erosion: an example from the Mitchell fluvial megafan, Queensland, Australia. *Earth Surface Processes and Landforms* 34, 1951-1969.
- Brown, E.T., Stallard, R.F., Larsen, M.C., Raisbeck, G.M. and Yiou, F. (1995) Denudation rates determined from the accumulation of in situ-produced ^{10}Be in the Luquillo Experimental Forest, Puerto Rico. *Earth and Planetary Science Letters* 129, 193-202.
- Brunauer, S., Emmett, P.H. and Teller, E. (1938) Adsorption of gases in multimolecular layers. *Journal of the American Chemical Society* 60, 309-319.
- Caitcheon, G.G., Olley, J.M., Pantus, F., Hancock, G. and Leslie, C. (2012) The dominant erosion processes supplying fine sediment to three major rivers in tropical Australia, the Daly (NT), Mitchell (Qld) and Flinders (Qld) Rivers. *Geomorphology* 151, 188-195.
- Cartwright, J. (1962) Particle shape factors. *Annals of Occupational Hygiene* 5, 163-171.
- Chabaux, F., Riotte, J. and Dequincey, O. (2003) U-Th-Ra fractionation during weathering and river transport. *Reviews in Mineralogy and geochemistry* 52, 533-576.
- Cheng, H., Edwards, R.L., Hoff, J., Gallup, C.D., Richards, D.A. and Asmerom, Y. (2000) The half-lives of uranium-234 and thorium-230. *Chemical Geology* 169, 17-33.

Chivas, A.R., Garcia, A., van der Kaars, S., Couapel, M.J.J., Holt, S., Reeves, J.M., Wheeler, D.J., Switzer, A.D., Murray-Wallace, C.V., Benerjee, D., Price, D.M., Wang, S.X., Pearson, G., Edgar, N.T., Beaufort, L., De Deckker, P., Lawson, E. and Cecil, C.B. (2001) Sea-level and environmental changes since the last interglacial in the Gulf of Carpentaria, Australia: An overview. *Quaternary International* 82-85, 19-46.

Church, M. and Slaymaker, O. (1989) Disequilibrium of Holocene sediment yield in glaciated British Columbia. *Nature* 337, 452-454.

Cohen, T.J., Jansen, J.D., Gliganic, L.A., Larsen, J.R., Nanson, G.C., May, J.-H., Jones, B.G. and Price, D.M. (2015) Hydrological transformation coincided with megafaunal extinction in central Australia. *Geology* 43, 195-198.

Coventry, R., Stephenson, P. and Webb, A. (1985) Chronology of landscape evolution and soil development in the upper Flinders River area, Queensland, based on isotopic dating of Cainozoic basalts. *Australian Journal of Earth Sciences* 32, 433-447.

Dahlkamp, F. (1993) *Geology of the uranium deposits*. Berlin, Springer Verlag.

De Deckker, P., Tapper, N. and van Der Kaars, S. (2003) The status of the Indo-Pacific Warm Pool and adjacent land at the Last Glacial Maximum. *Global and Planetary Change* 35, 25-35.

DeCelles, P. and Cavazza, W. (1999) A comparison of fluvial megafans in the Cordilleran (Upper Cretaceous) and modern Himalayan foreland basin systems. *Geological Society of America Bulletin* 111, 1315-1334.

Denniston, R.F., Wyrwoll, K.-H., Polyak, V.J., Brown, J.R., Asmerom, Y., Wanamaker, A.D., LaPointe, Z., Ellerbroek, R., Barthelmes, M. and Cleary, D. (2013) A stalagmite

record of Holocene Indonesian–Australian summer monsoon variability from the Australian tropics. *Quaternary Science Reviews* 78, 155-168.

DePaolo, D.J., Maher, K., Christensen, J.N. and McManus, J. (2006) Sediment transport time measured with U-series isotopes: Results from ODP North Atlantic drift site 984. *Earth and Planetary Science Letters* 248, 394-410.

Dequincey, O., Chabaux, F., Clauer, N., Sigmarsson, O., Liewig, N. and Leprun, J.C. (2002) Chemical mobilizations in laterites: evidence from trace elements and ^{238}U - ^{234}U - ^{230}Th disequilibria. *Geochimica et Cosmochimica Acta* 66, 1197-1210.

Dietrich, W.E., Dunne, T., Humphrey, N.F. and Reid, L.M. (1982) Construction of sediment budgets for drainage basins. *Sediment budgets and routing in forested drainage basins*, 5-23.

Dietrich, W.E., Reiss, R., Hsu, M.L. and Montgomery, D.R. (1995) A process-based model for colluvial soil depth and shallow landsliding using digital elevation data. *Hydrological processes* 9, 383-400.

Dosseto, A. (2014) Chemical Weathering (U-Series), in: Rink, W.J., Thompson, J. (Eds.), *Encyclopedia of Scientific Dating Methods*. Springer Netherlands, pp. 1-28.

Dosseto, A., Bourdon, B., Gaillardet, J., Maurice-Bourgoin, L. and Allègre, C.J. (2006) Weathering and transport of sediments in the Bolivian Andes: Time constraints from uranium-series isotopes. *Earth and Planetary Science Letters* 248, 759-771.

Dosseto, A., Bourdon, B., Joron, J.L. and Dupré, B. (2003) U-Th-Pa-Ra study of the Kamchatka arc: New constraints on the genesis of arc lavas. *Geochimica et Cosmochimica Acta* 67, 2857-2877.

Dosseto, A., Bourdon, B. and Turner, S.P. (2008a) Uranium-series isotopes in river materials: Insights into the timescales of erosion and sediment transport. *Earth and Planetary Science Letters* 265, 1-17.

Dosseto, A., Buss, H.L. and Chabaux, F. (2014) Age and weathering rate of sediments in small catchments: The role of hillslope erosion. *Geochimica et Cosmochimica Acta* 132, 238-258.

Dosseto, A., Buss, H.L. and Suresh, P.O. (2012) Rapid regolith formation over volcanic bedrock and implications for landscape evolution. *Earth and Planetary Science Letters* 337-338, 47-55.

Dosseto, A., Hesse, P.P., Maher, K., Fryirs, K. and Turner, S. (2010) Climatic and vegetation control on sediment dynamics during the last glacial cycle. *Geology* 38, 395-398.

Dosseto, A. and Schaller, M. (2016) The erosion response to Quaternary climate change quantified using uranium isotopes and in situ-produced cosmogenic nuclides. *Earth-Science Reviews* 155, 60-81.

Dosseto, A., Turner, S., Buss, H.L. and Chabaux, F. (2007) The timescale of sediment transport in a small tropical watershed. *Geochim. Cosmochim. Acta* 71, A972.

Dosseto, A., Turner, S.P. and Chappell, J. (2008b) The evolution of weathering profiles through time: New insights from uranium-series isotopes. *Earth and Planetary Science Letters* 274, 359-371.

Ewing, S.A., Paces, J.B., O'Donnell, J.A., Jorgenson, M.T., Kanevskiy, M.Z., Aiken, G.R., Shur, Y., Harden, J.W. and Striegl, R. (2015) Uranium isotopes and dissolved organic carbon in loess permafrost: Modeling the age of ancient ice. *Geochimica et Cosmochimica Acta* 152, 143-165.

Eyal, Y. and Fleischer, R.L. (1985a) Preferential leaching and the age of radiation damage from alpha decay in minerals. *Geochimica et Cosmochimica Acta* 49, 1155-1164.

Eyal, Y. and Fleischer, R.L. (1985b) Timescale of natural annealing in radioactive minerals affects retardation of radiation-damage-induced leaching.

Farley, K.A., Wolf, R.A. and Silver, L.T. (1996) The effects of long alpha-stopping distances on (U + Th)/He ages. *Geochimica et Cosmochimica Acta* 60, 4223-4229.

Field, C., Barros, V., Dokken, D., Mach, K., Mastrandrea, M., Bilir, T., Chatterjee, M., Ebi, K., Estrada, Y. and Genova, R. (2014) IPCC, 2014: Climate Change 2014: Impacts, Adaptation, and Vulnerability. Part A: Global and Sectoral Aspects. Contribution of Working Group II to the Fifth Assessment Report of the Intergovernmental Panel on Climate Change. Cambridge University Press, Cambridge, United Kingdom and New York, NY, USA.

Fleischer, R.L. (1980) Isotopic disequilibrium of uranium: Alpha-recoil damage and preferential solution effects. *Science* 207, 979-981.

Fleischer, R.L. (1982) Alpha-recoil damage and solution effects in minerals: uranium isotopic disequilibrium and radon release. *Geochimica et Cosmochimica Acta* 46, 2191-2201.

Folk, R. (1974) *Petrology of Sedimentary Rocks*. Hemphill Publishing Company, Austin, Texas.

Gentili, J. (1971) Dynamics of the Australian troposphere. *World Survey of Climatology: Climates of Australia and New Zealand*, 53-117.

Gilbert, J. (1845) Diary of the Port Essington Expedition, 18 Sept. 1844-28 June 1845. Mitchell Library: State Library of New South Wales.

Gleyzes, C., Tellier, S. and Astruc, M. (2002) Fractionation studies of trace elements in contaminated soils and sediments: a review of sequential extraction procedures. *TrAC Trends in Analytical Chemistry* 21, 451-467.

Haberle, S.G. (2005) A 23,000-yr pollen record from Lake Euramoo, Wet Tropics of NE Queensland, Australia. *Quaternary Research* 64, 343-356.

Handley, H.K., Turner, S., Afonso, J.C., Dosseto, A. and Cohen, T. (2013a) Sediment residence times constrained by uranium-series isotopes: A critical appraisal of the comminution approach. *Geochimica et Cosmochimica Acta* 103, 245-262.

Handley, H.K., Turner, S., Berlo, K., Beier, C. and Saal, A.E. (2011) Insights into the Galápagos plume from uranium-series isotopes of recently erupted basalts. *Geochemistry, Geophysics, Geosystems* 12, Q0AC14.

Handley, H.K., Turner, S.P., Dosseto, A., Haberlah, D. and Afonso, J.C. (2013b) Considerations for U-series dating of sediments: Insights from the Flinders Ranges, South Australia. *Chemical Geology* 340, 40-48.

Hashimoto, T., Aoyagi, Y., Kudo, H. and Sotobayashi, T. (1985) Range calculation of alpha-recoil atoms in some minerals using LSS-theory. *Journal of Radioanalytical and Nuclear Chemistry Articles* 90, 415-438.

Heimsath, A.M., Chappell, J., Spooner, N.A. and Questiaux, D.G. (2002) Creeping soil. *Geology* 30, 111-114.

Heimsath, A.M., Dietrich, W.E., Nishiizumi, K. and Finkel, R.C. (1997) The soil production function and landscape equilibrium. *Nature* 388, 358-361.

Heimsath, A.M., Fink, D. and Hancock, G.R. (2009) The ‘humped’ soil production function: eroding Arnhem Land, Australia. *Earth Surface Processes and Landforms* 34, 1674-1684.

Henderson, G.M. (2002) Seawater ($^{234}\text{U}/^{238}\text{U}$) during the last 800 thousand years. *Earth and Planetary Science Letters* 199, 97-110.

Herman, F., Seward, D., Valla, P.G., Carter, A., Kohn, B., Willett, S.D. and Ehlers, T.A. (2013) Worldwide acceleration of mountain erosion under a cooling climate. *Nature* 504, 423-426.

Hilton, R.G., Gaillardet, J., Calmels, D. and Birck, J.-L. (2014) Geological respiration of a mountain belt revealed by the trace element rhenium. *Earth and Planetary Science Letters* 403, 27-36.

Hilton, R.G., Galy, A., Hovius, N., Horng, M.J. and Chen, H. (2011) Efficient transport of fossil organic carbon to the ocean by steep mountain rivers: An orogenic carbon sequestration mechanism. *Geology* 39, 71-74.

Huang, W.H. and Walker, R.M. (1967) Fossil alpha-particle recoil tracks: a new method of age determination. *Science (New York, N.Y.)* 155, 1103-1106.

Jones, J. (1981) The estimation of long range dispersion and deposition of continuous releases of radionuclides to atmosphere. National Radiological Protection Board.

Kershaw, A., Van Der Kaars, S. and Flenley, J. (2007a) The Quaternary history of far eastern rainforests, *Tropical Rainforest Responses to Climatic Change*. Springer, pp. 77-115.

Kershaw, A.P., Bretherton, S.C. and van der Kaars, S. (2007b) A complete pollen record of the last 230 ka from Lynch's Crater, north-eastern Australia. *Palaeogeography, Palaeoclimatology, Palaeoecology* 251, 23-45.

Kigoshi, K. (1971) Alpha-recoil thorium-234: Dissolution into water and the uranium-234/uranium-238 disequilibrium in nature. *Science* 173, 47-48.

Kump, L.R., Brantley, S.L. and Arthur, M.A. (2000) Chemical weathering, atmospheric CO₂, and climate, pp. 611-667.

Lal, D. (1991) Cosmic ray labeling of erosion surfaces: in situ nuclide production rates and erosion models. *Earth and Planetary Science Letters* 104, 424-439.

Langmuir, D. (1978) Uranium solution-mineral equilibria at low temperatures with applications to sedimentary ore deposits. *Geochimica et Cosmochimica Acta* 42, 547-569.

Latham, A. and Schwarcz, H. (1987) On the possibility of determining rates of removal of uranium from crystalline igneous rocks using U-series disequilibria—1: a U-leach model, and its applicability to whole-rock data. *Applied Geochemistry* 2, 55-65.

Larsen, I.J., Montgomery, D.R. and Korup, O. (2010). Landslide erosion controlled by hillslope material. *Nature Geoscience*, 3, 247-251.

Lee, S.Y. and Baik, M.H. (2009) Uranium and other trace elements' distribution in Korean granite: implications for the influence of iron oxides on uranium migration. *Environmental geochemistry and health* 31, 413-420.

Lee, V.E. (2009) Radiogenic Isotope Geochemistry and the Evolution of the Earth's Surface and Interior. PhD Thesis at the University of California, Berkeley.

Lee, V.E., DePaolo, D.J. and Christensen, J.N. (2010) Uranium-series comminution ages of continental sediments: Case study of a Pleistocene alluvial fan. *Earth and Planetary Science Letters* 296, 244-254.

Leichhardt, L. (1847) *Journal of an Overland Expedition in Australia, from Moreton Bay to Port Essington:... During the Years 1844-1845*. T. & W. Boone.

Leier, A.L., DeCelles, P.G. and Pelletier, J.D. (2005) Mountains, monsoons, and megafans. *Geology* 33, 289-292.

Leleyter, L. and Probst, J.L. (1999) A new sequential extraction procedure for the speciation of particulate trace elements in river sediments. *International Journal of Environmental Analytical Chemistry* 73, 109-128.

Lindhard, J. and Scharff, M. (1961) Energy dissipation by ions in the keV region. *Physical Review* 124, 128.

Ma, L., Chabaux, F., West, N., Kirby, E., Jin, L. and Brantley, S. (2013) Regolith production and transport in the Susquehanna Shale Hills Critical Zone Observatory, Part 1: Insights from U-series isotopes. *Journal of Geophysical Research F: Earth Surface* 118, 722-740.

Magee, J.W., Miller, G.H., Spooner, N.A. and Questiaux, D. (2004) Continuous 150 ky monsoon record from Lake Eyre, Australia: insolation-forcing implications and unexpected Holocene failure. *Geology* 32, 885-888.

Maher, K., DePaolo, D.J. and Christensen, J.N. (2006) U-Sr isotopic speedometer: Fluid flow and chemical weathering rates in aquifers. *Geochimica et Cosmochimica Acta* 70, 4417-4435.

Malmon, D.V., Dunne, T. and Reneau, S.L. (2003) Stochastic theory of particle trajectories through alluvial valley floors. *The Journal of Geology* 111, 525-542.

Mann, M.E., Bradley, R.S. and Hughes, M.K. (1999) Northern hemisphere temperatures during the past millennium: inferences, uncertainties, and limitations. *Geophysical research letters* 26, 759-762.

Maroulis, J.C. and Nanson, G.C. (1996) Bedload transport of aggregated muddy alluvium from Cooper Creek, central Australia: A flume study. *Sedimentology* 43, 771-790.

Mathieu, D., Bernat, M. and Nahon, D. (1995) Short-lived U and Th isotope distribution in a tropical laterite derived from granite (Pitinga river basin, Amazonia, Brazil): application to assessment of weathering rate. *Earth and Planetary Science Letters* 136, 703-714.

Matmon, A., Bierman, P.R., Larsen, J., Southworth, S., Pavich, M., Finkel, R. and Caffee, M. (2003) Erosion of an ancient mountain range, the Great Smoky Mountains, North Carolina and Tennessee. *American Journal of Science* 303, 817-855.

Miller, G.H., Fogel, M.L., Magee, J.W., Gagan, M.K., Clarke, S.J. and Johnson, B.J. (2005) Ecosystem Collapse in Pleistocene Australia and a Human Role in Megafaunal Extinction. *Science* 309, 287-290.

Miller, G.H., Magee, J.W. and Jull, A.J.T. (1997) Low-latitude glacial cooling in the Southern Hemisphere from amino-acid racemization in emu eggshells. *Nature* 385, 241-244.

Montgomery, D.R. (2007) Soil erosion and agricultural sustainability. *Proceedings of the National Academy of Sciences of the United States of America* 104, 13268-13272.

- Muller, J., McManus, J.F., Oppo, D.W. and Francois, R. (2012) Strengthening of the Northeast Monsoon over the Flores Sea, Indonesia, at the time of Heinrich event 1. *Geology* 40, 635-638.
- Nanson, G.C., Jones, B.G., Price, D.M. and Pietsch, T.J. (2005) Rivers turned to rock: Late Quaternary alluvial induration influencing the behaviour and morphology of an anabranching river in the Australian monsoon tropics. *Geomorphology* 70, 398-420.
- Nanson, G.C., Price, D.M. and Short, S.A. (1992) Wetting and drying of Australia over the past 300 ka. *Geology* 20, 791-794.
- Nanson, G.C., Price, D.M., Short, S.A., Young, R.W. and Jones, B.G. (1991) Comparative uranium-thorium and thermoluminescence dating of weathered Quaternary alluvium in the tropics of northern Australia. *Quaternary Research* 35, 347-366.
- Nichols, K.K., Bierman, P.R., Hooke, R.L., Clapp, E.M. and Caffee, M. (2002) Quantifying sediment transport on desert piedmonts using ^{10}Be and ^{26}Al . *Geomorphology* 45, 105-125.
- Nichols, K.K., Bierman, P.R. and Rood, D.H. (2014) ^{10}Be constrains the sediment sources and sediment yields to the Great Barrier Reef from the tropical Barron River catchment, Queensland, Australia. *Geomorphology* 224, 102-110.
- Nott, J. and Price, D. (1999) Waterfalls, floods and climate change: evidence from tropical Australia. *Earth and Planetary Science Letters* 171, 267-276.
- O'Connor, T.P. and Kester, D.R. (1975) Adsorption of copper and cobalt from fresh and marine systems. *Geochimica et Cosmochimica Acta* 39, 1531-1543.

Olley, J., Murray, A., Mackenzie, D. and Edwards, K. (1993) Identifying sediment sources in a gullied catchment using natural and anthropogenic radioactivity. *Water Resources Research* 29, 1037-1043.

Pavich, M.J. (1989) Regolith residence time and the concept of surface age of the Piedmont "Peneplain". *Geomorphology* 2, 181-196.

Pavich, M.J., Brown, L., Harden, J., Klein, J. and Middleton, R. (1986) ^{10}Be distribution in soils from Merced River terraces, California. *Geochimica et Cosmochimica Acta* 50, 1727-1735.

Phillips, J.D., Marden, M. and Gomez, B. (2007) Residence time of alluvium in an aggrading fluvial system. *Earth Surface Processes and Landforms* 32, 307-316.

Portenga, E.W. and Bierman, P.R. (2011) Understanding Earth's eroding surface with ^{10}Be . *GSA Today* 21, 4-10.

Raymo, M. and Ruddiman, W.F. (1992) Tectonic forcing of late Cenozoic climate. *Nature* 359, 117-122.

Reeves, J.M., Bostock, H.C., Ayliffe, L.K., Barrows, T.T., De Deckker, P., Devriendt, L.S., Dunbar, G.B., Drysdale, R.N., Fitzsimmons, K.E., Gagan, M.K., Griffiths, M.L., Haberle, S.G., Jansen, J.D., Krause, C., Lewis, S., McGregor, H.V., Mooney, S.D., Moss, P., Nanson, G.C., Purcell, A. and van der Kaars, S. (2013) Palaeoenvironmental change in tropical Australasia over the last 30,000 years – a synthesis by the OZ-INTIMATE group. *Quaternary Science Reviews* 74, 97-114.

Reeves, J.M., Chivas, A.R., García, A., Holt, S., Couapel, M.J.J., Jones, B.G., Cendón, D.I. and Fink, D. (2008) The sedimentary record of palaeoenvironments and sea-level change in

the Gulf of Carpentaria, Australia, through the last glacial cycle. *Quaternary International* 183, 3-22.

Reneau, S.L., Dietrich, W.E., Donahue, D.J., JULL, A.T. and Rubin, M. (1990) Late Quaternary history of colluvial deposition and erosion in hollows, central California Coast Ranges. *Geological Society of America Bulletin* 102, 969-982.

Riebe, C.S., Kirchner, J.W. and Finkel, R.C. (2003) Long-term rates of chemical weathering and physical erosion from cosmogenic nuclides and geochemical mass balance. *Geochimica et Cosmochimica Acta* 67, 4411-4427.

Riebe, C.S., Kirchner, J.W., Granger, D.E. and Finkel, R.C. (2001) Minimal climatic control on erosion rates in the Sierra Nevada, California. *Geology* 29, 447-450.

Ritchie, J.C., Spraberry, J.A. and McHenry, J.R. (1974) Estimating soil erosion from the redistribution of fallout ¹³⁷Cs. *Soil Science Society of America Journal* 38, 137-139.

Roberts, R.G., Flannery, T.F., Ayliffe, L.K., Yoshida, H., Olley, J.M., Prideaux, G.J., Laslett, G.M., Baynes, A., Smith, M.A. and Jones, R. (2001) New ages for the last Australian megafauna: continent-wide extinction about 46,000 years ago. *Science* 292, 1888-1892.

Rosholt, J.N. (1983) Isotopic composition of uranium and thorium in crystalline rocks. *Journal of Geophysical Research* 88, 7315-7330.

Rule, S., Brook, B.W., Haberle, S.G., Turney, C.S., Kershaw, A.P. and Johnson, C.N. (2012) The aftermath of megafaunal extinction: ecosystem transformation in Pleistocene Australia. *Science* 335, 1483-1486.

Schultz, M.K., Burnett, W.C. and Inn, K.G.W. (1998) Evaluation of a sequential extraction method for determining actinide fractionation in soils and sediments. *Journal of Environmental Radioactivity* 40, 155-174.

Scott, M., Rotter, R. and Salter, P. (1985) Transport of fallout plutonium to the ocean by the Mississippi River. *Earth and Planetary Science Letters* 75, 321-326.

Semkow, T.M. (1991) Fractal model of radon emanation from solids. *Physical Review Letters* 66, 3012-3015.

Shellberg, J., Brooks, A. and Spencer, J. (2010) Land-use change from indigenous management to cattle grazing initiates the gulying of alluvial soils in northern Australia, 19th World Congress of Soil Science, Soil Solutions for a Changing World, pp. 1-6.

Shulmeister, J. (1992) A Holocene pollen record from lowland tropical Australia. *The Holocene* 2, 107-116.

Suppiah, R. (1992) The Australian summer monsoon: a review. *Progress in Physical Geography* 16, 283-318.

Suresh, P., Dosseto, A., Hesse, P. and Handley, H. (2014) Very long hillslope transport timescales determined from uranium-series isotopes in river sediments from a large, tectonically stable catchment. *Geochimica et Cosmochimica Acta* 142, 442-457.

Syvitski, J.P., Vörösmarty, C.J., Kettner, A.J. and Green, P. (2005) Impact of humans on the flux of terrestrial sediment to the global coastal ocean. *Science* 308, 376-380.

Tessier, A., Campbell, P.G.C. and Bisson, M. (1979) Sequential extraction procedure for the speciation of particulate trace metals. *Analytical Chemistry* 51, 844-851.

Tieh, T.T. and Ledger, E.B. (1981) Fission track study of uranium in two granites of central Texas. *Contributions to Mineralogy and Petrology* 76, 12-16.

Torgersen, T., Hutchinson, M.F., Searle, D.E. and Nix, H.A. (1983) General bathymetry of the Gulf of Carpentaria and the Quaternary physiography of Lake Carpentaria. *Palaeogeography, Palaeoclimatology, Palaeoecology* 41, 207-225.

Torgersen, T., Luly, J., De Deckker, P., Jones, M., Searle, D., Chivas, A. and Ullman, W. (1988) Late Quaternary environments of the Carpentaria basin, Australia. *Palaeogeography, Palaeoclimatology, Palaeoecology* 67, 245-261.

Trimble, S.W. (1977) The fallacy of stream equilibrium in contemporary denudation studies. *American Journal of Science* 277, 876-887.

Turney, C.S.M., Kershaw, A.P., Clemens, S.C., Branch, N., Moss, P.T. and Keith Fifield, L. (2004) Millennial and orbital variations of El Niño/Southern Oscillation and high-latitude climate in the last glacial period. *Nature* 428, 306-310.

van Der Kaars, S. and De Deckker, P. (2002) A Late Quaternary pollen record from deep-sea core Fr10/95, GC17 offshore Cape Range Peninsula, northwestern Western Australia. *Review of Palaeobotany and Palynology* 120, 17-39.

van der Kaars, S., De Deckker, P. and Gingele, F.X. (2006) A 100 000-year record of annual and seasonal rainfall and temperature for northwestern Australia based on a pollen record obtained offshore. *Journal of Quaternary Science* 21, 879-889.

Vigier, N., Bourdon, B., Lewin, E., Dupré, B., Turner, S., Chakrapani, G.J., van Calsteren, P. and Allègre, C.J. (2005) Mobility of U-series nuclides during basalt weathering: An example from the Deccan Traps (India). *Chemical Geology* 219, 69-91.

Vigier, N., Bourdon, B., Turner, S. and Allègre, C.J. (2001) Erosion timescales derived from U-decay series measurements in rivers. *Earth and Planetary Science Letters* 193, 549-563.

Vigier, N., Burton, K.W., Gislason, S.R., Rogers, N.W., Duchene, S., Thomas, L., Hodge, E. and Schaefer, B. (2006) The relationship between riverine U-series disequilibria and erosion rates in a basaltic terrain. *Earth and Planetary Science Letters* 249, 258-273.

Visser, K., Thunell, R. and Stott, L. (2003) Magnitude and timing of temperature change in the Indo-Pacific Warm Pool during deglaciation. *Nature* 421, 152-155.

von Blanckenburg, F., Bouchez, J. and Wittmann, H. (2012). Earth surface erosion and weathering from the ^{10}Be (meteoric)/ ^9Be ratio. *Earth and Planetary Science Letters*, 351, 295-305.

Von Blanckenburg, F., Bouchez, J., Ibarra, D.E. and Maher, K. (2015). Stable runoff and weathering fluxes into the oceans over Quaternary climate cycles. *Nature Geoscience*, 8, 538-542.

Wallbrink, P. and Murray, A. (1993) Use of fallout radionuclides as indicators of erosion processes. *Hydrological Processes* 7, 297-304.

Walling, D.E. (1983) The sediment delivery problem. *Journal of Hydrology* 65, 209-237.

Weissmann, G.S., Hartley, A.J., Nichols, G.J., Scuderi, L.A., Olson, M., Buehler, H. and Banteah, R. (2010) Fluvial form in modern continental sedimentary basins: Distributive fluvial systems. *Geology* 38, 39-42.

Wende, R., Nanson, G. and Price, D. (1997) Aeolian and fluvial evidence for Late Quaternary environmental change in the east Kimberley of Western Australia. *Australian Journal of Earth Sciences* 44, 519-526.

West, A.J., Galy, A. and Bickle, M. (2005) Tectonic and climatic controls on silicate weathering. *Earth and Planetary Science Letters* 235, 211-228.

West, N., Kirby, E., Bierman, P., Slingerland, R., Ma, L., Rood, D. and Brantley, S. (2013) Regolith production and transport at the Susquehanna Shale Hills Critical Zone Observatory, part 2: insights from meteoric ^{10}Be . *Journal of Geophysical Research: Earth Surface* 118, 1877-1896.

White, A.F., Blum, A.E., Schulz, M.S., Bullen, T.D., Harden, J.W. and Peterson, M.L. (1996) Chemical weathering rates of a soil chronosequence on granitic alluvium: I. Quantification of mineralogical and surface area changes and calculation of primary silicate reaction rates. *Geochimica et Cosmochimica Acta* 60, 2533-2550.

White, A.F. and Peterson, M. (1990) Role of reactive-surface-area characterization in geochemical kinetic models, *Chemical Modeling of Aqueous Systems II*. American Chemical Society, pp. 461-475.

Willenbring, J.K. and von Blanckenburg, F. (2010). Long-term stability of global erosion rates and weathering during late-Cenozoic cooling. *Nature*, 465, 211-214.

Willenbring, J.K., Codilean, A.T. and McElroy, B. (2013) Earth is (mostly) flat: Apportionment of the flux of continental sediment over millennial time scales. *Geology* 41, 343-346.

Williams, M., Cook, E., van der Kaars, S., Barrows, T., Shulmeister, J. and Kershaw, P. (2009) Glacial and deglacial climatic patterns in Australia and surrounding regions from 35 000 to 10 000 years ago reconstructed from terrestrial and near-shore proxy data. *Quaternary Science Reviews* 28, 2398-2419.

Wittmann, H., von Blanckenburg, F., Guyot, J.L., Maurice, L. and Kubik, P.W. (2009) From source to sink: Preserving the cosmogenic ^{10}Be -derived denudation rate signal of the Bolivian Andes in sediment of the Beni and Mamoré foreland basins. *Earth and Planetary Science Letters* 288, 463-474.

Wolanski, E. (1993) Water circulation in the Gulf of Carpentaria. *Journal of Marine Systems* 4, 401-420.

Wyrwoll, K.-H. and Miller, G.H. (2001) Initiation of the Australian summer monsoon 14,000 years ago. *Quaternary International* 83, 119-128.

2. Evaluating the removal of non-detrital matter from soils and sediment using uranium isotopes

Ashley Neil Martin^{1,*}, Anthony Dosseto¹ and Leslie P.J. Kinsley²

¹Wollongong Isotope Geochronology Laboratory, School of Earth & Environmental Sciences, University of Wollongong, Wollongong, NSW 2522, Australia.

²Research School of Earth Sciences, Australian National University, Canberra, ACT 0200, Australia.

*Corresponding author

Email: anm724@uowmail.edu.au

Telephone: (+61 2) 4221 3382

2.1 Abstract

The time elapsed since detrital minerals were reduced to $<63\ \mu\text{m}$ by weathering can be constrained by applying the comminution dating method, which is based on the ($^{234}\text{U}/^{238}\text{U}$) activity ratio and surface area properties of the detrital minerals. In order to constrain an accurate age, the detrital minerals should be isolated and non-detrital matter present must be completely removed. Here we evaluate current sample pre-treatment procedures for removing non-detrital matter using uranium isotopes. The ($^{234}\text{U}/^{238}\text{U}$) activity ratio of the solid residue decreased stepwise throughout sequential extraction procedures, which is attributed to the removal of non-detrital matter. Despite heterogeneity observed in the untreated samples, the final ($^{234}\text{U}/^{238}\text{U}$) activity ratio of solid residues from replicate experiments were within analytical error. This shows that the ($^{234}\text{U}/^{238}\text{U}$) activity ratio of the detrital minerals is consistent following removal of non-detrital matter. The addition of a complexing agent (sodium citrate) to extraction reagents decreased the readsorption of uranium, but did not affect the final ($^{234}\text{U}/^{238}\text{U}$) activity ratio. Mild HF/HCl etching experiments showed that the ($^{234}\text{U}/^{238}\text{U}$) activity ratio can be further decreased following sequential extraction. Particle-size distribution measurements revealed that the decrease in the ($^{234}\text{U}/^{238}\text{U}$) activity ratio is likely due to the dissolution of clay minerals. Mild HF/HCl etching of a rock standard also revealed a small amount of preferential leaching of ^{234}U ($<1\%$). The inferred comminution ages are generally beyond the limit of the technique (1000 ka). By assuming an initial activity ratio of 0.95 to account for preferential leaching effects, the ages of samples following sequential extraction were within analytical error. Mild HF/HCl etching following sequential extraction results in older ages, which is attributed to the further removal of clay minerals. We recommend sequential extraction followed by mild HF/HCl etching as sample pre-treatment for comminution dating studies.

Keywords: uranium; uranium-series isotopes; comminution age; sequential extraction.

2.2 Introduction

The uranium-series (U-series) isotopes are fractionated by chemical and physical weathering, and undergo radioactive decay on timescales relevant to Earth-surface processes (10^3 – 10^6 a). The *comminution dating* technique is a developing application of the U isotopes, which calculates the time elapsed since fine-grained, detrital minerals were reduced to $<63 \mu\text{m}$ by weathering (DePaolo et al., 2006). This is based on the *direct ejection* of ^{234}U (via the short-lived ^{234}Th) from detrital minerals following the alpha decay of ^{238}U (Kigoshi, 1971). Direct ejection leads to the formation of a ^{234}U -depleted rind on the surface of detrital grains (Figure 2.1); however, this ^{234}U -depleted rind is only measureable in fine-grained particles ca. $<63 \mu\text{m}$ due to their large surface-area-to-volume-ratio. Comminution ages (t) are calculated from the ($^{234}\text{U}/^{238}\text{U}$) activity ratio of the detrital minerals (A_{meas}), the initial activity ratio of parent material (assumed to be 1, A_0), the decay constant of ^{234}U (λ_{234}), and the *direct-recoil fraction* (f_α), which represents the number of ^{234}U nuclides directly-ejected out of the grain. The equation for calculating an age is shown in Equation 1 (DePaolo et al., 2006):

$$t = -\frac{1}{\lambda_{234}} \ln \left[\frac{A_{\text{meas}} - (1 - f_\alpha)}{A_0 - (1 - f_\alpha)} \right] \quad (1)$$

- ($^{234}\text{U}/^{238}\text{U}$) = 1: The ‘inner-core’ of detrital minerals.
- ($^{234}\text{U}/^{238}\text{U}$) < 1: The ‘outer-rind’ of the detrital minerals (ca. 50 nm).
- ▨ ($^{234}\text{U}/^{238}\text{U}$) > 1: Non-detrital matter comprised either surface coatings on detrital minerals or aggregates.
- ★ ^{234}U nuclides (via the short-lived ^{234}Th)
- ^{238}U nuclides

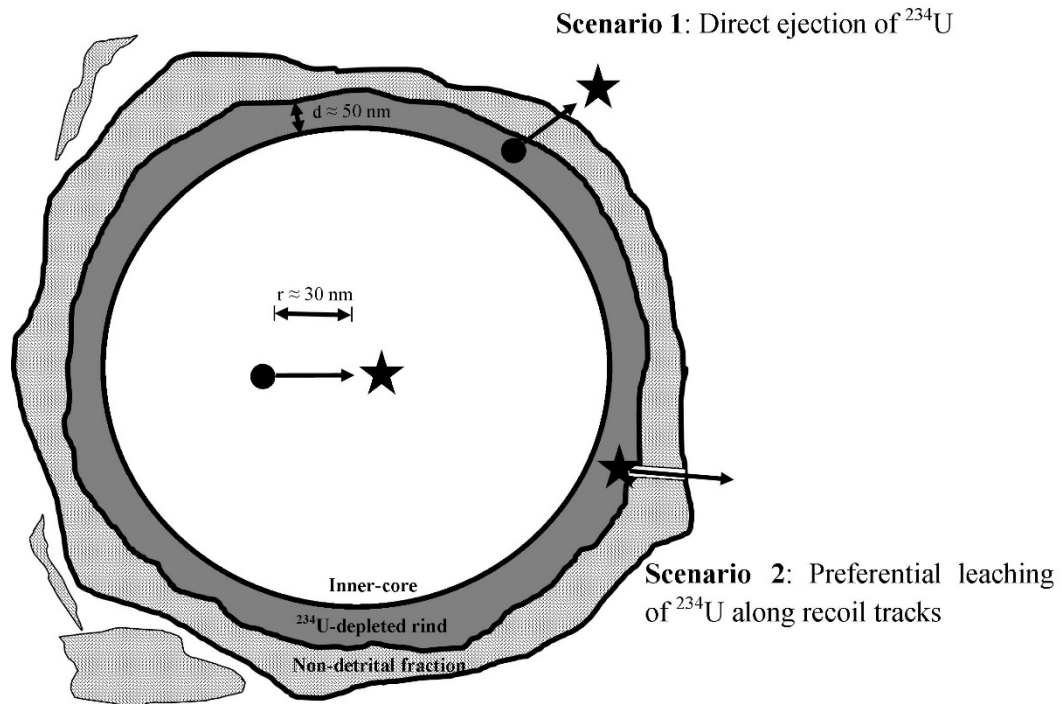


Figure 2.1 The three domains present in soils and sediment in terms of their respective ($^{234}\text{U}/^{238}\text{U}$) activity ratios and the two scenarios for ^{234}U -depletion: 1) direct ejection of ^{234}U (via the short-lived ^{234}Th); and 2) preferential leaching of ^{234}U from alpha-recoil tracks which are embedded as a result of direct ejection of ^{234}U from adjacent grains.

The technique has thus far been successfully applied to a North Atlantic marine core (DePaolo et al., 2006), palaeochannel deposits in south-eastern Australia (Dosseto et al., 2010), and ice cores in Antarctica (Aciego et al., 2011). Lee et al. (2010) attempted to calibrate the calculation of the direct-recoil fraction by assuming the transport time of glacial sediment was negligible. However, inferred comminution ages were less than the depositional ages, and a surface roughness factors was required to correct this. Comminution

dating was applied to an alluvial deposit in the Flinders Ranges, southern Australia using the fractal direct-recoil model (Handley et al., 2013b). Inferred ages were less than depositional ages, and decreased with depth. This was attributed to sediment samples comprising a mixture of fluvial sediment material and aeolian material. Inferred comminution ages of sediment from palaeochannel deposits in the Lake Eyre basin, central Australia were also less than depositional ages (Handley et al., 2013a). Furthermore, ages could not be produced for many samples as the direct-recoil fraction could not account for the measured ($^{234}\text{U}/^{238}\text{U}$) activity ratio. Comminution dating of sediments from the Lake Eyre basin is likely complicated by the fact that clay minerals travel as mud aggregates, and are resistant to disaggregation (Maroulis and Nanson, 1996). This shows that the comminution dating approach is currently only useful as a relative proxy for discerning between extreme variations in sediment transport (e.g. DePaolo et al., 2006; Dosseto et al., 2010), and measuring the release of ^{234}U from solids to the surrounding medium (e.g. Aciego et al., 2011; Bourdon et al., 2009). Further development is required to calculate reliable ages. For instance, a standardised sample pre-treatment method has not been developed. This is required to remove ^{234}U -rich non-detrital matter such as carbonates, iron oxides, and organic matter, and clay minerals (Andersson et al., 2001; Andersson et al., 1998; Paces et al., 2013; Plater et al., 1992; Porcelli et al., 1997). The U isotope composition of these phases is not related to the ^{234}U -depletion in detrital minerals, which is due to the direct ejection of ^{234}U . Thus non-detrital matter must be completely removed in order for ages calculated using the comminution dating technique to be reliable. Here we evaluate current sample pre-treatment procedures for removing non-detrital matter.

Sequential extraction procedures are currently used in comminution dating studies to remove non-detrital matter, and isolate the detrital minerals. It is difficult to compare results from different studies as each comminution dating study has used different sample pre-treatment methods: DePaolo et al. (2006) used a modified sequential extraction procedure based on

Tessier et al. (1979), and a further 1.5 M HCl leach; Dosseto et al. (2010) removed organic matter by ashing at 550°C followed by a 1.5 M HCl leach; Lee et al. (2010) used a modified sequential extraction procedure based on Tessier et al. (1979); while Handley et al. (2013a; 2013b) used a modified sequential extraction procedure based on Schultz et al. (1998). Blanco et al. (2004) attempted to compare the extraction of U using Tessier et al. (1979) and Schultz et al. (1998) (Table 2.1). However, the overall extraction of U was similar and only the distribution of U in each fraction varied between the two procedures. Furthermore, repeat experiments showed that the differences between the two procedures were not statistically significant. Here we attempt to evaluate the removal of non-detrital matter using U isotopes in order to develop a standardised procedure for the comminution dating technique. Furthermore, we measure the surface area properties of the detrital minerals in order to assess the effect of sample pre-treatment on the resulting comminution ages.

2.3 Conceptual model

The alpha decay of ^{238}U results in three theoretical domains in soils and sediment, with distinct ($^{234}\text{U}/^{238}\text{U}$) activity ratios, as shown in Figure 2.1.

Domain 1: ($^{234}\text{U}/^{238}\text{U}$) = 1

The inner-core of detrital minerals has the same isotopic composition as unweathered bedrock, and is in *secular equilibrium* whereby ($^{234}\text{U}/^{238}\text{U}$)_{S.E.} = 1. A system is in secular equilibrium if it has not undergone isotopic fractionation for at least four half-lives of the daughter nuclide. As the half-life of ^{234}U is $245,250 \pm 490$ a (Cheng et al., 2000), the inner-core of the detrital minerals will be in secular equilibrium if undisturbed for ca. 1 Ma (i.e. not exposed to weathering solutions).

Domain 2: ($^{234}\text{U}/^{238}\text{U}$) < 1

The outer ca. 50 nm ('outer-rind') of detrital minerals is ^{234}U -depleted due to the direct ejection of ^{234}U , which occurs on a length scale of ca. 30 nm in silicates (Hashimoto et al., 1985). Preferential leaching of ^{234}U from alpha-recoil tracks can also lead to ^{234}U -depletion by : i) the removal of embedded ^{234}U which is directly-ejected from adjacent grains (Figure 2.1); and/ or ii) the exposure of recoil tracks to weathering solutions as a result of mineral dissolution (Fleischer, 1980). This ^{234}U -depleted, outer-rind is only measureable in fine-grained detrital minerals (ca. <63 μm) where the surface-area-to-volume ratio is large enough.

Domain 3: ($^{234}\text{U}/^{238}\text{U}$) > 1

Non-detrital matter consists of authigenic weathering products (e.g. organic matter, carbonates etc.) and clay minerals. Natural waters are enriched in ^{234}U due to alpha-recoil effects (Kigoshi, 1971) and non-detrital matter is generally ^{234}U -rich (Andersson et al., 1998; Plater et al., 1992). Furthermore, organic colloidal particles (e.g. humic compounds) have a high affinity for U and are also ^{234}U -rich (Andersson et al., 2001; Porcelli et al., 1997). Thus, non-detrital matter generally has an activity ratio of ($^{234}\text{U}/^{238}\text{U}$) > 1.

Considering these three domains of ($^{234}\text{U}/^{238}\text{U}$) activity ratios, Lee (2009) suggested that the removal of non-detrital matter could be monitored by measuring the ($^{234}\text{U}/^{238}\text{U}$) activity ratio of the solid residue throughout a procedure. The removal of non-detrital matter should decrease the ($^{234}\text{U}/^{238}\text{U}$) activity ratio of the solid residue. The minimum ($^{234}\text{U}/^{238}\text{U}$) activity ratio should represent the optimal isolation of the detrital minerals. Any subsequent increase from this minimum value would imply dissolution of the ^{234}U -depleted outer-rind, and/or readsorption of released ^{234}U (Figure 2.2). An additional decrease in the ($^{234}\text{U}/^{238}\text{U}$) activity ratio following a sample pre-treatment procedure suggests that the removal of non-detrital matter was not complete.

In this study, firstly we monitored the ($^{234}\text{U}/^{238}\text{U}$) activity ratio by sampling an aliquot of the solid residue throughout a sequential extraction procedure. Repeat experiments were conducted to assess if the isotopic composition of the detrital minerals is consistent in separate sample aliquots. Mild HF etching was carried out to partially dissolve the outer-rind of the detrital minerals and determine the minimum ($^{234}\text{U}/^{238}\text{U}$) activity ratio. Finally, we evaluated the various sample pre-treatment procedures used in comminution age studies thus far using the ($^{234}\text{U}/^{238}\text{U}$) activity ratio.

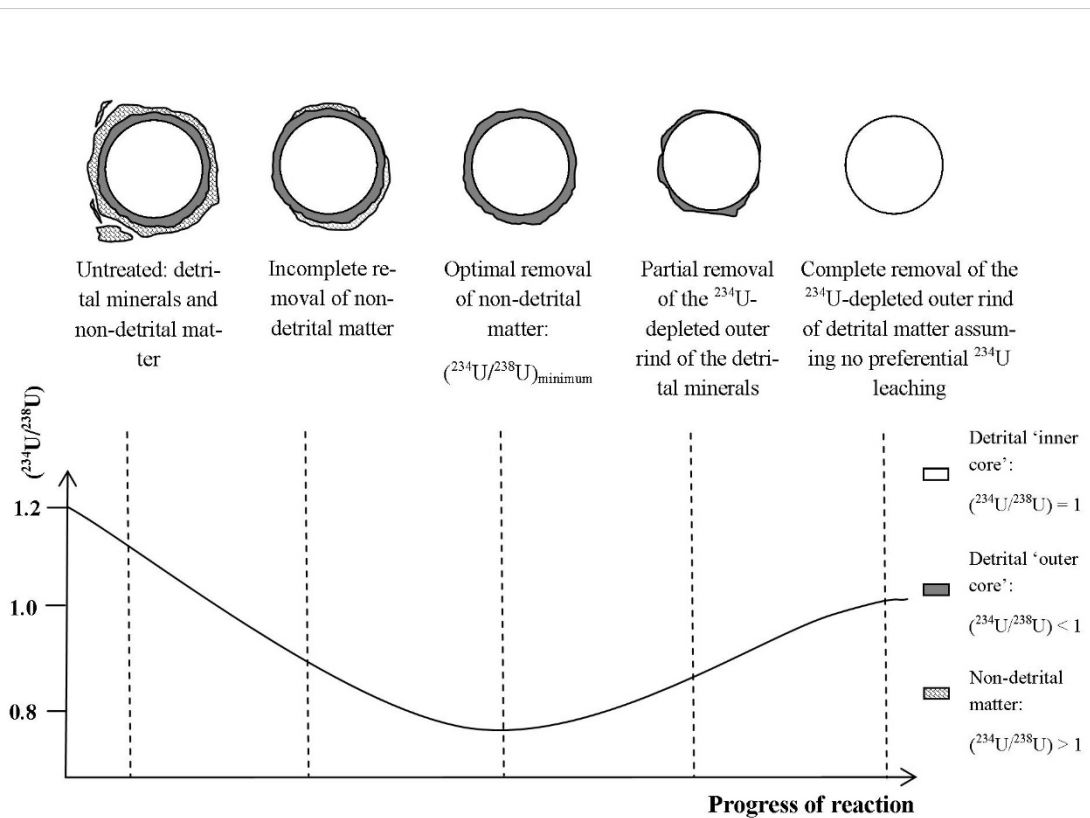


Figure 2.2 The hypothetical progression of the ($^{234}\text{U}/^{238}\text{U}$) activity ratio of the solid residue during the removal of non-detrital matter from the detrital minerals (modified from Lee, 2009).

2.4 Experimental methods and approach

A soil sample was collected from temperate rainforest on the Illawarra escarpment close to Otford, New South Wales, Australia (34.21°S 151.00°E 176m AMSL). The soil is a yellow podzol, which is developed over Triassic Sydney Basin Hawkesbury Sandstone (Young, 1982). The uppermost O-horizon was not sampled (0-0.1 m) and soil was collected from the A-horizon at a depth of 0.1 – 0.5 m. Suspended river sediment was sampled from the Leichhardt River from the Gulf of Carpentaria drainage basin in northern Australia (GOC-R16, Chapter 3), and marine sediment from core MD-32 (MD32-4a, Chapter 4) in the corresponding Gulf of Carpentaria sedimentary basin (Chivas et al., 2001). All samples were wet-sieved at 63 μm using deionised H_2O . The <63 μm fraction was retained, dried in an oven at 50 °C and homogenised by gentle mixing with an agate mortar and pestle. Experiments were carried out with 2 g aliquots of dry, homogenised sample. An orbital shaker at 200 rpm was used to agitate samples for experiments at room temperature and experiments requiring higher temperatures were carried out on a hotplate, and shaken manually every hour. The solid and aqueous phases were separated by centrifugation at 7000 rpm for 10 minutes. The aqueous phase was removed using disposable Pasteur pipettes (previously-rinsed with 2 % HNO_3) and retained for later analysis. After each step, the solid residues were rinsed twice with 10 mL 18.2 M Ω H_2O before collecting 100 mg aliquots for later analysis. In Experiments 1, 2, and 4 the leached sediment was dried and weighed after each step to determine the mass of the material removed by each step of the procedures.

The following operationally-defined phases are removed in the sequential extraction procedure from Tessier et al. (1979) and Schultz et al. (1996) (herein referred to as Tessier's and Schultz' procedure, respectively): the *exchangeable fraction* (F1), which refers to elements adsorbed to mineral surfaces; the *acid-soluble fraction* (F2), which is dissolved by acidic solutions and targets carbonate minerals such as calcite and dolomite; the *reducible fraction* (F3), which targets iron and manganese oxides, hydroxides, and oxyhydroxides,

with the use of a chemical reducing agent; and the *oxidisable fraction* (F4), which is removed by chemical or physical oxidation and targets organic matter. The remaining material following the removal of these operationally-defined fractions is referred to as the *residual fraction*, which should represent the detrital minerals. The reagents and conditions for each sequential extraction procedure are shown in Table 2.1.

Table 2.1 Reagents and conditions used in the sequential extraction procedures developed by Tessier et al. (1979) and Schultz et al. (1998).

Target phase	Reagents and Conditions	
	Tessier et al. (1979) ^a	Schultz et al. (1998) ^{a,b}
Water-soluble	8 mL H ₂ O	20 mL H ₂ O
(F0)	Room temp./1 h	Overnight
Exchangeable	8 mL 1 M MgCl ₂ at pH 7	20 mL 0.4 M MgCl ₂ at pH 5
(F1)	Room temp./1 h	Room temp./1 h
Acid-soluble	8 mL NaOAc/AcOH at pH 5	20 mL 1 M NaOAc/AcOH at pH 4
(F2)	Room temp./6 h	Room temp./2 h*
Reducible	20 mL 0.04 M NH ₂ OH.HCl/ AcOH at pH 2	20 mL 0.04 M NH ₂ OH.HCl/ AcOH at pH 2
(F3)	96 °C/5 h	Room temp./5 h
Oxidisable	8 mL 0.02 M HNO ₃ / H ₂ O ₂ at pH 2 85°C/2 h	20 mL NaOCl at pH 7.5
(F4)	3 mL H ₂ O ₂ at pH 2 85 °C/3 h	96 °C/ 0.5 h*
	5 mL 3.2 M NH ₄ OAc in HNO ₃ 20% diluted to 20 mL with H ₂ O Room temp./30 min	

^aReagent volumes for 1 g of sample.

^bThe order of extraction modified so that the oxidisable (F4) fraction is removed before F2 and F3.

*Extractions repeated twice.

In Exp. 1, the soil sample was leached according to Lee (2009), which utilises a modified version of Tessier's procedure (herein referred to as 'Lee's procedure'). In comparison to Tessier's procedure, Lee's procedure replaces MgCl₂ with 1 M Mg(NO₃)₂ for the removal of the exchangeable fraction. This is because the chloride ion has been shown to remove non-detrital matter from other phases (Leleyter and Probst, 1999).

In Exp. 2, we tested how the addition of sodium citrate to reagent solutions affects U removal in sequential extraction procedures. Extraction solutions are expected to be ^{234}U -rich and thus readsorption of U should be minimised. Sodium citrate has been shown to be the most effective complexing agent for U (Lozano et al., 2011). In Exp. 2, the same reagents and conditions were used as Exp. 1, except for the addition of 10 mg of sodium citrate per gram of sample to the reagent solution at the start of each reaction.

In Exp. 3, following sequential extraction, mild HF/HCl etching was carried out at room temperature using 20 mL 0.3 M HF/0.1 M HCl per gram of sample. This was carried out in order to partially dissolve the outer-rind of detrital minerals, increase the ($^{234}\text{U}/^{238}\text{U}$) activity ratio and find the minimum activity ratio (Figure 2.2). Sodium citrate was added to the solution using 10 mg of sodium citrate per gram of sample. A solution of 0.3 M HF/0.1 M HCl was chosen as mild HCl can remove any other non-detrital matter remaining following sequential extraction (Sutherland, 2002). The soil sample used in Exp. 3 was initially leached using the sequential extraction procedure in Exp. 1. During mild HF/HCl etching, aliquots of the solid residue and aqueous solution were taken at 0, 2, 4, 8, and 24 h. In Exp. 3, the river sediment, marine sediment and rock standard BCR-2 were also leached using the mild HF/HCl etching procedure. Shorter reaction times (<6 h) than for the soil sample were chosen as our results showed that prolonged periods of etching (24 h) did not change the ($^{234}\text{U}/^{238}\text{U}$) activity ratio.

In Exp. 4, the soil sample was leached using Schultz' procedure (Table 2.1). In Experiments 5 and 6, we tested the removal of non-detrital matter using other procedures which have been used in comminution age studies. In Exp. 5, the soil sample was leached by ashing in a furnace at 550°C as recommended by Heiri et al. (2001) and then leached using 16 mL $\text{Mg}(\text{NO}_3)_2$ at room temperature for 50 mins, as recommended by Lee (2009). In Exp. 6, the soil sample was leached by single-acid-extraction using 40 mL of 0.5 M HCl at room temperature for 1 h, as recommended by Sutherland et al. (2002). In Exp. 7, the soil sample

was initially leached using the procedure in Exp. 1 and then leached sequentially by the following procedures: i) ashing in a furnace and rinsed with 16 mL $\text{Mg}(\text{NO}_3)_2$ at room temperature for 50 min; ii) 40 mL of 0.04 M $\text{NH}_2\text{OH} \cdot \text{HCl}$ / AcOH at pH 2, and 96°C for 5 h; and iii) 40 mL of 0.5 M HCl at room temperature for 1 h.

X-ray diffraction analysis was carried out to assess if changes in the activity ratio are a result of the preferential dissolution of clay minerals, and the particle size distribution was measured in order to monitor changes in the particle size. It is important to understand how sample pre-treatment procedures affect not only the ($^{234}\text{U}/^{238}\text{U}$) activity ratio, but also the surface area properties. Thus the Brunauer–Emmett–Teller (BET) specific surface area (S_{BET}) and fractal dimension were measured. Ages were calculated using the fractal direct-recoil model presented in Bourdon et al. (2009). This takes into account the BET specific surface area (S_{BET}), density of solid phase (ρ), recoil length using a value of 30 nm for ^{234}Th (Hashimoto et al., 1985) (R), the fractal dimension (D), and diameter of the adsorbate gas (a), as shown in Equation 2:

$$f_{\alpha} = \frac{1}{4} S_{\text{BET}} \rho R \left[\frac{2^{D-1}}{4-D} \left(\frac{a}{R} \right)^{D-2} \right] \quad (2)$$

The C constant was also calculated from the BET equation, which provides information on the interaction between the adsorbate (N_2) and the mineral surface. As N_2 has a molecular quadrupolar moment (Buckingham et al., 1968), it is energetically favourable for N_2 to adsorb on polar surfaces, such as silicate minerals, which leads to a higher C constant. Adsorption onto non-polar surfaces, such as organic matter results in a lower C constant (Mayer, 1994). The C constant is also related to the extent of microporosity; a higher C constant indicates a greater degree of microporosity (Hudec, 2008).

2.5 Analytical techniques

The chemicals used in sequential extraction procedures were as follows (grade and supplier shown in brackets, respectively): glacial AcOH (Reagent grade, ThermoFisher), NH₄OAc (TraceSELECT>99.9999%, Sigma-Aldrich), NH₂.OH.HCl (TraceSELECT>99.9999%, Sigma-Aldrich), HF 32 % (Suprapur, Merck), H₂O₂ 30 % (Reagent grade, Merck), Mg(NO₃)₂ (Suprapur, Merck), HNO₃ 69 % (ACS Reagent, Merck), NaOAc (Analytical reagent, Merck), Na(citrate) (Analytical reagent, Sigma-Aldrich) and NaOCl 5-6 % (Analytical reagent, Sigma-Aldrich). In all experiments, 18.2 MΩ H₂O from a Milli-Q® Gradient A10® filtration system was used.

Strong acid dissolution of solid residues were carried out at Wollongong Isotope Geochronology Laboratory, University of Wollongong. Prior to dissolution, ca. 100 mg of material was weighed and a known amount of ²²⁹Th–²³⁶U tracer was added. Samples were dissolved in a solution of 2.5 mL 32 % HF and 0.5 mL 69 % HNO₃, heated overnight at 100°C, and dried to incipient dryness. Following this, 3 mL of 32 % HCl was added and where necessary, H₃BO₃ was added to dissolve fluorides. The samples were heated overnight at 80°C and dried to incipient dryness. Following this, 0.5 mL 69 % HNO₃ was added, dried at 100°C to incipient dryness and this step was repeated twice. For isotopic measurements, 2 mL of 1.5 M HNO₃ was added following dissolution and the solutions were sonicated for 15 min, and heated at 100°C, to ensure re-dissolution. For isotopic measurements, U was separated by standard chromatographic techniques using a TRU resin (Eichrom) as described in Luo et al. (1997). The ²³⁴U/²³⁸U ratios were measured using a ThermoFisher Neptune Plus Multi-Collector Inductively-Coupled-Plasma-Mass Spectrometer at the Research School of Earth Sciences, Australian National University. Mass bias and SEM/Faraday cup yield were corrected by standard bracketing using synthetic standard U010 and the accuracy of standard bracketing was checked using U005A. Accuracy was assessed by analysing a rock standard (BCR-2, U.S. Geological Survey)

known to be in secular equilibrium whereby $(^{234}\text{U}/^{238}\text{U})_{\text{S.E.}} = 1$. For isotopic dilution measurements, the $(^{236}\text{U}/^{238}\text{U})$ activity ratio was tail corrected by measuring the intensity at 235.5 and 236.5 amu. The weighted average $(^{234}\text{U}/^{238}\text{U})$ activity ratios was 1.003 ± 0.004 ($n = 2$) and the weighted average U concentrations was 1.72 ± 0.01 ppm ($n = 2$) which are all within error of recommended values (Wilson, 1997).

For acid digestion and column chromatography, the following chemicals were used: HCl 32 % (Suprapur, Merck), HF 32 % (Suprapur, Merck) and HNO_3 69 % (Suprapur, Merck). All dilutions were made using $18.2 \text{ M}\Omega$ H_2O from a Milli-Q® Gradient A10® filtration system.

For sequential extraction solutions, U concentrations were determined by dilution and using calibration curves of known concentration. The U concentrations were not determined by isotopic dilution due to difficulties in separating U from sequential extraction reagents with high cation concentrations. Solutions were diluted in 2 % v/v HNO_3 to ensure major ion concentrations reagents in solutions were <1 ppm, with the following dilutions factors: 48600 for $\text{Mg}(\text{NO}_3)_2$, 92000 for NaOAc/AcOH , 14200 for $\text{NH}_2\text{OH}.\text{HCl}/\text{AcOH}$, 405 for H_2O_2 , 60600 for NH_4OAc , 625 for 0.3 M HF/0.1 M HCl etching solutions, and 7500 for NaOCl . Concentrations were analysed on an Agilent 7500 Series Inductively-Coupled Plasma Mass Spectrometer at UOW and calculated quantitatively by constructing a calibrations curve using 6 standards with U concentrations ranging from 0 to 100 ppb. Total procedure blanks were ≤ 34 pg for U.

For X-ray diffraction measurements, samples were crushed to <4 mm with a Tollmill crusher (TEMA). The samples were then mounted in aluminium holders and placed in a Phillips 1130/90 diffractometer with Spellman DF3 generator set to 1 kW. They were loaded and analysed through an automatic sample holder. The 1 kW energy is achieved by setting the diffractometer to 35 kV and 28.8 mA. Samples were analysed between 4 and 70° 2-theta at 2° per minute with a step size of 0.02. Traces were produced through a GBC 122 control

system and analysed using Traces, μ PDSM and SIROQUANT softwares. Error was assessed by the chi-squared (χ^2) value which compares the observed data (measured XRD spectrum) with expected data (hypothetical XRD spectrum according to user-selected minerals). Particle size distributions were measured by laser diffraction using a Malvern Mastersizer 2000 particle size analyser by dispersing a few mg of sample in H₂O. Surface area measurements were determined by N₂ gas adsorption using a Quantachrome iQ surface area analyser. Samples were degassed for 3 h at 200 °C. The specific surface area (S_{BET}) was determined using 5-7 adsorption points from the partial pressure (P/P_0) range 0.05-0.30 and adjusted for the best fit of the Multi-point BET equation ($R^2 > 0.9999$). The fractal dimension was determined using the Neimark-Kiselev Method (Neimark, 1990).

2.6 Results

2.6.1 Uranium isotope and concentration measurements

Heterogeneity is observed for the ($^{234}\text{U}/^{238}\text{U}$) activity ratio and U concentration of the <63 μm fraction of the untreated soil (Table 2.2).

Table 2.2 ($^{234}\text{U}/^{238}\text{U}$) activity ratio, and U concentration of the untreated soil (< 63 μm fraction).

Sample	($^{234}\text{U}/^{238}\text{U}$)	U (ppm)
A	0.993 ± 0.002	2.7 ± 0.1
B	1.080 ± 0.001	2.4 ± 0.1
C	0.996 ± 0.002	3.2 ± 0.1
Average ^a	1.019 ± 0.002	2.6 ± 0.1

A, B and C represent dissolution of separate aliquots and error shown represents 2σ internal standard error.

^aWeighted average value (2σ , $n = 3$)

In Exp. 1, sequential extraction was carried out using Lee's procedure. The ($^{234}\text{U}/^{238}\text{U}$) activity ratio of the solid residue decreased stepwise following removal of each fraction (except the acid soluble fraction), to a final value of 0.939 ± 0.003 . The final activity ratio of a repeat experiment was within analytical error (Figure 2.3A). A total of 32 ± 2 wt. % of U

was extracted and the majority of U was found in the reducible and oxidisable fractions (Figure 2.3B). The ($^{234}\text{U}/^{238}\text{U}$) activity ratio of the solid residue of rock standard BCR-2 following sequential extraction using Lee's procedure was 1.003 ± 0.004 .

In Exp. 2, sequential extraction was carried out using Lee's procedure with sodium citrate added to each reagent as a complexing agent. The ($^{234}\text{U}/^{238}\text{U}$) activity ratio of the solid residue decreased sequentially following removal of each fraction to 0.938 ± 0.005 and the final activity ratio of a repeat experiment was within analytical error (Figure 2.3A). In Exp. 2, the proportion of U extracted increased by 47%, compared to Exp. 1. The majority of U was extracted in the acid-soluble, reducible and oxidisable fractions (Figure 2.3B).

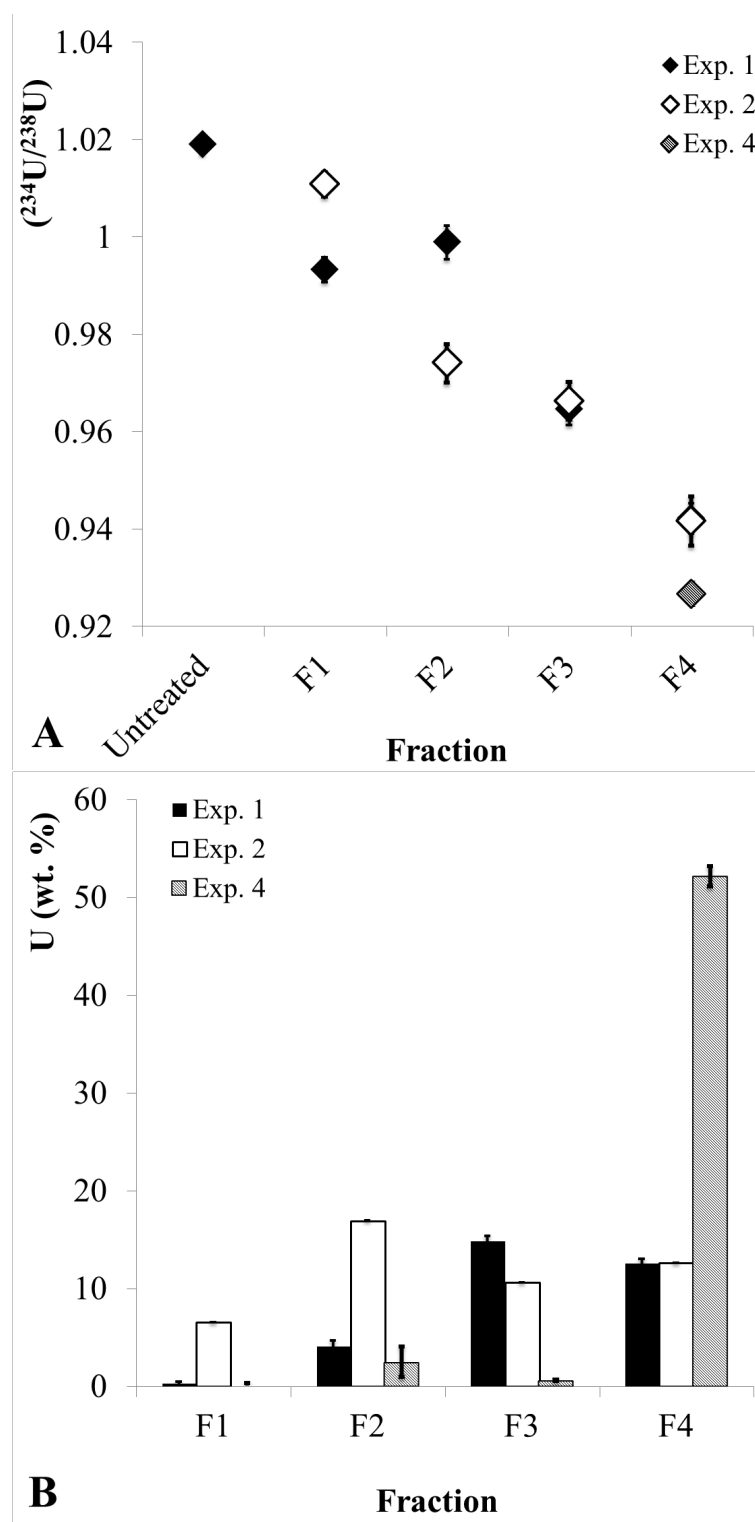
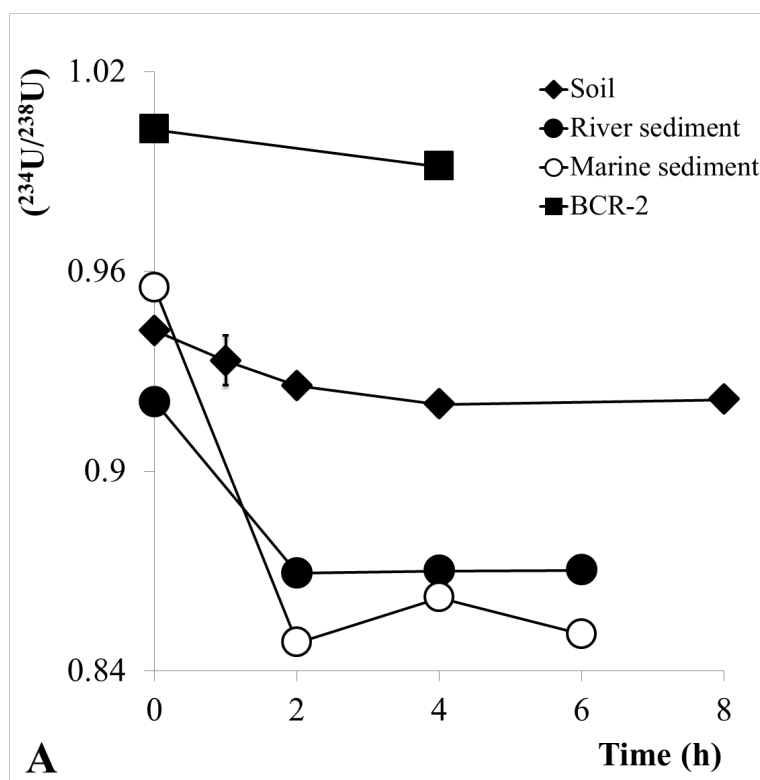


Figure 2.3A) $(^{234}\text{U}/^{238}\text{U})$ activity ratio of the solid residues; B) Percentage of U extracted in reagent solutions (relative to the amount of U in the untreated sample). All error bars represent 2σ internal standard error. Operationally-defined fractions are: exchangeable (F1), acid-soluble (F2), reducible (F3), oxidisable (F4) and refractory (F5). The error shown represents the 2σ internal standard error.

In Exp. 3, the ($^{234}\text{U}/^{238}\text{U}$) activity ratio decreased from 0.939 ± 0.003 following sequential extraction to a minimum of 0.917 ± 0.003 after 4 h of mild HF/HCl etching (Figure 2.4A). Mild HF/HCl etching extracted a further 6 ± 0 wt. % of U after 24 h (Figure 2.4B). In Exp. 3, the mild HF/HCl etching procedures was also tested on river and marine sediments. The minimum ($^{234}\text{U}/^{238}\text{U}$) activity ratio was found after sequential extraction and 2 h of etching for both the river and marine sediments (Figure 2.4A). Sequential extraction and 4 h of mild HF/HCl etching procedure on rock standard BCR-2 decreased the ($^{234}\text{U}/^{238}\text{U}$) activity ratio to 0.991 ± 0.002 (Figure 2.4A). A summary of the leaching and etching experiments carried out on BCR-2 are given in Table 2.3.



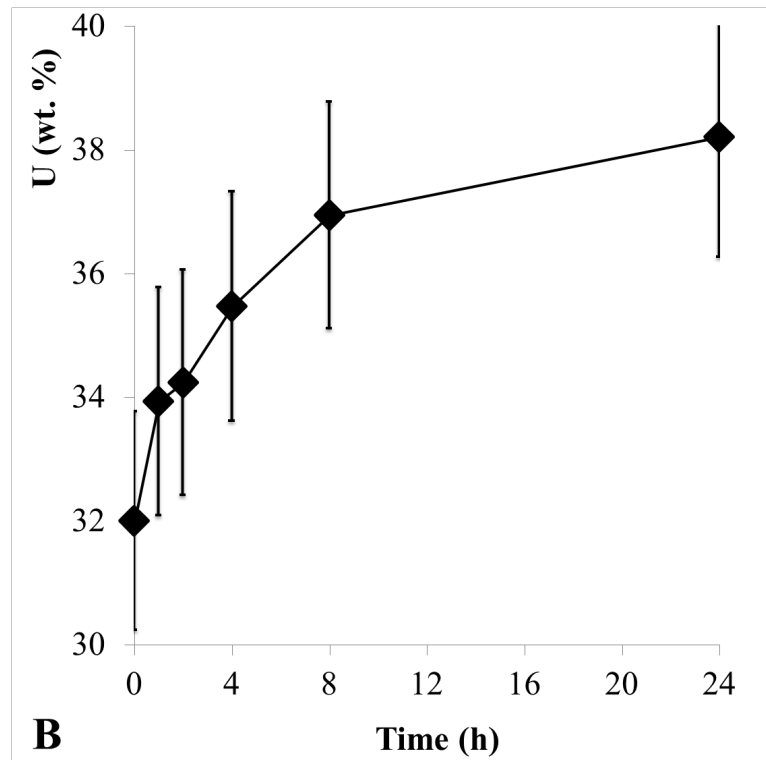


Figure 2.4A) ($^{234}\text{U}/^{238}\text{U}$) activity ratios of the solid residues following mild HF/HCl etching in Exp. 3 on the soil sample (diamonds), river sediment (filled circles), marine sediment (unfilled circles) and rock standard BCR-2 (squares); B) The percentage of U extracted in reagent solutions in Exp. 3 using the soil sample (relative to the amount of U in the untreated sample). All error bars represent 2σ internal standard error and most are hidden by the symbols.

Table 2.3 ($^{234}\text{U}/^{238}\text{U}$) activity ratio of rock standard BCR-2 following leaching experiments

Pre-treatment step	($^{234}\text{U}/^{238}\text{U}$)
Untreated	1.003 ± 0.004 (n = 2)
Sequential extraction	1.003 ± 0.004
mild HF/HCl etching	0.991 ± 0.002

In Exp. 4, the final activity ratio following sequential extraction using Schultz' procedure was 0.927 ± 0.003 , which is lower than the final activity ratios in Exp. 1 and 2 (Figure 2.3A). The majority of U was extracted in the oxidisable fraction (Figure 2.3B). In Exp. 5, the final activity ratio following ashing at 550°C and a 1 M $\text{Mg}(\text{NO}_3)_2$ rinse was 0.974 ± 0.002 . In Exp. 6, the final activity ratio following single-acid extraction using 0.5 M HCl was 0.969 ± 0.002 . In Exp. 7, additional leaching experiments were carried out sequentially following sequential extraction in Exp. 1. The activity ratio decreased from 0.939 ± 0.005 to 0.936 ± 0.002 following additional ashing and a $\text{Mg}(\text{NO}_3)_2$ rinse, and to 0.933 ± 0.002 following an additional $\text{NH}_2\text{OH} \cdot \text{HCl}$ leach. The activity ratio then remained within analytical error following single-acid extraction using 0.5 M HCl. A summary of the activity ratios following experiments with the soil sample is shown in Table 2.4.

Table 2.4 ($^{234}\text{U}/^{238}\text{U}$) activity ratios and the cumulative percentage of U extracted (relative to the amount of U in the untreated soil) in Experiments 1 – 7.

Experiment	Experiment summary	Fractions removed	($^{234}\text{U}/^{238}\text{U}$)	U (wt. %)
1	Sequential extraction procedure from Lee (2009)	F1	0.990 ± 0.003	0.27 ± 0.18
		F1, F2	0.996 ± 0.003	4.4 ± 0.7
		F1, F2, F3	0.961 ± 0.003	19 ± 1
		F1, F2, F3 and F4	0.939 ± 0.003	32 ± 2
		F1, F2, F3 and F4 (replicate)	0.935 ± 0.003	n/a
2	Sequential extraction procedure from Lee (2009) + sodium citrate	F1	1.007 ± 0.003	6.5 ± 0.6
		F1, F2	0.971 ± 0.003	24 ± 2
		F1, F2, F3	0.963 ± 0.003	35 ± 2
		F1, F2, F3 and F4	0.938 ± 0.005	47 ± 2
		F1, F2, F3 and F4 (replicate)	0.931 ± 0.003	n/a
3 (0 h)	Sequential extraction procedure from Lee (2009) + mild HF/HCl etch	F1, F2, F3, F4	0.939 ± 0.003	32 ± 2
3 (1 h)			0.930 ± 0.007	34 ± 2
3 (2 h)			0.923 ± 0.003	34 ± 2
3 (4 h)		F1, F2, F3, F4 and F5	0.917 ± 0.003	35 ± 2
3 (8 h)			0.919 ± 0.003	37 ± 2
3 (24 h)			0.923 ± 0.004	38 ± 2
4	Sequential extraction procedure from Schultz et al. (1998)	F1, F2, F3 and F4	0.927 ± 0.003	55 ± 3
5	Ashing and MgNO_3 rinse	F4	0.974 ± 0.002	n/a
6	0.5 M HCl	F2	0.969 ± 0.002	n/a
7	Additional leaching experiments following sequential extraction	F1	0.936 ± 0.002	n/a
		F1 and F3	0.933 ± 0.002	n/a
		F1, F3 and F2	0.933 ± 0.002	n/a

Experiments were conducted on the soil sample and the operationally-defined fractions are: exchangeable (F1), acid-soluble (F2), reducible (F3), oxidisable (F4) and refractory (F5). Error shown represents 2σ internal standard error. Values in brackets for Exp. **3** represent duration of mild HF/HCl etching.

2.6.2 Physical Analyses

Sequential extraction procedures resulted in a total loss of ca. 100 mg g⁻¹ of sample (Table 2.5). In each experiment, the removal of the exchangeable fraction did not result in significant mass loss (< 2 mg g⁻¹). In Exp. 1 and 4, the majority of mass was removed in the reducible fraction and in Exp. 2, the majority of mass was removed in the oxidisable fraction. The proportion of mass removed in Exp. 1 and 2 is highly variable.

Table 2.5 Amount of mass removed per gram of soil in Experiments 1, 2, 4, and 5.

Fraction ^a	Exp. 1	Exp. 2	Exp. 4	Exp. 5
F1	1.1	0.40	1.9	n/a
F2	7.0	20	11	n/a
F3	60	31	70	n/a
F4	41	32	13	64
Total	110	83	96	64

^aOperationally-defined fractions are: exchangeable (F1), acid-soluble (F2), reducible (F3), oxidisable (F4) and refractory (F5).

In Exp. 1, sequential extraction decreased the relative volume of particles <10 µm and concurrently decreased particles >10 µm (Figure 2.5). In contrast, in Exp. 3, mild HF/HCl etching following sequential extraction decreased the relative volume of particles <10 µm and increased particles >10 µm.

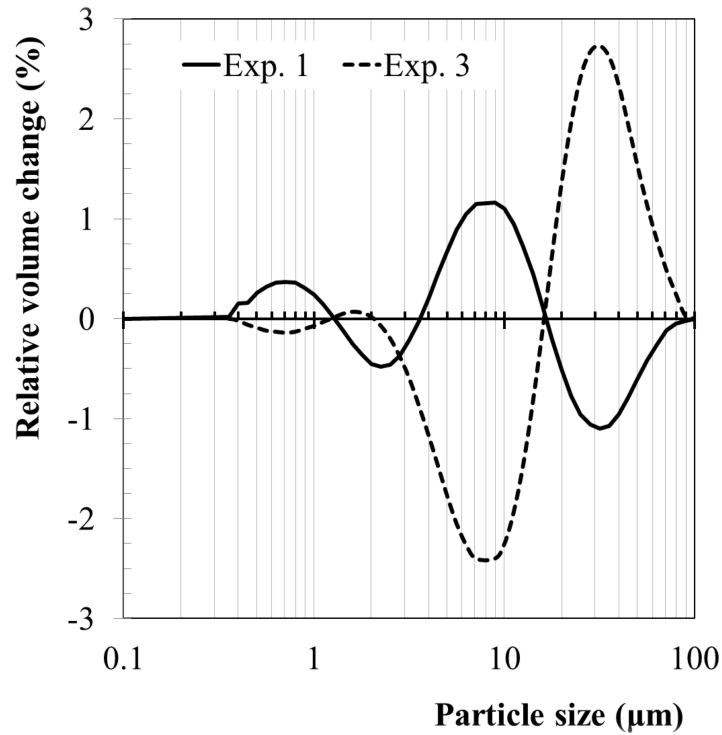


Figure 2.5 Relative volume change as a function of particle size following: sequential extraction in Exp. 1, compared to the <63 μm fraction of the untreated soil, and mild HF/HCl etching in Exp. 3 (24 h), compared to the particle-size distribution following sequential extraction in Exp. 1.

The mineralogy of the soil sample was determined before and after sequential extraction in Exp. 1 by X-ray diffraction. The mineralogy of the <63 μm fraction of the untreated soil is mainly quartz (72 %), kaolinite (11 %) with small amounts (<5 %) of illite, muscovite, zircon, magnetite, chlorite, ilmenite and rutile ($\chi^2 = 3.2$). These results are consistent with the quartzose sandstone lithology from which the soil is derived. The mineralogy remained unchanged following sequential extraction in Exp. 1 ($\chi^2 = 8.58$): quartz (74 %), and kaolinite (8 %) and small amounts (<6 %) of illite, muscovite zircon, magnetite, chlorite, ilmenite and rutile.

The effect of sample pre-treatment on the surface area properties was tested on the soil sample (Table 2.6). Sequential extraction increased S_{BET} in both Exp. 1 and 4. In Exp. 3, mild HF/HCl etching initially increased S_{BET} following 4 h of etching and subsequently

decreased following 24 h of etching. The fractal dimension of the soil remained unchanged following Lee's procedure in Exp. 1, but decreased following Schultz' procedure in Exp. 4. In Exp. 3, mild HF/HCl etching decreased the fractal dimension. Sequential extraction increased the C constant in Exp. 1 and 4. In Exp. 3, mild HF/HCl etching initially decreased the C constant following 4 h of etching, and then increased following 24 h of etching.

Table 2.6 Particle size and surface area properties of the <63 μm fraction of the untreated soil sample, and following Experiments 1, 3 and 4.

Experiment	Mean diameter	S_{BET}	D	C constant
Untreated	5.9	16	2.70	96
1	4.8	21	2.70	110
2	5.1	n/a	n/a	n/a
3 (4 h)	n/a	23	2.57	86
3 (24 h)	3.4	14	2.57	130
4	n/a	27	2.52	140
Estimated uncertainty	n/a	$\pm 0 \%$	$\pm 4.86 \%$	$\pm 3 \%$

Estimated uncertainty calculated from 2σ external standard error of replicate analyses. S_{BET} represents the specific surface area, and D represents the fractal dimension. Numbers in brackets for Exp. 3 represent the duration of etching.

2.7 Discussion

2.7.1 Validation of the methodology

Lee (2009) proposed that the removal of non-detrital matter from fine-grained soils and sediment (<63 μm) can be monitored by measuring the ($^{234}\text{U}/^{238}\text{U}$) activity ratio of the solid residue (Figure 2.2). We tested this by measuring the ($^{234}\text{U}/^{238}\text{U}$) activity ratio of the solid residue throughout sequential extraction procedures, and observed the sequential decrease of the activity ratio in Experiments 1 and 2 (Figure 2.3). Tests on rock standard BCR-2, which is known to be in secular equilibrium (Sims et al., 2008), showed that sequential extraction does not result preferential leach ^{234}U from damaged lattice sites (Exp. 1, Table 2.3). Suresh

et al. (2014) found that rock standards were within 1% of secular equilibrium following sequential extraction, which was considered acceptable in terms of analytical uncertainty. X-ray diffraction measurements showed that the decrease in the ($^{234}\text{U}/^{238}\text{U}$) activity ratio cannot be attributed to the preferential dissolution of ^{234}U -rich clay minerals. Furthermore, particle size distribution measurements also showed that there is a relative increase in particles $<10\text{ }\mu\text{m}$ (Figure 2.5), which suggests that the dissolution of clay minerals is minimal. The increase in particles $<10\text{ }\mu\text{m}$ following sequential extraction is attributed to the break-up of large aggregates which are cemented by organic and inorganic coatings (Horowitz and Elrick, 1987). Thus the decrease of the ($^{234}\text{U}/^{238}\text{U}$) activity ratio throughout sequential extraction is attributed to the removal of authigenic weathering products and organic matter.

Heterogeneity is observed in U concentrations and ($^{234}\text{U}/^{238}\text{U}$) activity ratios in the 3 aliquots of the untreated soil samples (Table 2.2). We attribute this to variable amounts of non-detrital matter in the different aliquots. It is difficult to avoid such heterogeneity as grinding would affect S_{BET} and the resulting comminution age calculations. Furthermore, grinding would create fresh mineral surfaces, which would alter mineral reactivity with reagents. Despite this, the final ($^{234}\text{U}/^{238}\text{U}$) activity ratios were remarkably similar between replicates and different experiments following sequential extraction (Figure 2.3A, Table 2.4). Firstly, this suggests that despite variations in the amount of U removed in each operationally-defined fraction using Lee's and Schultz' procedures (Figure 2.3B), the overall removal of U is consistent, as observed in Blanco et al. (2004). Secondly, and importantly, the U isotope composition of the detrital minerals following sequential extraction appears to be homogeneous.

2.7.2 The addition of a complexing agent

Readsorption of U during sequential extraction procedures could artificially increase the ($^{234}\text{U}/^{238}\text{U}$) activity ratio of the detrital minerals. The addition of sodium citrate as a

complexing agent increased the percentage of U extracted in the exchangeable and acid-soluble fraction (Exp. 2, Figure 2.3B). The percentage of U extracted in the exchangeable fraction with the addition of sodium citrate is high in comparison to other studies (6.5 wt. %), which report <1 wt. % of U extracted (Aubert et al., 2004; Virtanen et al., 2013). This suggests that either: i) sodium citrate is extracting U from other non-detrital phases; or ii) the proportion of U extracted in the exchangeable fraction in other studies has been consistently underestimated due to readsorption. The increased extraction of U from the exchangeable fraction does not affect the ($^{234}\text{U}/^{238}\text{U}$) activity ratio, which suggests that this material has a similar activity ratio to the untreated soil. The extraction of U in the acid-soluble fraction increases over fourfold following the addition of sodium citrate to sequential extraction reagents (Figure 2.3B). It should be noted that the increased extraction of U in the acid-soluble fraction could be due to a greater initial amount of carbonates in the soil aliquot used. This is evidenced by the higher ($^{234}\text{U}/^{238}\text{U}$) activity ratio following removal of the exchangeable fraction in Exp. 2. However, the ($^{234}\text{U}/^{238}\text{U}$) activity ratio decreased in Exp. 2, whereas the activity ratio remained within analytical error without the addition of sodium citrate in Exp. 1 (Figure 2.3A). This suggests U is readsorbed without the addition of a complexing agent. The final activity ratio following sequential extraction with, and without the addition of sodium citrate were within analytical error (Figure 2.3A). This suggests that U readsorbed during the removal of the acid-soluble fraction is removed later in the procedure.

2.7.3 Mild HF/HCl etching procedure

To assess whether the removal of non-detrital matter following sequential extraction is complete, a previously-leached sample was etched using a solution of 0.3 M HF/0.1 M HCl following sequential extraction. Mild HF/HCl etching further decreased the ($^{234}\text{U}/^{238}\text{U}$) activity ratio and the minimum was found following 4 h of etching. This decrease in the activity ratio indicates that the removal of non-detrital matter by sequential extraction was

incomplete (Figure 2.2). Particle size distribution measurements revealed a relative decrease in particles $<10\text{ }\mu\text{m}$ following a prolonged duration of etching. This suggests that the decrease in the activity ratio can at least partly be attributed to the dissolution of ^{234}U -rich clay minerals. As the U isotope composition of clay minerals is not related to the direct ejection of ^{234}U , they should be removed from samples for the comminution dating technique.

Mild HF/HCl etching decreased ($^{234}\text{U}/^{238}\text{U}$) activity ratio also of the river sediment, marine sediment, and rock standard. The ($^{234}\text{U}/^{238}\text{U}$) activity ratio of rock standard BCR-2 following 4 h of etching decreased to 0.992 ± 0.002 . This indicates that mild HF/HCl etching results in some preferential leaching of ^{234}U (Figure 2.1). As rock standards represent freshly-crushed rock, which have large amounts of fresh surface area, our experiment likely overestimates the preferential leaching of ^{234}U . Freshly-exposed surfaces contain labile ^{234}U , which is easily removed by weathering solutions, and leaching experiments suggest that these labile nuclides are removed in the natural environment within ca. 200 a (Fleischer, 1980). As it is likely that this fraction of labile ^{234}U would be instantly lost on the geological timescale, the comminution age technique must attempt to take preferential leaching into account in order to calculate reliable ages.

In addition to the preferential leaching of ^{234}U and the dissolution of clay minerals, it is possible that mild HF/HCl etching also removes refractory non-detrital matter. Other studies observe that a proportion of organic matter is refractory, resistant to ashing and chemical oxidation procedures, and is only removable by HF treatment (Kaiser and Guggenberger, 2003; Kleber et al., 2005; Mayer, 1994; Mikutta et al., 2006; Outola et al., 2009). The resistant nature of this refractory organic matter is due to: i) micropores limiting diffusion of solutions into pores (Mikutta and Mikutta, 2006); ii) reactive hydroxyl groups on mineral surfaces stabilising organic matter (Mikutta et al., 2006); iii) chemical oxidation by H_2O_2 forming more resistant phases (Mikutta et al., 2005).

Mild HF/HCl etching is therefore recommended following sequential extraction with Tessiers' procedure, and the procedure is shown in Table 2.7. The additional operationally-defined fraction removed by HF/HCl etching is referred to as the *resistant* phase (F5).

Table 2.7 Recommended sample pre-treatment procedure

Target phase	Reagents and Conditions ^{a,b}
Water-soluble (F0)	8 mL H ₂ O Room temp./1 h
Exchangeable (F1)	8 mL 1 M MgCl ₂ at pH 7 Room temp./1 h
Acid-soluble (F2)	8 mL NaOAc/AcOH at pH 5 Room temp./6 h
Reducible (F3)	20 mL 0.04 M NH ₂ OH.HCl/AcOH at pH 2 96 °C/5 h 8 mL 0.02 M HNO ₃ /H ₂ O ₂ at pH 2 85°C/2 h
Oxidisable (F4)	3 mL H ₂ O ₂ at pH 2 85 °C/3h 5 mL 3.2 M NH ₄ OAc in HNO ₃ 20% diluted to 20 mL with H ₂ O Room temp./30 min
Resistant (F5)	20 mL 0.1 M HF/0.3 HCl

^aReagent volumes for 1 g of sample.

^b10 mg per gram of sample of Na(cit) added to the reagent at the start of the reaction.

2.7.4 Evaluation of other procedures

The effectiveness of sample pre-treatment procedures used in comminution studies was assessed using U isotopes. The greatest decrease of the ($^{234}\text{U}/^{238}\text{U}$) activity ratio, and the highest percentage of U extracted, was observed in Exp. 4 using the procedure from Schultz et al. (1998). This is attributed to the increased effectiveness of NaOCl for removing the oxidisable fraction in comparison to H_2O_2 , which has also been shown elsewhere (Mikutta et al., 2005).

Ashing followed by a $\text{Mg}(\text{NO}_3)_2$ rinse decreased the activity ratio and appears to effectively remove the oxidisable fraction (Exp. 5, Table 2.4). Lee (2009) found that removal of the oxidisable fraction using H_2O_2 and ashing were similarly effective. However, the most effective method of removing organic matter appears to be using NaOCl.

The decrease in the ($^{234}\text{U}/^{238}\text{U}$) activity ratio following removal of the acid-soluble fraction using 0.5 M HCl is similar to the decrease using NaOAc/AcOH and sodium citrate. However, the decrease in the activity ratio following single-acid extraction is greater than using NaOAc/AcOH without sodium citrate (Exp. 2). This is further evidence that readsorption of U occurs with NaOAc/AcOH and no complexing agent. The much higher reagent-volume-to-sample ratio in single-acid extraction, compared to the NaOAc/AcOH solution likely inhibits the readsorption of U (20 vs 8 mL g^{-1}). These results are in contrast to Lee (2009) who found that single-acid extraction of alluvial sediment, under the same reactions conditions, increased the ($^{234}\text{U}/^{238}\text{U}$) activity ratio. This was attributed to the dissolution of the ^{234}U -depleted, outer-rind of the detrital minerals due to an insignificant amount of non-detrital matter present.

A previously-leached sample was subject to further leaching to determine the nature of the residual non-detrital matter following sequential extraction. The ($^{234}\text{U}/^{238}\text{U}$) activity ratio is unchanged following ashing and a $\text{Mg}(\text{NO}_3)_2$ leach, and decreased following an additional

NH₂OH.HCl/ AcOH leach (Exp. 7, Table 2.4). This indicates that a proportion of the non-detrital matter remaining after sequential extraction is reducible and could be the result of either: 1) incomplete removal of Fe/Mn oxides during sequential extraction; or 2) the stabilisation of poorly-crystalline material during H₂O₂ oxidation (Mikutta et al., 2005).

2.7.5 The effect of sequential extraction and etching procedures on the surface properties of soil

The effect of sample pre-treatment on the surface area properties of the soil was assessed. Sequential extraction increases S_{BET} of the soil sample (Exp. 1 and 4, Table 2.6), which is explained by increased pore space availability following removal of non-detrital matter, and is referred to as *occluded surface area* (Kaiser and Guggenberger, 2003; Mayer, 1994). This suggests that the majority of non-detrital matter removed during sequential extraction is low-surface area material, such as organic matter. Initially, S_{BET} increased following sequential extraction short durations of mild HF/HCl etching and then decreased following a longer duration of etching (Exp. 3, Table 2.6). This suggests that mild HF/HCl etching initially removes low surface area material, such as organic matter, which is followed by the removal of high surface-area material, such as clay minerals.

Sequential extraction increased the C constant (Exp. 1 and 4, Table 2.6), which suggests that the coverage of the surface of silicate minerals by organic matter is decreased (Mayer, 1994). The C constant initially decreased following sequential extraction and short durations of mild HF/HCl, and then increased following a longer duration of etching. This suggests that polar material and/or micropores are initially removed during etching and long durations remove non-polar material such as organic matter.

The fractal dimension remained constant following sequential extraction in Exp. 1, and decreased following mild HF/HCl etching and sequential extraction in Exp. 4 (Table 2.6).

Fractal behaviour in sediment is attributed to the presence of clay minerals, and authigenic weathering products (Krohn, 1988a; Krohn, 1988b; Wong et al., 1986). The development of porosity of minerals has also been shown to exhibit fractal behaviour (Katz and Thompson, 1985). The lack of decrease in the fractal dimension following sequential extraction indicates that the removal of non-detrital matter in Exp. 1 is incomplete. Alternatively, the increased porosity available to N₂ following the removal of non-detrital matter could be limiting the observed decrease in the fractal dimension. The decrease in the fractal dimension following mild HF/HCl etching indicates the removal of non-detrital matter and/or clay minerals.

Sequential extraction using the procedure from Schultz et al. (1998) leads to the highest S_{BET} and C constant, and lowest fractal dimension (Exp. 4, Table 2.6). These results indicate that this procedure represents the optimal balance between preserving the surface morphology of detrital minerals, and removing non-detrital matter.

2.7.6 Calculated ages

The ages inferred by the comminution dating approach are strongly dependent on the surface area properties of the detrital minerals. Here, we show the effect of sample pre-treatment on the calculated age using the fractal direct-recoil model. The inferred ages are generally >1000 ka, which is beyond the limit of the technique (Table 2.8). However, it is unlikely that the activity ratio of the starting material is 1 due to the preferential leaching of ²³⁴U (as discussed in Section 2.6.3). Using the activity ratio of the rock standard following sequential leaching and mild HF/HCl etching as the initial activity ratio (0.992), the ages are still beyond the limit of the technique. Assuming a hypothetical initial activity ratio of 0.95 is required for the ages to become ‘plausible’ i.e. within the limit of the technique. The ages of samples using different sequential extraction procedures are within error of each other (Exp. 1 and 4, Table 2.8). Mild HF/HCl etching following sequential extraction leads to much

older ages, which is due to: i) further removal of ^{234}U -rich non-detrital matter; and ii) lower S_{BET} following the removal of high surface-area clay minerals. The presence of clay minerals will lead to artificially low ages and may explain why inferred comminution ages from Handley et al. (2013b) for clay-rich sediment from the Flinders Ranges in South Australia were much lower than the depositional ages.

Table 2.8 Comminution ages calculated following the various sample pre-treatment procedures.

Experiment	$(^{234}\text{U}/^{238}\text{U})$	f_a	t (ka)	t (ka)	t (ka)
1	0.939 ± 0.003	0.043	>1,000	>1,000	330 ± 57
3 (4 h)	0.917 ± 0.003	0.069	>1,000	>1,000	>1000
3 (24 h)	0.923 ± 0.004	0.042	>1,000	>1,000	520 ± 36
4	0.927 ± 0.003	0.094	530 ± 46	490 ± 46	260 ± 46

^aInitial ($^{234}\text{U}/^{238}\text{U}$) activity ratio (A_0)

2.8 Conclusions

Sequential extraction resulted in a stepwise decrease of the ($^{234}\text{U}/^{238}\text{U}$) activity ratio of the solid residue following the removal of the operationally-defined, non-detrital phases. X-ray diffraction and particle size distribution measurements revealed that this decrease of the activity ratio during sequential extraction is due to the removal of authigenic weathering products and organic matter. These results validate the proposal by Lee (2009) that the removal of non-detrital matter can be monitored by measuring the ($^{234}\text{U}/^{238}\text{U}$) activity ratio of the solid residue (<63 μm fraction). Despite heterogeneous amounts of U in untreated soil aliquots, the activity ratios of samples following replicate sequential extraction experiments are similar. This suggests that the removal of non-detrital matter by sequential extraction procedures is consistent. Furthermore, this also suggests that the ($^{234}\text{U}/^{238}\text{U}$) activity ratio of the detrital minerals is homogeneous following sequential extraction.

The addition of a complexing agent (sodium citrate) to the sequential extraction reagents increased the proportion of U extracted in the exchangeable and acid-soluble fraction. However, this did not affect the final ($^{234}\text{U}/^{238}\text{U}$) activity ratio at the end of the procedure. This suggests that readsorbed U is removed later in the procedure. The addition of sodium citrate to sequential extraction reagents increases the overall extraction of U, and is thus recommended.

Mild HF/HCl etching further decreased the ($^{234}\text{U}/^{238}\text{U}$) activity ratio following sequential extraction, and this was also observed for river and marine sediments. Particle size distribution measurements show a relative decrease in particles $<10\text{ }\mu\text{m}$, which suggests that mild HF/HCl etching likely dissolves clay minerals. The U isotope and surface area composition of clay minerals are not related to the loss of ^{234}U by direct ejection, and thus should be removed for the comminution dating technique. Mild HF/HCl etching following sequential extraction on a rock standard revealed a small amount of preferential leaching of ^{234}U ($<1\%$). However, this likely represents a maximum loss of ^{234}U as rock standards are finely ground rock. In any case, the preferential leaching of ^{234}U likely occurs in most weathering environments, and further development of the comminution dating technique must account for this. Efforts must be made to quantify the loss of labile ^{234}U , which could be achieved with mild HF/HCl etching experiments. Although mild HF/HCl etching may induce a small amount of preferential leaching, mild HF/HCl etching following sequential extraction is recommended (Table 2.9).

Table 2.9 Recommended sample pre-treatment procedure for comminution dating.

Target phase	Reagents and Conditions ^{a,b}
Water-soluble (F0)	8 mL H ₂ O
Exchangeable (F1)	8 mL 1 M MgCl ₂ at pH 7
Acid-soluble (F2)	8 mL NaOAc/AcOH at pH 5
Reducible (F3)	20 mL 0.04 M NH ₂ OH.HCl/AcOH at pH 2 8 mL 0.02 M HNO ₃ /H ₂ O ₂ at pH 2
Oxidisable (F4)	3 mL H ₂ O ₂ at pH 2 5 mL 3.2 M NH ₄ OAc in HNO ₃ 20% diluted to
Resistant (F5)	20 mL 0.1 M HF/0.3 HCl

^aReagent volumes for 1 g of sample.

^b10 mg per gram of sample of Na(cit) added to the reagent at the start of the reaction.

Evaluation of current sample pre-treatment methods in terms of the (²³⁴U/²³⁸U) activity ratio reveals that the sequential extraction procedure from Schultz et al. (1998) is the most effective. This is attributed to NaOCl removing the oxidisable fraction more efficiently than H₂O₂, which has also been shown in other studies. Further work should therefore involve testing the mild HF/HCl etching procedure with Schultz' procedure.

Sequential extraction increased the specific surface area (S_{BET}), which is attributed to the increased porosity following the removal of non-detrital matter from the detrital minerals. Furthermore, sequential extraction increased the C constant suggesting a decreased coverage of detrital minerals by organic matter. The fractal dimension was unchanged following sequential extraction using Lee's procedure, but decreased using Schultz' procedure. As non-detrital matter is expected to have a high fractal dimension, this suggests the latter procedure removes non-detrital matter more effectively. Mild HF/HCl resulted in an initial increase in S_{BET} and subsequent decrease which is attributed to the removal of non-detrital matter and then clay minerals. The fractal dimension also decreases following etching, which suggests further removal of non-detrital matter and clay minerals.

The majority of inferred ages are beyond the limit of the technique (1000 ka). Assuming an initial ($^{234}\text{U}/^{238}\text{U}$) activity ratio of 0.95 is required for ages to be within the limit of the technique, which is much lower than the ^{234}U -depletion observed in the rock standard following mild HF/HCl etching and sequential leaching. Constraining the ($^{234}\text{U}/^{238}\text{U}$) activity ratio of the parent material should therefore be a necessary component of future work. Inferred ages are within analytical error following different sequential extraction procedures, but mild HF/HCl etching following sequential extractions leads to much older ages. This is attributed to the lower activity ratio and surface area following the removal of non-detrital matter. These results explain why comminution ages less than the depositional age were inferred in previous studies. Further work should involve testing the different sample pre-treatment procedures on a sample dated by other geochronological methods, similar to the approach by Lee et al. (2010) for refining calculation of the direct-recoil fraction.

Acknowledgements

This study was supported by an ARC Future Fellowship FT0990447 to AD and a University of Wollongong postgraduate scholarship award to ANM. We thank Lili Yu for technical support running the Q-ICP-MS and Amy Dougherty for fieldwork assistance. Davide Menozzi, Maxime Aubert and Monika Markowska are thanked for providing helpful discussions with the preparation of the manuscript. Allan Chivas is also thanked for helpful discussions and providing the river sediment and marine sediment samples.

References

Aciego, S., Bourdon, B., Schwander, J., Baur, H. and Forieri, A. (2011) Toward a radiometric ice clock: Uranium ages of the Dome C ice core. *Quaternary Science Reviews* 30, 2389-2397.

Andersson, P.S., Porcelli, D., Gustafsson, Ö., Ingri, J. and Wasserburg, G.J. (2001) The importance of colloids for the behavior of uranium isotopes in the low-salinity zone of a stable estuary. *Geochimica et Cosmochimica Acta* 65, 13-25.

Andersson, P.S., Porcelli, D., Wasserburg, G.J. and Ingri, J. (1998) Particle Transport of ^{234}U - ^{238}U in the Kalix River and in the Baltic Sea. *Geochimica et Cosmochimica Acta* 62, 385-392.

Aubert, D., Probst, A. and Stille, P. (2004) Distribution and origin of major and trace elements (particularly REE, U and Th) into labile and residual phases in an acid soil profile (Vosges Mountains, France). *Applied Geochemistry* 19, 899-916.

Blanco, P., Vera Tomé, F. and Lozano, J.C. (2004) Sequential extraction for radionuclide fractionation in soil samples: A comparative study. *Applied Radiation and Isotopes* 61, 345-350.

Bourdon, B., Bureau, S., Andersen, M.B., Pili, E. and Hubert, A. (2009) Weathering rates from top to bottom in a carbonate environment. *Chemical Geology* 258, 275-287.

Cheng, H., Edwards, R.L., Hoff, J., Gallup, C.D., Richards, D.A. and Asmerom, Y. (2000) The half-lives of uranium-234 and thorium-230. *Chemical Geology* 169, 17-33.

Chivas, A.R., Garcia, A., van der Kaars, S., Couapel, M.J.J., Holt, S., Reeves, J.M., Wheeler, D.J., Switzer, A.D., Murray-Wallace, C.V., Benerjee, D., Price, D.M., Wang, S.X., Pearson, G., Edgar, N.T., Beaufort, L., De Deckker, P., Lawson, E. and Cecil, C.B. (2001) Sea-level and environmental changes since the last interglacial in the Gulf of Carpentaria, Australia: An overview. *Quaternary International* 82-85, 19-46.

DePaolo, D.J., Maher, K., Christensen, J.N. and McManus, J. (2006) Sediment transport time measured with U-series isotopes: Results from ODP North Atlantic drift site 984. *Earth and Planetary Science Letters* 248, 394-410.

Dosseto, A., Hesse, P.P., Maher, K., Fryirs, K. and Turner, S. (2010) Climatic and vegetation control on sediment dynamics during the last glacial cycle. *Geology* 38, 395-398.

Fleischer, R.L. (1980) Isotopic disequilibrium of uranium: Alpha-recoil damage and preferential solution effects. *Science* 207, 979-981.

Handley, H.K., Turner, S., Afonso, J.C., Dosseto, A. and Cohen, T. (2013a) Sediment residence times constrained by uranium-series isotopes: A critical appraisal of the comminution approach. *Geochimica et Cosmochimica Acta* 103, 245-262.

Handley, H.K., Turner, S.P., Dosseto, A., Haberlah, D. and Afonso, J.C. (2013b) Considerations for U-series dating of sediments: Insights from the Flinders Ranges, South Australia. *Chemical Geology* 340, 40-48.

Hashimoto, T., Aoyagi, Y., Kudo, H. and Sotobayashi, T. (1985) Range calculation of alpha-recoil atoms in some minerals using LSS-theory. *Journal of Radioanalytical and Nuclear Chemistry Articles* 90, 415-438.

Heiri, O., Lotter, A.F. and Lemcke, G. (2001) Loss on ignition as a method for estimating organic and carbonate content in sediments: Reproducibility and comparability of results. *Journal of Paleolimnology* 25, 101-110.

Horowitz, A.J. and Elrick, K.A. (1987) The relation of stream sediment surface area, grain size and composition to trace element chemistry. *Applied Geochemistry* 2, 437-451.

Hudec, P. (2008) Zeolites and related materials: Trends, targets and challenges, Proceedings of the 4th International FEZA Conference Sensitivity of the C-constant of BET-isotherm to the content of micropore volume in mesoporous matrix. *Studies in surface science and catalysis* 174, 981-984.

Kaiser, K. and Guggenberger, G. (2003) Mineral surfaces and soil organic matter. *European Journal of Soil Science* 54, 219-236.

Katz, A.J. and Thompson, A. (1985) Fractal sandstone pores: implications for conductivity and pore formation. *Physical Review Letters* 54, 1325.

Kigoshi, K. (1971) Alpha-recoil thorium-234: Dissolution into water and the uranium-234/uranium-238 disequilibrium in nature. *Science* 173, 47-48.

Kleber, M., Mikutta, R., Torn, M.S. and Jahn, R. (2005) Poorly crystalline mineral phases protect organic matter in acid subsoil horizons. *European Journal of Soil Science* 56, 717-725.

Krohn, C.E. (1988a) Fractal measurements of sandstones, shales, and carbonates. *Journal of Geophysical Research: Solid Earth* (1978–2012) 93, 3297-3305.

Krohn, C.E. (1988b) Sandstone fractal and Euclidean pore volume distributions. *Journal of Geophysical Research: Solid Earth* 93, 3286-3296.

Lee, V.E. (2009) Radiogenic Isotope Geochemistry and the Evolution of the Earth's Surface and Interior. PhD Thesis at the University of California, Berkeley.

Lee, V.E., DePaolo, D.J. and Christensen, J.N. (2010) Uranium-series comminution ages of continental sediments: Case study of a Pleistocene alluvial fan. *Earth and Planetary Science Letters* 296, 244-254.

Leleyter, L. and Probst, J.L. (1999) A new sequential extraction procedure for the speciation of particulate trace elements in river sediments. *International Journal of Environmental Analytical Chemistry* 73, 109-128.

Lozano, J.C., Blanco Rodríguez, P., Vera Tomé, F. and Calvo, C.P. (2011) Enhancing uranium solubilization in soils by citrate, EDTA, and EDDS chelating amendments. *Journal of Hazardous Materials* 198, 224-231.

Luo, X., Rehkämper, M., Lee, D.-C. and Halliday, A.N. (1997) High precision $^{230}\text{Th}/^{232}\text{Th}$ and $^{234}\text{U}/^{238}\text{U}$ measurements using energy filtered ICP magnetic sector multiple collector mass spectrometry. *International Journal of Mass Spectrometry and Ion Processes* 171, 105-117.

Mayer, L.M. (1994) Surface area control of organic carbon accumulation in continental shelf sediments. *Geochimica et Cosmochimica Acta* 58, 1271-1284.

Mikutta, R., Kleber, M., Kaiser, K. and Jahn, R. (2005) Review: Organic matter removal from soils using hydrogen peroxide, sodium hypochlorite, and disodium peroxodisulfate. *Soil Science Society of America journal* 69, 120-135.

Mikutta, R., Kleber, M., Torn, M.S. and Jahn, R. (2006) Stabilization of soil organic matter: Association with minerals or chemical recalcitrance? *Biogeochemistry* 77, 25-56.

Mikutta, R. and Mikutta, C. (2006) Stabilization of Organic Matter at Micropores (≤ 2 nm) in Acid Forest Subsoils. *Soil Science Society of America journal* 70, 2049-2056.

Neimark, A. (1990) Thermodynamic method for calculating surface fractal. *JETP Lett* 51.

Outola, I., Inn, K., Ford, R., Markham, S. and Outola, P. (2009) Optimizing standard sequential extraction protocol with lake and ocean sediments. *Journal of Radioanalytical and Nuclear Chemistry*, Articles 282, 321-327.

Paces, J.B., Nichols, P.J., Neymark, L.A. and Rajaram, H. (2013) Evaluation of Pleistocene groundwater flow through fractured tuffs using a U-series disequilibrium approach, Pahute Mesa, Nevada, USA. *Chemical Geology* 358, 101-118.

Plater, A.J., Ivanovich, M. and Dugdale, R.E. (1992) Uranium series disequilibrium in river sediments and waters: the significance of anomalous activity ratios. *Applied Geochemistry* 7, 101-110.

Porcelli, D., Andersson, P.S., Wasserburg, G.J., Ingri, J. and Baskaran, M. (1997) The importance of colloids and mires for the transport of uranium isotopes through the Kalix River watershed and Baltic Sea. *Geochimica et Cosmochimica Acta* 61, 4095-4113.

Schultz, M.K., Burnett, W.C. and Inn, K.G.W. (1998) Evaluation of a sequential extraction method for determining actinide fractionation in soils and sediments. *Journal of Environmental Radioactivity* 40, 155-174.

Suresh, P.O., Dosseto, A., Handley, H.K. and Hesse, P.P. (2014) Assessment of a sequential phase extraction procedure for uranium-series isotope analysis of soils and sediments. *Applied Radiation and Isotopes* 83, 47-55.

Sutherland, R.A. (2002) Comparison between non-residual Al, Co, Cu, Fe, Mn, Ni, Pb and Zn released by a three-step sequential extraction procedure and a dilute hydrochloric acid leach for soil and road deposited sediment. *Applied Geochemistry* 17, 353-365.

Tessier, A., Campbell, P.G.C. and Bisson, M. (1979) Sequential extraction procedure for the speciation of particulate trace metals. *Analytical Chemistry* 51, 844-851.

Virtanen, S., Vaaramaa, K. and Lehto, J. (2013) Fractionation of U, Th, Ra and Pb from boreal forest soils by sequential extractions. *Applied Geochemistry* 38, 1-9.

Wilson, S.A. (1997) The collection, preparation and testing of USGS reference material BCR-2. U.S. Geological Survey Open-File Report 98.

Wong, P.-z., Howard, J. and Lin, J.-S. (1986) Surface Roughening and the Fractal Nature of Rocks. *Physical Review Letters* 57, 637-640.

Young, R. (1982) Soils of the Illawarra region. *Wollongong Studies in Geography*, 10.

3. Controls on ($^{234}\text{U}/^{238}\text{U}$) in fine-grained sediments from the Gulf of Carpentaria, tropical northern Australia

Ashley N. Martin^{1,2*}, Anthony Dosseto^{1,2}, Jan-Hendrik May^{1,2}, John Jansen^{1,2,3}, Leslie P. J. Kinsley⁴, and Allan R. Chivas²

¹*Wollongong Isotope Geochronology Laboratory, School of Earth & Environmental Sciences, University of Wollongong, NSW 2522, Australia.*

²*GeoQUEST Research Centre, School of Earth & Environmental Sciences, University of Wollongong, NSW 2522, Australia.*

³*Institute of Earth & Environmental Science, University of Potsdam, 14476 Potsdam, Germany.*

⁴*Research School of Earth Sciences, Australian National University, Canberra, ACT 0200, Australia.*

*Corresponding author:

Email: anm724@uowmail.edu.au

Telephone: (+61 2) 4221 3382

Abstract

Uranium (U) isotopes are useful for constraining the timescales of weathering and erosion processes. The ($^{234}\text{U}/^{238}\text{U}$) activity ratio of fine-grained detrital minerals has been proposed to record the time elapsed since the grains were reduced to $<63\text{ }\mu\text{m}$, which is termed the *comminution dating* technique. Applied to fluvial systems, comminution ages are inferred to represent sediment residence times in catchments. However, there are uncertainties in input parameters, e.g. the estimation of the direct-recoil fraction, and knowledge of the initial ($^{234}\text{U}/^{238}\text{U}$) activity ratio of the parent material, which is typically assumed to be in secular equilibrium. Here we measure the ($^{234}\text{U}/^{238}\text{U}$) activity ratios of the $<63\text{ }\mu\text{m}$ detrital fraction of river sediments from seven large catchments in the Gulf of Carpentaria drainage basin, northern Australia. Bedrock was sampled from catchment headwaters to assess the initial activity ratio of the parent material and the specific surface area and fractal dimension were measured for all sediments to calculate the direct-recoil fraction. The ($^{234}\text{U}/^{238}\text{U}$) activity ratios of visibly-unweathered rock samples ranged from 0.817 – 1.045, suggesting that the parent material is not in secular equilibrium in our study area. Higher specific surface areas and lower ($^{234}\text{U}/^{238}\text{U}$) were measured for sediments from the southern catchments. Considerations of the mass fluxes from dust deposition vs fluvial erosion suggest that the aeolian fraction of sediments could be up to 24%. Thus, sediment residence times in our study area are considered to represent fluvial-aeolian processes. Inferred sediment residence times in catchments ranged from <1 to $190\pm 80\text{ ka}$. The average sediment residence time was $88 \pm 35\text{ ka}$, suggesting that catchments may be currently reworking of sediment that was accumulated over the last glacial cycle, which was a period of reduced rainfall and fluvial activity in N Australia. This highlights that the long duration of sedimentary storage in large, low-relief shield basins.

Keywords: comminution age, uranium-series isotopes, sediment residence time, secular equilibrium.

3.1 Introduction

The breakdown of bedrock to soils and sediments provides material for chemical weathering, regulating atmospheric CO₂ levels on geological timescales (Berner et al., 1983; Gaillardet et al., 1999; Kump et al., 2000; West et al., 2005). Mountainous areas have high erosion rates, and provide the majority of sediment (Milliman and Syvitski, 1992; Syvitski et al., 2005), but weathering in these regions is kinetically limited (Stallard, 1985; West et al., 2005). Although low-relief areas have lower erosion rates, silicate minerals undergo more complete weathering (Frings et al., 2015; Lupker et al., 2012). If weathering reactions are still occurring during intervals of temporary storage (Bouchez et al., 2012), this has implications for global CO₂ drawdown as the magnitude of sediment exchange between the channel and floodplain can exceed the annual sediment flux in large fluvial systems e.g. the Amazon River (Dunne et al., 1998). The average residence time of sediment in hillslope-fluvial systems is therefore a key parameter in determining the relationship between silicate weathering, climate change, and CO₂ drawdown.

Sediment can be transported by multiple pathways in hillslope-fluvial systems (*sediment-routing system*), which accounts for the time spent by sediment particles in each temporary reservoir from inception at the soil-bedrock interface until long-term sequestration e.g. in a sedimentary basin (Allen, 2008; Malmgren et al., 2003). The total duration of this process at a given location is referred to as the *sediment residence time* (Figure 3.1). By relating the residence time of sediments to geomorphic and climatic parameters of hillslope and fluvial systems, a better understanding of how variations in sediment transport influence the global weathering cycle can be achieved. Accurately constraining the sediment residence time is complicated by the nature of mass wasting and fluvial processes which continually transport, deposit and remobilise material. Dating techniques such as optically stimulated luminescence can estimate the age of deposition, but properly constraining the sediment residence time of fluvial systems would require a catchment-wide assessment of

depositional ages (e.g. Phillips et al., 2007), and this is logistically impractical. Modelling suggests that the residence time of sediments in large river systems could be up to 1 Ma (Castelltort and Van Den Driessche, 2003; Métiévier and Gaudemer, 1999); however, these estimates require validating by empirical measurements.

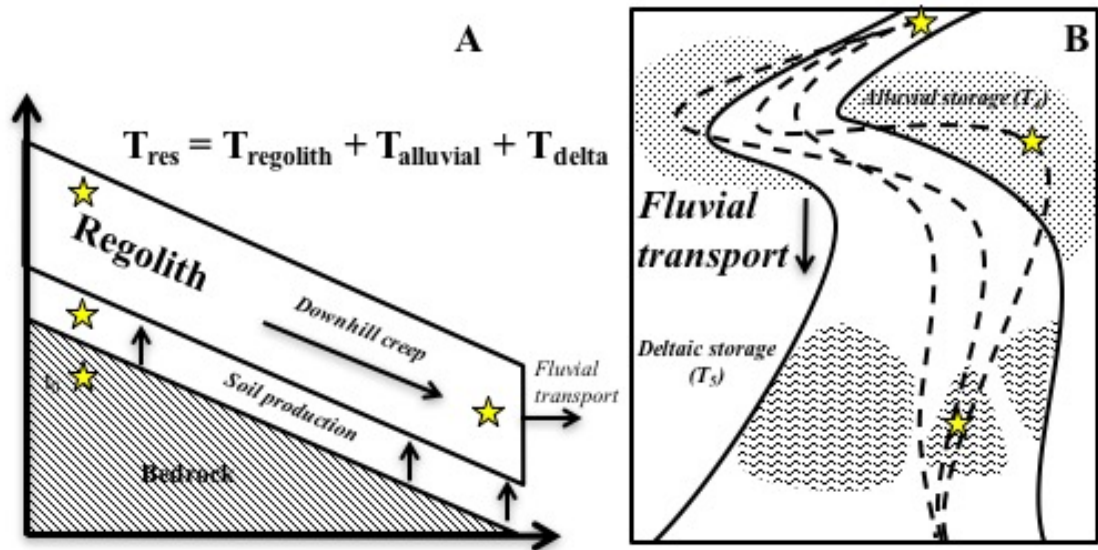


Figure 3.1A) Sketch depicting the sediment residence time (T_{res}) of a hillslope section depicting the potential pathways of sediment particles (stars) from incipient bedrock weathering, soil production, and creep during regolith storage ($T_{regolith}$); B) Sketch (oblique view) of the fluvial system depicting potential routes (dashed lines) of sediment particles during fluvial transport including alluvial storage ($T_{alluvial}$), and deltaic storage (T_{delta}) (modified from Malmon et al., 2003).

Uranium-series (U-series) isotopes undergo radioactive decay on timescales relevant to Earth-surface processes (10^3 to 10^6 a), and are fractionated by weathering processes (Chabaux et al., 2003). U-series disequilibria in soils and/or sediments yields the time elapsed since the onset of U and Th isotope fractionation by chemical weathering (see Dosseto et al., 2008 for a comprehensive review), which is referred to as the *weathering age* (Dosseto et al., 2012). Comminution dating is a developing application of U isotopes, which aims to constrain the time elapsed since sediment particles were reduced to $<63 \mu\text{m}$ in size (DePaolo et al., 2006). This is based on the loss of ^{234}U (via the short-lived ^{234}Th) by direct

recoil during the alpha-decay of ^{238}U (Kigoshi, 1971). This depletion of ^{234}U is only measurable in fine-grained minerals with high surface-area-to-volume ratios, typically $<63\ \mu\text{m}$ in size (DePaolo et al., 2006). A comminution age (t) can be calculated using the following equation:

$$t = \frac{-1}{\lambda_{234}} \ln \left[\frac{A - (1 - f_\alpha)}{A_0 - (1 - f_\alpha)} \right] \quad (1)$$

where A is the measured ($^{234}\text{U}/^{238}\text{U}$) activity ratio, A_0 is the initial ($^{234}\text{U}/^{238}\text{U}$) activity ratio of the parent material (e.g. bedrock or grains $>63\ \mu\text{m}$ in size), λ_{234} is the decay constant of ^{234}U (in a^{-1}) and f_α is the direct-recoil fraction. The latter represents the fraction of ^{234}U (via the short-lived ^{234}Th) nuclides lost by direct recoil from the solid phase to the surrounding medium and is estimated from the geometric properties of grains (DePaolo et al., 2006). The initial activity ratio of the parent material is typically assumed to be ($^{234}\text{U}/^{238}\text{U}$) = 1 (parentheses denote activity ratios) since secular equilibrium is achieved in systems that remain closed (no weathering reactions occur) for approximately four half-lives of the daughter nuclide (Chabaux et al., 2003). The half-life of ^{234}U is $245,250 \pm 490\ \text{a}$ (Cheng et al., 2000), and thus, the parent material will be in secular equilibrium if undisturbed for $\sim 1\ \text{Ma}$.

Applied to sediment in transit through hillslope and fluvial systems, comminution ages ideally represent the time elapsed since the breakdown of bedrock to form $<63\ \mu\text{m}$ grains. Comminution dating has been successfully applied to a marine core from the North Atlantic (DePaolo et al., 2006), ice cores in Antarctica (Aciego et al., 2011) permafrost in Greenland (Ewing et al., 2015), and palaeo-channel deposits in south-eastern Australia (Dosseto et al., 2010). However, some studies of alluvial deposits inferred comminution ages that were generally lower than depositional ages (Handley et al., 2013a; Handley et al., 2013b; Lee et al., 2010). This is impossible since comminution ages integrate sedimentary storage and

sediment transport, suggesting a systematic issue in the interpretation and/or modelling of comminution ages.

A major source of uncertainty is the assumption that the source rocks are in secular equilibrium. U isotope disequilibrium in rocks or grains $>63\ \mu\text{m}$ in size can arise from preferential leaching of ^{234}U from lattice sites damaged by recoil during the alpha decay of ^{238}U , which can occur on rapid timescales ($<200\ \text{a}$, Fleischer, 1980). Volcanic rocks are generally in secular equilibrium, e.g. the Galápagos islands (Handley et al., 2011), Puerto Rico (Chabaux et al., 2013), Cameroon (Pelt et al., 2013), and North America (Sims et al., 2008; Wilson, 1997), although a slight depletion of ^{234}U was observed in young volcanic rocks from the Kamchatka arc province (Dosseto and Turner, 2014). In contrast to volcanic rocks, ($^{234}\text{U}/^{238}\text{U}$) activity ratios significantly less than unity have been measured in visibly “unweathered” sedimentary, metamorphic and granitic rocks (Bourdon et al., 2009; Dosseto and Riebe, 2011; Handley et al., 2013b; Landström et al., 2001; Rosholt, 1983). This questions the starting point for U isotope fractionation in non-volcanic catchments. The validity of the secular equilibrium assumption may also be a function of erosion rates and the weathering environment. For instance, DePaolo et al. (2012) found that glacial outwash sediments, which are expected to have short transport times and closely represent the parent material, were in secular equilibrium.

Here we measure U isotope for eighteen river sediments from seven catchments draining to the Gulf of Carpentaria, northern Australia to infer sediment residence times. The Gulf of Carpentaria drainage basin is geologically diverse and provides an ideal study area to evaluate the assumption that the source rocks are in secular equilibrium. Thus, a range of bedrock samples were collected from catchment headwaters. In addition, the geometric properties (surface area, fractal dimension, and surface roughness), and mineralogy of river sediments were measured for each sample to reduce uncertainty in comminution age parameters that are typically assumed. Fluvial sediments were collected at various points

within catchments to assess intra-catchment variation in sediment residence times. Comminution ages should increase linearly downstream if sediment transport in catchments is a first-order diffusive process, as shown by modelling (Castelltort and Van Den Driessche, 2003; Métivier and Gaudemer, 1999), and U-series measurements in the Bolivian Andres (Dosseto et al., 2006). In addition, the Gulf drainage basin spans ten degrees of latitude from the tropical north to semi-arid south, with mean annual rainfall varying from >1700 to <400 mm a⁻¹ (BOM, 2009). The large difference in rainfall for the Gulf catchments allows us to assess the relationship between sediment residence times and climate. We first describe general trends in U isotopes and geometric properties of river sediments in northern Australia. Based on the (²³⁴U/²³⁸U) activity ratios of bedrock samples, we then consider whether the assumption that the source rocks are in secular equilibrium. Finally, we infer comminution ages for catchments as sediment residence times.

3.2 Study area

The Gulf of Carpentaria is a large, epicontinental sea in tropical northern Australia straddling the Pacific Ocean to the east and the Indian Ocean to the west (Figure 3.2). Regional denudation rates are considered to be slow. Measurements of cosmogenic nuclides (¹⁰Be, ²⁶Al) on bedrock surfaces in northern and central Australia indicate erosion rates of <4 m Ma⁻¹ (Belton et al., 2004; Bierman and Caffee, 2002), and catchment-wide rates of 15 – 20 m Ma⁻¹ are reported for streams draining to the Coral Sea in northeastern Australia (Nichols et al., 2014). Such rates are comparable with rates of ca. 20 m Ma⁻¹ measured by dating basalt surfaces in the Flinders River (Coventry et al., 1985), one of our study catchments. Another study of basalt surfaces in central Queensland estimated the rate of soil production to be even lower at 0.30 m Ma⁻¹ (Pillans, 1997).

Seven large catchments draining to the eastern shores of the Gulf were sampled (340,000 km² in total), namely the Archer, Mitchell, Staaten, Gilbert, Norman, Leichhardt and

Flinders Rivers (Figure 3.2). Much of the landscape is regolith mantled, even in the uplands (Figure 3.2C). The vegetation is mainly *Eucalyptus* and *Acacia* woodland, and pollen evidence suggests the current vegetation in the region was established by 7.5 ka (Shulmeister, 1992). Rivers are generally sand-dominated, low sinuosity, and anabranching, with channels flanked by extensive floodplains comprising overbank muds and muddy-sands (Nanson et al., 1991). Floodplain deposits in the Gilbert River have a well-established chronology and are generally Late Quaternary, reflecting alternating wet interglacial and dry glacial intervals throughout this period (Nanson et al., 1992). These deposits comprise coarse sands from ca. 120 – 85 ka (Nanson et al., 2005), muddy-sands from 65 – 50 ka, muds at 50 ka, and post-LGM sands (Nanson et al., 2005). In the Gilbert River, indurated alluvium that is mainly calcrete/gypcrete has produced local rapids, waterfalls and gorges (Nanson et al., 2005).

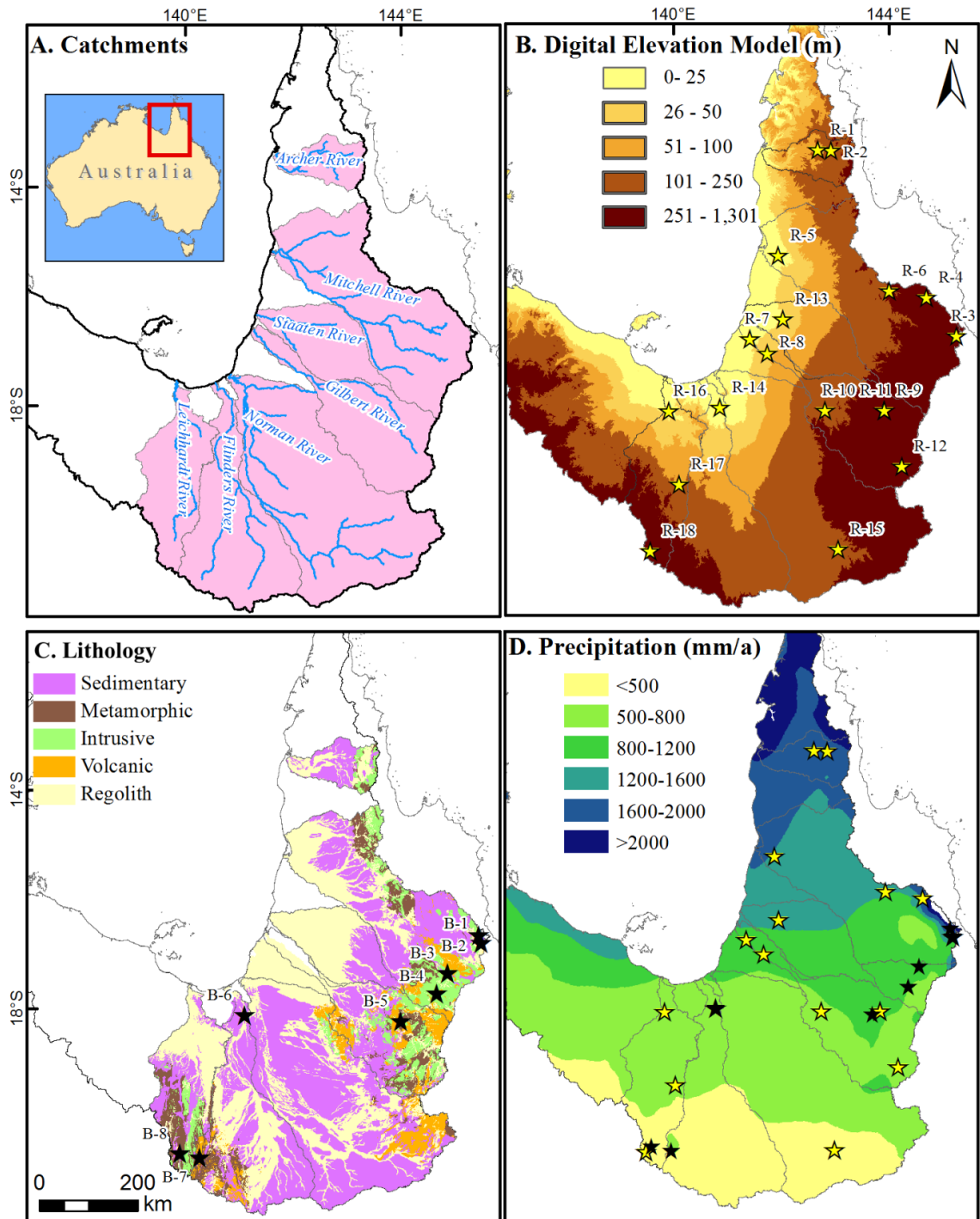


Figure 3.2. Spatial data for the Gulf of Carpentaria drainage basin including: A) Major channels (5th order streams and above) and labelled drainage basins (areas shown in pink); B) Digital elevation model (Gallant et al., 2014) with labelled sediment sampling sites (yellow stars); C) Catchment lithology with labelled sampling sites of bedrock (black stars) (Raymond et al., 2012); and D) Mean annual rainfall (BOM, 2009).

Catchment lithology varies greatly due to the complex and long tectonic history of the North Queensland that commenced in the Proterozoic Era (Withnall and Cranfield, 2013). The Archer River drains the metamorphic rocks of the Coen Inlier. The most common rocks are the Palaeozoic Sefton Metamorphics (predominantly schist, quartzite, limestone, marble and calc-silicates), and the high-grade metamorphic rocks of the Paleoproterozoic Yambo Subprovince (Withnall and Cranfield, 2013). The Mitchell River drains the Hodgkinson Province of the Mossman Orogen (Withnall and Cranfield, 2013). These rocks are predominately Carboniferous sedimentary rocks (quartzo-feldspathic arenite and mudstone), with granitic intrusions (Champion and Bultitude, 2013). The Staaten River drains the Neogene to Quaternary Wyaaba Beds, which are a mix of poorly-sorted clayey quartzose sand, sandstone, granule conglomerate and interbedded sandy claystone. The upper Staaten River drains Mesoproterozoic meta-sedimentary rocks of the Staaten Metamorphic Group (Raymond et al., 2012). The Gilbert River and Norman River drain the respective eastern and western sides of the Georgetown Inlier (Raymond et al., 2012). This is dominated by variably metamorphosed Proterozoic sedimentary and volcanic rocks with granitic intrusions (Champion and Bultitude, 2013). In the uplands, there are a high proportion of basaltic rocks from Cenozoic lava flows that are up to 160 km long (Stephenson and Griffin, 1976). The Flinders River catchment mainly drains Cretaceous sandstones and shales of the Galilee Basin, with a small number of Cenozoic basalt flows in the uplands (Withnall and Cranfield, 2013). The Leichhardt River drains the Mount Isa Inlier, which is a complex series of fold belts, and felsic/mafic intrusions into Proterozoic basement rocks (Withnall and Cranfield, 2013). Typical rocks types are granite, quartzite, gneiss, schist, amphibolite, phyllite, limestone and shale (Raymond et al., 2012).

Fluvial megafans are developed in the lower portions of several catchments indicating that such areas predominantly function as long-term sediment sinks. These are especially well-developed on the Mitchell River (<200 masl) where a large (31,000 km²) fan has formed as a

result of variations in sea-level and climate change from the Pliocene to present (Brooks et al., 2009). There is also a large fan in the Gilbert River where the lowermost 200 km consists of anabranching channels and associated deltaic deposits (Nanson et al., 1991).

Rivers flow in response to monsoonal rains, which are generally from December to March (Reeves et al., 2008). A strong rainfall gradient spans the study area from the north ($>2400 \text{ mm a}^{-1}$) to the south ($<600 \text{ mm a}^{-1}$, Figure 3.2D). The region experiences an average of two cyclones per year, which may be lower than at any period over the past 0.5 – 1.5 ka (Haig et al., 2014).

The 18 sampled sub-catchments have catchment areas ranging from 34 – 50,800 km^2 , average slope values from 1 to 10% using a three arc-second DEM (Jarvis et al., 2008), average slope values 2.6 to 15% using a one arc-second DEM (Gallant et al., 2014), and mean discharge values from 7.3 to 9800 $\text{m}^3 \text{ s}^{-1}$ (DNRM, 2014) (Table 3.1). Mean annual rainfall in the sub-catchments varies from 440 to 1740 mm (BOM, 2009).

Table 3.1 Morphometric parameters for each sub-catchment: catchment area (A), average slope, mean annual rainfall (P), discharge (Q), and lithology.

Sample	Catchment	A ^a	Slope ^a	P ^b	Q ^c	Lithology (% of catchment area) ^d							
		(km ²)	(%)	(mm a ⁻¹)	(m ³ s ⁻¹)	Mudstone	Other sedimentary	Granitic	Marble	Metamorphic	Regolith	Felsic volcanics	Mafic volcanics
R-1	Archer	3,350	5	1,740	1,150	0	0	14	0	68	18	0	0
R-2	Archer	2,890	5	1,670	995	0	0	42	0	24	33	0	0
R-3	Mitchell	34	6	1,380	12	58	0	5	0	0	36	0	0
R-4	Mitchell	540	8	1,730	184	14	49	36	0	0	1	0	0
R-5	Mitchell	46,300	6	916	159,00	7	34	20	0	8	20	9	2
R-6	Mitchell	3900	10	1,190	1340	4	84	8	0	0	1	0	2
R-7	Gilbert	26,000	3	841	17,500	0	1	1	0	0	2	0	0
R-8	Gilbert	25,300	4	841	17,100	6	17	24	3	10	20	7	11
R-9	Gilbert	9,360	5	841	6,310	0	4	34	9	16	20	4	13
R-10	Gilbert	11,000	4	841	7,400	15	40	15	4	8	11	7	0
R-11	Gilbert	9,330	5	841	6,300	0	4	34	9	16	20	4	13
R-12	Gilbert	59	6	800	40	0	0	38	22	19	22	0	0
R-13	Staaten	6,710	1	1,050	4,530	0	52	0	0	0	48	0	0
R-14	Flinders	50,800	1	564	3,580	14	30	4	2	7	40	1	1
R-15	Norman	17,300	2	650	1,220	34	16	4	0	2	18	0	26
R-16	Leichhardt	23,800	4	564	818	4	29	5	2	25	25	8	1
R-17	Leichhardt	8,660	6	473	2,980	5	13	11	6	35	10	17	2
R-18	Leichhardt	501	5	440	172	10	6	24	0	55	3	0	2

Data from ^aJarvis et al. (2008), ^bBOM (2009), ^cDNRM (2014), ^dRaymond et al. (2012).

3.3 Methods

3.3.1 Sample collection

Bedrock samples were collected from natural outcrops, and road cuts in the headwaters of the study catchments in August 2012 (sampling locations shown in Figure 3.2C). Care was taken to avoid visibly weathered material and ca. 1 kg of material was sampled. River sediment was collected from eighteen sites across seven catchments (sampling sites shown in Figure 3.2B), during the dry season (austral winter) in two field campaigns: May 2004 (R-1, 2, 5, 6, 7, 8, 10, 13, 14, and 16) and August 2012 (R-3, 4, 9, 11, 12, 15, 17, and 18). Samples were collected from: i) mud drapes deposited during falling flood stages (e.g. Figure 3.3B); ii) sandy bedload sub-samples amalgamated along ca. 100 m reaches (Figure 3.3C). Grain size distribution measurements showed no difference in the mean diameter of mud drape vs bedload samples, suggesting that these samples are comparable.

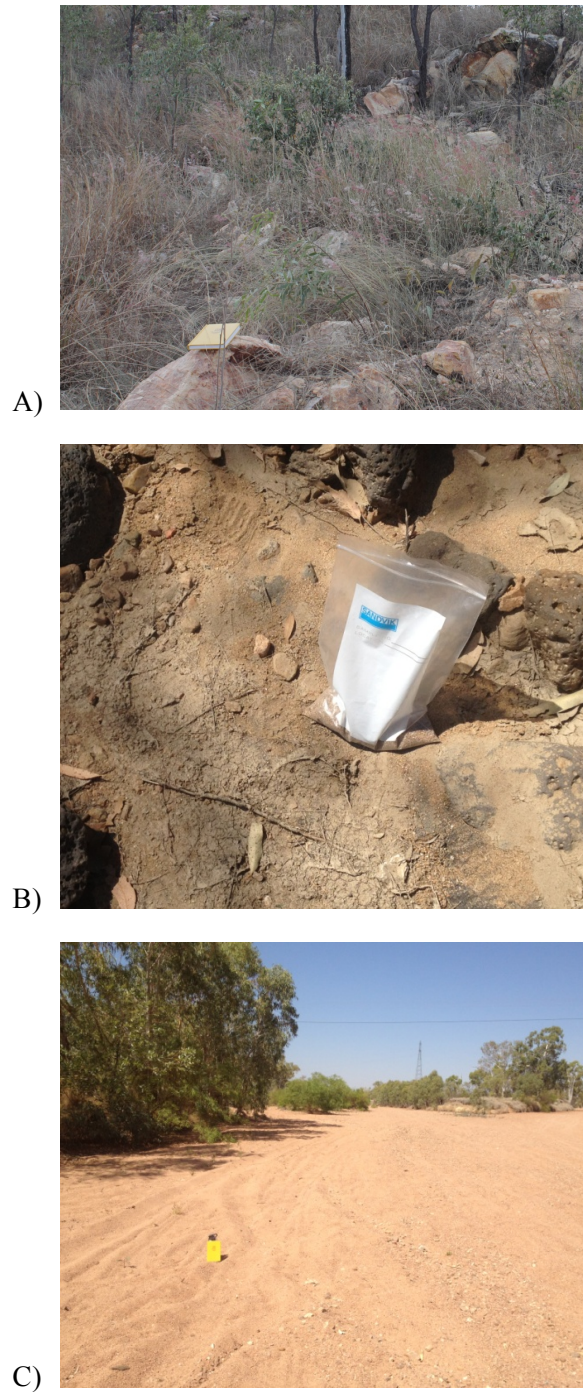


Figure 3.3A) Bedrock outcrop sampled from the Flinders River catchment (B-6, 17°44.21'S 144°32.01'E); B) Mud drapes (R-12, Einasleigh River, 19°12.38'S 144°22.70'E); and C) Sediment sampled from a 100 m reach of a dry channel (R-18, Leichhardt River, 20°46.63'S 139°29.69'E).

3.3.2 Sample preparation and analytical techniques

Rocks were split using a rock saw, and one half of the sample was analysed. Around 10 g of sample was further split by rock saw from the inner portions of the rock samples and then crushed to powder using a tungsten carbide TEMA® T100 laboratory disc mill. Sediments were wet-sieved at 63 µm using deionised water; the <63 µm fraction was retained, dried in an oven at 50 °C and homogenised by gentle mixing using an agate mortar and pestle. Sequential extraction was conducted on 2 g of dry sample following the procedure of Lee (2009). Sample pre-treatment methods developed in Chapter 2 were not utilised as the work in this Chapter was undertaken simultaneously. Solid and aqueous phases were centrifuged at 7000 rpm for 10 min.

Particle size analysis of leached sediments was conducted using a Malvern Mastersizer 2000 by dispersing a few mg of sample in water and reported values representing the average of three replicate measurements. BET surface area measurements were determined by N₂ gas adsorption using a Quantachrome iQ surface area analyser at the Wollongong Isotope and Geochronology Laboratory at the University of Wollongong. Samples were degassed for 3 h at 200 °C and S_{BET} was determined using 5 – 7 adsorption points from the partial pressure (P/P_0) range 0.05 – 0.30 and adjusted for the best fit of the multi-point BET plot ($R^2 > 0.9999$).

For X-ray diffraction (XRD) measurements, samples were crushed to <4 mm with a Tollmill crusher (TEMA). The samples were then mounted in aluminium holders and placed in a Phillips 1130/90 diffractometer with Spellman DF3 generator set to 1 kW. They were loaded and analysed through an automatic sample holder. The 1 kW energy is achieved by setting the diffractometer to 35 kV and 28.8 mA. Samples were analysed between 4 and 70° 2-theta at 2° per minute with a step size of 0.02. Traces were produced through a GBC 122 control system and analysed using Traces, µPDSM and SIROQUANT softwares. Error was assessed

by the chi-squared (χ^2) value which compares the observed data (measured XRD spectrum) with expected data (hypothetical XRD spectrum according to user-selected minerals). Only data from experiments with $\chi^2 < 5$ were accepted.

Prior to acid dissolution, ca. 100 mg of material was weighed and spiked with a ^{229}Th – ^{236}U tracer for isotopic dilution at the Wollongong Isotope and Geochronology Laboratory at the University of Wollongong. Samples were dissolved by adding 2.5 mL 32 % HF and 0.5 mL 69 % HNO_3 and heated overnight at 100°C. Once dry, 3 mL of 6 M HCl was added, with H_3BO_3 added to dissolve fluorides where necessary, heated at 80°C overnight and dried. Following this, 0.5 mL 69 % HNO_3 was added, and dried at 100°C and this step was repeated. To prepare samples for column chromatography, 2 mL of 1.5 M HNO_3 was added and the solutions were sonicated for 15 min and heated at 100°C to ensure re-dissolution. Total procedural blanks were <140 pg for U. For isotopic measurements, U was separated by standard chromatographic techniques using a TRU resin (Eichrom) as described in Luo et al. (1997). The $^{234}\text{U}/^{238}\text{U}$ ratios were measured using a ThermoFisher Neptune Plus Multi-Collector Inductively-Coupled-Plasma-Mass Spectrometer (MC-ICP-MS) at the Research School of Earth Sciences, Australian National University. Mass bias and SEM/Faraday cup yield were corrected by standard bracketing using synthetic standards CRM U005A and CRM U010 (NBL, 2008a; NBL, 2008b). For isotopic dilution measurements, the $^{236}\text{U}/^{238}\text{U}$ activity ratio was corrected for the tail contribution of ^{238}U by measuring the intensities at 235.5 and 236.5 and using a linear interpolation to calculate the mass at 236.045568. Accuracy of measurements was assessed by analysing a gravimetric rock standard (BCR-2, U.S. Geological Survey) known to be in secular equilibrium whereby $(^{234}\text{U}/^{238}\text{U})_{\text{S.E.}} = 1$. The measured $(^{234}\text{U}/^{238}\text{U})$ activity ratios were within 0.6 % of this value (1.004 ± 0.002 and 1.006 ± 0.002). The measured U concentrations (ppm) were 1.70 ± 0.01 and 1.84 ± 0.01 ppm which are all within error of recommended values (Wilson, 1997).

3.3.3 Spatial Analysis

Digital elevation analyses were conducted with Arc GIS 10TM using the 3 arc-second (ca. 90 m²) resolution Shuttle Radar Topography Mission (SRTM) dataset (Jarvis et al., 2008). To assess whether the 3 arc second DEM underestimated calculated slopes values, slope values were re-calculated using a 1 arc-second DEM (Gallant et al., 2014). To examine the topographic attributes of the vast, low gradient valleys, a Multi-resolution Index of Valley Bottom Flatness (MrVBF) was obtained from the ‘Multi-resolution Valley Bottom Flatness (3 arc-second resolution) dataset which uses an algorithm to identify valley bottoms in digital elevation models (Gallant and Dowling, 2003). High values of MrVBF indicate a larger proportion of low gradient areas, and low values indicate a larger proportion of high gradient values. Geological information was obtained in digital format from the ‘Surface Geology of Australia 1:1 million scale dataset 2012 edition’ (Raymond et al., 2012). Rainfall data were extracted from ‘Gridded Average Rainfall’ dataset (BOM, 2009), which is based on data collected from ca. 6300 stations across Australia from 1961 to 1990. Vegetation density data were obtained from the ‘Vegetation Post-European Settlement (1988)’ dataset from Geoscience Australia (Australia, 2003), and is expressed in terms of the proportion of the ground that is shaded by the tallest stratum at midday in four bands: 1) <10%, 2) 10 – 30%; 3) 30 – 70%; and 4) 70%. Streamflow data were obtained from the Queensland Government (DNRM, 2014), and regional discharge to drainage area relationships were derived for each study catchment via least squares regression (Figure 3.4). Note that streamflow data were only available for one site in the Staaten River and these were included in the model for the Gilbert River.

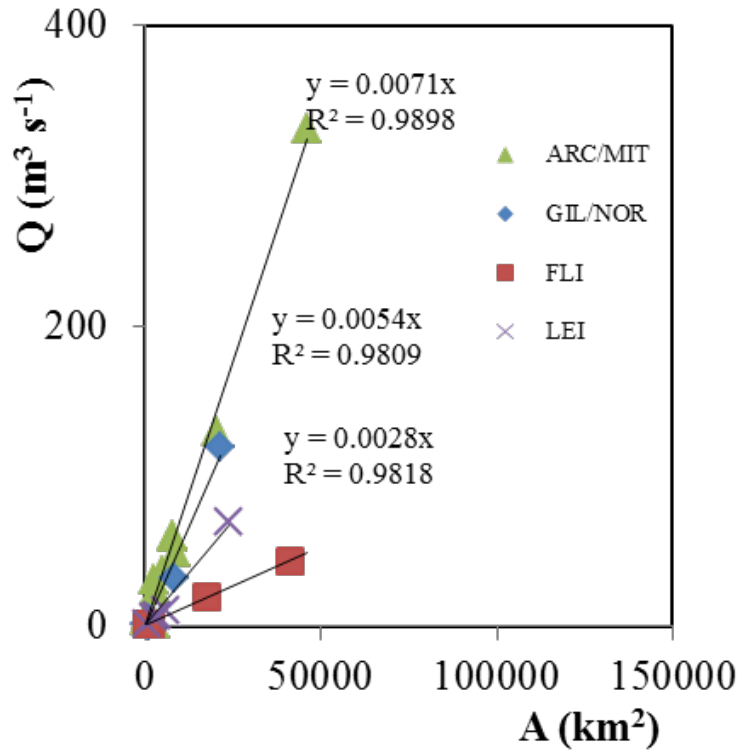


Figure 3.4. Linear regression models of catchment area (A) vs mean discharge (Q) for the following basins (DNRM, 2014): Archer/Mitchell (ARC/MIT), Gilbert/Staaten/Norman (GIL/NOR), Flinders (FLI), Leichhardt (LEI) Rivers.

3.3.4 Statistical analyses

Beta distributions were modelled in R 3.3.0 using the *pbeta* and *dbeta* functions ($n = 1,000$). Distributions were parameterised using positive shape factors α : number of positive outcomes and β : number of negative outcomes to calculate the probability that bedrock samples will be in secular equilibrium. Pearson's correlation matrices were calculated using XLSTAT. Pearson's correlation coefficient (ρ) is calculated by dividing the covariance of independent variables by the product of their standard deviations (Pearson, 1909); p-values were calculated to test the null hypothesis that the coefficients are not significantly different from $\rho = 0$. Bootstrap uncertainty estimates were calculated using XLSTAT (Resampled statistics Bootstrap), which is based on the method outlined by Efron (1993).

3.4 Results and discussion

3.4.1 Detrital uranium in river sediments

Measured ($^{234}\text{U}/^{238}\text{U}$) activity ratios ranged from 0.817 – 1.045 ($n = 18$, Table 3.2), which covers the range of previously measured ($^{234}\text{U}/^{238}\text{U}$) activity ratios for leached suspended sediments from temperate, semi-arid and arid Australia (Dosseto et al., 2010; Handley et al., 2013a; Handley et al., 2013b) (Figure 3.5). The measured ($^{234}\text{U}/^{238}\text{U}$) appear to be less variable in temperate rivers; for instance, the ($^{234}\text{U}/^{238}\text{U}$) of leached suspended sediment from the modern Murrumbidgee River in temperate Australia ranged from just 0.941 – 0.949, and the interquartile range of the $<63\ \mu\text{m}$ fraction of palaeo-channel deposits from the Murrumbidgee River was 0.004 ($n = 15$) (Dosseto et al., 2010). In contrast, ($^{234}\text{U}/^{238}\text{U}$) of leached suspended sediment from semi-arid and arid Australia were more variable (Handley et al., 2013a; Handley et al., 2013b). Highly variable ($^{234}\text{U}/^{238}\text{U}$) activity ratios of sediments may be related to high discharge variability in tropical monsoonal (Table 3.4) and semi-arid environments.

The minimum ($^{234}\text{U}/^{238}\text{U}$) for leached suspended sediment from Gulf catchments was lower than any previously measured value for leached sediment in Australia (Dosseto et al., 2010; Handley et al., 2013a; Handley et al., 2013b). This is surprising considering that other studies include leached sediment samples with depositional ages of up to $100 \pm 10\ \text{ka}$, which are expected to show lower ($^{234}\text{U}/^{238}\text{U}$) due to the loss of ^{234}U by direct recoil during sedimentary storage. This could suggest that Gulf sediments have longer residence times ($>100\ \text{ka}$) that exceed those in temperate, semi-arid and arid Australia. Alternatively, this could reflect the enhanced loss of ^{234}U from bedrock in tropical monsoonal vs temperature/semi-arid Australia. This is unlikely since the Australian continent is generally ancient and characterised by low denudation rates (Bierman and Caffee, 2002; Belton et al.,

2004), and ^{234}U depletion was measured in rocks from semi-arid Australia (Handley et al., 2013b).

The U concentrations ranged from 0.3 – 16.3 ppm (Table 3.2). Higher U concentrations of sediments are associated with larger mean grain sizes ($\rho = 0.56$, $p = 0.023$). Typically, U concentrations of bulk sediments grains are inversely correlated with grain size (Megumi and Mamuro, 1977; Megumi et al., 1982), which is attributed to U associated with secondary minerals and coatings and the greater surface-area-to-volume ratio of smaller grains. However, non-detrital matter was already removed during sample pre-treatment and hence this relationship was not observed. To a lesser extent, higher U concentrations are also associated with higher percentages of feldspar minerals ($\rho = 0.51$, $p = 0.042$).

Higher weighted average ($^{234}\text{U}/^{238}\text{U}$) activity ratios (0.980 vs 0.913) and higher average U concentrations (6.1 vs 2.5 ppm) were measured for the northern (N) vs southern (S) catchments draining to the Gulf (Table 3.6). Catchments were defined as N or S according to whether the latitude of the river mouth was above or below 16.5°S. This is a useful marker since the N catchments generally drain east to west and the S catchments below 16.5°S drain to a northerly direction.

The ($^{234}\text{U}/^{238}\text{U}$) of river sediments from the Gilbert River were highly variable (0.817 – 0.967, Table 3.2). Repeat sampling of a channel in the Gilbert River in two field campaigns during 2004 and 2012 yielded activity ratios of 0.967 ± 0.004 and 0.856 ± 0.007 (R-9 and R-11, Table 3.2). This suggests that sediment transport history of sediment grains in the Gilbert River are highly variable. Firstly, this may be due to highly variable discharge of the Gilbert River, which is controlled by variations in monsoonal rainfall (Reeves et al., 2008), and results in frequent channel abandonments (Nanson et al., 2005). Secondly, the actively-eroding floodplain units in the Gilbert River typically comprise muddy sands from 65 – 50 ka, muds from 50 ka, and post-LGM sands (Nanson et al., 2005). If loss of ^{234}U is occurring

by direct recoil and/or preferential leaching during alluvial storage, these units each contain sediments with distinct ($^{234}\text{U}/^{238}\text{U}$). Alternatively, sediment sourced from alluvial reworking vs hillslope erosion would also produce sediments with distinct ($^{234}\text{U}/^{238}\text{U}$). The discussion of sediment transport processes in the Gulf of Carpentaria drainage basin is therefore limited to catchment-wide processes.

Table 3.2. U concentration, U isotope, surface area, mineralogy, and particle size data for <63 µm river sediments.

Sample	Catchment	(²³⁴ U/ ²³⁸ U) ^a	U ^a (ppm)	Quartz ^b (%)	Feldspar ^b (%)	Mica ^b (%)	Accessory ^b (%)	Clays ^b (%)	Recoil length ^c (nm)	Density ^d (cm ³ g ⁻¹)	d ^e	S _{BET} ^f (m ² g ⁻¹)	D ^g	λ ^h	A ₀ ⁱ	f _a ^{jk}	t _{comm} ^k (ka)
R-1 ^l	Archer	1.045 ± 0.003	6.08 ± 0.11	n/a	n/a	n/a	n/a	n/a	28	2.7	14	n/a	n/a	n/a	0.989	n/a	<1
R-2 ^l	Archer	1.018 ± 0.002	16.2 ± 0.19	41	43	7.7	2.6	5.8	27	2.7	23	16	2.6	34	0.958	0.04	<1
R-3 ^m	Mitchell	0.908 ± 0.001	3.25 ± 0.02	72	12	11	2.3	2.6	27	2.7	12	17	2.5	22	0.920	0.06	33 ± 14
R-4 ^m	Mitchell	0.915 ± 0.002	3.84 ± 0.02	57	13	23	1.3	5.5	27	2.6	16	13	2.6	24	0.953	0.04	100 ± 43
R-5 ^l	Mitchell	0.903 ± 0.002	3.03 ± 0.03	65	9.1	17	1.1	8.3	28	2.5	16	8.5	2.4	14	0.968	0.05	170 ± 74
R-6 ^l	Mitchell	0.861 ± 0.002	3.05 ± 0.02	40	19	10	0.4	30	27	2.0	19	14	2.7	28	0.988	0.03	450 ± 220
R-7 ^l	Gilbert	0.961 ± 0.004	3.64 ± 0.02	61	14	18	2.3	5.4	27	2.6	17	16	2.4	26	0.964	0.08	5 ± 2
R-8 ^l	Gilbert	0.949 ± 0.002	1.76 ± 0.18	63	11	17	2.9	6.7	27	2.6	12	34	2.7	44	0.965	0.07	31 ± 14
R-9 ^l	Gilbert	0.967 ± 0.004	2.44 ± 0.02	18	20	32	5.4	26	27	2.2	20	24	2.5	43	0.967	0.10	<1
R-10 ^l	Gilbert	0.817 ± 0.002	4.88 ± 0.02	67	8.0	22	0.7	2.7	27	2.7	16	4.3	2.1	8.1	0.961	0.06	580 ± 300
R-11 ^m	Gilbert	0.856 ± 0.007	5.99 ± 0.02	32	26	13	2.7	26	28	2.1	27	36	2.7	92	0.967	0.08	300 ± 140
R-12 ^m	Gilbert	0.945 ± 0.002	3.17 ± 0.01	37	47	3.0	4.4	9.1	29	2.5	24	33	2.8	77	0.954	0.06	19 ± 8
R-13 ^l	Staaten	1.000 ± 0.003	3.69 ± 0.03	n/a	n/a	n/a	n/a	n/a	28	n/a	22	12	2.3	25	1.000	0.08	18 ± 7
R-14 ^l	Flinders	0.957 ± 0.002	1.79 ± 0.02	n/a	n/a	n/a	n/a	n/a	28	n/a	8.5	49	2.7	47	0.983	0.09	45 ± 19
R-15 ^m	Norman	0.922 ± 0.002	1.88 ± 0.02	35	20	18	2.6	24	28	2.3	8.2	78	3.0	71	0.930	0.08	17 ± 7
R-16 ^l	Leichhardt	0.921 ± 0.002	0.30 ± 0.02	70	15	8.6	8.1	3.0	28	2.9	9.6	41	2.7	44	0.987	0.08	130 ± 54
R-17 ^m	Leichhardt	0.943 ± 0.007	2.82 ± 0.05	37	22	22	2.3	17	27	2.4	11	70	2.9	81	0.981	0.10	64 ± 27
R-18 ^l	Leichhardt	0.931 ± 0.002	3.04 ± 0.02	65	15	14	1.8	5.0	28	2.7	15	35	2.8	53	0.967	0.05	81 ± 36

^a2σ internal standard error; ^breplicate measurement of R-13 (n = 2, external error = 1.5%); ^cdetermined by XRD; ^destimated from mineral abundances and average values for density and recoil length given in Table 3.8; ^ed: mean diameter; ^fS_{BET}: specific surface area (external error = 17 %); ^gD: fractal dimension (external error = 12 %); ^hλ = S_{BET}/S_{geo}; ^jCalculated using Equation 3; ^kError calculated according to Table 3.10; ^lsample collected in May 2004, ^msample collected in August 2012.

Table 3.3 Pearson's correlation matrix^a for measured parameters for <63 µm river sediments

Variables	(²³⁴ U/ ²³⁸ U)	U	d ^b	<2 µm	S _{BET} ^c	D ^d	Quartz ^e	Feldspars ^e	Mica ^e	Accessory minerals ^e (wt. %)	Non-silicate minerals ^e (wt. %)
		(ppm)	(µm)	(%)	(m ² g ⁻¹)		(wt. %)	(wt. %)	(wt. %)		
(²³⁴ U/ ²³⁸ U)	1.00	0.29	-0.06	0.32	0.23	0.34	-0.22	0.42	-0.06	0.35	-0.13
U (ppm)	0.29	1.00	0.56	-0.41	-0.33	-0.19	-0.10	0.51	-0.33	-0.11	-0.23
d ^b (µm)	-0.06	0.56	1.00	-0.78	-0.49	-0.26	-0.50	0.59	-0.19	-0.10	-0.22
<2 µm (%)	0.32	-0.41	-0.78	1.00	0.58	0.38	0.04	-0.20	0.09	0.35	0.44
S _{BET} ^c (m ² g ⁻¹)	0.23	-0.33	-0.49	0.58	1.00	0.81	0.05	0.06	-0.23	0.57	0.22
D ^d	0.34	-0.19	-0.26	0.38	0.81	1.00	-0.09	0.30	-0.45	0.40	0.28
Quartz ^e (wt. %)	-0.22	-0.10	-0.50	0.04	0.05	-0.09	1.00	-0.61	-0.20	-0.17	-0.39
Feldspars ^e (wt. %)	0.42	0.51	0.59	-0.20	0.06	0.30	-0.61	1.00	-0.51	0.26	0.04
Mica ^e (wt. %)	-0.06	-0.33	-0.19	0.09	-0.23	-0.45	-0.20	-0.51	1.00	-0.14	-0.01
Accessory minerals ^e (wt. %)	0.35	-0.11	-0.10	0.35	0.57	0.40	-0.17	0.26	-0.14	1.00	-0.24
Non-silicate minerals ^e (wt. %)	-0.13	-0.23	-0.22	0.44	0.22	0.28	-0.39	0.04	-0.01	-0.24	1.00

^aValues in bold are significant at the level p < 0.05, ^bd: mean diameter, ^cS_{BET}: specific surface area, ^dD: fractal dimension, and ^emineral abundances determined by XRD.

Table 3.4 U isotope and concentration data for <63 µm river sediments from the northern and southern catchments draining to the Gulf of Carpentaria

Catchment	$(^{234}\text{U}/^{238}\text{U})^a$	$[\text{U}]^{a,b}$
		(ppm)
Archer River (n = 2)	1.000	11.16
Mitchell River (n = 5)	0.896	3.41
Staaten River (n = 1)	1.000	3.70
Average northern catchments (n = 8)	0.980	6.09
Gilbert River (n = 6)	0.898	3.65
Norman River (n = 1)	0.922	1.88
Flinders River (n = 1)	0.957	1.80
Leichhardt River (n = 4)	0.897	2.75
Average southern catchments (n = 12)	0.913	2.52

^aBased on data from Table 3.2; and ^bweighted average activity ratio based on measured U concentrations.

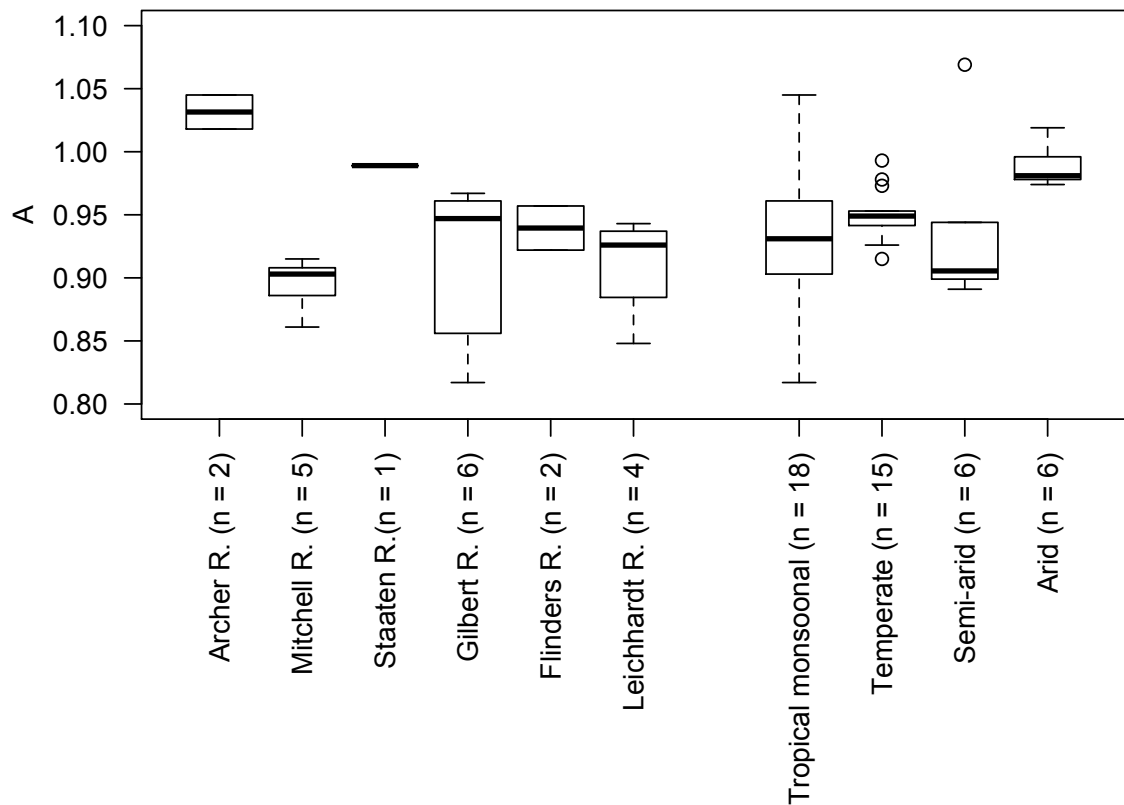


Figure 3.5 Box plot of ($^{234}\text{U}/^{238}\text{U}$) activity ratios (A) for $<63\ \mu\text{m}$ river sediments from the tropical monsoonal Gulf (this study), Murrumbidge River in southeastern Australia (Dosseto et al., 2010), Flinders Ranges in semi-arid South Australia (Handley et al., 2013b), and Cooper Creek in arid central Australia (Handley et al., 2013a). Outliers (outside 1.5 times the interquartile range) are represented as open circles. Upper and lower limits represent the interquartile range.

3.1.1 Geometric properties of detrital river sediments

Mean grain size diameters ranged from 8.2 to $27\ \mu\text{m}$, specific surface areas from 4.3 to $78\ \text{m}^2\ \text{g}^{-1}$, and the fractal dimension from 2.1 to 3.0 , whereby 3.0 represents the theoretical maximum (Table 3.2). Lower mean grain sizes are correlated with the percentage of $<2\ \mu\text{m}$ material ($\rho = -0.78$, $p < 0.001$), but not the specific surface areas of sediments (Table 3.3). However, the percentage of $<2\ \mu\text{m}$ material was associated with specific surface areas of sediment ($\rho = 0.58$, $p = 0.019$). The imperfect relationship between mean grain size and specific surface area for river sediments can be explained by the creation of surface

roughness during weathering and erosion (Anbeek 1992). Surface area created during silicate weathering is typically due to the formation of mesopores (Brantley and Mellott, 2000; Mayer, 1994; Titley et al., 1987), which are pore spaces with diameters ranging from 2 – 50 nm (Sing, 1985). The amount of porosity can be considered in terms of surface roughness (λ), which represents the ratio between specific surface areas of sediment measured using gas adsorption (S_{BET}) compared to the geometric surface area of a perfect sphere ($S_{geo} = 4\pi r^2$), given as $\lambda = S_{BET}/S_{geo}$ (Helgeson et al., 1984). The surface roughness of leached sediment from the Gulf catchments ranged from 8 – 92 (Table 3.2); this range is higher than freshly-ground minerals, which equal an average of 7 over a range of particle sizes (Brantley and Mellott, 2000; White and Peterson, 1990). The surface roughness of minerals is supposed to correlate with grain size (Anbeek, 1992; Anbeek et al., 1994; Lee et al., 2010). However, no relationship between mean grain size and surface roughness was found in this study, which may be because this relationship is mineral-dependent. Assuming this relationship for bulk fluvial sediment samples may therefore be invalid. Surface roughness values were reasonably correlated to fractal dimensions ($R^2 = 0.56$, Figure 3.6), suggesting that the fractal dimension is a reasonable proxy for estimating the surface roughness of fluvial sediments.

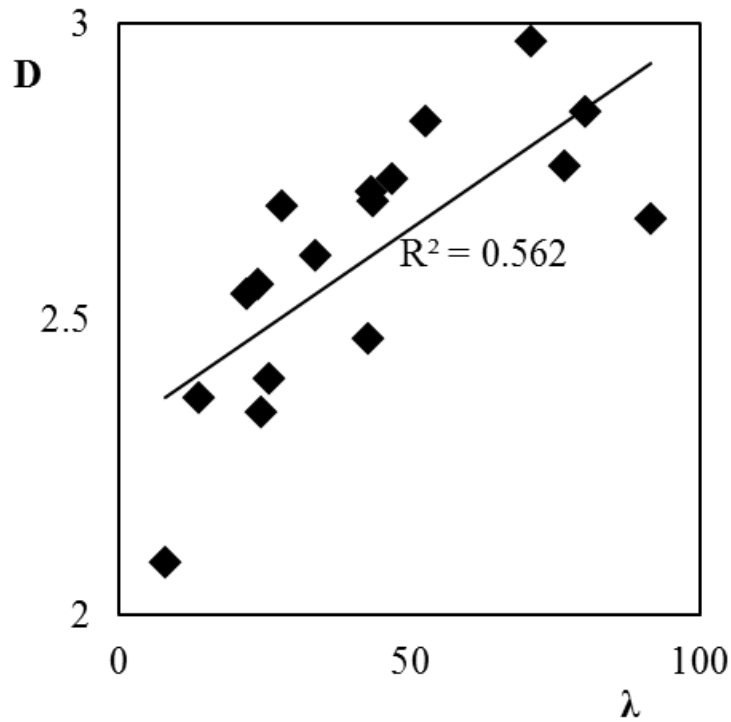


Figure 3.6 Surface roughness (λ) vs fractal dimension (D) for fluvial sediments from the Gulf of Carpentaria drainage basin

3.1.2 Initial ($^{234}\text{U}/^{238}\text{U}$) activity ratio of source rocks

Only two of the eight surface bedrock samples were in secular equilibrium (Table 3.5), with the ($^{234}\text{U}/^{238}\text{U}$) activity ratios ranging from 0.795 to 1.011. Replicate measurements on separate aliquots of B-6 yielded activity ratios of 1.007 ± 0.003 and 1.007 ± 0.002 . This indicates that the results are repeatable and there is insignificant heterogeneity in bedrock samples. Therefore, the assumption that all source rocks are in secular equilibrium at the soil-bedrock interface does not appear valid in our study area. Here we consider if there are any relationship between ($^{234}\text{U}/^{238}\text{U}$) activity ratios and lithology. Volcanic rocks are not considered since they are generally in secular equilibrium. Granitic rocks are discussed separately to sedimentary and metamorphic rocks due to their different formation mechanisms.

3.1.2.1 Influence of lithology

The ($^{234}\text{U}/^{238}\text{U}$) activity ratios of sedimentary and metamorphic rocks from the Gulf catchments were significantly lower ($p = 0.047$) for fine-grained rocks, (B-1 and B-4), compared to coarse-grained rocks (B-5, 6 and 8, Table 3.3). This difference is more significant ($p = 0.028$) when including rocks (shales, siltstone, quartzite) measured in other studies (Ma et al., 2010; Handley et al., 2013b; Menozzi, 2016, Table 3.4). As direct-recoil is dependent on grain size (Kigoshi, 1971), this could suggest that the magnitude of ^{234}U depletion in rocks is related to grain size. This hypothesis requires that fine-grained rocks are sufficiently permeable for the preferential leaching of ^{234}U to occur by water/pore fluid flow. Firstly, more samples are required as this grain size hypothesis is based on a limited sample database, and secondly, it could be biased by the number of quartzite samples ($n = 2$, Table 3.5), which is a coarse-grained metamorphic rock. However, sandstones appear to be generally in secular equilibrium ($n = 2$, Table 3.5), which supports the grain size hypothesis, but more sandstone samples are required. It is also possible to infer the activity ratio of the source rocks in catchments that are dominated by a single lithology. In the predominantly metamorphic Archer River catchment (Table 3.1), two sediments yielded activity ratios close to unity (R-1 and R-2, Table 3.5). This may provide further evidence to support the hypothesis that coarse-grained metamorphic rocks are generally in secular equilibrium.

Granitic rocks appear to be particularly susceptible to preferentially leaching of ^{234}U . This is based on both granitic rocks analysed in this study, and granitic rocks sampled from depths of up to 2800 m (Landström et al., 2001; Rosholt, 1983). This could be because the majority of U in granites is hosted at grain boundaries and in microfractures (Tieh and Ledger, 1981), and in accessory minerals, such as zircon. Zircons have high U concentrations up to 7,000 ppm and can be highly damaged by alpha recoil, i.e. metamictization (Balan et al., 2001). Since ^{234}U is easily leached from damaged recoil sites by water (Fleischer, 1980), fluid flow preferentially leach ^{234}U without significantly altering the host rock undergoing by chemical

weathering. Based on two granite samples from our study area, the weighted average activity ratio of granites in our study area is cautiously estimated to be 0.930 ± 0.003 ($n = 2$, Table 3.5).

3.1.2.2 Tectonic controls

Despite widespread evidence for ^{234}U depletion in rocks, glacial outwash sediments ($<63\ \mu\text{m}$ fraction) draining granitic, metamorphic, and sedimentary rocks were in secular equilibrium (DePaolo et al., 2012). Glacial outwash sediments are assumed to closely represent the source rocks following comminution due to a negligible transport time and minimal chemical alteration since comminution/glacial erosion. Since sediments represent an average composition of the source rocks they drain, rock outcrops could be systematically biased to lower ($^{234}\text{U}/^{238}\text{U}$) than the rock average. This may be because rock outcrops erode at a slower rate than the surrounding landscape (Bierman and Caffee, 2002). This could prolong oxidative weathering reactions and further promote the preferential leaching of ^{234}U (Petit et al., 1985). Bedrock outcrops also tend to be associated with fault lines; for instance, most bedrock outcrops sampled in this study were located near major fault lines (Figure 3.8). Fault movement fractures rocks (Molnar et al., 2007), which increases water fracture flow and could facilitate the preferential leaching of ^{234}U (Fleischer, 1980). These effects could be amplified in our study area by 1) low uplift and low denudation rates in northern Australia throughout the Quaternary (Bierman and Caffee, 2002; Belton et al., 2004), 2) the high proportion of old Proterozoic rocks in the Gulf drainage basin (Raymond et al., 2012), and 3) the complex tectonic history of North Queensland during the past 1,800 Ma, including rifting and volcanism associated with the breakup of Rodinia at $\sim 800\ \text{Ma}$ (Withnall and Cranfield, 2013).

Table 3.5 The ($^{234}\text{U}/^{238}\text{U}$) activity ratios of bedrock samples

Sample ID	Location	($^{234}\text{U}/^{238}\text{U}$) ^b	Lithology ^c	Grain size	Source
GOC-B-1	Mitchell River, N Australia	0.843 ± 0.003	mudstone	fine	this study
GOC-B-2	Mitchell River, N Australia	0.850 ± 0.002	granite	medium	this study
GOC-B-3	Mitchell River, N Australia	0.979 ± 0.004	granite	medium	this study
GOC-B-4	Mitchell River, N Australia	0.795 ± 0.001	rhyolite	fine	this study
GOC-B-5	Gilbert River, N Australia	1.011 ± 0.002	schist	coarse	this study
GOC-B-6^a	Flinders River, N Australia	1.007 ± 0.003	sandstone	coarse	this study
GOC-B-7	Flinders River, N Australia	0.963 ± 0.002	dolerite	coarse	this study
GOC-B-8	Leichhardt River, N Australia	1.004 ± 0.002	amphibolite	coarse	this study
WP-Q1	Flinders Ranges, S Australia	0.971 ± 0.003	quartzite	coarse	Handley et al. (2013b)
HK-Q1	Flinders Ranges, S Australia	0.966 ± 0.002	quartzite	coarse	Handley et al. (2013b)
GS-S1	Flinders Ranges, S Australia	0.940 ± 0.002	shale	fine	Handley et al. (2013b)
BRA-SS1	Flinders Ranges, S Australia	0.912 ± 0.002	siltstone	fine	Handley et al. (2013b)
DC1	Susquehanna Shale Hills, US	0.996 ± 0.002	shale	fine	Ma et al. (2010)
STD	Southern Highlands, SE Australia	1.022 ± 0.002	sandstone	coarse	Menozi (2016)

^aRepeat (separate aliquot) measurement of B-6 (n = 2); ^b2σ internal standard error; and ^cRaymond et al. (2012).

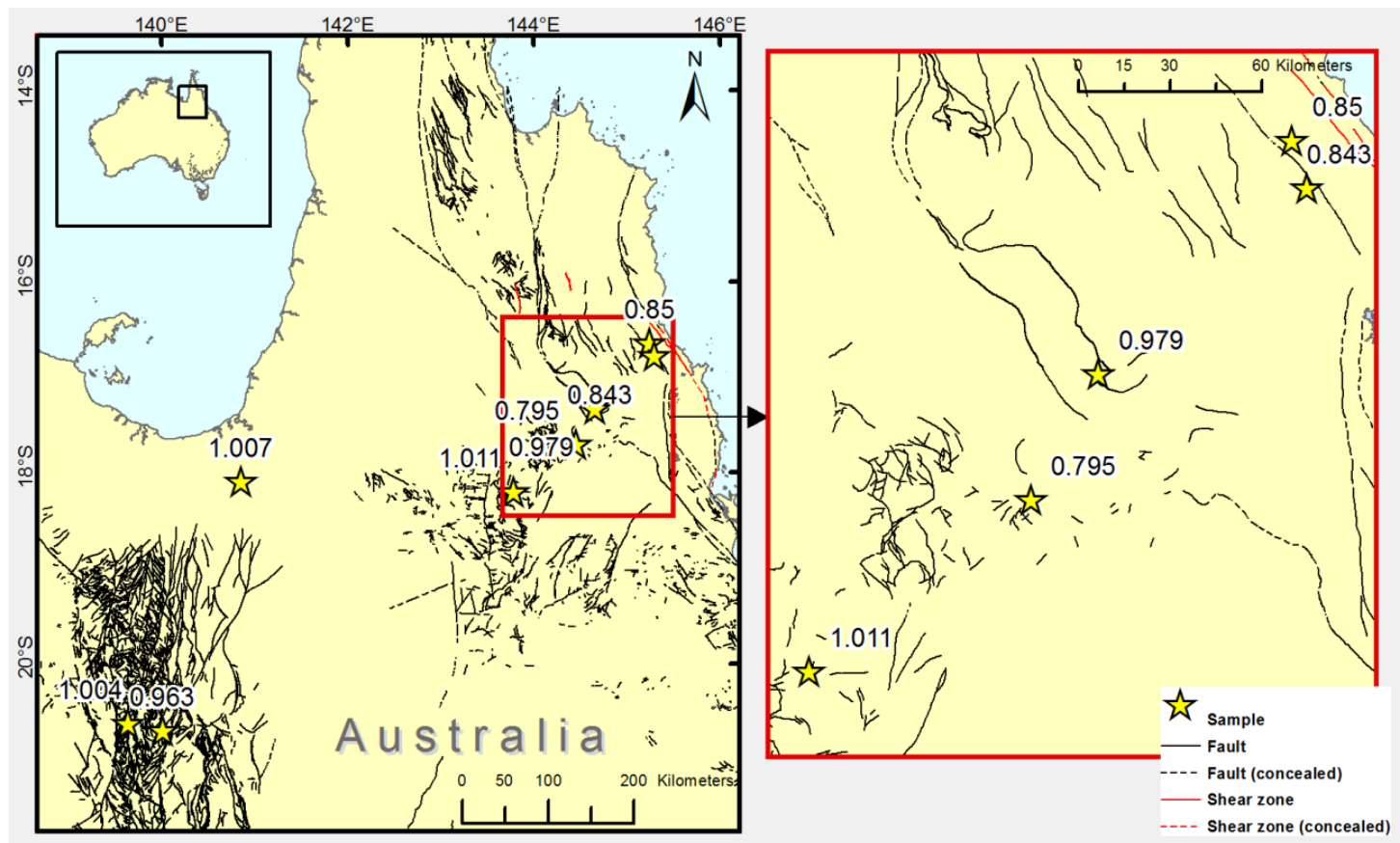


Figure 3.7 Bedrock sampling sites (stars) with the ($^{234}\text{U}/^{238}\text{U}$) activity ratio shown above. Solid black lines represent faults, dashed black lines represent concealed faults, red lines represent shear zones and the dashed red lines represent concealed shear zones. Geological data are derived from Raymond et al. (2012).

3.1.2.3 Initial activity ratio for catchments in the Gulf of Carpentaria drainage basin

Given the range of ($^{234}\text{U}/^{238}\text{U}$) measured in rocks from catchment headwaters ($A_0 = 0.795 - 1.011$, Table 3.5), the assumption that the source rocks are in secular equilibrium is not valid for the Gulf catchments. To estimate the initial activity ratio (A_0), bootstrap resampling was conducted using the measured activity ratios of rocks. The bootstrap mean A_0 for the Gulf catchments is estimated to be 0.944 ± 0.056 ($p = 0.05$, Table 3.6). Seven out of eighteen river sediments had ($^{234}\text{U}/^{238}\text{U}$) activity ratios greater than 0.944 (Table 3.2). Since comminution dating measures the decrease in ($^{234}\text{U}/^{238}\text{U}$) over time, $A_0 = 0.944$ would yield “negative” comminution ages for these samples. Therefore, the bootstrap mean cannot be applied a large and geologically diverse area, such as the Gulf of Carpentaria drainage basin. A better approach may be estimating A_0 using the proportion of each rock type in the catchment (Table 3.1), and the typical ($^{234}\text{U}/^{238}\text{U}$) for different rock types (Table 3.7). Following this approach, the estimated A_0 for catchments ranged from 0.920 to 1.000 (Table 3.2), and were all less the measured activity ratios for river sediments.

Table 3.6 Bootstrap results for measured initial activity ratios of bedrock samples^a

Mean (original)	Mean (bootstrap)	Lower bound (bootstrap)	Upper bound (bootstrap)
0.940 ± 0.086 ^b	0.944 ± 0.056 ^b	0.880	1.000

^aSeed (random numbers) = 1,642,145,353, p = 0.05; and ^b1σ standard deviation.

Table 3.7 Average (²³⁴U/²³⁸U) activity ratios of bedrock samples

Lithology	(²³⁴ U/ ²³⁸ U)
mudstone/siltstone	0.843 ± 0.064 ^a
sandstone	1.000 ± 0.011 ^{a,b}
igneous	0.931 ± 0.004 ^a
volcanic	1.000 ± 0.004 ^c
metamorphic	1.000 ± 0.023 ^a

Data sourced from: ^aTable 3.5, ^bMenozzi (2016); ^cHandley et al. (2011), Chabaux et al. (2013), and Pelt et al. (2013); and ^d1σ standard deviation.

3.1.3 Direct-recoil fraction of ²³⁴U in river sediments

The *direct-recoil fraction* (f_a) represents the number of ²³⁴U (via the short-lived ²³⁴Th) nuclides directly ejected out of the grain during the alpha decay of ²³⁸U. The direct-recoil fraction represents the number of can be estimated using a geometric model (DePaolo et al., 2006; Dosseto et al., 2010; Lee et al., 2010), but there are large uncertainties in inferred ages due to assumptions for particle shape factors and aspect ratios (Handley et al, 2013a). A better approach utilises the Brunauer–Emmett–Teller (BET) specific surface area (Maher et al., 2006), which measures the amount of a gas sorbed onto a surface over a range of pressures (Brunauer et al., 1938). However, gas sorption measurements overestimate the direct-recoil fraction by measuring the surface area on the length-scale of the selected gas molecule, typically nitrogen (d = 0.3 nm), which is two orders of magnitude smaller than the recoil length (typically 27 nm, Table 3.2). The overestimated direct-recoil fraction can be corrected using the fractal dimension (D) (Semkow, 1991; Bourdon et al., 2009), which is a measure of self-similarity that can be used as a proxy for surface roughness (Mandelbrot,

1983). The fractal dimension ranges from 2.0 (unweathered grain with no roughness equivalent to a 2D shape) to 3.0 (maximum roughness equivalent to a 3D shape). The fractal model for estimating the direct-recoil model is given as:

$$f_{\alpha} = \frac{1}{4} S_{BET} \rho R \left[\frac{2^{D-1}}{4-D} \left(\frac{a}{R} \right)^{D-2} \right] \quad (3)$$

where S_{BET} is the specific surface area (in $\text{m}^2 \text{g}^{-1}$), D is the fractal dimension, ρ is the density of the solid phase (in $\text{m}^3 \text{g}^{-1}$), and is R recoil length (in m), a represents diameter of the N_2 molecule (in m). The recoil length is a function of mineral density, ranging from 22 nm for heavy minerals (e.g. zircon), 27 nm for quartz, to 30 nm for feldspars (Hashimoto, 1985; Dosseto and Schaller, 2016). Recoil length and mineral density were estimated for each river sediment based on the sample mineralogy (Table 3.1), and reported values for specific minerals (Table 3.8). Estimated densities and recoil lengths for river sediments ranged from 2.0 to 2.7 $\text{cm}^3 \text{g}^{-1}$, and 27 to 29 nm. Finally, the estimated direct-recoil fractions ranged from 0.03 to 0.10 (Table 3.2). These are higher than glacial outwash sediments from the King River Fan, US (Lee et al., 2010), but lower than dust grains in the Dome C ice core, Antarctica (Aciego et al., 2011), and sediments from Site 984, North Atlantic (DePaolo et al., 2006) (Figure 3.8). The direct-recoil fraction range for the Gulf river sediments is very similar to river sediments from the Murrumbidgee River in temperate Australia (Dosseto et al., 2010), despite the latter having slightly large mean diameters (Figure 3.8).

Table 3.8 Recoil lengths for typical minerals/mineral groups

Mineral	Density (cm ³ /g)	Recoil length (nm)
Quartz ^a	2.65	27.2
Feldspars ^b	2.70	30.0
Micas ^c	2.95	24.7
Clays ^d	2.60	30.0
Heavy minerals ^e	4.50	22.7
Non-silicates/carbonates ^f	2.70	30.0

Density and recoil lengths from ^aHashimoto, 1985; ^balbite (Maher et al. 2006); ^caverage of biotite and muscovite (Hashimoto, 1985); ^dkaolinite (Maher et al. 2006); ^eaverage of monazite and zircon; and ^fcalcite (Maher et al. 2006).

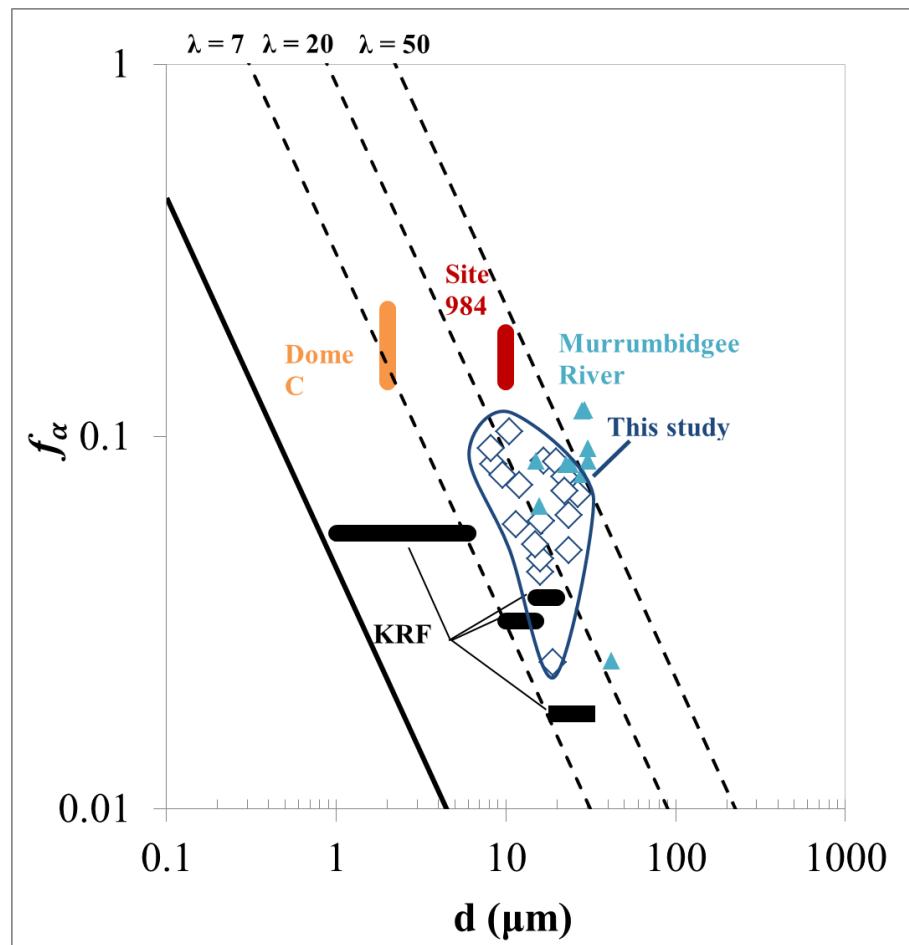


Figure 3.8 Direct-recoil fraction (f_α) as a function of mean grain diameter (d) for $<63 \mu\text{m}$ sediments measured in this study, Site 984 (DePaolo et al., 2006), KRF: King River Fan (Lee et al., 2010), Dome C ice core in Antarctica (Aciego et al., 2011), and the Murrumbidgee River (Dosseto et al., 2010).

3.1.4 Preferential leaching effects

Comminution ages could not be calculated for some samples using Equation 1 despite adjusting the initial activity ratio (samples R-3, -4, -5 and -6 from the Mitchell River, R-10 and R-11 from the Gilbert River, and R-18 from the Leichhardt River, Table 3.2). This is because the measured activity ratio A could not be accounted for by the direct-recoil fraction f_a in Equation 1, which must satisfy $A > (1 - f_a)$. For these sediments, the difference between the activity ratios that would be expected if direct-recoil fraction was the only process removing ^{234}U ($1 - A$) and the direct-recoil fraction ranged from 0.011 to 0.118 (Table 3.9). This suggests that 1) the direct-recoil fraction is underestimated, and/or 2) another process must account for the loss ^{234}U , e.g. preferential leaching. Scenario 1 seems unlikely given that the estimated direct-recoil fractions for river sediments lie within the range of previously reported values (Figure 3.9). In addition, low activity ratios were measured for rocks from catchments headwaters, suggesting that preferential leaching of ^{234}U is occurring (Table 3.5).

Table 3.9 The <63 μm river sediments from the Gulf of Carpentaria drainage basin for which the ($^{234}\text{U}/^{238}\text{U}$) activity ratios (A) could not be accounted for by the direct-recoil fraction (f_a)

Sample ID	Catchment	f_a	$1 - A$	$1 - A - f_a$
R-3	Mitchell River	0.063	0.092	0.029
R-4	Mitchell River	0.048	0.085	0.037
R-5	Mitchell River	0.054	0.097	0.043
R-6	Mitchell River	0.034	0.139	0.105
R-10	Gilbert River	0.065	0.183	0.118
R-11	Gilbert River	0.093	0.144	0.051
R-18	Leichhardt River	0.058	0.069	0.011

Preferential leaching can be accounted for by considering that the leaching rates of ^{234}U and ^{238}U are not equal and modifying Equation 1, given as (Dosseto and Schaller, 2016):

$$t_{comm} = -\frac{1}{\lambda_4 + \left(\frac{w_4}{w_8} - 1\right) w_8} \ln \left[\frac{\left(\frac{^{234}\text{U}}{^{238}\text{U}}\right) - \frac{(1-f_4)\lambda_4}{\lambda_4 + \left(\frac{w_4}{w_8} - 1\right) w_8}}{\left(\frac{^{234}\text{U}}{^{238}\text{U}}\right)_0 - \frac{(1-f_4)\lambda_4}{\lambda_4 + \left(\frac{w_4}{w_8} - 1\right) w_8}} \right] \quad (4)$$

where A is the measured ($^{234}\text{U}/^{238}\text{U}$) activity ratio, A_0 is the initial ($^{234}\text{U}/^{238}\text{U}$) activity ratio of the parent material (e.g. bedrock or grains $>63 \mu\text{m}$ in size), λ_{234} is the decay constant of ^{234}U (in a^{-1}), f_α is the direct-recoil fraction, and w_4 and w_8 are the leaching coefficients for ^{234}U and ^{238}U (in a^{-1}), respectively. Reported ^{238}U leaching coefficients for fine-grained sediments in tropical watersheds range from 4.4×10^{-6} to $9.9 \times 10^{-6} \text{ a}^{-1}$ (Table 3.9). The average of these leaching coefficients ($4.4 \times 10^{-6} \text{ a}^{-1}$) was adopted in this study. The ratio of the leaching coefficients, w_{234}/w_{238} , was assumed to be 1.1 ± 0.1 , similar to values measured in laboratory and field-based studies (Dequincey et al., 2002; Vigier et al., 2005; Dosseto et al., 2006a; Andersen et al., 2009; Dosseto et al., 2014). Thus, the preferential leaching of ^{234}U is accounted for by adopting a value greater than one for w_{234}/w_{238} .

Table 3.10 Reported leaching coefficients (w_{238}) for ^{238}U in tropical watersheds

Location	$w_8 \text{ (a}^{-1}\text{)}$	Reference
Amazon lowland rivers	4.4×10^{-6}	Dosseto et al. (2006a)
Deccan Traps, India	$6.9 - 9.9 \times 10^{-6}$	Vigier et al. (2005)
Puerto Rico	4.7×10^{-6}	Dosseto et al. (2014)
<i>Average</i>	5.7×10^{-6}	

3.1.5 Aeolian input

Australia is an ancient, low-relief and arid continent subject to active dust entrainment and dust deposition (Hesse and McTainsh, 2003; Hesse, 2010). Thus, a high proportion of the $<63 \mu\text{m}$ river sediments from the Gulf catchments may comprise deposited dust. The Gulf of Carpentaria drainage basin does not lie on active dust transport paths in Australia (Hesse and McTainsh, 2003), but is an active dust entrainment area with peak activity in the SW Gulf

catchments (McTainsh et al., 2011). The prevalent south-easterly trade winds during the dry season prevent dust from the arid Australian interior reaching the Gulf of Carpentaria drainage basin and the northerly monsoonal winds blow from tropical Papua New Guinea, which is not a major dust source (Hesse and McTainsh, 2003). The deposition of long-range fine dust ($d < 2 \mu\text{m}$) is not considered as this mainly comprises weathering products (Biscaye et al., 1997). These are typically enriched in ^{234}U with $(^{234}\text{U}/^{238}\text{U}) < 1$ (Aciego et al., 2015), and should be removed during the removal of non-detrital matter during sample pre-treatment. Therefore, the majority of dust in the Gulf catchments is expected to be locally derived from expansive floodplains that are sparsely vegetated during the dry season.

Dust contribution to river sediments in Gulf catchments was considered using dust deposition rates at Longreach during the dust storm season (August to November), which was $0.14 \text{ t km}^{-2} \text{ day}^{-1}$ (Hesse and McTainsh, 2003). This site is located $\sim 200 \text{ km}$ south of the Gulf of Carpentaria drainage basin and thus, represents a maximum dust deposition rate due to the closer proximity of this site to the arid Australian interior. An annual dust deposition rate of $12.8 \text{ t km}^{-2} \text{ a}^{-1}$ was estimated by considering that no dust is deposited outside of the dust storm season (Table 3.11). The mass fluxes derived from fluvial erosion was estimated by assuming a catchment-wide erosion rate of 20 mm ka^{-1} (Nichols et al., 2014), and an average mineral density of 2.7 kg m^{-3} (Table 3.11). By comparing the mass fluxes from fluvial erosion vs dust deposition, river sediments may comprise up to 24% deposited dust (Table 3.13). This value does not consider the temporal and spatial variability of dust deposition rates, but lies within the measured aeolian fraction of hillslopes in the Mojave Desert, southwestern U.S. (10 – 30 %, Crouvi et al., 2013).

A high proportions of $< 63 \mu\text{m}$ river sediments may comprise deposited dust. Thus, the U isotope composition and surface area properties of river sediments may represent fluvial-aeolian erosion processes. Higher dust deposition rates in the S vs N catchments (McTainsh et al., 2011) may explain the higher specific surface areas (Figure 3.7), and lower average

($^{234}\text{U}/^{238}\text{U}$) for the S vs N catchments (Table 3.4). Higher specific surface areas may be explained by the preferential erosion of fine-grained material. Similarly high specific surface areas ($\sim 70 \text{ m}^2 \text{ g}^{-1}$) were measured for cold-arid sediments from the Dry Valleys in Antarctica, which accumulate fine-grained dust sourced from glacial drift deposits (Marra et al., 2014). Lower average ($^{234}\text{U}/^{238}\text{U}$) may result from the aeolian reworking of older alluvial deposits. If sediments have undergone extended floodplain storage before wind-blown erosion, dust may exhibit lower ($^{234}\text{U}/^{238}\text{U}$) compared to river sediments in the active channel due to the loss of ^{234}U by direct-recoil and/or preferential leaching during alluvial storage (DePaolo et al., 2006; Dosseto et al., 2010).

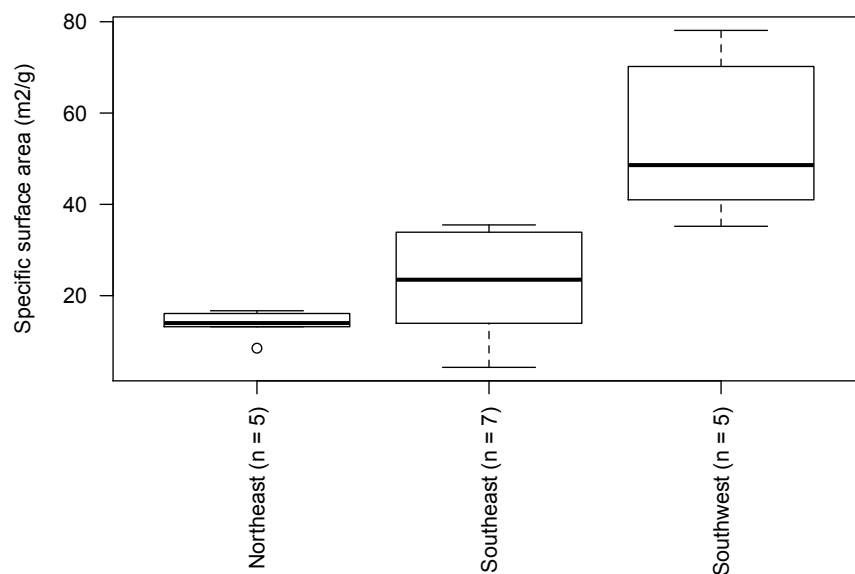


Figure 3.9 Box plot of specific surface area of sediments from the Gulf catchments where (in order from northeast to southwest) northeast: Archer River and Mitchell River, southeast: Staaten River and Gilbert River, and southwest: Norman River, Flinders River, and Leichhardt River.

Table 3.11 Relative contribution of denudation vs aeolian deposition to sediments in the Gulf of Carpentaria drainage basin

Source	Time period	Mass flux (kg km ² a ⁻¹)	Relative contribution (%)
Denudation ^a	present	54,000	76
Dust ^b	present	16,800	24
Denudation ^c	Last Glacial Maximum	54,000	24
Dust ^c	Last Glacial Maximum	168,000	76

^aA catchment-wide erosion rate of 20 mm ka⁻¹ and average mineral density of 2.7 kg m⁻³ was used to estimate the mass flux derived from denudation. ^bThe mass flux of dust was estimated using daily average dust deposition rate (0.14 t km⁻² day⁻¹) measured during the dust storm season (August – November) at Longreach, located in the southwest of our study area (Hesse and McTainsh, 2003). By considering that no dust is deposited outside of the dust storm season, the annual average dust deposition was estimated to be 12.8 t km⁻² a⁻¹. ^cEstimated by assuming that the dust flux was an order of magnitude greater during the LGM (Harrison et al., 2001), and the denudation flux was identical to the present flux.

3.1.6 Sediment residence times in the Gulf of Carpentaria drainage basin

Comminution ages were inferred using Equations 3 and 4 and ranged from <1 to 584 ka. Uncertainties in input parameters were accounted for by 1) adjusting the initial activity ratios for each sub-catchment based on measurements of rocks from the catchment headwaters (Table 3.5), 2) calculating the density and recoil length for each river sediment based on sample mineralogy (Table 3.2), and 3) accounting for preferential leaching effects by using a modified comminution age equation that considers leaching of ^{234}U and ^{238}U (Table 3.2). Uncertainties for each comminution age parameter for a river sediment (GOC-R-7) are given in Table 3.10. External uncertainties were calculated for all measured parameters from repeat measurements and uncertainty is expressed as 1σ relative standard deviation, RSD. The main source of uncertainty in comminution ages is associated with the estimation of the direct-recoil fraction (RSD: 27%), and the overall uncertainty is 39% RSD (Table 3.2).

The average sediment residence time in each catchment ranged from <1 to 190 ± 80 ka (Table 3.11). The shortest residence times were inferred for sediments from the Archer River, which had ($^{234}\text{U}/^{238}\text{U}$) close to secular equilibrium (Table 3.2). This suggests that an insufficient amount of time had elapsed since $<63 \mu\text{m}$ grains were formed for the loss of ^{234}U by direct recoil/preferential leaching to be significant. Faster sediment transport rates may be attributed to higher rainfall in the Archer River catchment (Figure 3.2). The longest residence times were inferred for sediments from the Mitchell River, which had a mean of 190 ± 80 ka (Table 3.11). In this catchment, long residence times were inferred both downstream and in smaller ($<600 \text{ km}^2$), upper catchments (Figure 3.10). Long sediment residence times in smaller catchments may indicate longer regolith storage times (T_1 and T_2 ,

Figure 3.1). This is consistent with long hillslope residence times (>200 ka) inferred in southeastern Australia (Dosseto et al., 2014; Suresh et al., 2014). However, sediment residence times were shorter for small catchments in landslide-prone areas of Puerto Rico (Dosseto et al., 2014). This is attributed to landslides sourcing younger sediment from deeper in the weathering profile; whereas near-surface soil erosion occurring in southeastern Australia mobilises older sediment that has spent longer in the weathering profile/hillslope. Understanding sediment-routing processes in hillslope-fluvial systems using comminution dating requires that sediment residence times in the weathering profile/hillslope must first be constrained.

The average sediment residence time for all study catchments weighted by catchment area was 88 ± 35 ka (Table 3.11). This approximately corresponds to the duration of the last glacial-interglacial cycle, and suggests that catchments are currently eroding material that was accumulated during the last glacial cycle. The northwards migration of the inter-tropical convergence zone (ITCZ) during the last glacial cycle resulted in reduced monsoonal rainfall in N Australia (De Deckker et al., 2002). Hence discharge and fluvial activity was reduced from Marine Isotope Stage (MIS) 5 to MIS 2 as shown by distinctive floodplain units in the Gilbert River (Nanson et al., 2005). Similarly long residence times (>100 ka) were inferred for $<63\mu\text{m}$ river sediments from both the tropical plains of the Amazon River (Dosseto et al., 2006a), and the Murrumbidgee River in temperate Australia (Dosseto et al., 2010). In contrast, regions that were glaciated during the LGM, such as Northern Canada, have sediment residence times that reflect the time elapsed since glaciation: 10–30 ka (Vigier et al., 2001). The long sediment residence times in low-relief, unglaciated, tectonically stable catchments may therefore reflect the accumulation of sediments during glacial periods.

Table 3.12 Comminution age parameters and associated uncertainties for river sediment GOC-R-7

Parameter	Units	Value	1 σ relative standard deviation (%)
Decay rate of ^{234}U , λ_{234}	a^{-1}	$2.829 \times 10^{-6} \pm 0.003 \times 10^{-6}$	0.10 ^a
Initial ($^{234}\text{U}/^{238}\text{U}$) activity ratio, A_0	dimensionless	0.980 ± 0.02	2.0 ^b
Measured ($^{234}\text{U}/^{238}\text{U}$) activity ratio, A	dimensionless	0.961 ± 0.014	1.5 ^c
Specific surface area of solid phase, S_{BET}	$\text{m}^2 \text{g}^{-1}$	16.5 ± 2.8	17 ^c
Fractal dimension of solid phase, D	dimensionless	2.4 ± 0.2	12 ^c
Diameter of a nitrogen molecule, a	nm	0.37 ± 0.01	1.4 ^d
Recoil length in solid phase, R	nm	27 ± 1	2.5 ^e
Density of solid phase, ρ	$\text{m}^3 \text{g}^{-1}$	2.6 ± 0.1	2.5 ^e
Leaching coefficient for ^{238}U , w_8	in a^{-1}	$5.7 \pm 1 \times 10^{-6}$	18
Ratio of leaching coefficients for ^{234}U and ^{238}U , w_4/w_8	dimensionless	1.1 ± 0.05	4.5
Direct-recoil fraction, f_a	dimensionless	0.08 ± 0.02	27 ^f
Comminution age, t_{comm}	ka	180 ± 70	43 ^f

^aCheng et al. (2000); ^bHandley et al. (2013a); ^cexternal error calculated from the standard deviation of repeat measurements;

^ecalculated from the square root of the sum of individual relative 1 σ standard deviations, ^dHirschfelder et al. (1964); estimated uncertainty associated with $\chi^2 = 5$ and $n = 1$ degrees of freedom for XRD experiments, and ^fcalculated from the square root of the sum of individual errors.

Table 3.13 The average residence time of <63 μm sediment in catchments draining to the Gulf of Carpentaria

Catchment	Average sediment residence time (ka)
Archer River	<1
Mitchell River	190 ± 80
Staaten River	18 ± 8
Gilbert River	160 ± 70
Flinders River	45 ± 20
Norman River	17 ± 7
Leichhardt River	95 ± 40
Weighted average ^a	88 ± 35

^aAverage weighted by catchment area for Archer River: 12,600 km^2 , Mitchell River 74,000 km^2 , Staaten River: 25,300 km^2 , Gilbert River: 26,600 km^2 , Flinders River: 110,000 km^2 , Leichhardt River: 33,000 km^2 , Norman River: 67,500 km^2 (Table 3.1).

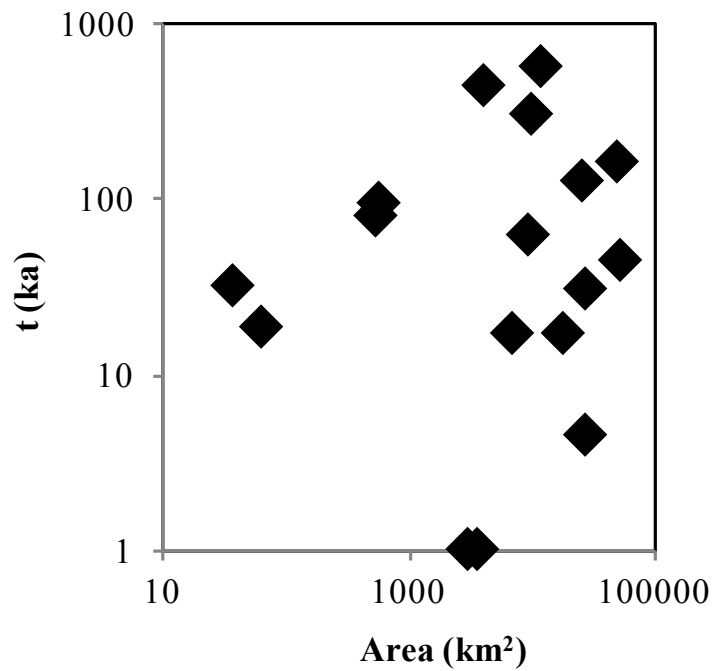


Figure 3.10 Sediment residence times as a function of catchment area in the Gulf of Carpentaria drainage basin

3.2 Conclusions

Comminution ages were inferred for seven catchments in the Gulf of Carpentaria drainage basin, northern Australia and ranged from <1 to 190 ± 80 ka. These comminution ages were inferred considering the various uncertainties regarding input parameters. Firstly, visibly unweathered rocks sampled from catchment headwaters were generally not in secular equilibrium. Thus, the assumption that the parent material is in secular equilibrium does not appear to be valid for catchments draining to the Gulf of Carpentaria. This was accounted for by calculating initial activity ratios for each sub-catchment considering the average ($^{234}\text{U}/^{238}\text{U}$) activity ratios of different rock types, and the proportion of each rock type in a given catchment. In addition, the density and recoil length were calculated for all river sediments based on sample mineralogy. Preferential leaching effects were accounted for by using a modified comminution age model that considers leaching of ^{234}U and ^{238}U . The effect of aeolian deposition on comminution ages in dust-prone Australia was considered using mass fluxes of dust deposition vs fluvial erosion. This approach predicts that

sediments may comprise up to 24% deposited dust. This is reflected by higher specific surface areas and lower mean grain sizes measured for sediments from more arid catchments, which is attributed to the deposition of fine-grained dust. Therefore, comminution ages of river sediments in northern Australia likely reflect fluvial-aeolian sediment transport processes.

The average sediment residence time (weighted by catchment area) for catchments in the Gulf of Carpentaria drainage basin was 88 ± 35 ka. This approximately corresponds to the duration of the last glacial-interglacial cycle, suggesting that catchments are currently eroding material that was accumulated during the last glacial cycle when rainfall and fluvial activity were generally reduced, and aeolian activity was enhanced. Similarly long sediment residence times have been reported in other low-relief, unglaciated, tectonically stable catchments. In such landscapes, the long sediment residence times may buffer the erosional response to short-term Quaternary climate fluctuations.

3.3 Acknowledgements

This study was supported by an Australian Research Council (ARC) Discovery grant (DP0990447) to AD and AC, Future Fellowship (FT0990447) to AD and a University of Wollongong postgraduate scholarship award to ANM. Tim Cohen and Alexandru Codilean, are thanked for helpful discussions of the manuscript. We thank NASA for providing DEM data from the CGIAR-CSI SRTM 90m Database (<http://srtm.csi.cgiar.org>), the Australian Bureau of Meteorology (www.bom.gov.au) for climate data, Geoscience Australia (www.ga.gov.au) for surface geology data, and the State of Queensland, Department of Natural Resources and Mines (<https://www.dnrm.qld.gov.au>) for streamflow data.

3.4 References

- Aciego, S., Bourdon, B., Schwander, J., Baur, H. and Forieri, A. (2011) Toward a radiometric ice clock: Uranium ages of the Dome C ice core. *Quaternary Science Reviews* 30, 2389-2397.
- Aciego, S.M., Aarons, S.M. and Sims, K.W.W. (2015) The uranium-isotopic composition of Saharan dust collected over the central Atlantic Ocean. *Aeolian Research* 17, 61-66.
- Allen, P.A. (2008) From landscapes into geological history. *Nature* 451, 274-276.
- Anbeek, C. (1992) The dependence of dissolution rates on grain size for some fresh and weathered feldspars. *Geochimica et Cosmochimica Acta* 56, 3957-3970.
- Anbeek, C., Van Breemen, N., Meijer, E.L. and Van Der Plas, L. (1994) The dissolution of naturally weathered feldspar and quartz. *Geochimica et Cosmochimica Acta* 58, 4601-4613.
- Australia, G. (2003) *Vegetation - Post-European Settlement (1988)*. National Mapping Division, Geoscience Australia.
- Balan, E., Neuville, D.R., Trocellier, P., Fritsch, E., Muller, J.-P. and Calas, G. (2001) Metamictization and chemical durability of detrital zircon. *American Mineralogist* 86, 1025-1033.
- Belton, D.X., Brown, R.W., Kohn, B.P., Fink, D. and Farley, K.A. (2004) Quantitative resolution of the debate over antiquity of the central Australian landscape: implications for the tectonic and geomorphic stability of cratonic interiors. *Earth and Planetary Science Letters* 219, 21-34.
- Bern, C.R. (2009) Soil chemistry in lithologically diverse datasets: the quartz dilution effect. *Applied Geochemistry* 24, 1429-1437.

Berner, R.A., Lasaga, A.C. and Garrels, R.M. (1983) The carbonate-silicate geochemical cycle and its effect on atmospheric carbon dioxide over the past 100 million years. *American Journal of Science* 283, 641-683.

Bierman, P.R. and Caffee, M. (2002) Cosmogenic exposure and erosion history of Australian bedrock landforms. *Geological Society of America Bulletin* 114, 787-803.

Biscaye, P.E., Grousset, F.E., Revel, M., Van der Gaast, S., Zielinski, G.A., Vaars, A. and Kukla, G. (1997) Asian provenance of glacial dust (stage 2) in the Greenland Ice Sheet Project 2 Ice Core, Summit, Greenland. *Journal of Geophysical Research: Oceans* 102, 26765-26781.

Blake, D.H. (1987) *Geology of the Mount Isa Inlier and environments*, Queensland and Northern Territory. Bureau of Mineral Resources, Geology and Geophysics, Australia, Bulletin 225.

BOM (2009) Mean monthly and mean annual rainfall data (base climatological datasets) Bureau of Meteorology.

Bouchez, J., Gaillardet, J., Lupker, M., Louvat, P., France-Lanord, C., Maurice, L., Armijos, E. and Moquet, J.-S. (2012) Floodplains of large rivers: Weathering reactors or simple silos? *Chemical Geology* 332–333, 166-184.

Bourdon, B., Bureau, S., Andersen, M.B., Pili, E. and Hubert, A. (2009) Weathering rates from top to bottom in a carbonate environment. *Chemical Geology* 258, 275-287.

Brantley, S.L. and Mellott, N.P. (2000) Surface area and porosity of primary silicate minerals. *American Mineralogist* 85, 1767-1783.

Brooks, A.P., Shellberg, J.G., Knight, J. and Spencer, J. (2009) Alluvial gully erosion: an example from the Mitchell fluvial megafan, Queensland, Australia. *Earth Surface Processes and Landforms* 34, 1951-1969.

Brunauer, S., Emmett, P.H. and Teller, E. (1938) Adsorption of gases in multimolecular layers. *Journal of the American Chemical Society* 60, 309-319.

Bultitude, R.J., Rees, I.D., Garrad, P.D., Champion, D.C., and Fanning, C.M. (1996). Mossman second edition. Queensland 1:250 000 Geological Series—Explanatory Notes. Geological Survey of Queensland, Department of Minerals and Energy, Brisbane.

Castelltort, S. and Van Den Driessche, J. (2003) How plausible are high-frequency sediment supply-driven cycles in the stratigraphic record? *Sedimentary Geology* 157, 3-13.

Chabaux, F., Blaes, E., Stille, P., di Chiara Roupert, R., Pelt, E., Dosseto, A., Ma, L., Buss, H.L. and Brantley, S.L. (2013) Regolith formation rate from U-series nuclides: Implications from the study of a spheroidal weathering profile in the Rio Icacos watershed (Puerto Rico). *Geochimica et Cosmochimica Acta* 100, 73-95.

Chabaux, F., Riotte, J. and Dequincey, O. (2003) U-Th-Ra fractionation during weathering and river transport. *Reviews in Mineralogy and Geochemistry* 52, 533-576.

Champion, D.C. and Bultitude, R.J. (2013). The geochemical and Sr Nd isotopic characteristics of Paleozoic fractionated S-types granites of north Queensland: Implications for S-type granite petrogenesis. *Lithos*, 162, 37-56.

Cheng, H., Edwards, R.L., Hoff, J., Gallup, C.D., Richards, D.A. and Asmerom, Y. (2000) The half-lives of uranium-234 and thorium-230. *Chemical Geology* 169, 17-33.

Cohen, T.J., Jansen, J.D., Gliganic, L.A., Larsen, J.R., Nanson, G.C., May, J.-H., Jones, B.G. and Price, D.M. (2015) Hydrological transformation coincided with megafaunal extinction in central Australia. *Geology* 43, 195-198.

Coventry, R., Stephenson, P. and Webb, A. (1985) Chronology of landscape evolution and soil development in the upper Flinders River area, Queensland, based on isotopic dating of Cainozoic basalts. *Australian Journal of Earth Sciences* 32, 433-447.

De Deckker, P., Tapper, N. and van Der Kaars, S. (2002) The status of the Indo-Pacific Warm Pool and adjacent land at the Last Glacial Maximum. *Global and Planetary Change* 35, 25-35.

DePaolo, D.J., Lee, V.E., Christensen, J.N. and Maher, K. (2012) Uranium comminution ages: Sediment transport and deposition time scales. *Comptes Rendus - Geoscience* 344, 678-687.

DePaolo, D.J., Maher, K., Christensen, J.N. and McManus, J. (2006) Sediment transport time measured with U-series isotopes: Results from ODP North Atlantic drift site 984. *Earth and Planetary Science Letters* 248, 394-410.

DNRM (2014) Water monitoring portal State of Queensland (Department of Natural Resources and Mines).

Dosseto, A., Bourdon, B. and Turner, S.P. (2008) Uranium-series isotopes in river materials: Insights into the timescales of erosion and sediment transport. *Earth and Planetary Science Letters* 265, 1-17.

Dosseto, A., Buss, H.L. and Chabaux, F. (2014) Age and weathering rate of sediments in small catchments: The role of hillslope erosion. *Geochimica et Cosmochimica Acta* 132, 238-258.

Dosseto, A., Buss, H.L. and Suresh, P.O. (2012) Rapid regolith formation over volcanic bedrock and implications for landscape evolution. *Earth and Planetary Science Letters* 337-338, 47-55.

Dosseto, A., Hesse, P.P., Maher, K., Fryirs, K. and Turner, S. (2010) Climatic and vegetation control on sediment dynamics during the last glacial cycle. *Geology* 38, 395-398.

Dosseto, A. and Riebe, C.S. (2011) Inception! timescale of chemical weathering during the early stages of water–rock interaction. *Mineral. Mag.* 3, 776.

Dosseto, A. and Turner, S. (2014) Reappraisal of uranium-series isotope data in Kamchatka lavas: implications for continental arc magma genesis. *Geological Society, London, Special Publications* 385, 103-116.

Duce, R. (1995) Sources, distributions, and fluxes of mineral aerosols and their relationship to climate. *Aerosol forcing of climate* 6, 43-72.

Dunne, T., Mertes, L.A.K., Meade, R.H., Richey, J.E. and Forsberg, B.R. (1998) Exchanges of sediment between the flood plain and channel of the Amazon River in Brazil. *Bulletin of the Geological Society of America* 110, 450-467.

Efron, B.T. (1993) An introduction to the bootstrap. *Monographs on Statistics and Applied Probability* 57.

Ewing, S.A., Paces, J.B., O'Donnell, J.A., Jorgenson, M.T., Kanevskiy, M.Z., Aiken, G.R., Shur, Y., Harden, J.W. and Striegl, R. (2015) Uranium isotopes and dissolved organic carbon in loess permafrost: Modeling the age of ancient ice. *Geochimica et Cosmochimica Acta* 152, 143-165.

Farley, K.A., Wolf, R.A. and Silver, L.T. (1996) The effects of long alpha-stopping distances on (U-Th)/He ages. *Geochimica et Cosmochimica Acta* 60, 4223-4229.

Fleischer, R.L. (1980) Isotopic disequilibrium of uranium: Alpha-recoil damage and preferential solution effects. *Science* 207, 979-981.

Frings, P.J., Clymans, W., Fontorbe, G., Gray, W., Chakrapani, G., Conley, D.J. and De La Rocha, C. (2015) Silicate weathering in the Ganges alluvial plain. *Earth and Planetary Science Letters* 427, 136-148.

Gaillardet, J., Dupré, B., Louvat, P. and Allégre, C. (1999) Global silicate weathering and CO₂ consumption rates deduced from the chemistry of large rivers. *Chemical Geology* 159, 3-30.

Gallant, J., Wilson, N., Dowling, T., Read, A. and Inskip, C. (2014) SRTM-derived 1 Second Digital Elevation Models Version 1.0. Commonwealth of Australia (Geoscience Australia)

Gallant, J.C. and Dowling, T.I. (2003) A multiresolution index of valley bottom flatness for mapping depositional areas. *Water Resources Research* 39, ESG41-ESG413.

Haig, J., Nott, J. and Reichert, G.-J. (2014) Australian tropical cyclone activity lower than at any time over the past 550-1,500 years. *Nature* 505, 667-671.

Handley, H.K., Turner, S., Afonso, J.C., Dosseto, A. and Cohen, T. (2013a) Sediment residence times constrained by uranium-series isotopes: A critical appraisal of the comminution approach. *Geochimica et Cosmochimica Acta* 103, 245-262.

Handley, H.K., Turner, S., Berlo, K., Beier, C. and Saal, A.E. (2011) Insights into the Galápagos plume from uranium-series isotopes of recently erupted basalts. *Geochemistry, Geophysics, Geosystems* 12, Q0AC14.

Handley, H.K., Turner, S.P., Dosseto, A., Haberlah, D. and Afonso, J.C. (2013b) Considerations for U-series dating of sediments: Insights from the Flinders Ranges, South Australia. *Chemical Geology* 340, 40-48.

Hashimoto, T., Aoyagi, Y., Kudo, H. and Sotobayashi, T. (1985) Range calculation of alpha-recoil atoms in some minerals using LSS-theory. *Journal of Radioanalytical and Nuclear Chemistry Articles* 90, 415-438.

Helgeson, H.C., Murphy, W.M. and Aagaard, P. (1984) Thermodynamic and kinetic constraints on reaction rates among minerals and aqueous solutions. II. Rate constants, effective surface area, and the hydrolysis of feldspar. *Geochimica et Cosmochimica Acta* 48, 2405-2432.

Hesse, P.P. and McTainsh, G.H., 2003. Australian dust deposits: modern processes and the Quaternary record. *Quaternary Science Reviews*, 22, 2007-2035.

Hesse, P.P. (2010) The Australian desert dunefields: formation and evolution in an old, flat, dry continent. *Geological Society, London, Special Publications* 346, 141-164.

Hesse, P.P. and McTainsh, G.H. (2003) Australian dust deposits: modern processes and the Quaternary record. *Quaternary Science Reviews* 22, 2007-2035.

Hirschfelder, J., Bird, R.B. and Curtiss, C.F., 1964. *Molecular theory of gases and liquids*.

Jarvis, A., Reuter, H.I., Nelson, A. and Guevara, E. (2008) Hole-filled SRTM for the globe Version 4. available from the CGIAR-CSI SRTM 90m Database (<http://srtm.csi.cgiar.org/>).

Kigoshi, K. (1971) Alpha-recoil thorium-234: Dissolution into water and the uranium-234/uranium-238 disequilibrium in nature. *Science* 173, 47-48.

Kump, L.R., Brantley, S.L. and Arthur, M.A. (2000) Chemical weathering, atmospheric CO₂, and climate, pp. 611-667.

Landström, O., Tullborg, E.-L. and Eriksson, G. (2001) Effect of glacial/post-glacial weathering compared with hydrothermal alteration - implications for matrix diffusion. . Swedish Nuclear Fuel and Waste Management Co.

Lee, V.E. (2009) Radiogenic Isotope Geochemistry and the Evolution of the Earth's Surface and Interior. PhD thesis, University of California, Berkeley, USA.

Lee, V.E., DePaolo, D.J. and Christensen, J.N. (2010) Uranium-series comminution ages of continental sediments: Case study of a Pleistocene alluvial fan. *Earth and Planetary Science Letters* 296, 244-254.

Luo, X., Rehkämper, M., Lee, D.-C. and Halliday, A.N. (1997) High precision ²³⁰Th/²³²Th and ²³⁴U/²³⁸U measurements using energy filtered ICP magnetic sector multiple collector mass spectrometry. *International Journal of Mass Spectrometry and Ion Processes* 171, 105-117.

Lupker, M., France-Lanord, C., Galy, V., Lavé, J., Gaillardet, J., Gajurel, A.P., Guilmette, C., Rahman, M., Singh, S.K. and Sinha, R. (2012) Predominant floodplain over mountain weathering of Himalayan sediments (Ganga basin). *Geochimica et Cosmochimica Acta* 84, 410-432.

Ma, L., Chabaux, F., Pelt, E., Blaes, E., Jin, L. and Brantley, S. (2010) Regolith production rates calculated with uranium-series isotopes at Susquehanna/Shale Hills Critical Zone Observatory. *Earth and Planetary Science Letters* 297, 211-225.

- Magee, J.W., Miller, G.H., Spooner, N.A. and Questiaux, D. (2004) Continuous 150 ky monsoon record from Lake Eyre, Australia: insolation-forcing implications and unexpected Holocene failure. *Geology* 32, 885-888.
- Maher, K., DePaolo, D.J. and Christensen, J.N. (2006) U-Sr isotopic speedometer: Fluid flow and chemical weathering rates in aquifers. *Geochimica et Cosmochimica Acta* 70, 4417-4435.
- Malmon, D.V., Dunne, T. and Reneau, S.L. (2003) Stochastic theory of particle trajectories through alluvial valley floors. *The Journal of Geology* 111, 525-542.
- Mandelbrot, B.B. (1983) *The Fractal Geometry of Nature*. Macmillan.
- Marra, K.R., Soreghan, G.S., Madden, M.E.E., Keiser, L.J. and Hall, B.L. (2014) Trends in grain size and BET surface area in cold-arid versus warm-semiarid fluvial systems. *Geomorphology* 206, 483-491.
- Martin, A.N., Dosseto, A. and Kinsley, L.P.J. (2015) Evaluating the removal of non-detrital matter from soils and sediment using uranium isotopes. *Chemical Geology* 396, 124-133.
- Matmon, A., Bierman, P.R., Larsen, J., Southworth, S., Pavich, M., Finkel, R. and Caffee, M. (2003) Erosion of an ancient mountain range, the Great Smoky Mountains, North Carolina and Tennessee. *American Journal of Science* 303, 817-855.
- Mayer, L.M. (1994) Surface area control of organic carbon accumulation in continental shelf sediments. *Geochimica et Cosmochimica Acta* 58, 1271-1284.
- McTainsh, G., O’Loingsigh, T. and Strong, C., Update of Dust Storm Index (DSI) maps for 2005 to 2010 (2011). Department of the Environment and Energy. December 2011.

Megumi, K. and Mamuro, T. (1977) Concentration of uranium series nuclides in soil particles in relation to their size. *J Geophys Res* 82, 353-356.

Megumi, K., Oka, T., Yaskawa, K. and Sakanoue, M. (1982) Contents of natural radioactive nuclides in soil in relation to their surface area. *Journal of Geophysical Research* 87, 10857-10860.

Menozi, D (2016) Assessment of sequential extraction and mineral separation for studying uranium-series isotopes in Regolith, Doctor of Philosophy thesis, School of Earth and Environmental Sciences, University of Wollongong, 2016.

Métivier, F. and Gaudemer, Y. (1999) Stability of output fluxes of large rivers in south and east Asia during the last 2 million years: Implications on floodplain processes. *Basin Research* 11, 293-303.

Milliman, J.D. and Syvitski, J.P.M. (1992) Geomorphic/tectonic control of sediment discharge to the ocean: the importance of small mountainous rivers. *The Journal of Geology* 100, 525-544.

Molnar, P., Anderson, R.S. and Anderson, S.P. (2007) Tectonics, fracturing of rock, and erosion. *Journal of Geophysical Research* 112, F03014.

Nanson, G.C., Jones, B.G., Price, D.M. and Pietsch, T.J. (2005) Rivers turned to rock: Late Quaternary alluvial induration influencing the behaviour and morphology of an anabranching river in the Australian monsoon tropics. *Geomorphology* 70, 398-420.

Nanson, G.C., Price, D.M. and Short, S.A. (1992) Wetting and drying of Australia over the past 300 ka. *Geology* 20, 791-794.

Nanson, G.C., Price, D.M., Short, S.A., Young, R.W. and Jones, B.G. (1991) Comparative uranium-thorium and thermoluminescence dating of weathered Quaternary alluvium in the tropics of northern Australia. *Quaternary Research* 35, 347-366.

Nichols, K.K., Bierman, P.R. and Rood, D.H. (2014) ^{10}Be constrains the sediment sources and sediment yields to the Great Barrier Reef from the tropical Barron River catchment, Queensland, Australia. *Geomorphology* 224, 102-110.

Pearson, K. (1909) On a new method of determining correlation between a measured character a, and a character b, of which only the percentage of cases wherein b exceeds (or falls short of) a given intensity is recorded for each grade of a. *Biometrika* 7, 96-105.

Pelt, E., Chabaux, F., Stille, P., Innocent, C., Ghaleb, B., Gérard, M. and Guntzer, F. (2013) Atmospheric dust contribution to the budget of U-series nuclides in soils from the Mount Cameroon volcano. *Chemical Geology* 341, 147-157.

Petit, J., Langevin, Y. and Dran, J. (1985) Radiation-enhanced release of uranium from accessory minerals in crystalline rocks. *Geochimica et Cosmochimica Acta* 49, 871-876.

Phillips, J.D. (2003) Sources of nonlinearity and complexity in geomorphic systems. *Progress in Physical Geography* 27, 1-23.

Phillips, J.D., Marden, M. and Gomez, B. (2007) Residence time of alluvium in an aggrading fluvial system. *Earth Surface Processes and Landforms* 32, 307-316.

Pillans, B. (1997) Soil development at snail's pace: evidence from a 6 Ma soil chronosequence on basalt in north Queensland, Australia. *Geoderma* 80, 117-128.

Plater, A.J., Ivanovich, M. and Dugdale, R.E. (1992) Uranium series disequilibrium in river sediments and waters: the significance of anomalous activity ratios. *Applied Geochemistry* 7, 101-110.

Raymond, O.L., Liu, S., Gallagher, R., Zhang, W. and Highet, L.M. (2012) Surface Geology of Australia 1:1 million scale dataset 2012 edition. Geoscience Australia.

Reeves, J.M., Chivas, A.R., García, A., Holt, S., Couapel, M.J.J., Jones, B.G., Cendón, D.I. and Fink, D. (2008) The sedimentary record of palaeoenvironments and sea-level change in the Gulf of Carpentaria, Australia, through the last glacial cycle. *Quaternary International* 183, 3-22.

Rosholt, J.N. (1983) Isotopic composition of uranium and thorium in crystalline rocks. *Journal of Geophysical Research* 88, 7315-7330.

Semkow, T.M. (1991) Fractal model of radon emanation from solids. *Physical Review Letters* 66, 3012-3015.

Shulmeister, J. (1992) A Holocene pollen record from lowland tropical Australia. *The Holocene* 2, 107-116.

Sims, K.W.W., Gill, J.B., Dosseto, A., Hoffmann, D.L., Lundstrom, C.C., Williams, R.W., Ball, L., Tollstrup, D., Turner, S., Prytulak, J., Glessner, J.J.G., Standish, J.J. and Elliott, T. (2008) An inter-laboratory assessment of the thorium isotopic composition of synthetic and rock reference materials. *Geostandards and Geoanalytical Research* 32, 65-91.

Sing, K.S. (1985) Reporting physisorption data for gas/solid systems with special reference to the determination of surface area and porosity (Recommendations 1984). *Pure and Applied Chemistry* 57, 603-619.

Stephenson, P. and Griffin, T. (1976) Some long basaltic lava flows in north Queensland. *Volcanism in Australasia*, 41-51.

Suresh, P., Dosseto, A., Hesse, P. and Handley, H. (2014) Very long hillslope transport timescales determined from uranium-series isotopes in river sediments from a large, tectonically stable catchment. *Geochimica et Cosmochimica Acta* 142, 442-457.

Syvitski, J.P., Vörösmarty, C.J., Kettner, A.J. and Green, P. (2005) Impact of humans on the flux of terrestrial sediment to the global coastal ocean. *Science* 308, 376-380.

Tieh, T.T. and Ledger, E.B. (1981) Fission track study of uranium in two granites of central Texas. *Contributions to Mineralogy and Petrology* 76, 12-16.

Titley, J., Glegg, G., Glasson, D. and Millward, G. (1987) Surface areas and porosities of particulate matter in turbid estuaries. *Continental Shelf Research* 7, 1363-1366.

Von Blanckenburg, F., Bouchez, J., Ibarra, D.E. and Maher, K., 2015. Stable runoff and weathering fluxes into the oceans over Quaternary climate cycles. *Nature Geoscience*, 8, 538-542.

West, A.J., Galy, A. and Bickle, M. (2005) Tectonic and climatic controls on silicate weathering. *Earth and Planetary Science Letters* 235, 211-228.

White, A.F. and Peterson, M. (1990) Role of reactive-surface-area characterization in geochemical kinetic models, *Chemical Modeling of Aqueous Systems II*. American Chemical Society, pp. 461-475.

Willenbring, J.K. and von Blanckenburg, F., (2010). Long-term stability of global erosion rates and weathering during late-Cenozoic cooling. *Nature* 465, 211-214.

Wilson, S.A. (1997) The collection, preparation and testing of USGS reference material BCR-2. U.S. Geological Survey Open-File Report.

Withnall, I.W. and Cranfield, L.C. (2013). Geological Framework. Queensland Minerals.

4. Late Quaternary sediment dynamics inferred from U isotope variations in tropical monsoonal Australia

A. N. Martin^{1,2,*}, A. Dosseto^{1,2}, J.-H. May^{1,2}, L. Kinsley³, I. Karatchevtseva⁴, and A. R. Chivas²

¹*Wollongong Isotope Geochronology Laboratory, School of Earth and Environmental Sciences, University of Wollongong, NSW 2522, Australia.*

²*GeoQUEST Research Centre, School of Earth & Environmental Sciences, University of Wollongong, NSW 2522, Australia.*

³*Research School of Earth Sciences, Australian National University, Canberra, ACT 0200, Australia.*

⁴*Institute of Materials Engineering, Australian Nuclear Science and Technology Organisation, New Illawarra Road, Lucas Heights, NSW, 2234, Australia.*

*Corresponding author:

Email: anm724@uowmail.edu.au

Telephone: (+61 2) 4221 3382

Abstract

Uranium (U) isotopes (^{234}U and ^{238}U) in sedimentary deposits record the landscape response to Late Quaternary climate change. The comminution dating technique constrains the time elapsed since detrital minerals were reduced to $<63\ \mu\text{m}$ in size based on the ($^{234}\text{U}/^{238}\text{U}$) activity ratio (parentheses denote activity ratio) and surface area properties of the detrital minerals. Here we report ($^{234}\text{U}/^{238}\text{U}$) and surface area measurements of fine-grained detrital sediments from two sedimentary cores in the Gulf of Carpentaria, northern Australia that span the past 120 ka. The ($^{234}\text{U}/^{238}\text{U}$) were low during Marine Isotope Stage (MIS) 5 and MIS 1, but higher throughout much of MIS 2 to 4. In addition, many sediments deposited during glacial periods remained close to secular equilibrium. Lower ($^{234}\text{U}/^{238}\text{U}$) were then recorded following the termination of the Last Glacial Maximum (LGM) from around 20 ka onwards to present. Inferred comminution ages suggest an average sediment residence time of 41 ± 18 ka during MIS 5 and post-LGM, similar to the average sediment residence time inferred for modern rivers draining to the Gulf. However, residence times could not be calculated for sediments deposited during glacial periods due to their lack of ^{234}U depletion, suggesting rapid sediment transport. River sediments from the northern catchments were also close to secular equilibrium, suggesting this may be the dominant sediment source during glacial periods. This is consistent with a reduced sediment contribution from the S catchments due to the northwards migration of the Indo-Australian monsoon. Longer sediment residence times during interglacial periods suggest the reactivation of sediment contribution from the southern catchments (characterised by long residence times) due to the return of monsoonal rainfall. This supports previous findings that on larger scales, the main effect of Late Quaternary climate change is a reorganisation of the spatial distribution of discharge and sediment provenance. However, the global response of weathering, erosion and sediment transport processes to glacial-interglacial cycles is likely buffered by long sediment residence times in catchments.

4.1 Introduction

Earth's climate is regulated on long-term (>1 Ma) timescales by a negative feedback mechanism between continental chemical weathering and atmospheric carbon dioxide (CO_2) concentrations (Raymo et al., 1988; Ruddiman et al., 1997; Kump et al., 2000). It was supposed that an increase in sedimentation rates at 2-4 Ma was due to an increase in erosion rates caused by Quaternary glacial-interglacial climate variability (Zhang et al., 2001). However, recent sedimentation rates are faster than long-term rates due to the increased probability of integrating sedimentary hiatuses on longer timescales (Willenbring and von Blanckenburg, 2010). In fact, weathering fluxes inferred from the ratio of cosmogenic beryllium (^{10}Be) to mineral-derived ^9Be ($^{10}\text{Be}/^9\text{Be}$) suggest that the silicate weathering flux has been constant throughout the Quaternary (Willenbring and von Blanckenburg, 2010; von Blanckenburg et al., 2014). A stable weathering flux throughout the Late Quaternary is consistent with the relative stability of CO_2 concentrations throughout the past 600 ka (Zeebe and Caldeira, 2008). Landscapes may instead respond to glacial cycles by modulating the strength of the feedback between erosion, weathering and climate (Maher and Chamberlain, 2014; Caves et al., 2016). A key parameter for understanding the strength of the weathering feedback is the time spent by silicate minerals in the weathering zone. For instance, the supply of silicate cations will be exhausted in transport-limited environments with low erosion rates (Stallard, 1985; West et al., 2005), and climate-induced hydrological changes will have little effect on weathering fluxes (Maher and Chamberlain, 2014). In contrast, high erosion rates in weathering-limited environments will mean weathering fluxes are susceptible to hydrological changes (Stallard, 1985; West et al., 2005; Maher and Chamberlain, 2014).

Uranium (U) isotopes provide information on the residence time of soils and sediments in the weathering environment (Chabaux et al., 2003; Dosseto et al., 2008). Firstly, the initial ($^{234}\text{U}/^{238}\text{U}$) (where parentheses denote activity ratio) of unweathered material is known since

systems that remain closed, i.e. material that has not undergone weathering, for more than ~1 Ma are in secular equilibrium where $(^{234}\text{U}/^{238}\text{U}) = 1$. Lower activity ratios in detrital sediments are generated by: 1) recoil of ^{234}U (via short-lived ^{234}Th) following the alpha-decay into the surrounding medium, i.e. alpha recoil (Kigoshi, 1971), and 2) the preferential leaching of ^{234}U from lattice sites damaged by alpha recoil (Fleischer, 1980). These processes are particularly important in fine-grained detrital sediments due to their higher surface-area-to-volume ratios (Kigoshi, 1971; DePaolo et al., 2006). Therefore, the $(^{234}\text{U}/^{238}\text{U})$ activity ratios and geometric properties of fine-grained detrital sediments can be used to infer the time elapsed since the sediments became $<63\text{ }\mu\text{m}$, i.e. the comminution dating technique (DePaolo et al., 2006). By applying comminution dating to sedimentary deposits of known age, depositional ages can be subtracted from comminution ages to infer sediment residence times (DePaolo et al., 2006). In the North Atlantic, $(^{234}\text{U}/^{238}\text{U})$ and sediment residence times varied with glacial-interglacial cycles (DePaolo et al., 2006). This was attributed to sediment provenance oscillating between Iceland (short residence times) and continental Europe (long residence times). Sampling palaeochannel deposits from the Murrumbidgee River, southeastern Australia showed that $(^{234}\text{U}/^{238}\text{U})$ and sediment residence times were much lower during glacial compared to interglacial periods (Dosseto et al., 2010). This was also attributed to changes in sediment provenance between younger hillslopes during glacials and reworking of older floodplain deposits during interglacials. In the East China Sea, sediment residence times decrease from 14 ka onwards (Li et al., 2016). This was attributed to possibly reflect a change in sediment provenance from the Chinese mainland to Taiwan.

Here we assess the controls on $(^{234}\text{U}/^{238}\text{U})$ activity ratios of fine-grained sediments from two sedimentary cores in the Gulf of Carpentaria (herein termed ‘the Gulf’), northern Australia (Figure 4.1). Sediment depositional ages span the past 120 ka (Chivas et al., 2001; Reeves et al., 2008), which covers the last interglacial-glacial cycle. The Gulf basin is tectonically

stable and has a low gradient ($<0.1\%$), limiting incision during sea-level low stands (Woolfe et al., 1998; Chivas et al., 2001; Nanson et al., 2013). Low sea levels create an isolated waterbody known as *Lake Carpentaria* (Chivas et al., 2001). At its maximum extent (~ 59 m contour, Figure 4.1B), Lake Carpentaria was up to ~ 100 and ~ 200 km from the present shorelines of the northern (N) and southern (S) catchments, respectively (Figure 4.1B). The relative two-fold increase in the length of the S vs N catchments during glacial periods likely decreased their contribution to sedimentation in the Gulf/Lake Carpentaria. This effect is expected to be compounded by the northward migration of the inter-tropical convergence zone (ITCZ) (Schneider et al., 2014), which strongly reduced the discharge of southern catchments during the Last Glacial Maximum (Devriendt, 2011). Therefore, increased river channel lengths and reworking of older continental shelf sediments during glacial periods should result in lower ($^{234}\text{U}/^{238}\text{U}$) and longer sediment residence times. In contrast, a shift in sediment provenance to the N catchments should result in higher ($^{234}\text{U}/^{238}\text{U}$) during glacial periods.

We first present ($^{234}\text{U}/^{238}\text{U}$) activity ratios and surface area measurements of sediments from the Gulf. Hypotheses for down-core variations in ($^{234}\text{U}/^{238}\text{U}$) activity ratios are then considered in context of existing paleoenvironmental data (Chivas et al., 2001; Reeves et al., 2008), U data for modern fluvial sediments from catchments draining to the Gulf (Chapter 3), and Late Quaternary glacial-interglacial cycles. Finally, we infer residence times for sediments based on their ($^{234}\text{U}/^{238}\text{U}$) and geometric properties.

4.2 Study area

4.2.1 Hydrology of the Gulf

The Gulf of Carpentaria ('the Gulf') is an epicontinental sea located between Australia and New Guinea (Figure 4.1). The water body of the Gulf covers an area of ca. $230,000 \text{ km}^2$, has a maximum depth of ca. 70 m in the central-eastern section (Chivas et al., 2001), and it has

low relief bathymetry (Torgersen et al., 1983). The basin is semi-enclosed from the Coral Sea by the Torres Strait to the east (12 m water depth), and the Arafura Sea by the Arafura Sill to the west (53 m water depth). This is only a 4 m difference in water depth over ~40 km, which is a gradient of just ~1:10,000 and likely not enough gravity potential for slumping to occur. Diurnal tides enter the Gulf from the northwest and circulate clockwise; more frequent, semi-diurnal tides are also present, but are focussed on the northern section of the Gulf (Wolanski, 1993). North-westerly trade winds are prevalent during the summer monsoon and result in a clockwise circulation. Occasionally, weak south-easterly trade winds produce a counter-clockwise circulation. Overall, this results in a clockwise residual current. Seasonal changes in wind patterns create sea-level fluctuations of 0.5 m in coastal areas.

Modern sediment in the Gulf is primarily fluvial, with the eastern side of the Gulf drainage basin providing the bulk of the sediment (Preda and Cox, 2005). Terrigenous minerals predominantly comprise quartz, minor feldspars, and clays present in various abundances (Preda and Cox, 2005). There is a significant biogenic carbonate fraction which is more significant in the shallower water depths that have higher biological productivity (Preda and Cox, 2005). The clockwise current dominates marine sediment transport in the Gulf and finer-grained sediment deposited in the centre/northwest of the Gulf. Modern sedimentation rates in the Gulf below 40 m water depths are low (Reeves et al. 2008).



Figure 4.1A) The Gulf of Carpentaria with delineated catchment areas (red curves), major fluvial channels (blue lines), and core locations (+ symbols) shown; B) Sahul during Last Glacial Maximum when sea level was -125 m bpsl and where grey lines show modern shorelines; and C) Regional setting showing key palaeoclimate study sites. In all figures, the red line represents the Gulf of Carpentaria catchment area, and labelled dashed lines depict the -53 and -59 m contour lines.

4.2.2 Gulf of Carpentaria drainage basin

The Gulf drainage basin extends from tropical New Guinea at 8°S to the semi-arid Australia interior at 22°S. The Gulf of Carpentaria basin largely lies within the North Australian Craton. Maximum elevations of ca. 1600 m are found in the east of the drainage basin in the Hodgkinson Province, which straddles the Great Dividing Range and the Atherton Tableland. There are also a series of Cenozoic lava fields centred around the Great Dividing Range; for instance, the McBride Basalt Province, which covers an area of ca. 5,500 km² and has a maximum elevation of 1,020 m (Whitehead, 2010). The Mount Isa Province is located in the southwest of the basin and consists of a series of fold belts (Blake, 1987). West of the Mount Isa Province lies the McArthur Basin, which is sedimentary and mainly low relief (Rawlings, 1999). An area in the northern section of the drainage basin drains from New

Guinea; however, as this is a small area and low-relief, we assume that sediment contribution from New Guinea to the Gulf is negligible. No sediment yield data are available for these rivers, but our assertion is supported by New Guinea pollen from being absent in sediment cores from the Gulf (S. van der Kaars, personal communication), and the greater long-range transport potential of pollen vs sediment (Rousseau et al., 2006). Furthermore, the large Fly River drains east of into the Coral Sea (Figure 4.1), and is blocked from reaching the Gulf by the shallow Torres Strait (10 m water depth).

The climate across the Gulf drainage basin is largely tropical savannah with a mean annual rainfall across the basin of 779 mm a^{-1} , and 94% of rainfall occurring in the wet season from December to March (Reeves et al., 2008). The variation in monsoonal intensity leads to mean annual rainfall totals ranging from 330 – 1800 mm. Average evaporation rates across the basin are 1650 mm a^{-1} (Newell, 1973). Modern upland vegetation is mainly open sclerophyll woodlands of *Eucalyptus* and *Acacia*, and coastal areas comprise salt flats and mangrove forests (Shulmeister, 1992).

Twenty six catchments drain into the Gulf and major catchments are located in the southeast of the drainage basin, including the Mitchell, Gilbert, Norman and Flinders Rivers, with mean discharge values ranging from $100 - 500 \text{ m}^3 \text{ s}^{-1}$ (DNRM, 2014). Fluvial channels tend to be sand-dominated, low sinuosity, and anabranching; channels are commonly flanked by extensive floodplains comprising overbank muds and muddy sands (Nanson et al., 1991). Induration of alluvium in the Gilbert River has produced local rapids, waterfalls and gorges (Nanson et al., 2005).

Fluvial megafans have developed in the lower sections of some catchments, for instance, in the Mitchell River (Brooks et al., 2009), Flinders River (Weissmann et al., 2010), and Gilbert River (Nanson et al., 2005). Fluvial megafans are distinguished from alluvial fans by the increased frequency of water-lain deposits, large areas, and low slope (DeCelles and

Cavazza, 1999). These features tend to form on the fringes of tropical climatic belts in catchments that are characterised by large seasonal variations in discharge (Leier et al., 2005), such as catchments draining to the Gulf.

4.2.3 Palaeoclimate in northern Australia

Northern (N) Australia is generally inferred to be humid during interglacial periods and drier during glacial periods (Nanson et al., 2008; Nanson et al., 1992). Broadly, the N Australian climate was wetter during Marine Isotope Stage (MIS) 5, and then became arid during MIS 4 resulting in dune building and playa lake deflation (Bowler et al., 2001; Magee et al., 2004). A brief wet period occurred at the start of MIS 3 before there was a major hydrological shift at ~46 ka to more arid conditions across the Australian continent that coincided with the arrival of humans, extinction of megafauna, and vegetation change (Miller et al., 1999; Roberts et al., 2001; Cohen et al., 2015). The climate was relatively arid throughout MIS 2 until the reactivation of the monsoon following the Last Glacial Maximum (LGM) (Reeves et al., 2008; Tachikawa et al., 2009).

Key palaeoclimatic study areas in N Australia include alluvial deposits in the Gilbert River, and the Lake Eyre Basin (Figure 4.1C), which borders the Gulf drainage basin to the south. Pollen evidence is sourced from Lynch's Crater in northeastern Australia and a marine deposit offshore from Cape Range in northwestern Australia (Figure 4.1C). The following sedimentary environments in the Gulf have been proposed as a result of past variations in sea level: open-marine, shallow-marine (Torres Strait closed), brackish lake (Torres Strait and Arafura Sill closed), freshwater lake (herein termed 'Lake Carpentaria') and sub-aerial exposure (Chivas et al., 2001; Reeves et al., 2008).

4.2.3.1 MIS 5

The oldest recovered sedimentary deposits from the Gulf are dated to ca. 120 ka and are associated with MIS 5, in which the Gulf was an open-marine environment. Sea-level fell to approximately 45 m below present sea level (bpsl) in MIS-5d (116 – 103 ka), and subsequently rose during the MIS-5c high-stand (103–93 ka) (Lambeck and Chappell, 2001). In this period, the Gulf was a shallow marine environment and semi-enclosed by a land bridge at the Torres Strait (Chivas et al., 2001; Reeves et al., 2008). Data from the Huon Peninsula, Papua New Guinea indicate sea-level was around 20 m bpsl (Lambeck and Chappell, 2001). Falling sea-level during MIS-5b (93–85 ka) formed a semi-enclosed lagoon and rising sea-level during MIS-5a (85–74 ka) re-formed a shallow-marine environment.

4.2.3.2 MIS 4

Falling sea-level during the MIS 5/4 transition (ca. 74 – 72 ka) re-closed the Arafura sill and formed a brackish lagoon, with occasional sub-aerial exposure (Chivas et al., 2001; Reeves et al., 2008). Gypsum and carbonate layers in the Gulf indicate repeated cycles of inundation and evaporation, which could be due to annual cycles of freshwater input (Playà et al., 2007). A subsequent lack of freshwater input formed a saline mudflat without permanent water from 72 ka onwards.

4.2.3.3 MIS 3

Rising sea-levels during the MIS 4/3 transition (ca. 60 ka) led to estuarine conditions in the Gulf (Chivas et al., 2001; Reeves et al., 2008). A subsequent fall in sea level formed a brackish waterbody perched above sea level known as *Lake Carpentaria*, which persisted throughout MIS 3 (55 – 40 ka) with brief marine incursions (Chivas et al., 2001; Reeves et al., 2008; Devriendt, 2011).

4.2.3.4 MIS 2

A saline waterbody with a maximum depth of 5 m and periodic anoxia was established during MIS 2 (Chivas et al., 2001; Reeves et al., 2008). Following the LGM, Lake Carpentaria expanded to the -59 m contour, which would represent a lake with a surface area >100,000 km² and suggests that the precipitation/evaporation ratio during MIS 2 was more than twice that of present (Reeves et al., 2008). This period coincides with the onset of deglaciation in the tropics that corresponds to a warming of the Coral Sea and rising sea levels (Tachikawa et al., 2009). Lake Carpentaria then expanded to a maximum surface area of almost 200,000 km² at ~14 ka (Reeves et al., 2008).

4.2.3.5 MIS 1

Marine waters first re-entered the Gulf at 12.2 ka following transgression of the Arafura Sill, and marine waters transgressed the Torres Strait ca. 8 ka (Reeves et al., 2008). Modern vegetation in the Gulf was established around 7.5 ka indicating that the modern climate would have also been established around this time (Shulmeister, 1992),.

4.3 Methods

4.3.1 Sampling and sample preparation

Samples were collected using a piston-core system deployed from the research vessel *Marion Dufresne* in June 1997. The core samples were pre-sliced into 1 cm depth-interval segments and stored flat in transparent glass Petri dishes with tape-sealed lids at 4°C (Chivas et al., 2001). Samples were collected from sedimentary cores MD972132 and MD972133, hereafter referred to as ‘MD32’ and ‘MD33’ respectively. MD32 is located at a water depth of 64 m and 12°18.79'S 139°58.73'E, and MD33 is located at a water depth of 68 m and 12°23.55'S 140°20.32'E; MD33 is located ca. 40 km southeast of MD32 (Figure 4.1).

4.3.2 Analytical techniques

The samples were wet-sieved at 63 μm using deionised H_2O ; the $<63 \mu\text{m}$ fraction was retained, dried in an oven at 50 $^{\circ}\text{C}$ and homogenised by gentle mixing using an agate mortar and pestle. Sequential extraction was carried out using the procedure recommended by Lee (2009) on 2 g of dry, homogenised sample. The solid and aqueous phases were separated by centrifugation. Prior to strong acid dissolution, ca. 100 mg of material was weighed and a known amount of ^{229}Th – ^{236}U tracer was added. The samples were dissolved in 2.5 mL 32 % HF and 0.5 mL 69 % HNO_3 and heated overnight at 100 $^{\circ}\text{C}$. The sample solutions were dried to incipient dryness and this was followed by the addition of 3 mL 6 M HCl. Where necessary, H_3BO_3 was added to dissolve fluoride precipitates. The samples were heated at 80 $^{\circ}\text{C}$ overnight and dried to incipient dryness. To the residue, 0.5 mL 69 % HNO_3 was added and the solution dried at 100 $^{\circ}\text{C}$ to incipient dryness. This step was repeated and then 2 mL of 1.5 M HNO_3 was added to the residue. The solutions were sonicated for 15 min and heated at 100 $^{\circ}\text{C}$ to ensure re-dissolution. Total procedural blanks were $<34 \text{ pg}$ for U. For isotopic measurements, U was separated by standard chromatographic techniques using a TRU resin (Eichrom) as described in Luo et al. (1997). The $^{234}\text{U}/^{238}\text{U}$ ratios and U concentrations were measured using a ThermoFisher Neptune Plus Multi-Collector Inductively-Coupled-Plasma-Mass Spectrometer (MC-ICP-MS) at the Research School of Earth Sciences, Australian National University for MD32 and at the Wollongong Isotope Geochronology Laboratory, University of Wollongong for MD33. Isotopic measurements were carried out according to the procedure described in Sims et al. (2008). Mass bias and SEM/Faraday cup yield were corrected by standard bracketing using certified reference material (CRM) U010 (NBL, 2008a). The ^{236}U peak was corrected for tailing from the ^{238}U peak by subtracting values interpolated from signals measured at 235.5 and 236.5 amu. Accuracy of measurements was assessed by analysing CRM U005A (NBL 2008b), and a gravimetric rock standard (BCR-2, U.S. Geological Survey) known to be in secular equilibrium where $(^{234}\text{U}/^{238}\text{U}) = 1$. Measured $(^{234}\text{U}/^{238}\text{U})$ activity ratios of BCR-2 were

precise within 0.005% of secular equilibrium (0.999 ± 0.005 and 1.000 ± 0.001). The measured U concentrations were 1.70 ± 0.004 and 1.84 ± 0.005 ppm which are within error of recommended values for BCR-2 (Wilson, 1997).

BET surface area measurements were determined by nitrogen (N_2) gas adsorption using an Autosorb® Quantachrome iQ surface area analyser at the Australian National Science and Technology Organisation (ANSTO). Samples were degassed for 3 h at 200 °C. The BET surface area was determined using 5 – 7 adsorption points from the partial pressure (P/P_0) range 0.05 – 0.30 and adjusted for the best fit of the multi-point BET equation ($R^2 > 0.9999$). The fractal dimension of sediments was determined from the multi-point adsorption data using the Neimark-Kiselev Method (Neimark, 1990). The total pore volumes were determined from the single-point total pore volume of pores at a partial pressure (P/P_0) > 0.99.

4.3.3 Depositional age chronology

In MD32, a limited number of depositional ages (optically stimulated luminescence and thermoluminescence) were available below 370 cm. Thus, depositional ages of samples from units 4, 5 and 6 were inferred from the record of palaeoenvironmental and sea-level changes from Reeves et al. (2008). Unit 6d was inferred to represent the MIS 5.3 high-stand (103–93 ka BP), unit 6b represents rising sea-level in MIS 5a (85–74 ka BP), and unit 5 represents falling sea-level during the MIS 5/4 transition (ca. 74 – 72 ka). Above 370 cm in core MD32, linear regression models of radiocarbon ages were used to infer ages for samples (Figure 4.2A).

In MD33, depositional ages were limited below 200 cm, and for samples from units 3 and 4 they were inferred from the record of palaeoenvironmental and sea-level changes from Reeves et al. (2008). Above 200 cm in MD33, linear regression models of radiocarbon ages were also used to infer depositional ages for samples (Figure 4.2B).

Sedimentation rates were calculated for MD32 and MD33 using the depositional age chronologies developed in this study, based on radiocarbon ages and the palaeoenvironmental record (Figure 4.2). Sedimentation rates could not be calculated for modern samples of the cores due to reworking in the upper few centimeters; however, modern sedimentation rates in the Gulf are known to be low (Reeves et al., 2008). Sedimentation rates were not adjusted for core compaction and thus represent minimum estimates.

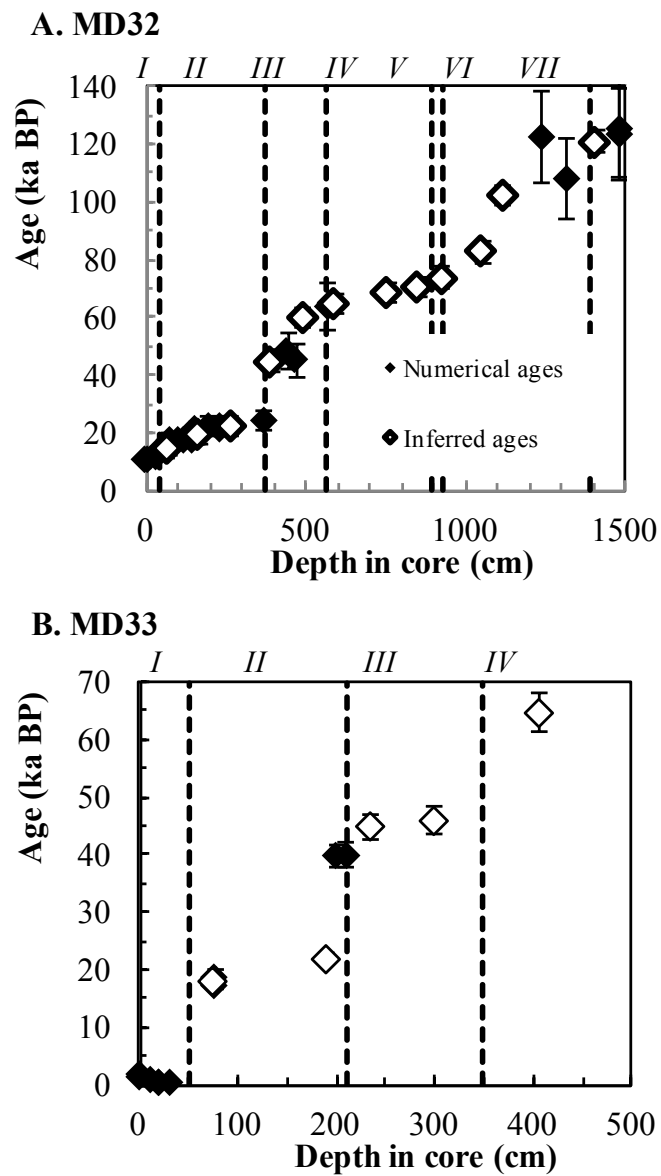


Figure 4.2A) Age-depth model for the Gulf of Carpentaria cores A) MD32 and B) MD33. The depositional ages are from Reeves et al. (2008) (◆), inferred depositional ages from the palaeo environmental record (◇), and stratigraphic units (italics). Error bars not shown are hidden by markers.

4.4 Results

4.4.1 Uranium isotopes

The ($^{234}\text{U}/^{238}\text{U}$) (where parentheses denote activity ratio) and U concentration measurements for thirteen leached sediment samples from cores MD32 and six samples from MD33 are given in Table 4.2. The depositional ages for MD32 and MD33 span 0 to 121 ± 14 ka, and 0 to 46 ± 2 ka, respectively (Table 4.2). The ($^{234}\text{U}/^{238}\text{U}$) for MD32 core sediments ranged from 0.990 to 1.110, whereas significantly lower ($^{234}\text{U}/^{238}\text{U}$) were measured for MD33: 0.830 to 0.944 ($p = 0.003$, Table 4.2). The difference in the range of measured values is surprising considering the cores are located within 50 km of each other and the Gulf presently covers an area of $\sim 500,000$ km (Figure 4.1). The ranges of activity ratios measured for MD32 and MD33 are similar to leached core sediments measured elsewhere: 0.917 to 1.04 for sediments from the East China Sea (Li et al., 2016), and 0.830 to 0.968 for sediments from the North Atlantic (DePaolo et al., 2006).

The activity ratio of the deepest core sediment was enriched in ^{234}U relative to secular equilibrium (MD32-7, Table 4.2). This can only be explained by 1) incomplete removal of ^{234}U -rich non-detrital matter during sample pre-treatment (Plater et al., 1992), and/or ii) implantation of ^{234}U nuclides from adjacent grains (Kigoshi, 1971). Since the specific surface area for MD32-7 was 50% lower than all other samples, the high activity ratio may be attributed to the formation of cements by early sedimentary diagenesis processes at depth (Michalopoulos and Aller, 1995, 2004). Cement phases are typically enriched in ^{234}U (Paces et al., 2013), and may be resistant to removal by sequential extraction. Alternatively, the decreased porosity could have increased the fraction of ^{234}U (via the short-lived ^{234}Th) nuclides that are implanted into surrounding silicate minerals instead of being ejected into air or water. Since implanted ^{234}U nuclides are labile (Fleischer, 1980), and would be leached by acidic solutions during sample pre-treatment (Section 4.3.2), this hypothesis suggests that recoil-damaged lattice sites in silicate minerals could be annealed during sedimentary

storage. This is reasonable considering that low temperature annealing of damaged lattice sites in silicates occurs on timescales of ~15 ka (Eyal and Fleischer, 1985), and MD32-7 has a depositional age of 120 ± 19 ka. Increased implantation of ^{234}U and subsequent annealing may also explain why many core sediments exhibited ($^{234}\text{U}/^{238}\text{U}$) activity ratios close to unity. This is despite long sedimentary storage times, e.g. ~80 ka for MD32-6b, and any time spent by sediment in catchments (Table 4.3).

The ($^{234}\text{U}/^{238}\text{U}$) of MD32 core sediments can be divided into two groups based on whether they were greater or lower than the activity ratio of modern sediment from the upper portion of MD32 (0.952 ± 0.002 , Table 4.1). Note that MD32-7 is regarded as an outlier and only core sediments deposited from 101 ± 4 ka to 20 ± 1 ka are discussed herein. Sediments with lower activity ratios were deposited at 101 ± 19 , 68 ± 4 , 19.9 ± 0.7 , 15 ± 1 , and 0 ka; whereas the activity ratios for all other sediments were closer to secular equilibrium. In core MD33, there was just one core sediment that exhibited a higher activity ratio than the modern sediment from the upper portion of MD32, which was deposited during MIS 2 at 25.4 ± 1.3 ka. An increase in activity ratios was recorded for both cores from the LGM towards the present, which peaked at approximately 19 – 23 ka in northern Australia (Williams et al., 2009). Higher ($^{234}\text{U}/^{238}\text{U}$) were recorded for sediments deposited at 22 ± 2 ka and 20 ± 1 ka in MD32, and 25 ± 1 ka and 16 ± 1 ka in MD33. However, unlike in MD32, lower ($^{234}\text{U}/^{238}\text{U}$) were recorded in MIS 3 at 42 ± 2 ka. The discordance in the records of MD32 and MD33 are discussed in Section 4.5.2.

The U concentrations in MD32 ranged from 1.37 – 2.00 ppm, except for MD32-1 and MD32-2c that yielded much higher U concentrations of 15.85 and 14.56 ppm, respectively. The U concentrations for sediments from core MD33 were generally higher and exhibited greater variability compared to MD32, ranging from 4.45 – 13.63 ppm. In both cores, U concentrations were similarly high in core sediments deposited at 0 ka, and 22 – 25 ka. However, in MD33, there was a peak in U concentrations at 46 ± 2 ka that does not seem to

correspond to MD32. Given that an immobile element, such as zirconium, was not measured, it is not possible to use the measured U concentrations to consider the relative gain/loss of U in sediments (Brimhall et al., 1992). Nevertheless, the large magnitude of change in U concentrations does suggest a change in sediment provenance. This is because the U budget of river sediments are mainly controlled by the relative proportion of accessory minerals, such as zircon and monazite, that are sorted during fluvial transport (Bosia et al., 2016). Possible changes in sediment provenance over the past 120 ka are discussed in Section 4.5.1.

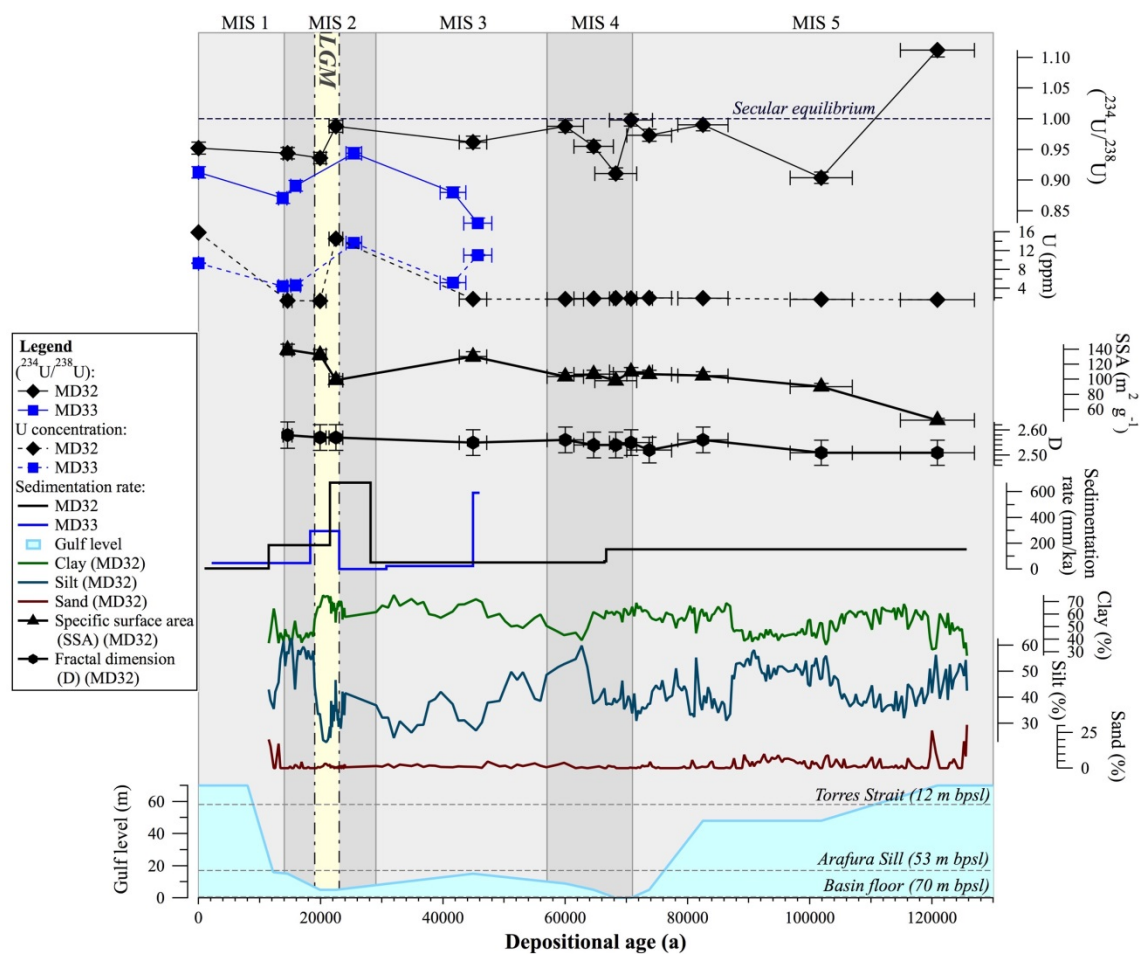


Figure 4.3 Uranium isotope data, sedimentation rates for cores MD32 and MD33 from the Gulf of Carpentaria. Gulf level represents the maximum water depth in the Gulf of Carpentaria. Particle size distribution and surface area data for core MD32.

Table 4.1 U and surface area measurements for <63 µm detrital core sediments from the Gulf of Carpentaria

Core	Depth in core (m)	Depositional age (ka) ^{a,b}	Sedimentary Unit	Depositional environment ^b	(²³⁴ U/ ²³⁸ U) ^c	U (ppm)	Mean diameter (µm) ^d	S _{BET} (m ² g ⁻¹) ^e	D ^e	Total pore volume (cm ³ g ⁻¹) ^f	f _a ^g
MD32	0	0	1	Open marine	0.952 ± 0.002	15.85 ± 0.05	20	n/a	n/a	0.32	0.40 ± 0.09 ^h
	0.67	15 ± 1	2a	Lacustrine	0.944 ± 0.003	1.44 ± 0.01	8	130 ± 27	2.58 ± 0.31	0.30	0.46 ± 0.10
	1.66	20 ± 1	2b	Lacustrine	0.936 ± 0.003	1.37 ± 0.01	5	130 ± 25	2.57 ± 0.31	0.22	0.44 ± 0.10
	2.66	22 ± 1	2c	Lacustrine	0.988 ± 0.002	14.56 ± 0.04	6	99 ± 19	2.57 ± 0.31	0.29	0.33 ± 0.08
	3.93	45 ± 2	3a	Lacustrine	0.962 ± 0.003	1.72 ± 0.01	5	130 ± 25	2.55 ± 0.31	0.23	0.46 ± 0.11
	4.92	60 ± 3	3b	Salt flat	0.988 ± 0.002	1.76 ± 0.01	7	104 ± 20	2.56 ± 0.31	0.25	0.36 ± 0.08
	5.91	65 ± 3	4a	with	0.955 ± 0.002	1.87 ± 0.01	6	94 ± 18	2.54 ± 0.31	0.22	0.38 ± 0.09
	7.58	68 ± 3	4c	episodic	0.911 ± 0.003	1.91 ± 0.01	6	98 ± 19	2.54 ± 0.31	0.20	0.36 ± 0.08
	8.52	71 ± 4	4d	inundation	0.998 ± 0.003	1.89 ± 0.01	4	110 ± 21	2.55 ± 0.31	0.27	0.39 ± 0.09
	9.26	74 ± 4	5	Lagoon	0.973 ± 0.002	2.00 ± 0.01	20	110 ± 20	2.52 ± 0.30	0.23	0.41 ± 0.09
	10.51	83 ± 4	6b	Shallow marine	0.990 ± 0.002	1.91 ± 0.01	16	110 ± 20	2.56 ± 0.31	0.19	0.37 ± 0.08
	11.18	102 ± 5	6d	Shallow marine	0.904 ± 0.003	1.69 ± 0.01	8	90 ± 17	2.51 ± 0.30	0.20	0.37 ± 0.08
	14.09	121 ± 4	7	Open Marine	1.110 ± 0.003	1.63 ± 0.01	10	46 ± 9	2.51 ± 0.30	0.18	0.18 ± 0.04
MD33	0	0	1	Open marine	0.913 ± 0.003	9.32 ± 0.02	29				
	0.65	14 ± 1	2b	Lacustrine	0.871 ± 0.004	4.45 ± 0.01	14				
	0.75	16 ± 1	2b	Lacustrine	0.891 ± 0.003	4.63 ± 0.01	11	n/a	n/a	n/a	0.40 ± 0.09 ^h
	1.82	25 ± 1	2c	Lacustrine	0.944 ± 0.002	13.63 ± 0.02	15				
	2.20	42 ± 2	3a	Lacustrine	0.880 ± 0.002	5.25 ± 0.01	11				
	2.82	46 ± 2	3b	Lacustrine	0.830 ± 0.001	11.05 ± 0.01	3				

^aInterpolated from Figure 4.2; ^bData from Reeves et al. (2008); ^c2σ standard error; ^dData from Chivas et al. (2001); ^eS_{BET}: specific surface areas and D: fractal dimension where uncertainty is expressed as external error based on standard deviation of repeat measurements of sample 4a (n = 2); ^fsingle-point total pore volume at P/P0 > 0.99; ^gf_a: direct-recoil fraction where uncertainty is expressed as the propagated error (discussed later); and ^hassumed value based on measured direct-recoil values from MD32.

4.4.2 Surface area measurements

The BET surface area measurements for thirteen leached sediment samples from core MD32 ranged from 90 – 134 m² g⁻¹ (Table 4.2). These values are an order of magnitude higher than common primary minerals, such as quartz and feldspars (Brantley and Mellott, 2000; White et al., 1996), and are attributed to the sediments being clay-rich (Reeves et al., 2008). The specific surface area and fractal dimension of core sediments both decreased with increasing depth in core (Table 4.2, Figure 4.3).

4.5 Discussion

4.5.1 Grain size variations

Late Quaternary sea-level fluctuations have resulted in marine, lacustrine, sub-aerially exposed salt flat and lagoonal environments in the Gulf (Chivas et al., 2001; Reeves et al., 2008). The individual hydrodynamic sorting characteristic of these environments will therefore affect the grain size distribution of sediments deposited in the Gulf. Since the loss of ²³⁴U by direct-recoil is grain-size dependent (Kigoshi, 1971), (²³⁴U/²³⁸U) activity ratios may be a function of sorting in the depositional environment in addition to changes in the rate of sediment transport. Grain size distributions of the bulk sediment fraction show that the mean diameter of MD32 core sediments ranged from 3 – 81 µm (Chivas et al., 2001), representing an approximate five-fold variations in the mean grain size diameter. Here we consider changes in the (²³⁴U/²³⁸U) activity ratios and direct-recoil fractions in terms of changes in the Gulf's depositional environment.

Sediments with the smallest mean diameter were deposited in Lake Carpentaria from 15±1 ka to 45 ±2 ka and from 60±2 ka to 72 ±2 ka when the Gulf existed as a salt flat (Table 4.1). This is attributed to a high proportion of clays (Figure 4.3), which could have been due to the settling out of fine-grained sediments in low-energy environments. Despite the narrow

range of mean grain diameter deposited during the lacustrine and salt flat phases (~8 to 10 μm), the ($^{234}\text{U}/^{238}\text{U}$) were highly variable (Figure 4.4a). Therefore, ($^{234}\text{U}/^{238}\text{U}$) are not simply a function of mean grain diameter for core sediments.

The coarsest sediments were deposited during the marine and lagoon phases of the Gulf (Table 4.1), which is consistent with these being higher energy depositional environments. These core sediments also exhibited generally higher activity ratios. The exception to this trend was MD32-6d, which was deposited at 102 ± 19 ka with a mean diameter of 8 μm – similar to sediments deposited in low energy environments. Interestingly, this sample also exhibited a much lower activity ratio compared to the coarser grained marine and lagoon core sediments.

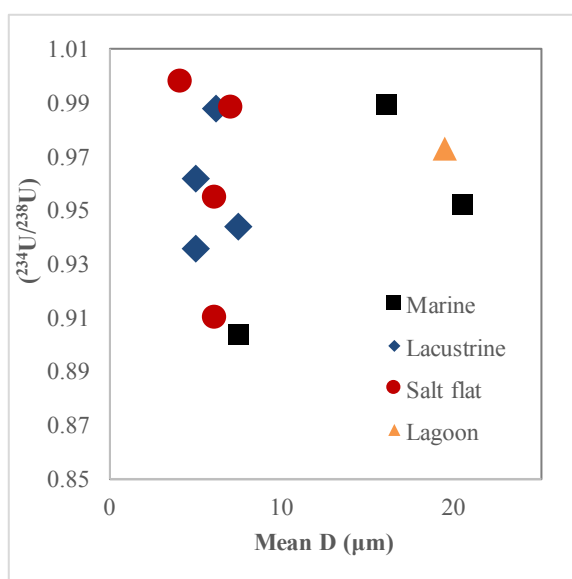


Figure 4.4 Mean diameter of MD32 core sediments as a function of the ($^{234}\text{U}/^{238}\text{U}$) activity ratio (errors not shown are within the marker size).

4.5.2 Reduced direct-recoil of ^{234}U in core sediments

The loss rate of ^{234}U in detrital sediments is controlled by their surface area properties (Kigoshi, 1971). The specific surface area and fractal dimension of sediments all decreased with increasing depth in the core (Figure 4.5). This can be explained by considering compaction processes occurring during sediment burial under pressure, which is shown by a decrease in the total pore volume of sediments with increasing depth in core (Table 4.2). Sediments are deposited with a specific surface area of $\sim 139 \text{ m}^2\text{g}^{-1}$, and this decreases by $\sim 5 \text{ m}^2\text{g}^{-1}$ per metre with increasing core depth ($R^2 = 0.673$), given as:

$$S_{BET} = 139 - 4.88x \quad (1)$$

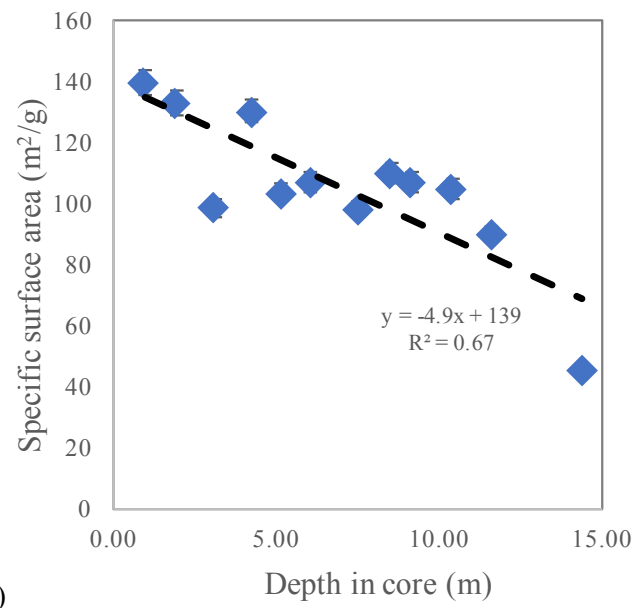
where S_{BET} is the specific surface area of sediments and x is the depth in core (in m). The relationship between fractal dimension of sediments and depth in core is given as:

$$D = 2.58 - 0.0048x \quad (2)$$

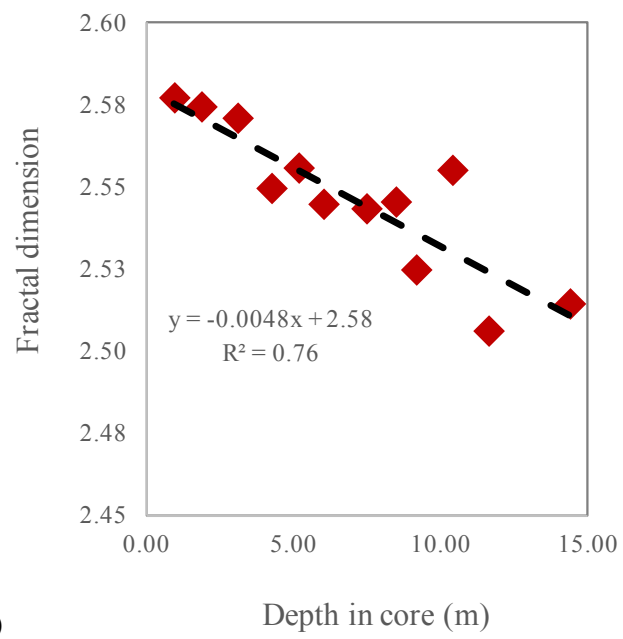
where D is the fractal dimension of sediments and x is the depth in core (in m). This suggests that compaction processes occurring during sediment burial alter the surface roughness, or self-similar, properties of weathered mineral surfaces.

Reduced porosity in consolidated sedimentary deposits may decrease the rate of ^{234}U loss by direct recoil in core sediments. This is because decreased sediment porosity should increase the implantation rate of ^{234}U into adjacent grains (Fleischer and Raabe, 1978). However, since implanted nuclides are labile and easily removed by water (Fleischer, 1980), a reduced loss of implanted ^{234}U nuclides in core sediments requires a decrease in water-rock interactions. This is possible in core MD32 considering the high proportion of clays in sediments, which are typically clayey-silt or silty-clay (Chivas et al., 2001). The low permeability of clays may therefore result in the clay-rich sediments acting as an aquitard

and limiting water flow through sediments (Neuzil, 1994). This may explain why some core sediments were close to secular equilibrium despite long sedimentary storage times, e.g. ~80 ka for MD32-6b (Table 4.1). Reduced direct-recoil may also explain why inferred comminution ages less than depositional ages have been reported (Handley et al., 2013a; Handley et al., 2013b; Li et al., 2016). Constraining comminution ages of sediments in consolidated sedimentary deposits based on their measured surface area properties is thus difficult. A better approach may be to infer comminution ages from the decrease in ($^{234}\text{U}/^{238}\text{U}$) activity ratios of core sediments with depositional age (DePaolo et al., 2006). However, this approach relies on a constant sediment provenance and uniform grain size.



a)



b)

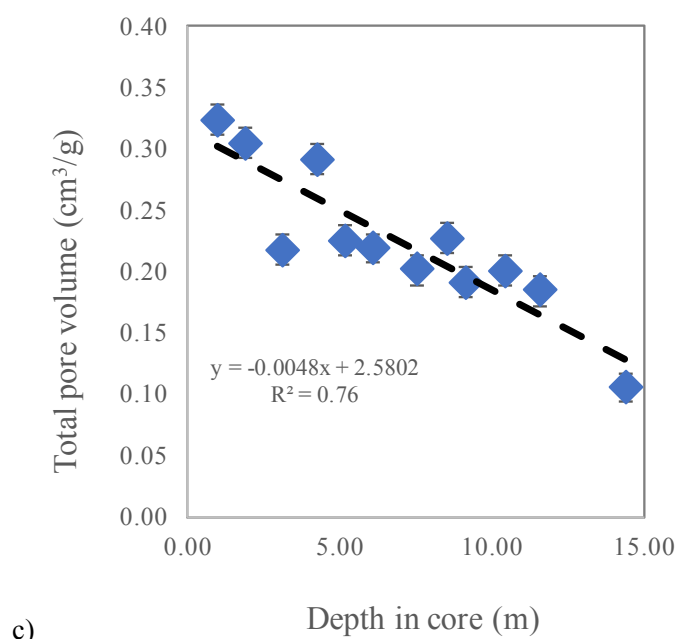


Figure 4.5a) Specific surface area, b) fractal dimension of $<63 \mu\text{m}$ sediments, and c) total pore volume as a function of depth in core MD32. Errors not shown are within the symbol size.

4.5.3 Comparison of two cores from the Gulf of Carpentaria

The ($^{234}\text{U}/^{238}\text{U}$) activity ratios of modern sediment from the upper few centimetres of cores MD32 and MD33 were significantly different (0.952 ± 0.002 vs 0.913 ± 0.003 , respectively, Table 4.6). This difference in ($^{234}\text{U}/^{238}\text{U}$) activity ratios is surprising considering that these cores are only located 40 km apart (Figure 4.1). This may be attributed to differences in mean grain sizes of core sediments from each core (Chivas et al., 2001). Both the mean grain size and maximum grain size of sediments from core MD33 are two-fold higher than MD32 (Table 4.2). Despite the large variation of grain sizes in both cores MD32 and MD33 with standard deviations of 9.7 and 25 μm , respectively (Table 4.2), this difference is significant ($p < 0.0001$, Table 4.2). This is counter-intuitive since coarser sediment grain sizes would be expected to have lower ($^{234}\text{U}/^{238}\text{U}$) (Kigoshi, 1971; DePaolo et al., 2006). This may suggest that the sediment provenance for MD32 and MD33 are distinct. Core MD33 may preferentially receive coarser-grained material due to its closer proximity (40 – 50 km) to the

eastern shoreline of the Gulf (the sediment source) compared to MD32. However, fluvial sediments from the N catchments exhibit lower ($^{234}\text{U}/^{238}\text{U}$) (Table 4.3), and MD33 core sediments would be expected to also exhibit a higher ($^{234}\text{U}/^{238}\text{U}$) (Table 4.3). Therefore, MD33 may receive sediments with a distinctly lower ($^{234}\text{U}/^{238}\text{U}$) from a source area that was not sampled in Chapter 3. This potential source could be the northern tip of the Cape York Peninsula, or the western shoreline of the Gulf (Figure 4.1).

In addition to differences in mean grain size, MD32 and MD33 also exhibit distinctive trends in sedimentation rates and ($^{234}\text{U}/^{238}\text{U}$) activity ratios. The different sedimentation rates for cores MD32 and M33 suggest that these cores record different events. For instance, sedimentation rates increased at around 45 ka in MD33, but not MD32 (Figure 4.3). This was accompanied by higher activity ratios in MD32 at 45 ± 2 ka, but not MD33 at 46 ± 2 ka. Clearly, a pulse of sediments with lower activity ratios reached MD33 but not MD32. This could be explained by different sediment transport processes from the delta to each core.

Table 4.2 Statistical summary of ($^{234}\text{U}/^{238}\text{U}$) activity ratios and mean grain size for cores MD32 and MD33

Parameter	Core	Sample size	Minimum	Maximum	Mean	Std. deviation
$(^{234}\text{U}/^{238}\text{U})$	MD32	13	0.904	1.112	0.970	0.052
	MD33	6	0.830	0.944	0.888	0.039
Grain size (μm)	MD32	300	3.0	81	9.8	9.7
	MD33	129	1.8	220	20	25

4.5.4 Comminution ages in the Gulf of Carpentaria

The ($^{234}\text{U}/^{238}\text{U}$) and surface area properties of detrital sediments were used to infer comminution ages (DePaolo et al., 2006). Preferential leaching of ^{234}U was accounted for given the ^{234}U depletion reported for source rocks in the Gulf of Carpentaria drainage basin (Chapter 3). This was accounted for in the comminution age model by considering that the leaching rates of ^{234}U and ^{238}U , given as (Dosseto and Schaller, 2016):

$$t_{comm} = -\frac{1}{\lambda_4 + \left(\frac{w_4}{w_8} - 1\right)w_8} \ln \left[\frac{\left(\frac{{}^{234}\text{U}}{{}^{238}\text{U}}\right) - \frac{(1-f_4)\lambda_4}{\lambda_4 + \left(\frac{w_4}{w_8} - 1\right)w_8}}{\left(\frac{{}^{234}\text{U}}{{}^{238}\text{U}}\right)_0 - \frac{(1-f_4)\lambda_4}{\lambda_4 + \left(\frac{w_4}{w_8} - 1\right)w_8}} \right] \quad (3)$$

where A is the measured (${}^{234}\text{U}/{}^{238}\text{U}$) activity ratio, A_0 is the initial (${}^{234}\text{U}/{}^{238}\text{U}$) activity ratio of the parent material (e.g. bedrock or grains $>63 \mu\text{m}$ in size), λ_{234} is the decay constant of ${}^{234}\text{U}$ (in a^{-1}), f_α is the direct-recoil fraction, and w_4 and w_8 are the leaching coefficients for ${}^{234}\text{U}$ and ${}^{238}\text{U}$ (in a^{-1}), respectively. The ${}^{238}\text{U}$ leaching coefficients for sediments were calculated from the average of values reported for tropical watersheds, which range from 4.4×10^{-6} to $9.9 \times 10^{-6} \text{ a}^{-1}$ (Table 4.3). The ratio of the leaching coefficients, w_{234}/w_{238} , was assumed to be 1.1 ± 0.1 , similar to values measured in laboratory and field-based studies (Dequincey et al., 2002; Vigier et al., 2005; Dosseto et al., 2006a; Andersen et al., 2009; Dosseto et al., 2014).

The direct-recoil fraction is typically estimated from measured surface area parameters. However, this approach appears invalid for sedimentary deposits in the Gulf due to the decrease in specific surface area and fractal dimension with increasing depth in core (Figure 4.5). Furthermore, the assumption that the source rocks in the Gulf drainage basin are in secular equilibrium is likely invalid due to the ${}^{234}\text{U}$ depletion measured in rocks from the catchment headwaters (Chapter 3). Uncertainties in comminution age parameters for the Gulf sediments are considered in the following sections.

Table 4.3 Reported leaching coefficients (w_{238}) for ${}^{238}\text{U}$ in tropical watersheds

Location	$w_8 \text{ (a}^{-1}\text{)}$	Reference
Amazon lowland rivers	4.4×10^{-6}	Dosseto et al. (2006a)
Amazon highland rivers	$4.0 - 6.0 \times 10^{-5}$	Dosseto et al. (2006a,b)
Deccan Traps, India	$6.9 - 9.9 \times 10^{-6}$	Vigier et al. (2005)
Puerto Rico	4.7×10^{-6}	Dosseto et al. (2014)
<i>Average</i>	<i>5.7×10^{-6}</i>	

4.5.4.1 Initial activity ratio of source rocks in the Gulf of Carpentaria drainage basin

The initial ($^{234}\text{U}/^{238}\text{U}$) activity ratio (A_0) of the parent material is typically assumed to equal one (DePaolo et al., 2006; Dosseto et al., 2010). However, rocks from the catchment headwaters of Gulf Carpentaria drainage basin exhibited $A_0 < 1$ (Chapter 3), and this assumption therefore appears to be invalid for our study area. Volcanic rocks and coarse-grained sedimentary/metamorphic rocks were more likely to be in secular equilibrium than granitic and fine-grained sedimentary rocks, such as mudstone (Chapter 3). Based on measured values for different rock types (Chapter 3), the average A_0 for the Gulf of Carpentaria drainage basin at present is estimated to be 0.975 ± 0.020 (Table 4.5). Since the northern and southern catchments are active during interglacials, the estimated average A_0 is expected to be similar to present ($A_0 = 0.975 \pm 0.020$, Table 4.5). However, the northward migration of the monsoon during glacial periods likely results in less sediment being sourced the S catchments. Therefore, the average A_0 in the Gulf during glacials will reflect the source rocks in the N catchments. By considering the proportion of rocks in the major N catchments (Archer River, Mitchell River and Staaten River), and the average ($^{234}\text{U}/^{238}\text{U}$) values for different rock types, the average A_0 during glacial periods is estimated to be 0.989 ± 0.020 (Table 4.4).

Table 4.4 Estimated initial activity ratio of source rocks in the Gulf of Carpentaria drainage basin during glacial vs interglacial periods

Source	Estimated initial ($^{234}\text{U}/^{238}\text{U}$) activity ratio
Northern and southern catchments ^a	0.975 ± 0.020
Northern catchments only ^b	0.989 ± 0.020

Initial activity ratio estimated by considering the proportion of different rock types in: ^aArcher River, Mitchell River, Staaten River, Gilbert River, Norman River, Flinders River, and Leichhardt River catchments and ^bArcher River only (Chapter 3). Average ($^{234}\text{U}/^{238}\text{U}$) values for rock types are: fine-grained sedimentary = 0.843, coarse-grained sedimentary = 1.000, metamorphic = 1.000, granitic = 0.931, volcanic = 1.000.

4.5.4.2 Direct-recoil fraction of core sediments in the Gulf of Carpentaria

The direct-recoil fraction can be calculated from the Brunauer–Emmett–Teller (BET) specific surface area, measured by N₂ gas sorption. However, the BET specific surface area is measured on the length scale of a N₂ molecule, which is an order of magnitude less than the length scale of direct recoil (ca. 30 nm, Hashimoto et al., 1985), and a correction is required (Bourdon et al., 2009). This can be achieved using the fractal dimension, which is a measure of self-similarity or surface roughness (Mandelbrot, 1983), and ranges from 2.0 (no roughness) to 3.0 (maximum roughness). The fractal direct-recoil model is given as (Bourdon et al., 2009):

$$f_{\alpha} = \frac{1}{4} S_{BET} \rho R \left[\frac{2^{D-1}}{4-D} \left(\frac{a}{R} \right)^{D-2} \right] \quad (4)$$

where S_{BET} is the specific surface area (in m² g⁻¹), ρ is the average mineral density (in g m⁻³), R is the recoil length (in m), D is the fractal dimension, and a is the diameter of the adsorbate gas (in m).

The usefulness of direct-recoil fraction estimates based on measured surface area parameters appears limited due to the decrease in specific surface area and fractal dimension with

increasing depth in core (Figure 4.5). Thus, direct-recoil fractions of core sediments were also estimated by plotting the ($^{234}\text{U}/^{238}\text{U}$) activity ratios as an exponential function of their depositional age (t_{sed}) and the ^{234}U decay rate (λ_{234}) to yield time evolution curves as straight lines (Figure 4.6). This approach assumes samples that yield linear evolution curves share the same sediment provenance. In the Gulf, these two different sediment sources are assumed to be 1) N and S catchments (similar to present), and 2) predominantly N catchments due to reduced contribution from S catchments (discussed later in Section 4.5.5). Core sediments were first divided into two groups based on whether their activity ratio was greater or less than the ($^{234}\text{U}/^{238}\text{U}$) activity ratio of modern sediment from the upper portion of MD32 (0.952 ± 0.002 , Table 4.1). There is a strong correlation ($R^2 = 0.97$) between ($^{234}\text{U}/^{238}\text{U}$) activity ratios and $\exp(-\lambda_{234}t_{\text{sed}})$ for sediments with ($^{234}\text{U}/^{238}\text{U}$) $< 0.952 \pm 0.002$ (Figure 4.6). Extrapolating this relationship to find the activity ratio at $\exp(-\lambda_{234}t_{\text{sed}}) = 1$ yields a direct-recoil fraction of 0.25. In contrast, there is no clear relationship between activity ratios and $\exp(-\lambda_{234}t_{\text{sed}})$ for core sediments with ($^{234}\text{U}/^{238}\text{U}$) $> 0.952 \pm 0.002$, which yielded activity ratios close to unity. The lack of relationship between activity ratios and $\exp(-\lambda_{234}t_{\text{sed}})$ could suggest that these sediments have different sediment provenance transport histories. This may be attributed to the variable contribution of sediments from the S catchments during glacial periods. This hypothesis is consistent with highly variable ostracod Mg/Ca, Na/Ca, Sr/Ca ratios and $\delta^{18}\text{O}$ values during the LGM, suggesting highly irregular rainfall patterns (Devriendt, 2011).

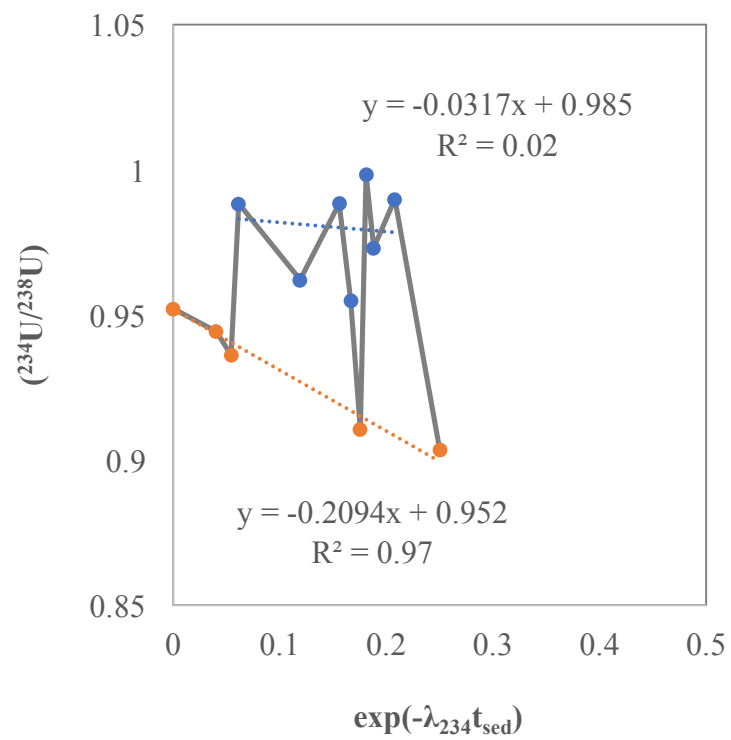


Figure 4.6 ($^{234}\text{U}/^{238}\text{U}$) as a function of the ^{234}U decay rate (in a^{-1}) and the depositional age (in ka) for the MD32 core sediments

4.5.4.3 Sediment residence times in the Gulf of Carpentaria

Comminution ages for sediments deposited during interglacials were calculated using Equation 3 (input parameters and associated uncertainties given in Table 4.5), and these ranged from 33 ± 15 to 135 ± 57 ka (Table 4.6). Sediment residence times were estimated by subtracting depositional ages from comminution ages and ranged from 33 ± 15 to 51 ± 22 ka (Table 4.6). These represent maximum estimates considering that the rate of ^{234}U loss (direct-recoil fraction) may have been higher before deposition (as discussed in Section 4.5.2). The sediment residence times during interglacials are similar considering uncertainties for comminution age parameters (Table 4.6), and yield an average of 41 ± 17 ka. This is within uncertainty of the average sediment residence time (88 ± 35 ka) for major catchments in the Gulf of Carpentaria drainage basin (Table 4.9). Since the average sediment residence time spans at least the LGM, this suggests that catchments are currently reworking material accumulated over the last glacial cycle during MIS 2-4.

Sediment residence times could not be inferred for sediments deposited during glacial periods. This is surprising considering the long sedimentary storage times of these sediments, e.g. the depositional age of MD32-6b is ~ 80 ka (Table 4.1). Comminution ages also could not be inferred for river sediments from the Archer River (Chapter 3), which is the most northerly catchment. This suggests sediment provenance shifts to the N catchments during glacial periods. Fast sediment transport rates are expected for the N catchments since they are characterised by smaller catchment areas, higher relief, and higher rainfall compared to the S catchments (Figure 4.1). Therefore, an insufficient amount of time may have elapsed since formation from the bedrock for these sediments to have lost significant amounts of ^{234}U .

The few applications of comminution dating studies to sedimentary deposits found large abrupt shifts in sediment residence times around glacial–interglacial transitions (DePaolo et

al., 2006; Dosseto et al., 2010; Li et al., 2016). Similarly in the Gulf of Carpentaria, the largest variation in residence times was found following the LGM. Such sudden changes in erosion timescales can only be explained by changes in sediment provenance. In the North Atlantic, sediment provenance oscillated between Iceland (short residence times) and continental Europe (long residence times). In the Murrumbidgee River, southeastern Australia, sediment provenance switched between younger hillslopes during glacials and reworking of older floodplain deposits during interglacials (Dosseto et al., 2010). In the East China Sea, sediment residence times decreased from 14 ka onwards (Li et al., 2016), possibly reflecting a change in sediment provenance from the Chinese mainland to Taiwan. In the Gulf of Carpentaria, changes in sediment provenance appear to be driven by the north/southward migration of the ITCZ, which controls the spatial distribution of monsoonal rainfall/discharge in the Gulf catchments. These findings imply that rather than affect global net erosion rates, Late Quaternary climate variability simply spatially reorganises the loci of erosion. This is consistent with stable silicate weathering fluxes throughout the Quaternary (Willenbring and von Blanckenburg, 2010; von Blanckenburg et al., 2014), and relatively CO₂ concentrations for the past 600 ka (Zeebe and Caldeira, 2008).

Table 4.5 Comminution age parameter uncertainties for core sediment MD32-6d

Parameter	Units	Value	1 σ relative standard deviation (%)
Decay rate of ^{234}U , λ_{234}	a^{-1}	$^{a}2.8286 \times 10^{-6} \pm 0.0028 \times 10^{-6}$	0.10
Initial ($^{234}\text{U}/^{238}\text{U}$) activity ratio, A_0 (dimensionless)	dimensionless	0.975 ± 0.02^b	2.0
Measured ($^{234}\text{U}/^{238}\text{U}$) activity ratio, A (dimensionless)	dimensionless	0.961 ± 0.014^c	1.5
Specific surface area of solid phase, S_{BET}	$\text{m}^2 \text{g}^{-1}$	16.5 ± 2.8^c	17.0
Fractal dimension of solid phase, D (dimensionless)	dimensionless	2.4 ± 0.2^c	12.0
Diameter of nitrogen, a	nm	0.37 ± 0.01	1.4
Recoil length in solid phase, R	nm	27 ± 1^d	2.5
Density of solid phase, ρ	$\text{m}^3 \text{g}^{-1}$	2.6 ± 0.1^d	2.5
Leaching coefficients for ^{238}U , w_8	in a^{-1}	$^{e}5.7 \pm 1 \times 10^{-6}$	17.5
Ratio of leaching coefficients for ^{234}U and ^{238}U , w_4/w_8	dimensionless	$^{e}1.1 \pm 0.05$	4.5
Direct-recoil fraction, f_a	dimensionless	0.25 ± 0.02	27.2 ^f
Comminution age, t_{comm}	ka	180 ± 70	42.6 ^f
Depositional age, t_{sed}	ka	$102 \pm 5^{a,b}$	4.9
Sediment residence time, t_{res}	ka	33 ± 14	42.9 ^g

^aCheng et al. (2000); ^bTable 4.4; ^cTable 4.1; ^destimated from average values in Chapter 3; ^eTable 4.3; ^f $\sqrt{\frac{\sigma_{S_{BET}}^2}{S_{BET}^2} + \frac{\sigma_{\rho}^2}{\rho^2} + 2\frac{\sigma_R^2}{R} + 3\frac{\sigma_D^2}{D}}$; ^g $\sqrt{\sigma_{t_{comminution}}^2 + \sigma_{t_{deposition}}^2}$.

Table 4.6 Sediment residence times for <63 μm sediments from core MD32 during interglacial periods in the Gulf of Carpentaria

Sample	Depositional age ^{a,b} (ka)	Comminution age ^c (ka)	Sediment residence times ^d (ka)
1	0	38 ± 16	38 ± 16
2a	15 ± 1	52 ± 16	37 ± 16
2b	20 ± 1	67 ± 20	47 ± 20
4c	68 ± 3	119 ± 50	51 ± 22
6d	102 ± 5	135 ± 57	33 ± 15
Average			41 ± 18

^aChivas et al. (2001); Reeves et al., (2008); ^ccomminution age calculated using Equation 4 and 5; and ^dCalculated by subtracting depositional age from comminution age. Uncertainty shown represents 1 σ standard deviation detailed in Table 4.5.

Table 4.7 Average sediment residence time of catchments in the Gulf of Carpentaria drainage basin (Chapter 3)

Catchment	Average sediment residence time (ka)
Archer River	<1
Mitchell River	190 ± 80
Staaten River	18 ± 8
Gilbert River	160 ± 67
Flinders River	45 ± 19
Norman River	17 ± 7
Leichhardt River	95 ± 40
<i>Weighted average^a</i>	88 ± 35

^aAverage weighted by catchment area for Archer River: 12,600 km², Mitchell River: 74,000 km², Staaten River: 25,300 km², Gilbert River: 26,600 km², Flinders River: 110,000 km², Leichhardt River: 33,000 km², Norman River: 67,500 km² (Chapter 3).

4.5.5 Variations in sediment provenance during glacial and interglacial periods

Sediment provenance of core sediments in the Gulf has likely varied over the last glacial-interglacial cycle due to the migration of the inter-tropical convergence zone (ITCZ) (Magee et al., 2004). Modern rainfall in the Gulf is mainly associated with the ITCZ, with approximately 94% of rainfall occurring during the austral summer monsoon (Reeves et al., 2008). The Gulf catchment area spans ten degrees of latitude and the increasing distance from the ITCZ results in a significant decrease in rainfall from north (N) to south (S) (Suppiah, 1992; Chivas et al., 2001). The discharge of the S catchments during the LGM was strongly reduced (Devriendt, 2011). Therefore, glacial-interglacial climate change has likely affected the relative contribution of the S and N catchments to sediment deposited in the Gulf. Here we assess potential changes in the relative contribution of N vs S catchments during the last interglacial-glacial cycle using the detrital sediment record of MD32 and MD33 core sediments. The relative contribution of the S catchments was assessed using spatial trends in (²³⁴U/²³⁸U) activity ratios of fluvial sediment from Gulf catchments (Chapter 3). Potential variations in the initial (²³⁴U/²³⁸U) activity ratios of bedrocks (parent material)

are not considered since this effect will be represented in the activity ratio of fluvial sediments.

Twenty fluvial sediments were sampled from seven major catchments across the Gulf (Chapter 3). The catchments were classified as N (Archer R., Mitchell River, Staaten R.) or S (Gilbert R., Norman R., Flinders R., and Leichhardt R.) based on their latitude (above or below 16.5°S). Sediments were mainly sampled from the eastern catchments, which are the major sediment sources to the Gulf at present (Preda and Cox, 2005). The weighted average ($^{234}\text{U}/^{238}\text{U}$) activity ratios (0.980 ± 0.003 vs 0.913 ± 0.003) and average U concentrations (6.09 ± 0.01 vs 2.52 ± 0.01 ppm) were higher for the N vs S catchments (Table 4.8).

Table 4.8 Average ($^{234}\text{U}/^{238}\text{U}$) activity ratios and U concentrations for <63 μm sediments from the northern and southern catchments draining to the Gulf

Catchment	$(^{234}\text{U}/^{238}\text{U})^a$	$[\text{U}]^{a,b}$
		(ppm)
Average northern catchments (n = 8)	0.980 ± 0.003^a	6.09 ± 0.01
Average southern catchments (n = 12)	0.913 ± 0.003^a	2.52 ± 0.01

^aBased on data from Chapter 3 (Table 3.2.1); and ^bweighted average activity ratio based on measured U concentrations.

A mass balance approach was used to predict the average ($^{234}\text{U}/^{238}\text{U}$) activity ratio of modern sediment deposited in the Gulf based on the sediment loads of the N and S catchments (Table 4.9). Sediment yields of the N and S catchments were modelled using catchment properties from Table 4.3, given as (Syvitski et al., 2003):

$$Q_s = \alpha_6 Q^{\alpha_7} R^{\alpha_8} e^{kT} \quad (5)$$

where Q is discharge (in $\text{m}^3 \text{a}^{-1}$), R is relief in (in m), T is the basin-average temperature (in °C), and Q_s is the long-term sediment load in (kg a^{-1}). The coefficients α_6 , α_7 , α_8 , and k are derived from the regression analysis of sediment load data from 36 rivers in the southern

hemisphere tropics (0 to 30°S) analysed by Syvitski et al., (2003). This model predicts the sediment load for the majority of rivers to within 20% of observed values (Syvitski et al., 2003). The predicted sediment loads and measured ($^{234}\text{U}/^{238}\text{U}$) for the N and S catchments were used in a mass balance approach to predict an average ($^{234}\text{U}/^{238}\text{U}$) activity ratio of for modern sediment deposited in the Gulf (Table 4.9).

$$r_N = \frac{Q_{SN}[U]_N}{Q_{STOT}[U]_{mix}} \quad (6)$$

where r_N (dimensionless), Q_{SN} , and $[U]_N$ are the mixing proportion (dimensionless), sediment yield (in kg/a) and U concentrations (in ppm) for the N catchments, and Q_{STOT} and $[U]_{mix}$ are the total sediment yield (in kg/a) and average U concentrations (in ppm) for the N and S catchments. The equation for modelling the ($^{234}\text{U}/^{238}\text{U}$) for modern sediment deposited in the Gulf is given as:

$$(^{234}\text{U}/^{238}\text{U})_{mix} = r_N \cdot (^{234}\text{U}/^{238}\text{U})_N + r_S \cdot (^{234}\text{U}/^{238}\text{U})_S \quad (7)$$

where r_N and r_S (dimensionless) are mixing proportions calculated using Equation 6, and $(^{234}\text{U}/^{238}\text{U})_N$ and $(^{234}\text{U}/^{238}\text{U})_S$ are the average activity ratios of the N and S catchments (Figure 4.8). The predicted ($^{234}\text{U}/^{238}\text{U}$) for modern sediment deposited in the Gulf was 0.962 ± 0.008 , which is within analytical error of the measured activity ratio of 0.952 ± 0.002 for modern sediment from the upper portion of MD32 (Table 4.1). Uncertainty in sediment loads were considered by allowing the predicted sediment load for the N or S catchments to vary by $\pm 20\%$, which yields a maximum uncertainty of ± 0.004 . Co-variations in discharge for the N and S catchments have no effect on the mass balance model. The total uncertainty in the predicted ($^{234}\text{U}/^{238}\text{U}$) (± 0.008) was estimated by combining individual uncertainties for the predicted sediment loads and measured activity ratios. The predicted ($^{234}\text{U}/^{238}\text{U}$) is significantly higher than the measured activity ratio of modern sediments from MD33 (0.913 ± 0.003 , Table 4.1). Therefore, MD32 is considered more representative of large-scale

processes operating in the Gulf catchments, or at least the major catchments studied in Chapter 3. This may be because MD32 is located closer to the centre of the Gulf, whereas MD33 is located 40 km closer to the shoreline (sediment source) (Figure 4.1); other potential explanations for the difference in activity ratios measured for cores MD32 and MD33 are discussed in Section 4.5.3. In addition, MD32 provides the longest and best preserved sedimentary record of cores collected in the Gulf (Chivas et al., 2001; Reeves et al., 2008).

Table 4.9 Sediment yield and input parameters, and mass balance mixing factors

Catchment	Catchment area (km ²) ^a	Average discharge (m ³ /a) ^b	Average relief (m) ^a	Sediment yield (kg/a) ^c	Mixing factor ^d	Average (²³⁴ U/ ²³⁸ U) activity ratio ^a
Northern	146,000	5.07 x10 ¹⁰	958	1.18 x10 ⁷	0.75	0.980 ± 0.004 ^a
Southern	450,000	2.52 x10 ¹⁰	839	7.56 x10 ⁶	0.25	0.913 ± 0.004 ^a
<i>Average</i>	<i>596,000</i>	<i>75,900</i>	<i>898</i>	<i>2,190</i>	-	<i>0.962 ± 0.008^e</i>

^abased on data from Chapter 3 (Table 3.2.1); ^bCendon et al., 2004; ^cSediment yield model for southern hemisphere tropical (<30° S) catchments (Syvitski et al., 2003); ^dMixing factors calculated using Equation 6; ^eTotal uncertainty estimated by considering both ±20% variation in predicted sediment loads and 2σ standard error uncertainty in measured activity ratios.

The effect of varying sediment provenance on the (²³⁴U/²³⁸U) activity ratios of sediments deposited in the Gulf was modelled by assuming that sediment yield remains constant for the N catchments and was variable for the S catchments. This assumption is based on trace element ratios in ostracods from MD32 that indicate water chemistry in Lake Carpentaria varied as result of changes in the discharge of the S catchments (Devriendt, 2011). By extension, it is assumed that changes in water chemistry in the Gulf are reflected in the sediment load. Sediment yields for the S catchments were calculated for different discharges, ranging from 10 to 400% of the modern discharge (Table 4.10). These sediments yields were then combined with (²³⁴U/²³⁸U) from the N and S catchments (Table 4.9) in a mass balance approach to calculate the average (²³⁴U/²³⁸U) in the Gulf (Table 4.10). The modelled (²³⁴U/²³⁸U) are given in Figure 4.7 as a function of discharge for the S catchments relative to modern discharge, which is inferred to represent the relative palaeodischarge of

the S catchments. Logarithmic regression ($R^2 = 0.982$) was used to relate the relative discharge of the S catchments to the ($^{234}\text{U}/^{238}\text{U}$) activity ratios of sediments deposited in the Gulf (Figure 4.7), given as:

$$(^{234}\text{U}/^{238}\text{U}) = 0.953 - 0.009 \ln(x), \quad x > 0 \quad (6)$$

where x represents the relative discharge of the S catchments relative to present and this is valid for the range $x > 0$. The relative palaeodischarge of the S catchments were then estimated from the ($^{234}\text{U}/^{238}\text{U}$) activity ratios of leached MD32 core sediments using Equation 6. Since ^{234}U is lost by direct recoil during sedimentary storage (see Section 4.5.4.2), the ($^{234}\text{U}/^{238}\text{U}$) of sediments at a given depth in the core will be lower than at the time of deposition. The ($^{234}\text{U}/^{238}\text{U}$) at the time of deposition was estimated using Equation 3, the sample depositional age as t , and the direct-recoil fractions constrained in Figure 4.6.

The estimated relative palaeodischarge of the S catchments over the past 120 ka ranged from 0.01 to 1 (Figure 4.8). Only order of magnitude changes in relative palaeodischarge were considered due to large uncertainty in palaeodischarge estimates. The estimated relative palaeodischarge of the S catchments was similar to modern at 15 ± 1 and 20 ± 1 ka, an order of magnitude lower at 101 ± 19 and 68 ± 4 ka, and two orders of magnitude lower at 22 ± 2 , 45 ± 2 , 60 ± 2 , 65 ± 2 , 71 ± 2 , 74 ± 3 , and 83 ± 3 ka (Table 4.1). These palaeodischarge interpretations are considered in terms of existing palaeoclimatic records in northern Australia in the following discussion.

Table 4.10 Predicted ($^{234}\text{U}/^{238}\text{U}$) in the Gulf as a function of the discharge of the northern (N) and southern (S) catchments relative to present

Relative discharge of S catchments	Discharge (N) (m^3/a)	Discharge (S) (m^3/a)	Sediment load ^a (N) (kt/a)	Sediment load ^a (S) (kt/a)	r^b (N)	r^b (S)	$(^{234}\text{U}/^{238}\text{U})^{c,d}$
4.00	5.07×10^{10}	1.01×10^{11}	1.18×10^7	1.86×10^7	0.48	0.52	0.945 ± 0.008^e
1.50	5.07×10^{10}	3.70×10^{10}	1.18×10^7	9.85×10^6	0.67	0.33	0.958 ± 0.008^e
1.00 ^c	5.07×10^{10}	2.52×10^{10}	1.18×10^7	7.56×10^6	0.75	0.25	0.963 ± 0.008^e
0.80	5.07×10^{10}	2.02×10^{10}	1.18×10^7	6.54×10^6	0.79	0.21	0.966 ± 0.008^e
0.60	5.07×10^{10}	1.51×10^{10}	$1.18\text{E}+07$	5.43×10^6	0.84	0.16	0.970 ± 0.008^e
0.50	5.07×10^{10}	1.26×10^{10}	$1.18\text{E}+07$	4.82×10^6	0.87	0.13	0.972 ± 0.008^e
0.25	5.07×10^{10}	6.30×10^9	$1.18\text{E}+07$	3.07×10^6	0.97	0.03	0.979 ± 0.008^e
0.10	5.07×10^{10}	2.52×10^9	$1.18\text{E}+07$	1.69×10^6	1.00	0.00	$0.985\text{g} \pm 0.008^e$

^aSediment yield model for southern hemisphere tropical (<30° S) catchments using parameters described in Table 4.9 (Syvitski et al., 2003); ^bMixing factors determined from sediment load of N and S catchments defined as $r_a = r_a/(r_a + r_b)$; ^cCalculated using mixing factors and average ($^{234}\text{U}/^{238}\text{U}$) of N and S catchments (Table 4.8); ^dTotal uncertainty estimated by considering both $\pm 20\%$ variation in predicted sediment loads and 2σ standard error uncertainty in measured activity ratios; ^eCendon et al., 2004.

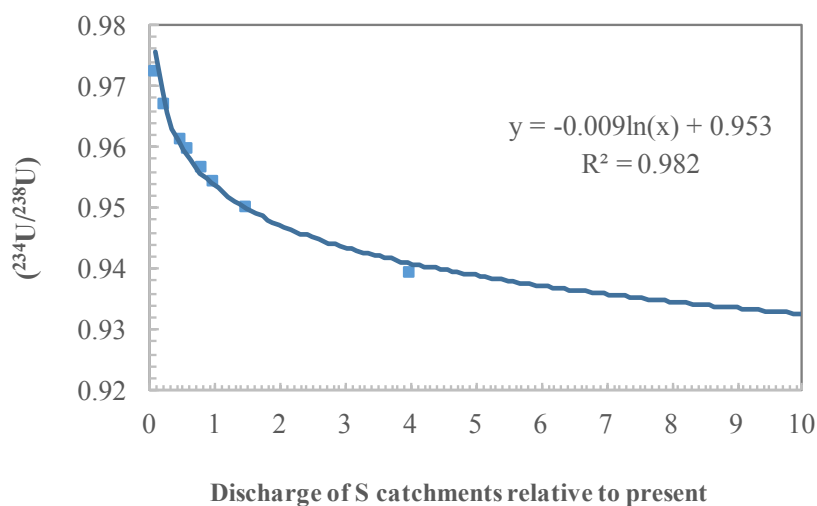


Figure 4.7 Modelled ($^{234}\text{U}/^{238}\text{U}$) activity ratios of sediments deposited in the Gulf as a function of the relative contribution of the south (S) catchments

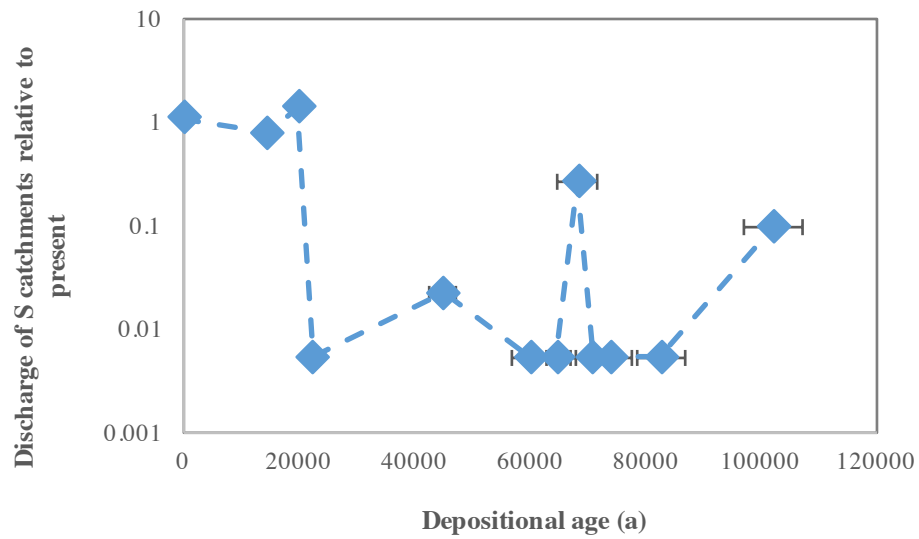


Figure 4.8 Predicted discharge of the southern (S) catchments relative to the modern discharge based on the ($^{234}\text{U}/^{238}\text{U}$) activity ratios of sediments deposited in MD32 and Equation 6. Only order of magnitude changes in relative palaeodischarge are considered due to large uncertainty in palaeodischarge estimates.

The relative palaeodischarge of the S catchments at 101 ± 19 ka is estimated to have been one order of magnitude less than at present, but an order of magnitude higher than the majority of MIS 2-4 (Figure 4.8). Fluvial activity during MIS-5d is indicated by alluvial deposits in the Gilbert River, which drains to the southern shore of the Gulf (Figure 4.1A) (Nanson et al., 2005). In addition, continuous filling of Lake Eyre, which lies to the south of the Gulf's drainage divide (Figure 4.1C), indicates that monsoonal rainfall extended to the currently arid Australian interior during MIS 5c (Magee et al., 2004). The lower palaeodischarge of the S catchments during MIS 5c relative to present may be due to sea-level being around -20 m bpsl (Lambeck and Chappell, 2001; Reeves et al., 2008), increasing the distance between the S catchments and the warm tropical seas (rainfall source) (De Deckker et al., 2003).

Reduced relative palaeodischarge of the S catchments inferred at 71 ± 2 , 74 ± 3 , and 83 ± 3 ka is consistent with the cessation of alluvial deposition in the Gilbert River from 85 to 65 ka (Nanson et al., 2005). In addition, Lake Eyre shallowed from 100 ka onwards and eventually dried at 75 – 70 ka, indicating the onset of aridification in the Australian interior (Magee et

al., 2004). These arid conditions likely resulted in low palaeodischarge of the S catchments during MIS 4.

A lower ($^{234}\text{U}/^{238}\text{U}$) activity ratio was then recorded at 68 ± 2 ka during MIS 4 and followed by higher activity ratios at 65 ± 2 and 60 ± 2 ka, suggesting a brief increase in the relative palaeodischarge of the S catchments at 68 ± 2 ka. The palaeoclimate in northern and central Australia during MIS 4 is poorly constrained, but appears to have been highly variable (Hesse et al., 2004). There is also evidence for a variable MIS 4 climate in the Gulf, which underwent periods of sub-aerially exposure (Reeves et al., 2008). Gypsum and carbonate layers in MD32 indicate repeated cycles of inundation and evaporation, which are likely due to cycles of freshwater input (Playà et al., 2007).

Sediment deposited at 45 ± 2 ka during MIS 3 exhibited a higher ($^{234}\text{U}/^{238}\text{U}$) activity ratio, indicating decreased palaeodischarge in the S catchments. Falling sea-level during MIS 3 resulted in a transition from estuarine conditions in the Gulf to the formation of a brackish waterbody perched above sea level known as *Lake Carpentaria* (Chivas et al., 2001; Devriendt, 2011; Reeves et al., 2008). There is widespread evidence for major hydrological shift towards arid conditions across Australia during MIS 3, e.g the drying out of Lake Eyre at 48 ± 2 ka (Cohen et al., 2015). This arid period also coincides with megafauna extinction in Lake Eyre (Miller et al., 2005; Miller et al., 1999), suggesting a major ecological change.

A high ($^{234}\text{U}/^{238}\text{U}$) activity ratio was recorded during MIS2 at 22 ± 2 ka, suggesting that the palaeodischarge of the S catchments remained low throughout MIS 2 and at the Last Glacial Maximum (LGM). There is widespread evidence for reduced rainfall during the MIS 2 and the LGM in northern Australia due to lower sea levels exposing the continental shelf (De Deckker et al., 2003; Yokoyama et al., 2001), and 1 – 3 °C cooler sea-surface temperatures (Reeves et al., 2013).

Lower ($^{234}\text{U}/^{238}\text{U}$) activity ratio recorded at 20 ± 1 ka indicates that the palaeodischarge of SW catchments increased by this time. Increased water levels in Lake Carpentaria suggest that a shift to wetter conditions in the Gulf by 19 ka (Reeves et al., 2008). Post-LGM alluvial deposits in the Gilbert River suggest that wetter conditions returned to the S catchments in the Gulf (Nanson et al., 2005). This hydrological shift could have been initiated by summer insolation, which was at a maximum in the Southern Hemisphere at 20 ka and could have increased monsoonal rainfall in northern Australia before widespread deglaciation (Tachikawa et al., 2009). Lower ($^{234}\text{U}/^{238}\text{U}$) activity ratio were also recorded at 15 ± 1 and 14 ± 1 ka in MD32 and MD33, respectively. At this time, Lake Carpentaria was freshwater and had expanded to a surface area of almost 200,000 km² (Reeves et al. 2008), suggesting the establishment of significantly wetter conditions post-LGM. This is consistent with flood deposits from northwestern Australia at 14 ka, suggesting that the monsoon was stronger than at present (Wyrwoll and Miller, 2001). In northeastern Australia, *Eucalyptus* woodland was not re-established until 17 ka in Lake Euramoo (Haberle, 2005), and 13 ka in Lynch's Crater (Kershaw et al., 2007b; Turney et al., 2004).

4.6 Conclusions and summary

The ($^{234}\text{U}/^{238}\text{U}$) and surface area properties of fine-grained detrital sediments from the Gulf of Carpentaria were measured to infer comminution ages and sediment residence times. The ($^{234}\text{U}/^{238}\text{U}$) of fine-grained detrital sediments from the Gulf of Carpentaria were low during MIS 5 and then increased during the MIS 5/4 transition, remaining high until MIS 2. Lower ($^{234}\text{U}/^{238}\text{U}$) were then recorded following the LGM from around 20 ka to present. Sediments deposited during glacial periods were close to secular equilibrium, despite sedimentary storage times of ~80 ka. This was attributed to reduced direct recoil because sediment porosity was inversely correlated with increasing depth in core. This may decrease the amount of ^{234}U nuclides lost by direct recoil to the surrounding medium, which could be instead implanted into adjacent grains. Moreover, this could explain the phenomenon of

“negative” sediment residence times reported elsewhere where inferred comminution ages are less than the depositional age.

Despite the range of depositional environment in the Gulf throughout the last glacial-interglacial cycle (open marine to lacustrine), variations in ($^{234}\text{U}/^{238}\text{U}$) and sediment residence times were not simply a function of grain size and/or the depositional palaeoenvironment. Another explanation for the variations in activity ratios is a change in sediment provenance between the N and S catchments due to the migration of the monsoon/ITCZ. This hypothesis is based on higher weighted average activity ratios of the N vs S catchments in the Gulf of Carpentaria drainage basin. Lower ($^{234}\text{U}/^{238}\text{U}$) activity ratios are inferred to represent sediment being sourced from both the N and S catchments, whereas higher ($^{234}\text{U}/^{238}\text{U}$) activity ratios are inferred to represent a decrease in the relative contribution of the S catchments. Based on the ($^{234}\text{U}/^{238}\text{U}$) of core sediments, the relative palaeodischarge of the S catchments is estimated to have varied by three orders of magnitude over the past 120 ka (Figure 4.8). The lowest relative palaeodischarge of the S catchments is estimated during glacial periods, which may have been 1/100th of the present discharge.

The average residence time for sediments from interglacial periods inferred by comminution dating was 41 ± 18 ka, which is similar to the average sediment residence time of catchments draining to the Gulf (88 ± 37 ka). This suggests that sediment transport processes during interglacials is dominated by the reworking of sediment accumulated over the last glacial cycle. Since the average sediment residence time is much longer than the timescale of Late Quaternary climate change (<20 ka), erosion and sediment transport processes during interglacial periods do not appear to be in steady state. In contrast, the activity ratios for sediments from glacial periods were close to secular equilibrium, suggesting that an insufficient amount of time elapsed between the formation of fine-grained sediment and deposition, i.e. rapid sediment transport. This is similar to river sediments from small N

catchments, which were also close to secular equilibrium, and is attributed to rapid sediment transport in small, wet catchments. Therefore, it is suggested that that sediment deposited in the Gulf during glacial periods is mainly sourced from the N catchments. In the Gulf of Carpentaria, it appears that Late Quaternary climatic variations rearrange the spatial distribution of discharge and the modern landscape is dominated by the reworking of sediment accumulated over the last glacial-interglacial climate change. In the Gulf of Carpentaria, changes in sediment provenance appear to be driven by the north/southward migration of the ITCZ, which controls the spatial distribution of monsoonal rainfall/discharge in the Gulf catchments. Other applications of comminution dating to sedimentary deposits also find that Quaternary glacial cycles mainly affect sediment provenance. Thus, Late Quaternary climate variability may simply spatially reorganise the erosion loci with no net increase in erosion rates. This is consistent with stable silicate weathering fluxes and atmospheric CO₂ concentrations throughout the Quaternary.

Acknowledgements

Laurent Devriendt is thanked for helpful discussions about the Gulf of Carpentaria. Monika Markowska is thanked for discussions with preparation of the manuscript. This study was supported by an Australian Research Council (ARC) Discovery grant (DP0990447), Future Fellowship (FT0990447) to AD and a University of Wollongong postgraduate scholarship award to ANM.

References

- Allen, P.A. (2008) From landscapes into geological history. *Nature* 451, 274-276.
- Anderson, S. P., Drever, J. I., & Humphrey, N. F. (1997). Chemical weathering in glacial environments. *Geology*, 25(5), 399-402.
- Blake, D.H. (1987) Geology of the Mount Isa Inlier and environments, Queensland and Northern Territory. Bureau of Mineral Resources, Geology and Geophysics, Australia, Bulletin 225.
- Bourdon, B., Bureau, S., Andersen, M.B., Pili, E. and Hubert, A. (2009) Weathering rates from top to bottom in a carbonate environment. *Chemical Geology* 258, 275-287.
- Bowler, J.M., Wyrwoll, K.-H. and Lu, Y. (2001) Variations of the northwest Australian summer monsoon over the last 300,000 years: the paleohydrological record of the Gregory (Mulan) Lakes System. *Quaternary International* 83, 63-80.
- Brooks, A.P., Shellberg, J.G., Knight, J. and Spencer, J. (2009) Alluvial gully erosion: an example from the Mitchell fluvial megafan, Queensland, Australia. *Earth Surface Processes and Landforms* 34, 1951-1969.
- Bull, W.B. (1991) Geomorphic responses to climatic change.
- Caitcheon, G.G., Olley, J.M., Pantus, F., Hancock, G. and Leslie, C. (2012) The dominant erosion processes supplying fine sediment to three major rivers in tropical Australia, the Daly (NT), Mitchell (Qld) and Flinders (Qld) Rivers. *Geomorphology* 151, 188-195.
- Cendón, D.I., Chivas, A.R. and García, A., 2004. Chemistry of the rivers in the Gulf of Carpentaria drainage division and possible correlations with the sedimentary record during

lake phases. 17th Australian Geological Convention. Dynamic Earth: Past, Present and Future. Hobart, Australia, 73, 228.

Cheng, H., Edwards, R.L., Hoff, J., Gallup, C.D., Richards, D.A. and Asmerom, Y. (2000) The half-lives of uranium-234 and thorium-230. *Chemical Geology* 169, 17-33.

Chivas, A.R., Garcia, A., van der Kaars, S., Couapel, M.J.J., Holt, S., Reeves, J.M., Wheeler, D.J., Switzer, A.D., Murray-Wallace, C.V., Benerjee, D., Price, D.M., Wang, S.X., Pearson, G., Edgar, N.T., Beaufort, L., De Deckker, P., Lawson, E. and Cecil, C.B. (2001) Sea-level and environmental changes since the last interglacial in the Gulf of Carpentaria, Australia: An overview. *Quaternary International* 82-85, 19-46.

Church, J. and Forbes, A. (1983) Circulation in the Gulf of Carpentaria. I. Direct observations of currents in the south-east corner of the Gulf of Carpentaria. *Marine and Freshwater Research* 34, 1-10.

Cohen, T. J., Jansen, J. D., Gliganic, L. A., Larsen, J. R., Nanson, G. C., May, J. H., and Price, D. M. (2015). Hydrological transformation coincided with megafaunal extinction in central Australia. *Geology*, 43, 195-198.

De Deckker, P., Corrège, T. and Head, J. (1991) Late Pleistocene record of cyclic eolian activity from tropical Australia suggesting the Younger Dryas is not an unusual climatic event. *Geology* 19, 602-605.

De Deckker, P., Tapper, N. and van Der Kaars, S. (2002) The status of the Indo-Pacific Warm Pool and adjacent land at the Last Glacial Maximum. *Global and Planetary Change* 35, 25-35.

DeCelles, P. and Cavazza, W. (1999) A comparison of fluvial megafans in the Cordilleran (Upper Cretaceous) and modern Himalayan foreland basin systems. *Geological Society of America Bulletin* 111, 1315-1334.

DePaolo, D.J., Maher, K., Christensen, J.N. and McManus, J. (2006) Sediment transport time measured with U-series isotopes: Results from ODP North Atlantic drift site 984. *Earth and Planetary Science Letters* 248, 394-410.

Devriendt, L.S.J. (2011) Late quaternary environment of Palaeolake Carpentaria inferred from the chemistry of ostracod valves. University of Wollongong, Wollongong.

Dietrich, W.E. and Perron, J.T. (2006) The search for a topographic signature of life. *Nature* 439, 411-418.

DNRM (2014) Water monitoring portal State of Queensland (Department of Natural Resources and Mines).

Dosseto, A., Hesse, P.P., Maher, K., Fryirs, K. and Turner, S. (2010) Climatic and vegetation control on sediment dynamics during the last glacial cycle. *Geology* 38, 395-398.

Dosseto, A., & Schaller, M. (2016). The erosion response to Quaternary climate change quantified using uranium isotopes and in situ-produced cosmogenic nuclides. *Earth-Science Reviews*, 155, 60-81.

Droxler, A.W. and Schlager, W. (1985) Glacial versus interglacial sedimentation rates and turbidite frequency in the Bahamas. *Geology* 13, 799-802.

Field, C., Barros, V., Dokken, D., Mach, K., Mastrandrea, M., Bilir, T., Chatterjee, M., Ebi, K., Estrada, Y. and Genova, R. (2014) IPCC, 2014: Climate Change 2014: Impacts, Adaptation, and Vulnerability. Part A: Global and Sectoral Aspects. Contribution of

Working Group II to the Fifth Assessment Report of the Intergovernmental Panel on Climate Change. Cambridge University Press, Cambridge, United Kingdom and New York, NY, USA.

Foster, G. L., & Vance, D. (2006). Negligible glacial–interglacial variation in continental chemical weathering rates. *Nature* 444, 918-921.

Gabet, E.J., Reichman, O. and Seabloom, E.W. (2003) The effects of bioturbation on soil processes and sediment transport. *Annual Review of Earth and Planetary Sciences* 31, 249-273.

Granger, D.E., Kirchner, J.W. and Finkel, R. (1996) Spatially averaged long-term erosion rates measured from in situ-produced cosmogenic nuclides in alluvial sediment. *The Journal of Geology* 104, 249-257.

Haberle, S.G. (2005) A 23,000-yr pollen record from Lake Euramoo, Wet Tropics of NE Queensland, Australia. *Quaternary Research* 64, 343-356.

Hancock, G., Evans, K., McDonnell, J. and Hopp, L. (2012) Ecohydrological controls on soil erosion and landscape evolution. *Ecohydrology* 5, 478-490.

Handley, H.K., Turner, S., Afonso, J.C., Dosseto, A. and Cohen, T. (2013) Sediment residence times constrained by uranium-series isotopes: A critical appraisal of the comminution approach. *Geochimica et Cosmochimica Acta* 103, 245-262.

Hashimoto, T., Aoyagi, Y., Kudo, H. and Sotobayashi, T. (1985) Range calculation of alpha-recoil atoms in some minerals using LSS-theory. *Journal of Radioanalytical and Nuclear Chemistry Articles* 90, 415-438.

Kershaw, A., Van Der Kaars, S. and Flenley, J. (2007a) The Quaternary history of far eastern rainforests, *Tropical Rainforest Responses to Climatic Change*. Springer, pp. 77-115.

Kershaw, A.P., Bretherton, S.C. and van der Kaars, S. (2007b) A complete pollen record of the last 230 ka from Lynch's Crater, north-eastern Australia. *Palaeogeography, Palaeoclimatology, Palaeoecology* 251, 23-45.

Kigoshi, K. (1971) Alpha-recoil thorium-234: Dissolution into water and the uranium-234/uranium-238 disequilibrium in nature. *Science* 173, 47-48.

Koppes, M.N. and Montgomery, D.R. (2009) The relative efficacy of fluvial and glacial erosion over modern to orogenic timescales. *Nature Geoscience* 2, 644-647.

Kump, L. R., Brantley, S. L., & Arthur, M. A. (2000). Chemical weathering, atmospheric CO₂, and climate. *Annual Review of Earth and Planetary Sciences*, 28, 611-667.

Lambeck, K. and Chappell, J. (2001) Sea level change through the last glacial cycle. *Science* 292, 679-686.

Landström, O., Tullborg, E.-L. and Eriksson, G. (2001) Effect of glacial/post-glacial weathering compared with hydrothermal alteration - implications for matrix diffusion. . Swedish Nuclear Fuel and Waste Management Co.

Lee, V.E. (2009) Radiogenic Isotope Geochemistry and the Evolution of the Earth's Surface and Interior. PhD Thesis at the University of California, Berkeley.

Leier, A.L., DeCelles, P.G. and Pelletier, J.D. (2005) Mountains, monsoons, and megafans. *Geology* 33, 289-292.

Li, C., Francois, R., Yang, S., Barling, J., Darfeuil, S., Luo, Y. and Weis, D. (2016) Constraining the transport time of lithogenic sediments to the Okinawa Trough (East China Sea). *Chemical Geology*.

Magee, J.W., Miller, G.H., Spooner, N.A. and Questiaux, D. (2004) Continuous 150 ky monsoon record from Lake Eyre, Australia: insolation-forcing implications and unexpected Holocene failure. *Geology* 32, 885-888.

Malmon, D.V., Dunne, T. and Reneau, S.L. (2003) Stochastic theory of particle trajectories through alluvial valley floors. *The Journal of Geology* 111, 525-542.

Mandelbrot, B.B. (1983) *The fractal geometry of nature*. Macmillan.

Martin, A.N., Dosseto, A., May, J.-H., Jansen, J., Kinsley, L.P.J. and Chivas, A.R. (2016 in prep.) Uranium comminution dating in slowly-eroding northern Australian.

Mayewski, P.A., Rohling, E.E., Curt Stager, J., Karlén, W., Maasch, K.A., David Meeker, L., Meyerson, E.A., Gasse, F., van Kreveland, S., Holmgren, K., Lee-Thorp, J., Rosqvist, G., Rack, F., Staubwasser, M., Schneider, R.R. and Steig, E.J. (2004) Holocene climate variability. *Quaternary Research* 62, 243-255.

Miller, G. H., Magee, J. W., Johnson, B. J., Fogel, M. L., Spooner, N. A., McCulloch, M. T., and Ayliffe, L. K. (1999). Pleistocene extinction of *Genyornis newtoni*: human impact on Australian megafauna. *Science*, 283, 205-208.

Milliman, J.D. and Syvitski, J.P.M. (1992) Geomorphic/tectonic control of sediment discharge to the ocean: the importance of small mountainous rivers. *The Journal of Geology* 100, 525-544.

Muller, J., McManus, J.F., Oppo, D.W. and Francois, R. (2012) Strengthening of the Northeast Monsoon over the Flores Sea, Indonesia, at the time of Heinrich event 1. *Geology* 40, 635-638.

Nanson, G.C., Jones, B.G., Price, D.M. and Pietsch, T.J. (2005) Rivers turned to rock: Late Quaternary alluvial induration influencing the behaviour and morphology of an anabranching river in the Australian monsoon tropics. *Geomorphology* 70, 398-420.

Nanson, G.C., Price, D.M., Jones, B.G., Maroulis, J.C., Coleman, M., Bowman, H., Cohen, T.J., Pietsch, T.J. and Larsen, J.R. (2008) Alluvial evidence for major climate and flow regime changes during the middle and late Quaternary in eastern central Australia. *Geomorphology* 101, 109-129.

Nanson, G.C., Price, D.M. and Short, S.A. (1992) Wetting and drying of Australia over the past 300 ka. *Geology* 20, 791-794.

Nanson, G.C., Price, D.M., Short, S.A., Young, R.W. and Jones, B.G. (1991) Comparative uranium-thorium and thermoluminescence dating of weathered Quaternary alluvium in the tropics of northern Australia. *Quaternary Research* 35, 347-366.

Nanson, R.A., Vakarelov, B.K., Ainsworth, R.B., Williams, F.M. and Price, D.M. (2013). Evolution of a Holocene, mixed-process, forced regressive shoreline: the Mitchell River delta, Queensland, Australia. *Marine Geology* 339, 22-43.

Neimark, A. (1990) Thermodynamic method for calculating surface fractal. *JETP Lett* 51.

New Brunswick Laboratory (2008a). Certificate of Analysis CRM U010. U.S. Department of Energy.

New Brunswick Laboratory (2008b). Certificate of Analysis CRM U005-A. U.S. Department of Energy.

Nott, J. (2006) Tropical cyclones and the evolution of the sedimentary coast of northern Australia. *Journal of Coastal Research*, 49-62.

Nott, J., Thomas, M. and Price, D. (2001) Alluvial fans, landslides and Late Quaternary climatic change in the wet tropics of northeast Queensland. *Australian Journal of Earth Sciences* 48, 875-882.

Playà, E., Cendón, D.I., Travé, A., Chivas, A.R. and García, A. (2007) Non-marine evaporites with both inherited marine and continental signatures: The Gulf of Carpentaria, Australia, at ~ 70 ka. *Sedimentary Geology* 201, 267-285.

Rawlings, D. (1999) Stratigraphic resolution of a multiphase intracratonic basin system: the McArthur Basin, northern Australia. *Australian Journal of Earth Sciences* 46, 703-723.

Raymo, M. E., Ruddiman, W. F., & Froelich, P. N. (1988). Influence of late Cenozoic mountain building on ocean geochemical cycles. *Geology* 16, 649-653.

Reeves, J.M., Chivas, A.R., García, A., Holt, S., Couapel, M.J.J., Jones, B.G., Cendón, D.I. and Fink, D. (2008) The sedimentary record of palaeoenvironments and sea-level change in the Gulf of Carpentaria, Australia, through the last glacial cycle. *Quaternary International* 183, 3-22.

Riebe, C.S., Kirchner, J.W., Granger, D.E. and Finkel, R.C. (2001) Minimal climatic control on erosion rates in the Sierra Nevada, California. *Geology* 29, 447-450.

Roberts, R. G., Flannery, T. F., Ayliffe, L. K., Yoshida, H., Olley, J. M., Prideaux, G. J., and Smith, B. L. (2001). New ages for the last Australian megafauna: continent-wide extinction about 46,000 years ago. *Science*, 292, 1888-1892.

Rose, C.W., Shellberg, J.G. and Brooks, A.P. (2015) Modelling suspended sediment concentration and load in a transport-limited alluvial gully in northern Queensland, Australia. *Earth Surface Processes and Landforms* 40, 1291-1303..

Rosholt, J.N. (1983) Isotopic composition of uranium and thorium in crystalline rocks. *Journal of Geophysical Research* 88, 7315-7330.

Rousseau, D.D., Schevin, P., Duzer, D., Cambon, G., Ferrier, J., Jolly, D. and Poulsen, U., (2006). New evidence of long distance pollen transport to southern Greenland in late spring. *Review of Palaeobotany and Palynology*, 141, 277-286.

Ruddiman, W. F., Raymo, M. E., Prell, W. L., & Kutzbach, J. E. (1997). The uplift-climate connection: a synthesis (pp. 471-515). Plenum Press, New York.

Schumm, S. (1968) Speculations concerning paleohydrologic controls of terrestrial sedimentation. *Geological Society of America Bulletin* 79, 1573-1588.

Schneider, T., Bischoff, T. and Haug, G.H. (2014). Migrations and dynamics of the intertropical convergence zone. *Nature* 513, 45-53.

Shellberg, J.G., Brooks, A.P. and Rose, C.W. (2013) Sediment production and yield from an alluvial gully in northern Queensland, Australia. *Earth Surface Processes and Landforms* 38, 1765-1778.

Shulmeister, J. (1992) A Holocene pollen record from lowland tropical Australia. *The Holocene* 2, 107-116.

Stallard, R. F. (1985). River chemistry, geology, geomorphology, and soils in the Amazon and Orinoco basins. In *The chemistry of weathering* (pp. 293-316). Springer Netherlands.

Tachikawa, K., Vidal, L., Sonzogni, C. and Bard, E. (2009) Glacial/interglacial sea surface temperature changes in the Southwest Pacific ocean over the past 360 ka. *Quaternary Science Reviews* 28, 1160-1170.

Thomas, M.F., Nott, J., Murray, A.S. and Price, D.M. (2007) Fluvial response to late Quaternary climate change in NE Queensland, Australia. *Palaeogeography, Palaeoclimatology, Palaeoecology* 251, 119-136.

Torgersen, T., Hutchinson, M.F., Searle, D.E. and Nix, H.A. (1983) General bathymetry of the Gulf of Carpentaria and the Quaternary physiography of Lake Carpentaria. *Palaeogeography, Palaeoclimatology, Palaeoecology* 41, 207-225.

Turney, C.S.M., Kershaw, A.P., Clemens, S.C., Branch, N., Moss, P.T. and Keith Fifield, L. (2004) Millennial and orbital variations of El Nino/Southern Oscillation and high-latitude climate in the last glacial period. *Nature* 428, 306-310.

van der Kaars, S., De Deckker, P. and Gingeles, F.X. (2006) A 100 000-year record of annual and seasonal rainfall and temperature for northwestern Australia based on a pollen record obtained offshore. *Journal of Quaternary Science* 21, 879-889.

Von Blanckenburg, F., Bouchez, J., Ibarra, D.E. and Maher, K., (2015). Stable runoff and weathering fluxes into the oceans over Quaternary climate cycles. *Nature Geoscience*, 8, 538-542.

Walling, D.E. (1983) The sediment delivery problem. *Journal of Hydrology* 65, 209-237.

Weissmann, G.S., Hartley, A.J., Nichols, G.J., Scuderi, L.A., Olson, M., Buehler, H. and Banteah, R. (2010) Fluvial form in modern continental sedimentary basins: Distributive fluvial systems. *Geology* 38, 39-42.

West, A. J., Galy, A., & Bickle, M. (2005). Tectonic and climatic controls on silicate weathering. *Earth and Planetary Science Letters* 235, 211-228.

Willenbring, J.K. and von Blanckenburg, F., (2010). Long-term stability of global erosion rates and weathering during late-Cenozoic cooling. *Nature* 465, 211-214.

Whitehead, P.W. (2010) The Regional Context of the McBride Basalt Province and the Formation of the Undara Lava Flows, Tubes, Rises and Depressions. *Proceedings 14th International Symposium on Vulcanospeleology*.

Wittmann, H., von Blanckenburg, F., Guyot, J.L., Maurice, L. and Kubik, P.W. (2009) From source to sink: Preserving the cosmogenic ^{10}Be -derived denudation rate signal of the Bolivian Andes in sediment of the Beni and Mamoré foreland basins. *Earth and Planetary Science Letters* 288, 463-474.

Wilson, S.A. (1997) The collection, preparation and testing of USGS reference material BCR-2. U.S. Geological Survey Open-File Report 98.

Wolanski, E. (1993) Water circulation in the Gulf of Carpentaria. *Journal of Marine Systems* 4, 401-420.

Woolfe, K.J., Larcombe, P., Naish, T. and Purdon, R.G. (1998). Lowstand rivers need not incise the shelf: an example from the Great Barrier Reef, Australia, with implications for sequence stratigraphic models. *Geology*, 26, 75-78.

Wyrwoll, K.-H. and Miller, G.H. (2001) Initiation of the Australian summer monsoon 14,000 years ago. *Quaternary International* 83, 119-128.

Yokoyama, Y., Esat, T.M. and Lambeck, K. (2001) Coupled climate and sea-level changes deduced from Huon Peninsula coral terraces of the last ice age. *Earth and Planetary Science Letters* 193, 579-587.

Zeebe, R.E. and Caldeira, K. (2008). Close mass balance of long-term carbon fluxes from ice-core CO₂ and ocean chemistry records. *Nature Geoscience*, 1, 312-315.

Zhang, P., Molnar, P. and Downs, W.R. (2001) Increased sedimentation rates and grain sizes 2–4 Myr ago due to the influence of climate change on erosion rates. *Nature* 410, 891-89.

5. Summary and future perspectives

To understand the potential landscape response to climate change, the timescales of Earth-surface processes must be constrained. In this thesis, various aspects of a developing geochronological tool, known as comminution dating, were evaluated and developed through laboratory experiments and field-based studies. In Chapter 2, sample pre-treatment methods were evaluated by monitoring the ($^{234}\text{U}/^{238}\text{U}$) activity ratio, and surface area properties of the detrital minerals. In Chapter 3, ($^{234}\text{U}/^{238}\text{U}$) activity ratio of bedrock and fluvial sediments were measured in catchments draining to the Gulf of Carpentaria to infer comminution ages. In Chapter 4, comminution dating was applied to sedimentary deposits of known age from the Gulf of Carpentaria to infer sediment residence times over the past 120 ka. The major findings, conclusions and future perspectives are summarised in this section.

5.1 Sampling and sample pre-treatment

Separate aliquots of an untreated soil sample exhibited heterogeneous ($^{234}\text{U}/^{238}\text{U}$) activity ratios. However, the ($^{234}\text{U}/^{238}\text{U}$) activity ratios of different aliquots of this soil sample were similar following sequential extraction. This is a key finding that indicates U isotope variability in soil samples could be due to non-detrital matter. Thus, isolating the detrital minerals in soil samples may be preferable to measuring bulk samples to obtain reproducible results. Separate aliquots of crushed rock samples from northern Australia also exhibited homogeneous ($^{234}\text{U}/^{238}\text{U}$) activity ratios. However, two aliquots of river sediment from northern Australia exhibited heterogeneous ($^{234}\text{U}/^{238}\text{U}$) activity ratios. This indicates that the natural U isotope variability of sediment on the catchment scale is not being addressed by only analysing one aliquot (discussed later in Section 5.4).

Sequential extraction, single-acid extraction, ashing in a furnace, and hydrofluoric (HF) acid etching techniques were tested on a soil sample to evaluate the optimum sample pre-

treatment for removing non-detrital matter. The ($^{234}\text{U}/^{238}\text{U}$) activity ratio decreased stepwise throughout a sequential extraction procedure, and this decrease is attributed to the removal of non-detrital matter. These results replicate findings by Lee (2009), and validate that the ($^{234}\text{U}/^{238}\text{U}$) activity ratio is a useful proxy for monitoring the removal of non-detrital matter from fine-grained detrital minerals. To dissolve the ^{234}U -depleted outer rind of detrital minerals, and increase the ($^{234}\text{U}/^{238}\text{U}$) ratio, an additional step was introduced where the sample is leached with mild HF/HCl. Applying this to soil and sediment samples further decreased the ($^{234}\text{U}/^{238}\text{U}$) activity ratio and it was shown that this was due to removal of clay minerals, which are ^{234}U -rich. Following mild HF/HCl etching, only a small increase in the ($^{234}\text{U}/^{238}\text{U}$) activity ratio was observed, which was within analytical error of the minimum ($^{234}\text{U}/^{238}\text{U}$) activity ratio. Etching experiments of longer duration (>24 h) should be conducted on a range of samples to test if the ($^{234}\text{U}/^{238}\text{U}$) activity ratio increases due to the removal of the ^{234}U -depleted rind and the activity ratio returns to unity.

Mild HF/HCl etching experiments were conducted on leached samples following the sequential extraction procedure from Tessier et al. (1979); however, evaluation of current sample pre-treatment methods revealed that the sequential extraction procedure from Schultz et al. (1998) was the most effective. Further work should, therefore, involve testing the mild HF/HCl etching procedure with the procedure from Schultz et al. (1998). This investigation should be extended by testing sample pre-treatment techniques on different sample types. For instance, the fractionation and speciation of U in the various non-detrital phases will depend on the depositional environment and parent lithology. The procedure developed in Chapter 2 represents a step towards the development of a standardised procedure, which is required for comminution ages to be cross-comparable.

In addition to decreasing the ($^{234}\text{U}/^{238}\text{U}$) activity ratio, sample pre-treatment procedures also affect the surface area properties of detrital minerals. This is important as the surface area parameters, such as surface area and fractal dimension, are used to estimate the direct-recoil

fraction using the BET and fractal models. For instance, in Chapter 2, different sample pre-treatment procedures resulted in variations in ($^{234}\text{U}/^{238}\text{U}$) activity ratios and surface area properties, which resulted in estimated ages ranging from 500 to 1000 ka. However, it is difficult to state which procedure results in the most “accurate” ages. Therefore, further work should involve testing the different sample pre-treatment procedures on a sample dated by other geochronological methods, similar to the approach by Lee et al. (2010), for refining calculation of the direct-recoil fraction.

Readsorption of released U during sample pre-treatment has been suggested as a potential issue for comminution dating. The addition of sodium citrate to sequential extraction reagents increased the overall extraction of U, but did not affect the final activity ratio. This suggests that readsorption was not an issue, but as the extraction of U was increased, its addition to sequential extraction reagents is thus recommended.

Some fluvial samples had ($^{234}\text{U}/^{238}\text{U}$) activity ratios greater than unity despite removing non-detrital matter by sequential extraction, resulting in negative calculated ages. In addition, some sediment samples from a sedimentary core in the Gulf of Carpentaria had comminution ages less than the depositional age. This is attributed to incomplete removal of ^{234}U -rich, non-detrital matter. Applying the new mild HF/HCl etching procedure to these samples following sequential leaching resulted in a further decrease of the ($^{234}\text{U}/^{238}\text{U}$) activity ratios. Following this, comminution ages were greater than depositional ages and sediment residence times could be calculated.

In summary, mild HF/HCl etching is recommended following sequential extraction, with sodium citrate added to reagents to inhibit readsorption of U. The recommended sample pre-treatment procedure for comminution dating is shown in Table 2.9.

Table 5.1 Recommended sample pre-treatment procedure for comminution dating.

Target phase	Reagents and Conditions ^{a,b}
Water-soluble (F0)	8 mL H ₂ O/Room temp./1 h
Exchangeable (F1)	8 mL 1 M MgCl ₂ at pH 7/Room temp./1 h
Acid-soluble (F2)	8 mL NaOAc/AcOH at pH 5/Room temp./6 h
Reducible (F3)	20 mL 0.04 M NH ₂ OH.HCl/ AcOH at pH 2/96 °C/5 h
Oxidisable (F4)	i) 8 mL 0.02 M HNO ₃ / H ₂ O ₂ at pH 2/85°C/2 h
	ii) 3 mL H ₂ O ₂ at pH 2/85 °C/3 h
	iii) 5 mL 3.2 M NH ₄ OAc in HNO ₃ 20% diluted to 20 mL with H ₂ O/Room temp./30 min
Resistant (F5)	20 mL 0.1 M HF 0.3 HCl/ Room temp./4 h

^aReagent volumes for 1 g of sample.

^b10 mg per gram of sample of Na(cit) added to the reagent at the start of the reaction.

5.2 Initial activity ratio of the parent material

The majority of near-surface rocks sampled from the Gulf of Carpentaria drainage basin in northern Australia were not in secular equilibrium and generally depleted in ²³⁴U. This indicates that ²³⁴U loss is occurring before the soil-bedrock interface, and/or following comminution to produce <63 µm minerals. The (²³⁴U/²³⁸U) activity ratios of sedimentary and metamorphic rocks from the Gulf of Carpentaria drainage basin were significantly lower (p = 0.047) for fine-grained rocks compared to coarse-grained rocks. This difference was more significant (p = 0.028) when including rocks (shales, siltstone, quartzite) measured in other studies (Table 5.2). As direct-recoil is dependent on grain size (Kigoshi, 1971), this could suggest that the magnitude of ²³⁴U depletion in rocks is related to grain size. This hypothesis requires that fine-grained rocks are sufficiently permeable for labile ²³⁴U to be removed by water/pore fluid flow. It is noted that this grain size hypothesis could be biased by the

number of quartzite samples (Table 5.2), which is a coarse-grained metamorphic rock. A sandstone rock was in secular equilibrium (Table 3.5), which may support the grain size hypothesis, but a greater sample size is clearly required. Despite the need for a greater sample size, the current sample database shows that assuming the initial activity ratio is in unity is not valid in all cases.

Granitic rocks appear particularly susceptible to preferentially leaching of ^{234}U based on evidence from this thesis and granite sampled from depths of up to 2800 m (Table 5.2). This could be because the majority of U in granites is hosted at grain boundaries and in microfractures (Tieh and Ledger, 1981). In addition, U is hosted in accessory minerals, such as zircon, which can have high U concentrations up to 7,000 ppm and can be highly damaged by alpha recoil, i.e. metamictization (Balan et al., 2001). Since ^{234}U is easily leached from damaged recoil sites by water, fluid flow preferentially leach ^{234}U without significantly altering the host rock undergoing by chemical weathering. These results suggest that comminution dating in granitic catchments should not assume that the initial activity ratio is in unity.

Despite widespread evidence for U isotope disequilibrium in bedrock in the literature and this study, a range of glacial sediments were in secular equilibrium (DePaolo et al., 2012). These glacial sediments are expected to have short transport time times since formation, and closely represent the U composition of the parent rocks. Therefore, the assumption that the initial activity ratio is unity is valid in some cases. Glacial sediments may be in secular equilibrium due to comminution by glacial grinding removing the ^{234}U -depleted outer-rind of mineral grains, i.e. resetting the radiometric clock.

In the Gulf of Carpentaria drainage basin, disequilibrium in the parent material was accounted for by calculating initial activity ratios for each sub-catchment considering the average ($^{234}\text{U}/^{238}\text{U}$) activity ratios of different rock types, and the proportion of each rock

type in catchments. Preferential leaching effects in river sediments were accounted for by using a modified comminution age model that considers leaching of ^{234}U and ^{238}U . This approach removes the need to assume that the parent material is in secular equilibrium. A larger dataset of rocks, with a larger range of lithologies, is required to reduce uncertainties in inferred comminution ages following this approach.

5.3 Sediment-routing system

Inferred comminution ages for catchments in the Gulf of Carpentaria drainage basin, northern Australia ranged from <1 to 190 ± 80 ka. The mean annual rainfall in the study catchments ranged from <400 mm a^{-1} to >1700 mm a^{-1} , but there was no clear relationship between comminution ages and rainfall. However, sediments from small, wet catchments from the tropical north of the drainage basin were close to secular equilibrium. This indicates that the river sediments in these catchments undergo minimal chemical alteration (no preferential leaching of ^{234}U) and that sediment transport is rapid (insufficient time for the loss of ^{234}U by direct recoil to become significant).

In the Gulf of Carpentaria drainage basin, large variations in comminution ages can be attributed to varying rock types, sediment mineralogy, and relief across catchments. In addition, sediment residence times may be complicated by the multiple pathways by which a sediment particle can be transported from source to sink i.e. the *sediment-routing system* (Allen, 2008; Malmgren et al., 2003). Although comminution dating provides an average transport time of sediment grains, obtaining comminution ages for only a few samples per catchment appears to be insufficient to address intra-catchment variability in large fluvial systems. This is indicated by replicate measurements not being repeatable for different sample aliquots, and repeat sampling of a sub-catchment in two separate field campaigns. Future work should ensure that variability is assessed by increasing the number of samples

in a catchment. This is necessary to place sediment residence times in the stochastic framework of the sediment-routing system.

The average sediment residence time for major catchments in the Gulf of Carpentaria drainage basin was 88 ± 35 ka vs 41 ± 17 ka for modern marine sediment in the Gulf of Carpentaria. This may suggest that the Gulf of Carpentaria preferentially receives sediment that is rapidly transported out of the drainage basin. Longer residence times for river sediment from the drainage basin may also show that lowland catchments are long-term sediment sinks. Sediment samples from the deltaic and shoreline areas of the Gulf of Carpentaria are required to further investigate sediment transport through deltas.

5.4 Comminution dating of sedimentary deposits

Comminution dating was applied to two sedimentary cores from the Gulf of Carpentaria in Chapter 4. Analytical considerations and geomorphic interpretations of comminution parameters are discussed in this section.

5.4.1 Reduced direct recoil in core sediments

Comminution dating was applied to two sedimentary cores from the Gulf of Carpentaria in Chapter 4. Firstly, many comminution ages were less than the depositional ages, resulting in “negative” sediment residence times. Negative ages have also been reported in other applications of comminution dating of core sediments (Handley et al., 2013a; Handley et al., 2013b; Lee et al., 2010; Li et al., 2016). A systematic problem with the interpretation of comminution ages may be that direct recoil is reduced following deposition. This is evidenced by the decrease in specific surface area, fractal dimension, and pore volume of core sediments with increasing depth in the Gulf of Carpentaria. Furthermore, the ($^{234}\text{U}/^{238}\text{U}$) activity ratio of some core sediments were close to secular equilibrium despite sedimentary storage times up to 80 ka. Reduced porosity in compacted core sediments could retain

implanted ^{234}U that are typically removed by water flow and result in activity ratios close to secular equilibrium. Clay-rich sedimentary deposits, such as those in the Gulf, may have low permeability and reduce water infiltration through core sediments.

5.4.2 Past variations in sediment residence times

The average residence time of sediments deposited during interglacial periods was 41 ± 17 ka. In contrast, sediment residence times could not be inferred for sediments deposited during glacial periods, despite some sediments having depositional ages up to ~ 80 ka. The average residence time of interglacial sediments is within uncertainty of the average residence time of river sediments (88 ± 35 ka) for major catchments in the Gulf of Carpentaria drainage basin (Table 4.9). Since the average sediment residence time spans at least the LGM, this suggests that catchments are currently reworking material accumulated over the last glacial cycle during MIS 2-4.

Previous successful applications of comminution dating have recognised large variations in sediment residence times may be due to changes in sediment provenance; for instance, Iceland vs continental Europe in the North Atlantic (DePaolo et al., 2006), and young hillslopes vs old alluvial deposits in the Murrumbidgee River (Dosseto et al., 2010). In the Gulf of Carpentaria, changes in sediment provenance appear to be driven by the north/southward migration of the ITCZ, which controls the spatial distribution of monsoonal rainfall/discharge in the Gulf catchments. This is based on the average ($^{234}\text{U}/^{238}\text{U}$) activity ratios of fluvial sediments from northern (N) and southern (S) catchments draining to the Gulf (Chapter 3). Lower ($^{234}\text{U}/^{238}\text{U}$) activity ratios are inferred to represent sediment being sourced from both the N and S catchments, whereas higher ($^{234}\text{U}/^{238}\text{U}$) activity ratios are inferred to represent a decrease in the relative contribution of the S catchments, i.e. decreased relative palaeodischarge of the southern catchments. Based on the ($^{234}\text{U}/^{238}\text{U}$) of core sediments, the relative palaeodischarge of the S catchments is estimated to have varied

by three orders of magnitude over the past 120 ka. The lowest relative palaeodischarge of the S catchments is inferred during glacial periods, and may have been 1/100th of the present discharge. There is significant uncertainty in these palaeodischarge estimates, but these calculations suggest that past variations in sediment residence times in the Gulf of Carpentaria are likely driven by changes in sediment provenance rather than intra-catchment variations in erosion. These findings imply that rather than affect global net erosion rates, Late Quaternary climate variability may simply spatially reorganise erosional loci. This is consistent with stable silicate weathering fluxes throughout the Quaternary (Willenbring and von Blanckenburg, 2010; von Blanckenburg et al., 2015), and relatively stable atmospheric CO₂ concentrations for the past 600 ka (Zeebe and Caldeira, 2008). This long-term stability may be the result of long duration of sediment transport in low-relief landscapes (~100 ka), which could buffer high frequency changes in climate.

5.5 Future work

Further work is required to reduce uncertainty in comminution ages. Key goals for future comminution dating studies are improving the estimation of the direct-recoil fraction, and assessing aeolian contribution. These are discussed in the following section.

5.5.1 Initial activity ratio of the parent material

All (²³⁴U/²³⁸U) activity ratio measurements for sedimentary, metamorphic and intrusive rocks are given in Table 5.2. Clearly, a larger range of lithologies is required to assess the (²³⁴U/²³⁸U) of rocks at Earth's surface. In particular, a greater number of granite samples are required since i) granitic rocks tend to exhibit (²³⁴U/²³⁸U) <1 (Table 5.2), and ii) the term “granite” covers a range of different rock types. For instance, granites can be sub-divided into I-type and S-types, which are derived by partial melting of igneous and sedimentary source rocks (Chappell and White, 2001). Furthermore, mafic and felsic granitic rocks have differing chemical composition and mineralogy that are likely important for U-series. The

U-rich mineral muscovite is common in the more felsic S-types, whereas U-rich biotite may be up to 35% more abundant in more mafic S-types (Chappell and White, 2001).

Determining the ($^{234}\text{U}/^{238}\text{U}$) activity ratio of $>63\ \mu\text{m}$ sediment grains (sand and pebbles) from active fluvial channels may be a convenient method to determine the representative composition of the source rocks on a catchment-wide scale. This would overcome the need to measure the numerous rock types in a given catchment. If sand and pebbles are not in secular equilibrium, the measured ($^{234}\text{U}/^{238}\text{U}$) could be used to accurately adjust the initial activity ratio for the silt fraction. A standard procedure for comminution dating of catchments could be to collect and analyse the silt, sand and pebbles.

Table 5.2 The ($^{234}\text{U}/^{238}\text{U}$) activity ratios of bedrock samples

Sample	Location	($^{234}\text{U}/^{238}\text{U}$) ^b	Lithology	Grain size	Source
GOC-B-1	Mitchell River, N Australia	0.843 ± 0.003	mudstone	fine	Chapter 3
GOC-B-2	Mitchell River, N Australia	0.850 ± 0.002	granite	medium	Chapter 3
GOC-B-3	Mitchell River, N Australia	0.979 ± 0.004	granite	medium	Chapter 3
GOC-B-4	Mitchell River, N Australia	0.795 ± 0.001	rhyolite	fine	Chapter 3
GOC-B-5	Gilbert River, N Australia	1.011 ± 0.002	schist	coarse	Chapter 3
GOC-B-6	Flinders River, N Australia	1.007 ± 0.003	sandstone	coarse	Chapter 3
GOC-B-7	Flinders River, N Australia	0.963 ± 0.002	dolerite	coarse	Chapter 3
GOC-B-8	Leichhardt River, N Australia	1.004 ± 0.002	amphibolite	coarse	Chapter 3
WP-Q1	Flinders Ranges, S Australia	0.971 ± 0.003	quartzite	coarse	Handley et al. (2013b)
HK-Q1	Flinders Ranges, S Australia	0.966 ± 0.002	quartzite	coarse	Handley et al. (2013b)
GS-S1	Flinders Ranges, S Australia	0.940 ± 0.002	shale	fine	Handley et al. (2013b)
BRA-SS1	Flinders Ranges, S Australia	0.912 ± 0.002	siltstone	fine	Handley et al. (2013b)
DC1	Susquehanna Shale Hills, US	0.996 ± 0.002	shale	fine	Ma et al. (2010)
STD	Southern Highlands, SE Australia	1.022 ± 0.002	sandstone	coarse	Menozi (2016)

^b2 σ internal standard error

5.5.2 Sediment budgeting and comminution dating

Sediment transport in geomorphic systems is generally non-linear and stochastic (Phillips, 2003). This may explain the highly variable comminution ages measured in catchments draining to the Gulf of Carpentaria, besides analytical uncertainties in comminution ages. Comminution dating should be combined with a detailed sediment budgeting approach to assess catchment (dis)connectivity, which considers longitudinal, lateral and vertical linkages in hillslope-fluvial systems (Fryirs, 2013; Fryirs and Brierley, 2001; Fryirs et al., 2007). This considers the probabilities of sediment exchange between the various sediment stores and sinks in a catchment, such as hillslope-channel and channel-floodplain connectivity. These various sediment stores should be sampled within a single catchment whilst controlling other variables, such as lithology. Hillslope-channel connectivity is controlled by the frequency of processes such as landslides (e.g., Korup, 2005), and alluvial gullying (e.g., Shellberg and Brooks, 2012). Channel-floodplain connectivity is mainly controlled by the frequency of floodplain inundation (Walling et al., 1998). In large river systems such as the Amazon River, sediment exchange between the channel and floodplain can exceed the annual sediment flux (Dunne et al., 1998). Future comminution age studies of fluvial systems should follow this sampling approach to overcome natural variability in transport histories of sediment grains.

5.5.3 Direct-recoil fraction

The direct-recoil fraction could be calibrated by calculating the direct-recoil fraction for old sediments that have been deposited for >1 Ma. This is because enough time has elapsed for steady-state disequilibrium to form and the direct-recoil fraction can be calibrated using depositional ages constrained by established techniques, e.g. optically-stimulated luminescence. This was attempted by Lee et al. (2010) with the study of glacially-derived sediments in an alluvial deposit. However, there is uncertainty in the assumption that the transport time was negligible. Furthermore, Lee et al. (2010), estimated the direct-recoil fraction using a geometric model, which has input variables that are hard to measure, e.g. aspect ratio, and must be assumed. The fractal direct-recoil model appears to better estimate the direct-recoil fraction, as shown by the comminution dating of ice cores (Aciego et al., 2011). An interesting experiment would be to estimate the direct-recoil fraction for the sediments analysed Lee et al. (2010) using the fractal model. Other future studies should apply the comminution dating technique directly to tephra, avalanche, and glacial moraine deposits of known age. In these cases, the time elapsed between comminution and deposition is minimal.

5.5.4 Aeolian input

Considerations of mass fluxes from dust deposition vs fluvial erosion predicted sediments in the Gulf of Carpentaria drainage basin may comprise up to 24% deposited dust. This is reflected by higher specific surface areas and lower mean grain sizes measured for sediments

from more arid catchments, which could be attributed to the deposition of fine-grained dust. The long average residence times inferred for river sediments in the Gulf of Carpentaria span at least the Last Glacial Maximum when dust fluxes are thought to have been an order of magnitude greater. Therefore, comminution ages of river sediments in northern Australia likely reflect fluvial-aeolian sediment transport processes, and should be considered as *fluvial-aeolian systems* (Liu and Coulthard, 2015). Untangling the links between fluvial and aeolian erosion processes requires a greater understanding of the U composition of dust. If the aeolian fluxes, and the U composition of aeolian material are known, comminution ages can be used to calculate the timescales of aeolian transport, and correct the sediment residence times of hillslope-fluvial systems.

5.6 Final conclusions

This thesis developed and tested various aspects of comminution dating through laboratory and field experiments. Sample pre-treatment methods were evaluated and a mild HF/HCl etching procedure step was introduced. Further experiments are required to further develop sample pre-treatment for comminution dating and experiments have been clearly outlined. Rocks, river sediments and core sediments were sampled in a source to sink assessment of the Gulf of Carpentaria drainage basin. The source rocks were generally not in secular equilibrium. Thus, this was accounted for by estimating the initial activity ratio of catchments. The average residence time for sediments deposited in the Gulf during interglacial periods was 41 ± 18 ka, which is similar to the average sediment residence time in

catchments in the Gulf of Carpentaria drainage basin (88 ± 37 ka). Sediment transport processes during interglacials may be dominated by the reworking of sediment accumulated over the last glacial cycle. In contrast, the activity ratios for sediments from glacial periods were close to secular equilibrium, suggesting that an insufficient amount of time elapsed between the formation of fine-grained sediment and deposition, i.e. rapid sediment transport. This is similar to river sediments from small N catchments, which were also close to secular equilibrium, and is attributed to rapid sediment transport in small, wet catchments. Therefore, sediments deposited in the Gulf during glacial periods could mainly be sourced from the N catchments. In the Gulf of Carpentaria, it appears that Late Quaternary climatic variations rearrange the spatial distribution of discharge and the modern landscape is dominated by the reworking of sediment accumulated over the last glacial-interglacial climate change. The long duration of sediment transport (~ 100 ka) in low-relief landscapes may provide a mechanism for buffering the landscape response to high frequency changes in climate.

5.7 References

- Aciego, S., Bourdon, B., Schwander, J., Baur, H. and Forieri, A. (2011) Toward a radiometric ice clock: Uranium ages of the Dome C ice core. *Quaternary Science Reviews* 30, 2389-2397.
- Allen, P.A. (2008) From landscapes into geological history. *Nature* 451, 274-276.

Balan, E., Neuville, D.R., Trocellier, P., Fritsch, E., Muller, J.-P. and Calas, G. (2001) Metamictization and chemical durability of detrital zircon. *American Mineralogist* 86, 1025-1033.

Chappell, B.W. and White, A.J.R., 2001. Two contrasting granite types: 25 years later. *Australian Journal of Earth Sciences* 48, 489-499.

DePaolo, D.J., Lee, V.E., Christensen, J.N. and Maher, K. (2012) Uranium comminution ages: Sediment transport and deposition time scales. *Comptes Rendus - Geoscience* 344, 678-687.

DePaolo, D.J., Maher, K., Christensen, J.N. and McManus, J. (2006) Sediment transport time measured with U-series isotopes: Results from ODP North Atlantic drift site 984. *Earth and Planetary Science Letters* 248, 394-410.

Dosseto, A., Buss, H.L. and Chabaux, F. (2014) Age and weathering rate of sediments in small catchments: The role of hillslope erosion. *Geochimica et Cosmochimica Acta* 132, 238-258.

Dosseto, A., Hesse, P.P., Maher, K., Fryirs, K. and Turner, S. (2010) Climatic and vegetation control on sediment dynamics during the last glacial cycle. *Geology* 38, 395-398.

Dosseto, A. and Riebe, C.S. (2011) Inception! timescale of chemical weathering during the early stages of water–rock interaction. *Mineral. Mag.* 3, 776.

Fryirs, K. (2013) (Dis) Connectivity in catchment sediment cascades: a fresh look at the sediment delivery problem. *Earth Surface Processes and Landforms* 38, 30-46.

Fryirs, K. and Brierley, G.J. (2001) Variability in sediment delivery and storage along river courses in Bega catchment, NSW, Australia: implications for geomorphic river recovery. *Geomorphology* 38, 237-265.

Fryirs, K.A., Brierley, G.J., Preston, N.J. and Kasai, M. (2007) Buffers, barriers and blankets: the (dis) connectivity of catchment-scale sediment cascades. *Catena* 70, 49-67.

Handley, H.K., Turner, S., Afonso, J.C., Dosseto, A. and Cohen, T. (2013a) Sediment residence times constrained by uranium-series isotopes: A critical appraisal of the comminution approach. *Geochimica et Cosmochimica Acta* 103, 245-262.

Handley, H.K., Turner, S.P., Dosseto, A., Haberlah, D. and Afonso, J.C. (2013b) Considerations for U-series dating of sediments: Insights from the Flinders Ranges, South Australia. *Chemical Geology* 340, 40-48.

Korup, O. (2005) Geomorphic imprint of landslides on alpine river systems, southwest New Zealand. *Earth Surface Processes and Landforms* 30, 783-800.

Lee, V.E., DePaolo, D.J. and Christensen, J.N. (2010) Uranium-series comminution ages of continental sediments: Case study of a Pleistocene alluvial fan. *Earth and Planetary Science Letters* 296, 244-254.

Li, C., Francois, R., Yang, S., Barling, J., Darfeuil, S., Luo, Y. and Weis, D. (2016) Constraining the transport time of lithogenic sediments to the Okinawa Trough (East China Sea). *Chemical Geology* 445, 199-207.

Malmon, D.V., Dunne, T. and Reneau, S.L. (2003) Stochastic theory of particle trajectories through alluvial valley floors. *The Journal of Geology* 111, 525-542.

Matmon, A., Bierman, P.R., Larsen, J., Southworth, S., Pavich, M., Finkel, R. and Caffee, M. (2003) Erosion of an ancient mountain range, the Great Smoky Mountains, North Carolina and Tennessee. *American Journal of Science* 303, 817-855.

Phillips, J.D., 2003. Sources of nonlinearity and complexity in geomorphic systems. *Progress in Physical Geography* 27, 1-23.

Schultz, M.K., Burnett, W.C. and Inn, K.G.W. (1998) Evaluation of a sequential extraction method for determining actinide fractionation in soils and sediments. *Journal of Environmental Radioactivity* 40, 155-174.

Shellberg, J. and Brooks, A. (2012) Alluvial Gully Erosion: A Dominant Erosion Process Across Tropical Northern Australia.

Suresh, P., Dosseto, A., Hesse, P. and Handley, H. (2014) Very long hillslope transport timescales determined from uranium-series isotopes in river sediments from a large, tectonically stable catchment. *Geochimica et Cosmochimica Acta* 142, 442-457.

Tieh, T.T. and Ledger, E.B. (1981) Fission track study of uranium in two granites of central Texas. *Contributions to Mineralogy and Petrology* 76, 12-16.

Von Blanckenburg, F., Bouchez, J., Ibarra, D.E. and Maher, K., (2015). Stable runoff and weathering fluxes into the oceans over Quaternary climate cycles. *Nature Geoscience*, 8, 538-542.

Walling, D.E., Owens, P.N. and Leeks, G.J.L. (1998) The role of channel and floodplain storage in the suspended sediment budget of the River Ouse, Yorkshire, UK. *Geomorphology* 22, 225-242.

Willenbring, J.K. and von Blanckenburg, F., (2010). Long-term stability of global erosion rates and weathering during late-Cenozoic cooling. *Nature* 465, 211-214.

Zeebe, R.E. and Caldeira, K. (2008). Close mass balance of long-term carbon fluxes from ice-core CO₂ and ocean chemistry records. *Nature Geoscience*, 1, 312-315.

6. Appendix A

This appendix includes a description of analytical techniques, data from procedure blanks and rock standards, field work notes, and data that was not reported in Chapters 2, 3 or 4.

6.1 Analytical techniques

This section describes sample preparation for the comminution dating technique. This includes laboratory techniques for isotopic analysis of uranium (U), and a brief theoretical description of analytical equipment is given.

6.1.1 Sample preparation

Soil and sediment samples were wet-sieved at 63 μm using deionised H_2O . The $<63 \mu\text{m}$ fraction was retained, dried in an oven at 50 $^{\circ}\text{C}$ and homogenised by gentle mixing with a mortar and pestle. This was followed by sequential extraction on a 2 g aliquot of dry, homogenised sample using the procedure from Lee (2009), which is shown in Table 6.1. The solid and aqueous phases were separated by centrifugation at 7000 rpm for 10 minutes. The aqueous phase was removed using disposable Pasteur pipettes. Details of mild HF/HCl etching experiments are given in Chapter 2.

Table 6.1 Sequential extraction procedure from Lee (2009) where the operationally-defined fractions are F0: water soluble F1: exchangeable, F2: acid soluble, F3: reducible, and F4: oxidisable.

Fraction	Reagent	Reaction conditions
F0	H ₂ O at pH 7	Room temp./1 h
F1	1 M Mg(NO ₃) ₂ at pH 7	Room temp./ 1 h
F2	NaOAc/ AcOH at pH 5	Room temp./ 6 h
F3	0.04 M NH ₂ OH.HCl/ AcOH at pH 2	96 °C/ 5 h
	0.02 M HNO ₃ / H ₂ O ₂ at pH 2	85°C/ 2 h
F4	H ₂ O ₂ at pH 2	85 °C/ 3h
	3.2 M NH ₄ OAc in 20% (V/V) HNO ₃	Room temp./ 0.5 h

6.1.2 Sample weighing

Silicate rock samples were dissolved using strong acids in screw-capped PFA (Teflon) vials on a hotplate. For strong acid dissolution, ca. 100 mg of material was weighed and spiked with 30 mg of ²²⁹Th–²³⁶U tracer. A tracer was added following laboratory techniques for determining U concentrations by isotopic dilution. However, both the volume and mass of soils and sediments change throughout sequential extraction, regolith transport, and fluvial transport. As U is fractionated by these processes, an immobile element, such as zirconium,

should be measured. As this was not carried out, U concentrations in different samples cannot be compared and these concentrations were not reported.

6.1.3 Acid dissolution

Silicate mineral samples were dissolved by heating with hydrofluoric acid (HF) and nitric acid (HNO₃). Silicate mineral dissolution using HF is stoichiometric and HF removes silicon, aluminium, and magnesium at rates proportional to their lattice concentrations (Kline and Fogler, 1981). To reduce the formation of stable fluoride compounds, and HF consumption, a strong acid such as HNO₃ is used to lower the pH and shift the equilibrium towards complexes coordinated by fewer fluorine atoms (Hekim and Fogler, 1977).

The samples were dissolved by adding 2.5 mL 32 % HF and 0.5 mL 69 % HNO₃ and heating overnight at 100°C. The samples were dried down to incipient dryness in a closed system and once dry, 3 mL of 32 % HCl was added. H₃BO₃ was added to dissolve fluorides where necessary. The samples were heated at 80°C overnight and dried down to incipient dryness in a closed system. Following this, 0.5 mL 69 % HNO₃ was added, dried down at 100°C to incipient dryness and this step was repeated. 2 mL of 1.5 M HNO₃ was added and the solutions were sonicated for 15 min and heated at 100°C to ensure re-dissolution.

6.1.4 Column chromatography

In order to accurately measure U isotopes by mass spectrometry, matrix interferences from other elements are removed by ion exchange chromatography. This technique involves a solid phase (resin) and a mobile phase (dissolved rock). The elements in the dissolved rock solution have different affinities for the resin and this is used to separate them. Depending on the affinity of the element for the resin, varying quantities of acid are used to remove them.

For separating U, an Eichrom TRU Resin is used, which is an octylphenyl-N,N-di-isobutyl carbamoylphosphine oxide (abbreviated CMPO) dissolved in tri-n-butyl phosphate (TBP). Tetravalent actinides (e.g. Th) show an extremely high retention on the column (Horwitz et al., 1993); however, U is http://www.eichrom.com/image/products/tru/fig3_lg.gif hexavalent under oxidising conditions and has approximately one order of magnitude lower retention. The acids used are shown in Table 6.2. Chromatography columns used were Bio-Spin® (#732-6025) columns with a working bed height of 3.7 cm and a 1.2 mL bed volume, which represents the volume of the column packed by the stationary phase (resin). The column chromatography procedure used was modified from the procedure in Luo et al. (1997) and is shown in Table 6.2.

Table 6.2 Column chromatography used to separate U, which is modified from Luo et al. (1997).

Reagent	Volume (mL)	Purpose
3 M HCl	6.0	
0.2 M HCl	6.0	Cleaning
0.1 M HCl/0.3 M HF	6.0	
1.5 M HNO ₃	9.0	Preconditioning
1.5 M HNO ₃	<4.0	Wash
1.5 M HNO ₃	4.0	
3 M HCl	4.5	Collect rare earth elements
0.2 M HCl	4.5	Collect Th
0.1 M HCl/0.3 M HF	8.0	Collect U

6.1.5 Mass spectrometry

6.1.5.1 *Multi-collector inductively-coupled-plasma mass spectrometry*

Multi-collector-inductively-coupled-plasma-mass-spectrometry (MC-ICPMS) was used for the high-precision isotopic analysis of U. This main advantage of MC-ICPMS vs other methods, such as thermal-ionisation mass spectrometer (TIMS), is the high ionisation efficiency of the argon (Ar) plasma for most elements.

The MC-ICPMS system comprises: i) a *sample inlet system* that is typically introduces a liquid via a nebuliser or a solid via laser ablation; ii) an *inductively-coupled-plasma* that is normally Ar; iii) an *ion transfer mechanism* that separates the internal vacuum from the external inlet system which is at atmospheric pressure ; and iv) a *mass analyser* that detects the abundances of ions. In MC-ICP-MS, a *magnetic sector* analyser accelerates ions through a magnetic field that separates ions on the basis of their mass to charge ratio (m/z). A series of *Faraday cups* are used to measure the signal of each isotope, and *ion counters*, such as a secondary electron multiplier (SEM), are used to analyse low intensity signals.

Drawbacks of MC-ICP-MS include (Albarède and Beard, 2004): i) the formation of ions with a range of kinetic energies that requires an electrostatic filter or *collision cell* to produce flat-topped peaks; ii) the production of doubly-charged ions that create isobaric interferences, and iii) instrumental mass bias, which can be further complicated by sample matrix effects.

Instrumental mass bias varies smoothly during the course of an analytical session, and can be corrected for by the *standard bracketing* method. Standard bracketing interpolates the mass bias of unknown sample by analysing a known standard before and after the sample during the analysis. The interpolated equation is given as (Albarède and Beard, 2004):

$$R_{sample} = R_{standard} \frac{r_{sample}}{\sqrt{r_{sample} \times r_{standard}}} \quad (1)$$

where R_{sample} is the corrected isotopic ratio of the sample, $R_{standard}$ is the known isotopic ratio of the standard, r_{sample} is the measured isotopic ratio of the sample, and $r_{standard}$ is the measured isotopic ratio of the standard. Synthetic standard U010 was used for standard bracketing, and accuracy was checked using synthetic standard U005A and rock standard BCR-2 (U.S. Geological Survey), which is known to be in secular equilibrium whereby $(^{234}\text{U}/^{238}\text{U}) = 1$.

6.1.5.2 *Quadrupole-inductively-coupled-plasma-mass-spectrometry*

Quadrupole inductively-coupled plasma mass spectrometry (Q-ICP-MS) was used for concentration determinations of U, Th and Nd. Similar to MC-ICP-MS system, the Q-ICP-MS system comprises: i) sample inlet system; ii) inductively-coupled-plasma of Ar; iii) ion transfer mechanisms that separates the internal vacuum from the external inlet system which is at atmospheric pressure ; and iv) mass analyser. In Q-ICP-MS, a *quadrupole* mass analyser separate ions based on their m/z by alternating electrical fields (AT, 2005); the

quadrupole can rapidly scan across a mass range of 2 – 260 amu and analyse each m/z of interest sequentially.

An aliquot of the digestion solution was taken prior to column chromatography, diluted in 2 % v/v HNO₃ and analysed on an Agilent 7500 Series Inductively-Coupled Plasma Mass Spectrometer (Q-ICP-MS). The concentrations of U were calculated quantitatively by constructing a calibrations curve, typically using ca. 6 – 8 standards with U concentrations ranging from 0 – 100 ppb.

6.1.6 Surface area analysis

To estimate the direct-recoil fraction, discussed in Section 1.x), surface area analysis to measure the Brunauer–Emmett–Teller (BET) specific surface area, and the fractal dimension.

6.1.6.1 BET theory

The surface area A_s of an adsorbent is calculated from the coverage of the monolayer by an adsorbed gas, given as (Brunauer et al., 1938; Sing, 1985):

$$A_s = n_m^a \times L \times a_m \quad (1)$$

where n_m^a is the monolayer capacity, L is the Avogadro constant, and a_m is the area of the adsorbed molecule. The specific surface area a_s refers to the unit mass of adsorbent:

$$a_s = \frac{A_m}{m} \quad (2)$$

where m is the adsorbent mass.

Adsorption-desorption isotherms can be classified into six types (Figure 6.1), and are outlined here (Sing, 1985). *Type I* isotherms are produced by microporous solids that have a small external surface area and large internal surface area. *Type II* isotherms are typical for non-porous or macroporous solids; the inflection at point B marks the point where monolayer coverage is complete and multilayer adsorption begins. *Type III* isotherms are rare and related to adsorbate-adsorbent interactions e.g. N₂ on polyethylene. *Type IV* isotherms are characterised by the divergence between the adsorption and desorption isotherms i.e. *hysteresis*, which is associated with capillary condensation in mesopores; as for type II isotherms, point B marks the point where monolayer coverage is complete. *Type V* isotherms are also rare and related to weak adsorbent-adsorbate interactions. *Type VI* isotherms are also rare and represent the “stepwise multilayer adsorption on a uniform non-porous surface”.

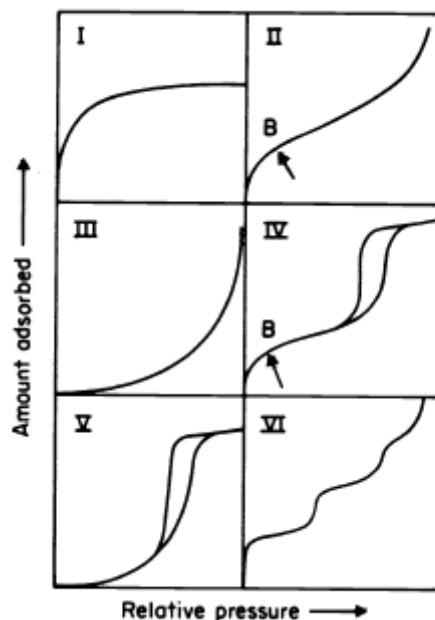


Figure 6.1 Various types of physisorption isotherms.

The BET equation is given as:

$$\frac{P}{n^a \cdot (P_0 - P)} = \frac{1}{n_m^a \cdot C} + \frac{(C-1)P}{n_m^a \cdot C P_0} \quad (3)$$

where n^a is the amount of gas adsorbed at the partial pressure P/P_0 and n_m^a is the monolayer capacity, and C is a constant. The C constant is related to the enthalpy of adsorption in the initially adsorbed layer. The BET equation is calculated from a linear plot of $P/n^a(P_0 - P)$ vs P/P_0 , which is normally range in the range $P/P_0 = 0.05 - 0.30$. The calculated amount of gas adsorbed is then used to calculate the surface area using Equation 1.

In this thesis, BET surface area measurements were determined by N₂ gas adsorption using a Quantachrome iQ surface area analyser. Samples were degassed for 3 h at 200 °C under vacuum to remove any adsorbed species from the adsorbent surface. The surface area was determined using 5 – 7 adsorption points from the partial pressure (P/P₀) range 0.05 – 0.30 and adjusted for the best fit of the Multi-point BET plot ($R^2 > 0.9999$).

6.1.6.2 Fractal dimension

Fractal geometry can be applied to take into account the surface roughness of sediment grains. The *fractal dimension* (D) takes into account the relationship between the surface area and the deviation from a perfect geometrical shape; this can take a value from 2 – 3. An ideal surface can be modelled by using simple geometric concepts e.g. the surface area of a cube is equivalent to $6L^2$ or $4\pi R^2$ for a sphere. For such surfaces $D = 2$ as the surface area is proportional to X^2 , where X is a characteristic dimension of the adsorbent. As the value of D approaches 3, more space it taken up by the surface area and essentially becomes three dimensional. The Neimark-Kiselev (NK) method was used to calculate the fractal dimension in thesis, as outlined in Section 1.x.

Avnir and Jaroniec (1989) proposed a modified version of the Dubinin-Radushkevich equation (Dubinin et al., 1979), which was similar to the Frenkel-Halsey-Hill (FHH) equation (Steele, 1974), and given as:

$$\theta = K \left[\ln \left(\frac{P_0}{P} \right) \right]^{-v} \quad (14)$$

$$v = 3 - D \quad (15)$$

where P_0/P is the relative pressure from gas sorption measurements, θ is the monolayer coverage, K is a constant, and D is the fractal dimension.

Alternatively, the fractal dimension can be calculated using the Neimark-Kiselev (NK) method, which is based on the thermodynamic relationship between the onset of capillary condensation and the adsorbate-vapour interface area (Neimark, 1992), given as:

$$S_{lg} = K(a_c)^{2-D} \quad (16)$$

where S_{lg} is the adsorbate-vapour interface area, a_c is the mean radius of curvature of the adsorbate-vapor interface, K is a constant; and D is the fractal dimension. The fractal dimension is calculated from a plot of $\log [S_{lg}]$ vs $\log [a_c]$, which should yield a straight line within the multilayer region of the isotherm.

Both methods of calculating the fractal dimension yield similar results for mesoporous samples (Jaroniec, 1995), with pore sizes ranging from 2 – 50 nm (Sing, 1985). However, the FHH equation should not be applied to microporous samples with pores <2 nm. In this thesis, the NK method was utilised as samples generally exhibited microporosity.

6.2 Analytical data

This section includes data from blanks and standards, and column chromatography yields for the procedure outlined in Section 6.1.4.

6.2.1 Blanks data

Total procedure blanks are conducted along with each sample batch. Blanks generally ranged from 1 – 34 pg of U, and the average was 66 pg ($n = 11$), as shown in Table 6.3. The higher average value was caused by blanks ranging from 166 – 395 pg of U in late 2013/early 2014, which was a laboratory-wide issue. Considering that most samples in these batches contained 2 – 3 ppm of U, and 100 mg aliquots of sample were analysed, this represents a maximum contribution of 0.2% U from contamination. Therefore, the input of U by contamination is regarded to have not significantly affected samples.

Table 6.3 Amount of U in total procedure blanks

Date of analysis	U (pg)
13/02/2012	34
2/03/2012	26
10/05/2012	4
8/02/2013	8
8/02/2013	2
26/07/2013	11
8/02/2013	6
26/07/2013	166
26/07/2013	395
3/10/2014	138
3/10/2014	4
3/10/2014	1
average	66.3

6.2.2 Standard data

To assess if laboratory techniques fractionate U isotopes e.g. during dissolution or chromatography, rock standards of known isotopic ratios were analysed. The rock standard used was BCR-2, which is a basalt sampled from Oregon, USA known to be in secular equilibrium whereby ($^{234}\text{U}/^{238}\text{U}$) = 1 (Wilson, 1997). The average ($^{234}\text{U}/^{238}\text{U}$) activity ratio of rock standard BCR-2 was 1.003 ± 0.003 (n=9) (Table 6.4), which is within error of secular equilibrium. This shows that acid dissolution and column chromatography did not fractionate ^{234}U and ^{238}U .

Table 6.4 ($^{234}\text{U}/^{238}\text{U}$) of rock standards shown with 2σ standard error.

Date of analysis	($^{234}\text{U}/^{238}\text{U}$)
28/03/2012	1.001 ± 0.007
27/03/2012	0.999 ± 0.005
5/05/2012*	0.987 ± 0.022
1/02/2013	1.007 ± 0.004
10/03/2013	1.012 ± 0.003
17/04/2013	1.009 ± 0.003
21/10/2013	1.006 ± 0.002
16/13/2013	1.004 ± 0.002
3/02/2014	1.004 ± 0.002
09/03/2015	1.000 ± 0.001
average	1.003 ± 0.003

*Samples reanalysed on the 21/10/2013

6.2.3 Chromatography

To test the separation of U, Th and Nd using the procedure outlined in Section 6.1.4, three aliquots of rock standard BCR-2 were dissolved, and element concentrations in each fraction were analysed. Only 35 % of U eluted was found in the relevant fraction (Table 6.5); however, this is not considered a problem as only ca. 10 ng of U in solution is required for analysis by MC-ICP-MS and ca. 300 ng of U are typically dissolved for most samples (considering an average U concentration of 3 ppm). Despite incomplete column yields, there is still ca. 100 ng of U for analysis. Furthermore, standard data show that chromatography procedures are not inducing fractionation between ^{234}U and ^{238}U (Table 6.4). In contrast,

89% of Th was found in the relevant fraction and a good separation was achieved. The separation of Nd is discussed later in Section 6.3.1.

Table 6.5 Percentage of U, Th, and Nd eluted in each fraction

Fraction	Reagent	Volume (mL)	U (%)	Th (%)	Nd (%)	Target elements
A	Sample loading	<4.0	11	4.8	5.1	-
B	1. 5M HNO ₃	4.0	18	4.0	4.2	-
C	1.5 M HNO ₃	4.5	0.14	0.09	5.7	-
D	3 M HCl	4.5	7.2	1.6	16	Nd and other rare earth elements
E	0.2 M HCl	8.0	29	89	69	Th
F	0.1 M HCl/0.3 M HF	<4.0	35	0.94	0.10	U

6.3 Field work

Field work was undertaken in August 2012 to collect bedrock and fluvial sediment from a range of catchments in the northeastern and southeastern sections of the Gulf of Carpentaria drainage basin. Samples are listed in chronological order of collection and all samples have the prefix GOC-R-# e.g. GOC-R-01 for fluvial sediment and GOC-B-# for bedrock samples.

6.3.1 Fluvial sediment

Fluvial sediment in Chapter 3 were collected in previous field trips by Allan R. Chivas and August 2012 by Ashley Martin, Anthony Dosseto, and Allan R. Chivas. Samples names and collection dates are given in Table 6.6. Sampling notes, GPS locations, photos of sampling locations, and specific sample dates are given in the following sections.

Table 6.6 Fluvial sediment samples collected

Field trip campaign	Sample#	Paper#
August 2012	GOC R-1	3
	GOC R-4	4
	GOC-R-7	11
	GOC R-20	12
	GOC R-19	15
	GOC R-15W	17
	GOC R-16	18
	GOC R-17	19
	GOC R-3	20
	GOC-D-1	21
	GOC-15E	22
May 2004	GOC 56	1
	GOC 3-2	2
	GOC 9-2	5
	GOC 50	6
	GR09	7
	GOC 10-2	8
	GOC 60-1	9
	GOC-59	10
	GOC-43	13
	GOC-12-2	14
	GOC-13-2	16

6.3.1.1 Lake Mitchell (R-01)

- Fluvial sediment collected from Big Mitchell Creek at the bridge crossing the road heading from Mareeba.
- GPS: 16°48'14.14"S 145°21'53.69"E
- Collected 21/8/12

- Upstream creek in Mitchell River catchment
- Catchment dammed upstream (Lake Mitchell) and has extensive wetlands surrounding the lake
- Big Mitchell Creek is a low gradient sandy creek ca. 4 m wide and dry. It widens at the bridge then narrows. Samples of sand and mud from the bridge taken



Figure 6.2 Upstream (A) and downstream (B) views from sample point for R-01

6.3.1.2 McLeod River (R-02)

- Two aliquots of fluvial sediment collected A: Wet and B: Dry
- Cobbles composed of greywacke and weathered granite also collected
- GPS: 16°29'59.49"S 145°0'3.84"E
- Collected 21/8/12
- A: Flowing river ca. 10 m wide and 0.2 – 1 m deep with 1 -2 m high banks.
- Sediment mainly coarse sand.
- Cobbles comprised of quartzite, granite and sedimentary sandstone/greywacke
- Collected 21/8/12



Figure 6.3 Downstream (A) upstream (B) views of McLeod River for wet sample R-02. Downstream (C) and upstream (D)

6.3.1.3 Mitchell River downstream (R-03)

- Fluvial sediment collected from dry river bed.
- GPS: 16°33'39.64"S 144°53'17.92"E
- Collected 21/8/12
- Dry, and wide channel (ca. 50 m), with low banks (ca. 2-3 m).
- Abundance of pebbles but the majority of these are SiO₂ rich and possibly silicified.
- Collected 21/8/12

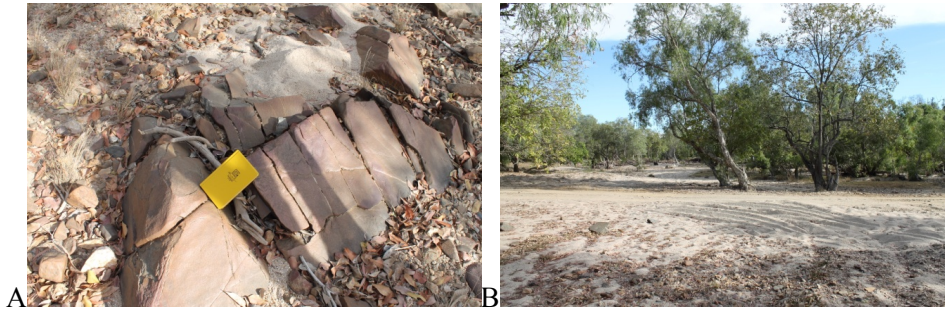


Figure 6.4

6.3.1.4 Palmer River (R-04)

- Fluvial sediment collected from dry channel bed.
- Mud sample also taken (R-04-mud)
- Cobbles (A, B)
- GPS: 16° 6'34.44"S 144°46'37.53"E
- Collected 22/8/12
- Dry, and wide channel (ca. 50 m), with low banks ca. 2-3 m.
- Extensively vegetated channel island
- Sediment mainly coarse sand
- Bedrock outcrops of greywacke
- 1 cm pebbles comprised of quartzite, greywacke and various metamorphic



Figure 6.5 Downstream (A) and upstream (B) views for the Palmer River (R-04)

6.3.1.5 Walsh River (R-05)

- River sediment
- Cobbles: Sandstone, greywacke, weathered granite
- GPS: 17° 7'14.78"S 145°16'14.20"E
- Collected 22/8/12
- Outcrops of Devonian/carboniferous greywacke from Hodgkinson formation
- 10 m high banks,
- Western channel still flowing with water depth of about 1 m.
- Channel gradient gradually increases eastward with sand/silt and then cobbles.

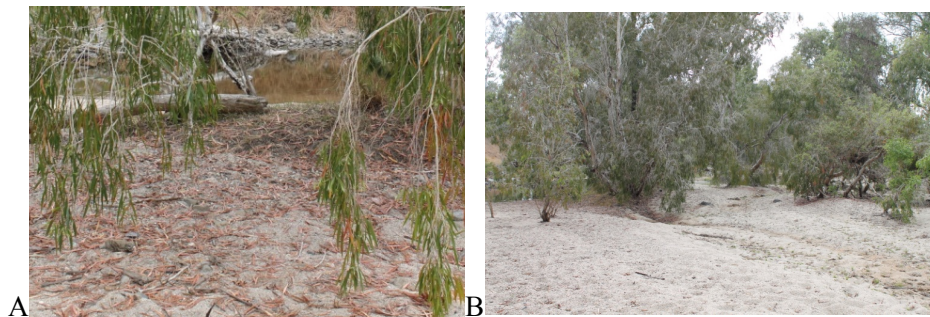


Figure 6.6

6.3.1.6 Lynd River (R-06)

- River sediment
- GPS: 17°49'56.69"S 144°26'45.39"E
- Collected 22/8/12
- Narrow river ca. 30 m

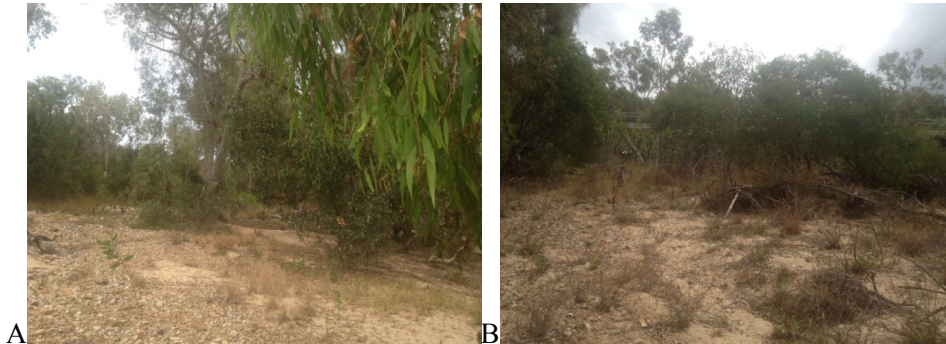


Figure 6.7 Downstream and B: Upstream

6.3.1.7 Einasleigh (R-07)

- River sediment
- River mud
- GPS: 18°11'7.83"S 144° 0'33.75"E
- Collected 23/8/12
- Will be hard to integrate samples due to size of the river

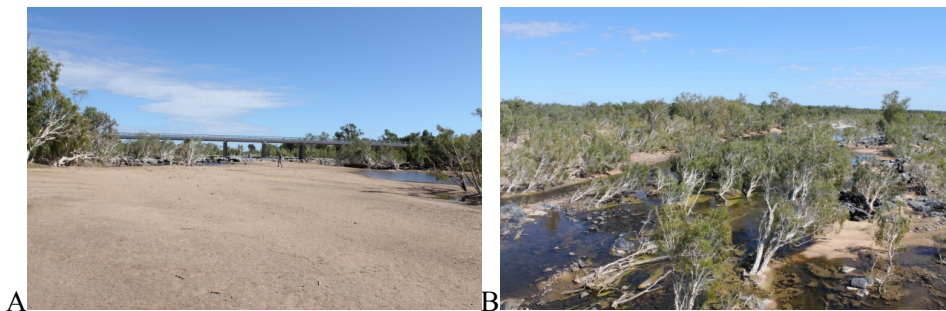


Figure 6.8 A: Upstream B: Downstream

6.3.1.8 Gilbert River (R-08)

- River sediment

- GPS: 18°11'57.31"S 142°52'33.59"E
- Collected 23/8/12
- Sand/silt river, no large cobbles, only pebbles
- Sampled eastern bank as still water flowing on the western side



Figure 6.9 Upstream (A) and downstream (B) views of sample location for GOC-R-8.

6.3.1.9 Gilbert River II at Strathmore HS (R-09)

- GPS: 17°51'41.77"S 142°32'41.36"E
- Collected 23/8/12
- Mud sample from water's edge
- Overbank deposit from eastern bank
- 200 m wide river gradually inclined from west to east and the water flows in the west, then sandy river bed to coarser river bed with cobbles



Figure 6.10 Upstream (A) and downstream (B) views of sample location for GOC-R-9.

6.3.1.10 *Dust sample (D-01)*

- GPS: Croydon to Strathmore HS
- Collected 23/8/12
- Road dust collected from 4WD

6.3.1.11 *Gilbert River III (R-10)*

- GPS: 17°10'11.18"S 141°45'53.26"E
- Mud and sediment
- Collected 26/8/12



Figure 6.11

6.3.1.12 *Maxwell creek (R-11)*

- GPS: 17°13'13.83"S 141°53'22.79"E
- Collected 26/8/12
- River sediment and mud/silt collected
- Sampled sand from bar and mud from pond



Figure 6.12 Upstream (A) and downstream (B) views of sample location for GOC-R-11.

6.3.1.13 *Fitzmaurice Creek (R-12)*

- GPS: 17°17'52.84"S 141°10'44.87"E
- Collected 26/8/12
- Meandering channel sampled from the Gilbert River fluvial megafan
- Channel depth of 1.3 m, banks of 2m and a width of 3 m
- OSL dates from Nanson 2005 (REF) indicate deposits are Holocene in age



Figure 6.13 Upstream (A) and downstream (B) views of sample location for GOC-R-16.

6.3.1.14 *Maxwell creek (R-13)*

- River sediment and mud/silt collected
- GPS: 17°28'17.64"S 141°10'46.97"E
- Collected 26/8/12
- Sampled sandbars from the flowing channel and coarser, dry channel to the south



Figure 6.14 Upstream (A) and downstream (B) views of sample location for GOC-R-13.

6.3.1.15 *Flinders River (R-14)*

- GPS: 18° 9'43.29"S 140°51'20.90"E
- River sediment and mud/silt collected
- Collected 26/8/12
- Sediment mostly comprised sand, with no cobbles
- Silt collected from top of rocks and mud collected from ponds
- Abundant bedrock outcrops



Figure 6.15 Sediment sampled from silt dried on the top of boulders.

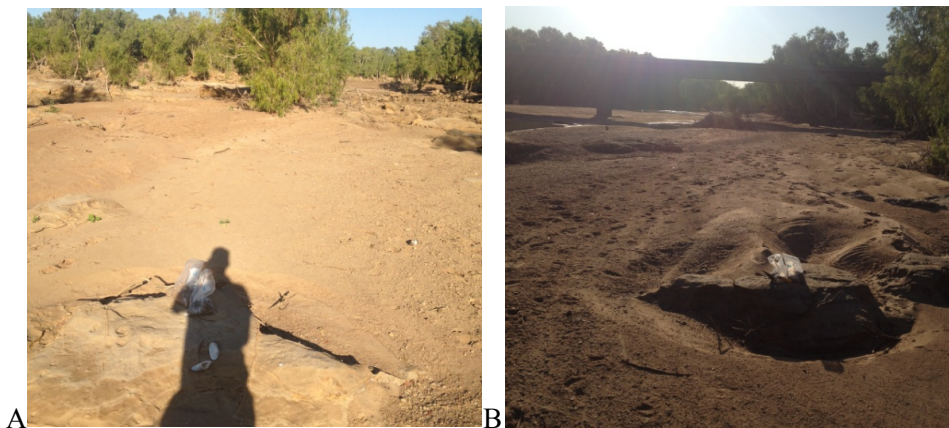


Figure 6.16 Upstream (A) and downstream (B) views of sample location for GOC-R-14.

6.3.1.16 *Leichardt River (R-15E and R-15W)*

- GPS: 19°33'53.97"S 140° 4'9.11"E
- Sampled river sediment and mud
- Collected 26/8/12
- Extensive vegetated section ca. 40 m between still-flowing water in west and dry section in east

- Sediment collected from both sides of the channel
- Muddy sediment sampled from what appears to be a hillslope gully



Figure 6.17 Upstream (A) and downstream (B) views of sample location for GOC-R-16W. C) Sample point for muddy “gully deposits” for “GOC-R-15E; and d) Side-view of “gully”.

6.3.1.17 *Upper Leichardt (R-16)*

- GPS: 20°46'37.86"S 139°29'41.50"E
- Sampled mud/silt downstream of bridge and cobbles also collected
- Collected 26/8/12
- Wide channel (83 m)
- Coarse-grained and pebbly sediment
- River anabranches 200 m upstream

- Abundant 4WD tracks in the channel which were not sampled



Figure 6.18 Upstream (A) and downstream (B) views of sample location for GOC-R-16.

6.3.1.18 *Eastern Leichardt (R-17)*

- GPS: 20°43'8.41"S 139°47'12.84"E
- Sand and mud sampled
- Collected 26/8/12
- Relatively-narrow channel (30 – 50 m)
- Abundant outcrops of metamorphic and granitic rock



Figure 6.19 A) Upstream view of sample location for GOC-R-17; B) Filled sample bag and typical example of sampled sediment for GOC-R-17.

6.3.1.19 *McKinley River (R-18)*

- GPS: 21°15'57.01"S 141°16'53.69"E
- Sampled river mud and sediment
- Collected 26/8/12
- Narrow channel (<30 m)
- Over-bank deposits present
- No cobbles, and sediment mainly comprised sand and silt

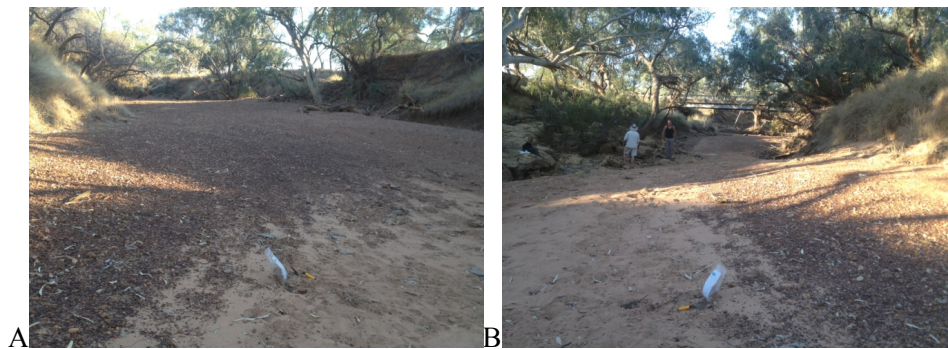


Figure 6.20 Upstream (A) and downstream (B) views of sample location for GOC-R-18.

6.3.1.20 *Flinders River (R-19)*

- GPS: 20°44'31.25"S 143° 9'40.02"E
- Sampled sediment from silt-crusts on the fluvial sand and mud from the water's edge of isolated pools
- Collected 30/08/12
- Main active channel still flowing with a depth of ca. 0.5 m
- Very silt/sandy and no cobbles
- Cross bedding present on banks



Figure 6.21A) Upstream view of sample location for GOC-R-19; B) Filled sample bag and typical example of sampled sediment for GOC-R-19.

6.3.1.21 *Upper Einasleigh River (R-20)*

- GPS: 19°12'23.01"S 144°22'4.25"E
- River sediment and mud from boulders from sand bars and silt dried on boulders
- Collected 31/08/12
- Channel ca. 50 – 75 m wide with a large number of basaltic boulders and outcrops.
- Sampled



Figure 6.22A) Upstream view of sample location for GOC-R-20; B) Filled sample bag and typical example of sampled sediment for GOC-R-20

6.3.2 Bedrock samples

A large number of bedrock samples (30) were collected during the field trip and only the bedrock samples analysed in Chapter 3 are described here. Different sample numbers were used in Chapter 3 in order to for them to be presented neatly; fieldwork sample numbers that correlate to numbers in Chapter 3 are given in Table x. Lithology of rocks was confirmed using a surface geology map (REF).

Table 6.7 Fieldwork numbers are corresponding sample numbers used in Chapter 3.

Fieldwork#	Manuscript#
1	1
2	2
5	3
6	4
10	5
14	6
14 (replicate)	7
20	8
22	9

6.3.2.1 Lake Mitchell Outcrop (B-1)

- GPS: 16°47'56.28"S 145°21'44.24"E
- Road cut with rocks dumped on top of the cut. Predominantly weathered sedimentary rock, likely to be greywacke from the Hodgekinson formation. Quartzite also seen.
- Sampled boulder from cut



Figure 6.23 A) Sampling point of GOC-B-1 from boulder shown by yellow notebook; B) Side-view of sample location for GOC-B-1

6.3.2.2 *Mount Molloy (B-2)*

- GPS: 16°39'38.87"S 145°18'45.88"E
- Granitic rocks taken from road cut.
- Grey porphyritic granite.
- Sampled boulder that apparently had been created during the road cut



Figure 6.24 Sampling point of GOC-B-2 from boulder shown by yellow notebook; B) Side-view of sample location for GOC-B-2

6.3.2.3 Road cut (B-5)

- GPS: 17°21'35.52"S 144°44'0.99"E
- Bedrock sampled from road cut
- Pink granite
- Granitic, aplitic dykes and intrusions present

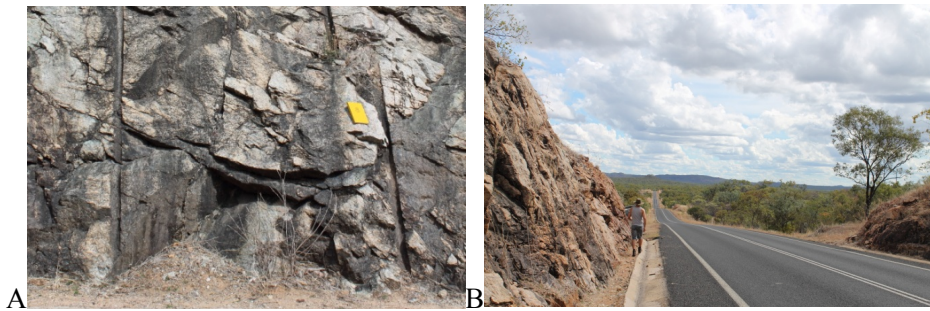


Figure 6.25 Sampling point of GOC-B-5 from road cut shown by yellow notebook; B) Side-view of sample location for GOC-B-5

6.3.2.4 Outcrop (B-06)

- GPS: 17°44'12.52"S 144°32'0.51"E
- Bedrock sampled from natural outcrop
- Pink/lucrocratic rhyolite
- Rock extremely weathered with pink banding (due to k-feldspar) and phenocrysts of quartz



Figure 6.26 Sampling point of GOC-B-6 from outcrop shown by yellow notebook.

6.3.2.5 Road cut (B-10)

- GPS: 18°15'9.63"S 143°51'22.14"E
- Bedrock sampled from old road cut
- Extensively-weathered granite

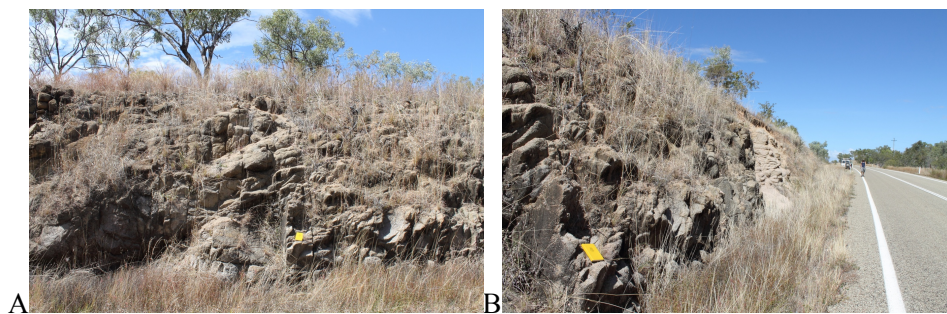


Figure 6.27 Sampling point of GOC-B-10 from road cut shown by yellow notebook; B) Side-view of sample location for GOC-B-10

6.3.2.6 Channel outcrop (B-14)

- GPS: 18° 9'42.99"S 140°51'23.72"E
- Natural outcrop in the Flinders River (see GOC-R-14 for pictures of sample site)
- Cretaceous sandstone
- Very weathered and friable rock

6.3.2.7 Road cut (B-20)

- GPS: 20°46'26.41"S 139°58'51.47"E
- Road cut outcrop
- Dolerite with quartz veins



Figure 6.28 Sampled rock for GOC-B-1; B) Side-view of sample location for GOC-B-01, as shown by the hammer.

6.3.2.8 Road cut (B-22)

- GPS: 20°41'51.85"S 139°35'35.76"E
- Bedrock sampled from road cut
- Meta-basalt with abundant veins of calcite, quartz-epidote and chlorite

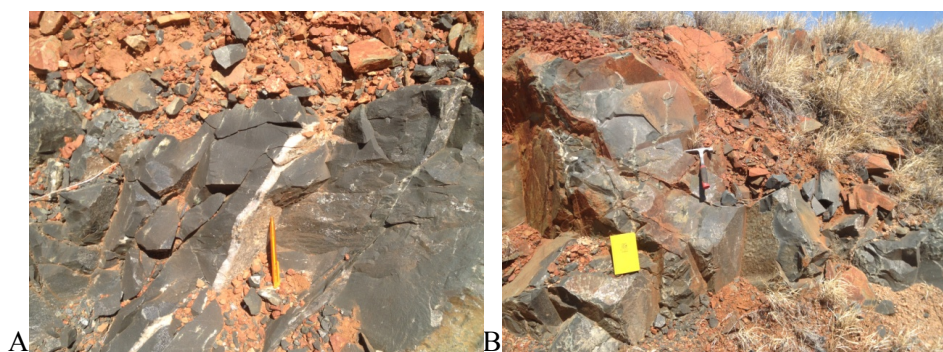


Figure 6.29 Sampling point of GOC-B-22 from road cut shown by yellow notebook; B) Side-view of sample location for GOC-B-22 shown by hammer.

6.4 Unreported experiments

6.4.1 Neodymium chromatography experiments

Sample pre-treatment for the comminution dating technique aims to isolate fine-grained detrital minerals by removing non-detrital matter (DePaolo et al., 2006). The neodymium (Nd) isotope composition of these phases can also provide valuable information about Earth-surface processes. Palaeoceanographic information is derived from the non-detrital fraction or authigenic component of marine sediments as the Nd isotope composition in the oceans is variable, and each water mass has its own Nd isotope signature (Piepgras and Wasserburg, 1980). The detrital fraction is derived from continental rocks and the Nd isotope composition is related to sediment provenance and sediment transport (Grousset et al., 1988). Therefore, Nd measurements could be combined with comminution dating by saving the REE fraction in column chromatography Table 6.2.

Column chromatography for Nd first requires the separation of rare earth elements and an additional column is required to separate light and heavy rare earth elements (Yang et al., 2010). Here the separation of rare earth elements by the procedure outlined in Table 6.2 was tested by analysing Nd concentrations. Three aliquots of rock standard BCR-2 were dissolved, and column fractions were collected throughout the chromatography procedure.

The separation of Nd was poor as only 16 % of Nd was found in the relevant fraction, and 69 % of Nd was found in the Th fraction (Table 6.5). If the same digest sample aliquot is to

be used for comminution dating and Nd measurements, further work is required to calibrate the columns for Nd separation. From this preliminary study as 5 – 11 % of each element are lost during sample loading. Therefore it appears that the column resin is saturated and either i) more resin should be used, or ii) less sample should be loaded. As the majority of Nd was found in the Th fraction, the volume and/or strength of the Nd reagent should be increased.

6.4.2 Sequential extraction experiments

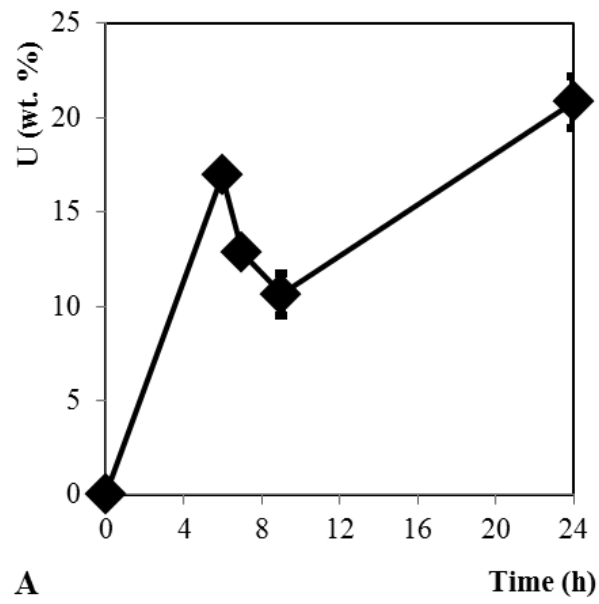
It is possible that sequential extraction procedures do not fully remove the non-detrital matter. The reaction times of the procedure suggested by Tessier et al. (1979) were varied in order to test the completeness of the extraction of U.

Removal of the acid-soluble fraction using a buffer solution of NaOAc/ AcOH extracted 16.9 ± 1.1 wt. % of U after the recommended 6 h, and increased to 20.8 ± 1.4 % of U after 24 h (Figure 6.30A). This is attributed to the possible extraction of the reducible and oxidisable fraction, which are thought to consist of metal oxides and organic matter respectively and are also likely acid-soluble.

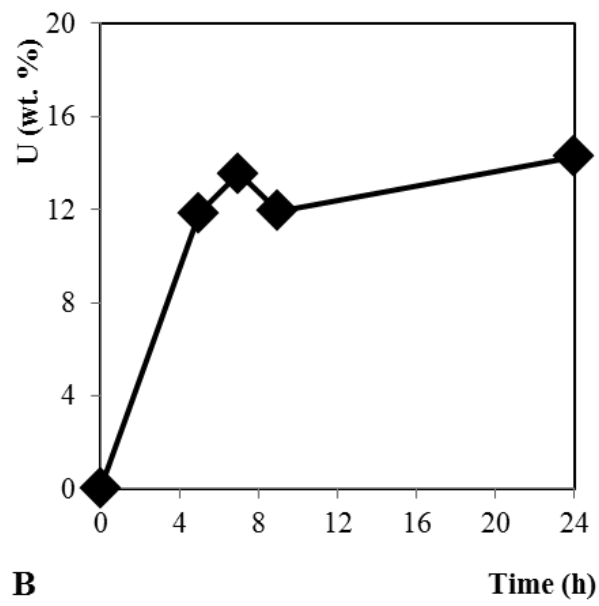
Removal of the reducible fraction using $\text{NH}_2\text{OH} \cdot \text{HCl}$ / AcOH extracted 11.9 ± 0.0 wt. % of U after the recommended 5 h, and increased to 14.3 ± 0.2 wt. % of U after 24 h (Figure 6.30B). As this reagent is acidic, it is possible that the increased extraction of U is due to the dissolution of organic matter.

Removal of the oxidisable fraction using $\text{H}_2\text{O}_2/\text{HNO}_3$ extracted 2.8 ± 0.1 % of U after 1.5 h, and remained constant after 3 h (Figure 6.30C). The second step in the removal of the oxidisable fraction, also using $\text{H}_2\text{O}_2/\text{HNO}_3$, extracted 3.9 ± 0.0 wt % of U after the recommended 3 h, which initially increased to 4.3 ± 0.0 wt. % of U after 4 h and then decreased to 0.9 ± 0.0 wt. % of U after 6 h (Figure 6.30D). This is attributed to the readsorption of U, despite using sodium citrate as a complexing agent.

In summary, longer reaction times for the acid-soluble and reducible fractions increased the extraction of U. However, both chemical reagents used in these extractions are acidic and it is not clear whether the reactions were incomplete, or U was being removed from other phases, which are also acid-soluble. Longer reaction times for removal of the oxidisable fraction did not increase the amount of U extracted, and reaction times appear sufficient.



A



B

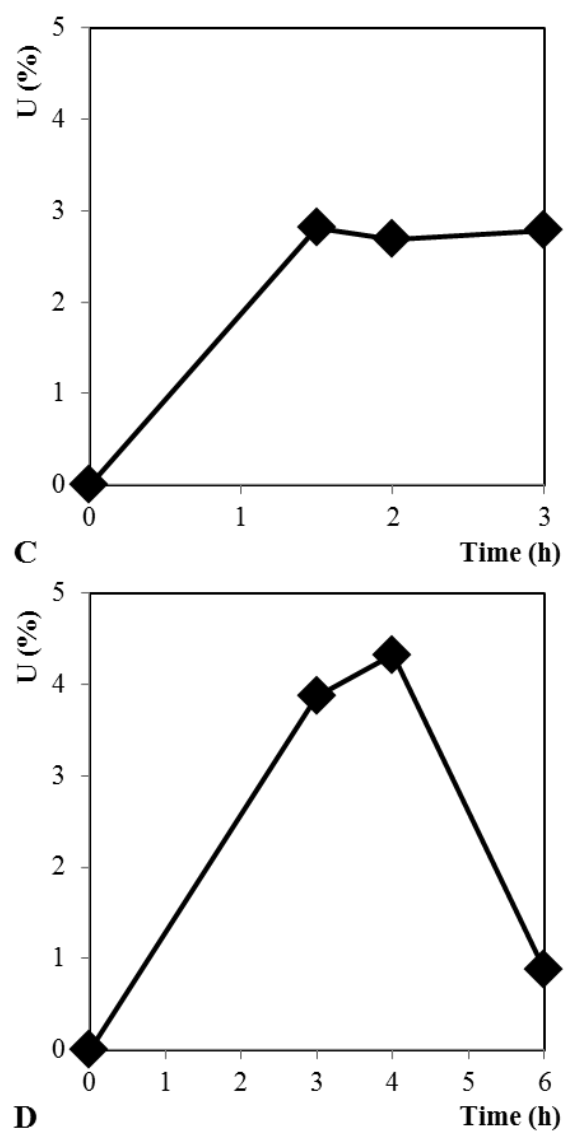


Figure 6.30 Percentage of U extracted into solution as a function of reaction time using the following reagents: A) NaOAc at 6, 8, 10 and 24 h; B) $\text{NH}_2\text{OH}.\text{HCl}$ at 5, 8, 10 and 24 h; C) $\text{H}_2\text{O}_2/\text{HNO}_3$ at 1, 2 and 3 h; D) $\text{H}_2\text{O}_2/\text{HNO}_3$ at 3, 4 and 5 h. The error bars represent 1σ standard deviation and where not shown, are hidden by the markers.

6.5 Uranium measurements summary

A summary of all ($^{234}\text{U}/^{238}\text{U}$) activity ratios and U concentrations for all samples from Chapters 2, 3, and 4 are given in Table 6.8, Table 6.9, and Table 6.10.

Table 6.8 ($^{234}\text{U}/^{238}\text{U}$) activity ratios and U concentrations for all samples from Chapter 2

Experiment	Experiment summary	Fractions removed	($^{234}\text{U}/^{238}\text{U}$) ^a	U (ppm)	Error (ppm) ^a
Untreated	Aliquot A	None	0.993 ± 0.002	3.20	0.01
	Aliquot B		1.080 ± 0.001	2.60	0.01
	Aliquot C		0.996 ± 0.002	2.44	0.01
1	Sequential extraction procedure from Lee (2009)	F1	0.990 ± 0.003	3.25	0.01
		F1, F2	0.996 ± 0.003	3.30	0.01
		F1, F2, F3	0.961 ± 0.003	2.35	0.01
		F1, F2, F3 and F4	0.939 ± 0.003	2.55	0.01
		F1, F2, F3 and F4	0.935 ± 0.003	2.69	0.01
2	Sequential extraction procedure from Lee (2009) + sodium citrate	F1	1.007 ± 0.003	3.13	0.01
		F1, F2	0.971 ± 0.003	2.38	0.01
		F1, F2, F3	0.963 ± 0.003	2.45	0.01
		F1, F2, F3 and F4	0.938 ± 0.005	2.46	0.00
		F1, F2, F3 and F4	0.931 ± 0.003	2.83	0.03
3 (1 h)	Mild HCl/HF etching following sequential extraction	F1, F2, F3, F4 and F5	0.930 ± 0.007	2.34	0.02
3 (2 h)			0.923 ± 0.003	2.54	0.01
3 (4 h)			0.917 ± 0.003	2.75	0.01
3 (8 h)			0.919 ± 0.003	2.94	0.01
3 (24 h)			0.923 ± 0.004	2.31	0.01
4	Sequential extraction procedure from Schultz et al. (1998)	F1, F2, F3 and F4	0.927 ± 0.003	2.38	0.01
5	Ashing and MgNO ₃ rinse	F4	0.974 ± 0.002	2.19	0.00
6	0.5 M HCl leaching	F2	0.969 ± 0.002	2.44	0.02
7	Additional leaching experiments following sequential extraction	F1	0.936 ± 0.002	2.58	0.01
		F1 and F3	0.933 ± 0.002	2.42	0.01
		F1, F3 and F2	0.933 ± 0.002	2.53	0.00

^a2σ standard error

Table 6.9 ($^{234}\text{U}/^{238}\text{U}$) activity ratios and U concentrations for all samples from Chapter 3

Sample	Catchment	($^{234}\text{U}/^{238}\text{U}$) ^a	U (ppm)	Error (ppm) ^a
B-1	Mitchell River	0.843 ± 0.003	2.92	0.01
B-2	Mitchell River	0.850 ± 0.002	1.61	0.01
B-3	Mitchell River	0.979 ± 0.004	2.60	0.00
B-4	Mitchell River	0.795 ± 0.001	5.27	0.01
B-5	Gilbert River	1.011 ± 0.002	0.64	0.02
B-6 ^a	Flinders River	1.007 ± 0.003	0.65	0.00
B-7	Flinders River	0.963 ± 0.002	3.20	0.00
B-8	Leichhardt River	1.004 ± 0.002	2.00	0.01
R-1	Archer	1.045 ± 0.003	6.08	0.31
R-2	Archer	1.018 ± 0.002	16.20	0.29
R-3	Mitchell	0.908 ± 0.001	3.25	0.79
R-4	Mitchell	0.915 ± 0.002	3.84	0.02
R-5	Mitchell	0.903 ± 0.002	3.03	0.03
R-6	Mitchell	0.861 ± 0.002	3.05	0.12
R-7	Gilbert	0.961 ± 0.004	3.64	0.00
R-8	Gilbert	0.949 ± 0.002	1.76	0.11
R-9	Gilbert	0.967 ± 0.004	2.44	0.22
R-10	Gilbert	0.817 ± 0.002	4.88	0.02
R-11	Gilbert	0.856 ± 0.007	5.99	0.01
R-12	Gilbert	0.945 ± 0.002	3.17	0.03
R-13	Staaten	1.000 ± 0.003	3.69	0.01
R-14	Flinders	0.957 ± 0.002	1.79	0.01
R-15	Norman	0.922 ± 0.002	1.88	0.01
R-16	Leichhardt	0.921 ± 0.002	0.30	0.01
R-17	Leichhardt	0.943 ± 0.007	2.82	0.01
R-18	Leichhardt	0.931 ± 0.002	3.04	0.01

^a2σ standard error

Table 6.10 ($^{234}\text{U}/^{238}\text{U}$) activity ratios and U concentrations for all samples from Chapter 4

Core	Sedimentary	($^{234}\text{U}/^{238}\text{U}$) ^a	U (ppm)	Error (ppm) ^a
MD32	1	0.952 ± 0.002	15.85	0.05
	2a	0.944 ± 0.003	1.44	0.01
	2b	0.936 ± 0.003	1.37	0.00
	2c	0.988 ± 0.002	14.56	0.04
	3a	0.962 ± 0.003	1.72	0.01
	3b	0.988 ± 0.002	1.76	0.00
	4a	0.955 ± 0.002	1.87	0.01
	4c	0.911 ± 0.003	1.91	0.01
	4d	0.998 ± 0.003	1.89	0.01
	5	0.973 ± 0.002	2.00	0.01
	6b	0.990 ± 0.002	1.91	0.00
	6d	0.904 ± 0.003	1.69	0.01
	7	1.110 ± 0.003	1.63	0.00
MD33	1	0.913 ± 0.003	9.32	0.02
	2b	0.871 ± 0.004	4.45	0.01
	2b	0.891 ± 0.003	4.63	0.01
	2c	0.944 ± 0.002	13.63	0.02
	3a	0.880 ± 0.002	5.25	0.01
	3b	0.830 ± 0.001	11.05	0.01

^a2σ standard error

References

Albarède, F., Beard, B., 2004. Analytical methods for non-traditional isotopes. *Reviews in Mineralogy and geochemistry* 55, 113-152.

AT, 2005. *Inductively Coupled Plasma Mass Spectrometry: A Primer*. Agilent Technologies.

Avnir, D., Jaroniec, M., 1989. An isotherm equation for adsorption on fractal surfaces of heterogeneous porous materials. *Langmuir* 5, 1431-1433.

Brunauer, S., Emmett, P.H., Teller, E., 1938. Adsorption of gases in multimolecular layers. *Journal of the American Chemical Society* 60, 309-319.

DePaolo, D.J., Maher, K., Christensen, J.N., McManus, J., 2006. Sediment transport time measured with U-series isotopes: Results from ODP North Atlantic drift site 984. *Earth and Planetary Science Letters* 248, 394-410.

Dubinin, M.M., Gregg, S., Sing, K., Stoeckli, H., 1979. *Characterization of porous solids*. Society of Chemical Industry, London, 1.

Grousset, F., Biscaye, P., Zindler, A., Prospero, J., Chester, R., 1988. Neodymium isotopes as tracers in marine sediments and aerosols: North Atlantic. *Earth and Planetary Science Letters* 87, 367-378.

Hekim, Y., Fogler, H.S., 1977. Acidization—VI: on the equilibrium relationships and stoichiometry of reactions in mud acid. *Chemical Engineering Science* 32, 1-9.

Horwitz, E.P., Chiarizia, R., Dietz, M.L., Diamond, H., Nelson, D.M., 1993. Separation and preconcentration of actinides from acidic media by extraction chromatography. *Analytica Chimica Acta* 281, 361-372.

Jaroniec, M., 1995. Evaluation of the fractal dimension from a single adsorption isotherm. *Langmuir* 11, 2316-2317.

Kline, W.E., Fogler, H.S., 1981. Dissolution of silicate minerals by hydrofluoric acid. *Industrial and Engineering Chemistry Fundamentals* 20, 155-161.

Lee, V.E., 2009. Radiogenic Isotope Geochemistry and the Evolution of the Earth's Surface and Interior. PhD Thesis at the University of California, Berkeley.

Luo, X., Rehkämper, M., Lee, D.-C., Halliday, A.N., 1997. High precision $^{230}\text{Th}/^{232}\text{Th}$ and $^{234}\text{U}/^{238}\text{U}$ measurements using energy filtered ICP magnetic sector multiple collector mass spectrometry. *International Journal of Mass Spectrometry and Ion Processes* 171, 105-117.

Neimark, A., 1992. A new approach to the determination of the surface fractal dimension of porous solids. *Physica A: Statistical Mechanics and its Applications* 191, 258-262.

Piegras, D.J., Wasserburg, G., 1980. Neodymium isotopic variations in seawater. *Earth and Planetary Science Letters* 50, 128-138.

Rosholt, J.N. (1983) Isotopic composition of uranium and thorium in crystalline rocks. *Journal of Geophysical Research* 88, 7315-7330.

Sing, K.S., 1985. Reporting physisorption data for gas/solid systems with special reference to the determination of surface area and porosity (Recommendations 1984). *Pure and applied chemistry* 57, 603-619.

Steele, W.A., 1974. The interaction of gases with solid surfaces.

Tessier, A., Campbell, P.G.C., Bisson, M., 1979. Sequential extraction procedure for the speciation of particulate trace metals. *Analytical Chemistry* 51, 844-851.

Wilson, S.A., 1997. The collection, preparation and testing of USGS reference material BCR-2. U.S. Geological Survey Open-File Report 98.

Yang, Y.-h., Zhang, H.-f., Chu, Z.-y., Xie, L.-w., Wu, F.-y., 2010. Combined chemical separation of Lu, Hf, Rb, Sr, Sm and Nd from a single rock digest and precise and accurate

isotope determinations of Lu–Hf, Rb–Sr and Sm–Nd isotope systems using Multi-Collector ICP-MS and TIMS. *International Journal of Mass Spectrometry* 290, 120-126.

7. Appendix B

Article below removed for copyright reasons, please refer to the citation.
This section contains the published manuscript of Chapter 2:

Martin, A.N., Dosseto, A., Kinsley, L.P.J., 2015. Evaluating the removal of non-detrital matter from soils and sediment using uranium isotopes. *Chemical Geology* 396, 124-133.